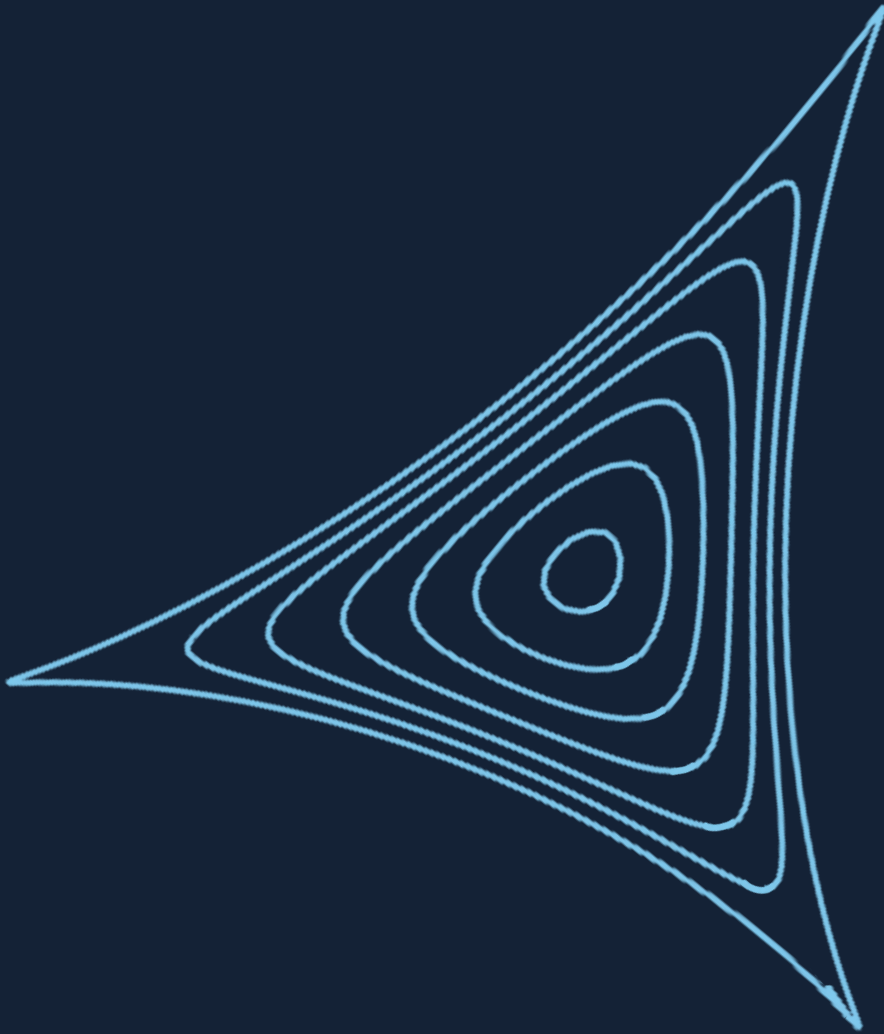


A PhD Thesis

Slow Extraction:

Upgrades for Next Ion Medical Machines at FLASH timescales



Rebecca Louise TAYLOR

Imperial College London
Physics Department

Supervised by:

J. Pasternak, K. Long - Imperial

E. Benedetto, M. Vretenar - CERN

Slow Extraction:

Upgrades for Next Ion Medical Machines
at FLASH timescales

Rebecca Louise TAYLOR

Under supervision of:

J. Pasternak, K. Long - Imperial College London

E. Benedetto, M. Vretenar - CERN

Examined by:

Z. Najmudin - Imperial College London

G. Franchetti - GSI & Goethe University Frankfurt

A thesis presented for the degree of Doctor of Philosophy

**Imperial College
London**

Physics Department

Faculty of Natural Sciences

Imperial College London

London

March 2024

Abstract

Slow resonant extraction is the control of resonant beams to extract a continuous rate of particles from the accelerator, over seconds. This technique is crucial for hadron therapy synchrotrons, where slowly extracted beams are scanned across tumour volumes. Recent radiobiological research demonstrates that ultra-high dose rates (UHDR) reduce tissue toxicities to healthy tissue, but causes damage to tumour tissue – known as the FLASH effect. This effect, and other open questions in ion radiobiology, motivates the next-generation of ion medical machines with flexible extraction methods. This thesis provides key results in areas of slow extraction, to be applied to the Next Ion Medical Machine Study (NIMMS).

It addresses upgrades to existing designs, considering $6\times$ higher emittances and $10\times$ faster timescales. The design for a new Helium Light Ion Compact Synchrotron (HeLICS), is introduced and the extraction is established for two working points. UHDR extraction is performed via quadrupole extraction and radiofrequency knock-out (RF-KO), for 60 s continuous spills, and spills with 10 lots of 3 ms bursts.

To study beams under RF-KO conditions, measurements performed at HIT, which displayed unusual tune responses, were reproduced in simulations. These simulations were expanded to single-particle dynamics to show how the tune coherence was a time-oscillating effect.

Impacts of higher order magnets were quantified at the CERN Proton Synchrotron (PS) with octupole-island trapping. Measurements with sextupole and octupole scans produced good agreement at 2 GeV and identified an offset at 24 GeV. Finely-tuned octupole strengths increase extracted beam density to reduce losses at the extraction septum by 15 % and at the first magnetic septum by 45 %, with increased global losses. Measurements demonstrated parabolic relations of octupole strength vs beam loss.

Finally, this thesis explored future conceptual methods and simulated the first resonant extraction from scaling fixed field accelerators for LhARA.

Statement of Originality: All work performed is the author's own, and anything else is appropriately referenced.

Direct collaborators of particular chapters/sections are written in SMALL CAPS at the beginning of where it pertains to.

Where content has been published in a journal, it follows the relevant copyright licences, and has been properly attributed in SMALL CAPS at the beginning of the section.

Thesis written in \LaTeX . Template and formatting of the \LaTeX document created by the author, but inspired by The Upstanding Citizens's Brigade Comedy Improvisation Manual (M. BESSER ET AL. 2013).

Please email taylor.r@cern.ch to request usage of the \LaTeX template for your own theses - if used or modified, please credit R. TAYLOR.

Images are the author's own, produced via *Inkscape*, *tikz* or *matplotlib*. For any exceptions, explicit permission has been obtained and the author has been clearly accredited in-text and in the figure.

Front cover title page made in *Canva*.

Copyright: 'The copyright of this thesis rests with the author. Unless otherwise indicated, its contents are licensed under a Creative Commons Attribution-Non Commercial 4.0 International Licence (CC BY-NC). Under this licence, you may copy and redistribute the material in any medium or format. You may also create and distribute modified versions of the work. This is on the condition that: you credit the author and do not use it, or any derivative works, for a commercial purpose. When reusing or sharing this work, ensure you make the licence terms clear to others by naming the licence and linking to the licence text. Where a work has been adapted, you should indicate that the work has been changed and describe those changes. Please seek permission from the copyright holder for uses of this work that are not included in this licence or permitted under UK Copyright Law.'

Acknowledgements:

There is a wide circle of people who have made this thesis worth writing. Let me first start by thanking Elena, and Maurizio, for having me on this project and supporting me for many years. Also the NIMMS team for our Tuesday lunchtimes that I always look forward to and Mariusz, for many of the initial ideas that this thesis rests on. And a special comment to Kristaps for our never-ending brainstorming. I am grateful to the wider slow extraction community - many of us did not meet until the final workshop, but our zoom correspondences and code sharing made me feel much more connected throughout the first few covid years. In particular Florian, Jiangyang, Elisabeth and also Cristopher - for our river-side accelerator chats.

I would like to give thanks to the PS Operators from 2021-2023. All who I worked with were enthusiastic to help, provided great entertainment during long night shifts, and were surprisingly relaxed about each new magnet that I tripped.

Appreciation goes to ABP and INC for adopting me into their group and building. For sure I could not do any of this without Aris, Heli, Carlo and Dora for catching up every day for tea and trauma-dumps.

My heartfelt thanks to all the LINACtors - our weekly workshops never failed to energize me. 2 years ago I would not have believed how big our little group has grown, and how much enthusiasm all of you bring to the community. In particular to the inhabitants of 8/1-006, Szymon & Fredrik for putting up with my barrage of questions every hour of every day - you both help me look forward to coming into work each day. Special shout out to Szymon for your invaluable XSuite magic and rocket-speed bug fixing.

Once more heads up to 5BB - yet another thesis down alongside the lot of you.

Finally, for everything else, I thank James. Every day you helped me fight all my doubts and insecurities, by reading every page, reviewing every presentation, colour-blind checking every plot. Now that this is published, I hope we can continue our dumb adventures stress-free.

*To Harry Derek Taylor. I wish you were still around to read this.
And in memory of Joe Robinson. I can only hope to cause chaos and
communicate science as flawlessly as you did.*

Contents

1	Hadron Therapy	22
1.1	Radiobiological Motivation: A Physicist's Approach	23
1.2	Current Status of Hadron Therapy	25
1.2.1	Ion Therapy	26
1.3	Beam Delivery	27
1.3.1	FLASH Therapy	29
1.4	Treatment from NIMMS	32
1.4.1	Open Questions in Hadron Therapy	33
	Bibliography	36
2	Accelerator Theory for Slow Extraction	40
2.1	Linear Beam Dynamics	41
2.1.1	The Beam	41
2.1.2	The Magnets	45
2.1.3	The Accelerator	47
2.2	Non-Linear Beam Dynamics	48
2.2.1	Tune and Resonances	48
2.2.2	Chromaticity	50
2.2.3	Higher order magnets	50
2.2.4	Hamiltonians	52
2.3	Slow Extraction Theory	53
2.3.1	Spiral Step	54
2.3.2	Phase Advances	55
2.3.3	Excitation Methods	56
2.3.4	Spill	57

2.3.5	Hardt Condition	58
2.4	Conclusion	59
2.4.1	Exceptions	59
2.4.2	Theory Discussion	60
	Bibliography	60
3	Review and Current Status of Slow Extraction	62
3.1	Introduction	63
3.2	Historical	63
3.2.1	With Quadrupole-driven Extraction	64
3.2.2	With Betatron Core	64
3.2.3	With RF-KO	65
3.3	Recent Developments	65
3.3.1	COSE	66
3.3.2	Advanced RF-KO	67
3.3.3	Empty-Bucket Channelling	68
3.3.4	Multi-Energy Extraction	68
3.3.5	Octupole Folding	69
3.3.6	Crystal Channelling	69
3.3.7	FLASH	70
3.4	Slow Extraction R&D at NIMMS	71
	Bibliography	72
4	Simulation Models & Reproducibility	76
4.1	Introduction to Accelerator Simulations	77
4.1.1	MADX & PTC	77
4.1.2	Maptrack	78
4.1.3	Xsuite	79
4.2	PIMMS Benchmarks	80
4.2.1	Tracking	81
4.2.2	Tune and Chromaticity	82
4.2.3	Betatron Core Simulations	83
4.2.4	Comparison with Literature	87

4.3	Simulation Discussion	89
	Bibliography	89
5	Dynamic Tune Analysis	92
5.1	Introduction to Frequency Analysis	93
5.1.1	NAFF	94
5.2	HIT Studies	95
5.2.1	Measurements	95
5.2.2	Whole-Beam Simulations	97
5.2.3	Single-Particle Dynamics	99
5.2.4	HIT Discussion	102
	Bibliography	103
6	Measurements of slow extraction with octupoles	104
6.1	Background	105
6.1.1	Proton Synchrotron	105
6.1.2	Methodology	106
6.2	Octupole Trapping	109
6.2.1	24 GeV: Simulations and Measurements	109
6.2.2	2 GeV: Simulations and Measurements	114
6.3	Beam Extraction Efficiency	116
6.3.1	Simulation indications	117
6.3.2	Measurements 2022	119
6.3.3	Measurements 2023	121
6.4	Chapter Approach & Conclusions	126
	Bibliography	129
7	Extraction from NIMMS Synchrotrons	130
7.1	From PIMMS to NIMMS: Upgrades for UHDRs	131
7.1.1	Betatron Core Extraction	131
7.1.2	Radiofrequency Knock-out Extraction	132
7.1.3	PIMMS to NIMMS Discussion	138
7.2	HeLICS: Helium Light-Ion Compact Synchrotron	139

7.2.1	Baseline Design and Optics	140
7.2.2	Extraction Configuration	141
7.2.3	Continuous UHDR for FLASH	145
7.2.4	Burst UHDR for FLASH	152
7.2.5	HeLICS Discussion	157
	Bibliography	158
8	Future Technologies	160
8.1	Future R&D of NIMMS	161
8.1.1	Superconducting Medical Machine	161
8.1.2	Proton Radiography	162
8.2	Ion Therapy Research Facility	163
8.2.1	Slow Extraction from Fixed Field Accelerators	165
8.2.2	Synchrotron Option	176
	Bibliography	177
9	Conclusions	180
9.1	Discussion	181
9.2	Key Results	184
	Bibliography	187
A	Appendix A: Simulation Models	188
A.1	MADX Momentum	188
A.2	Code Benchmarking	189
B	Appendix B: HeLICS - Extra Content	194
B.1	Initial lattice schematic	194
B.1.1	Analytical Investigation	196
B.2	RF-KO Controller Optimisation	198
B.2.1	Beam Physicist's Guide to Hand-Tuning PIDs	199
C	Appendix C: Proton Synchrotron	202
C.1	PS Methodology	202
C.2	Octupole Trapping Dynamics	205

C.3 Pole-Faced Windings	207
Bibliography	213

List of Figures

1.1 Dose deposition of 4 species of radiation throughout water, modelled in Geant4 (K. PAŁSKIS [6]). Normalised to maximal dose.	23
1.2 Schematic comparing transverse raster scanning (left) and spot scanning (right) with variable intensity (yellow to red)	28
2.1 Schematic of particle momentum vector in (x, z) plane. Defines angle x' as per the transverse & longitudinal canonical momentum (P_x, P_z)	42
2.2 Schematics of the four magnets types used in this thesis and their field lines: dipoles (blue), quadrupoles (yellow), sextupoles (red) and octupoles (orange). . .	45
2.3 Schematics of the two septum types used in this thesis and their field lines. Blue and orange represent opposite polarities, and red circles represents the beam trajectory.	46
2.4 Lattice and optics of PIMMS in horizontal (red) and vertical (blue) [15]	47
2.5 Diagram of resonance lines and their orders in horizontal & vertical tune space for the PIMMS lattice.	49
2.6 Contour plot of the Kobayashi-Hamiltonian equation in horizontal phase-space with (right) and without (left) octupoles	53
2.7 Tune-amplitude diagram of a beam near a driven third-order resonance for betatron core (left) and RF-KO (right) extraction	56
2.8 Contour plot of a grid of tracked particles in δp - A . Colourbar represents the turn where the particle is lost from 0 to 5000, where white is more stable, and green is less stable	59
4.1 The simulation tool used for each project, referenced by section number.	77
4.2 Schematic of the PIMMS synchrotron showing dipoles (cyan), quadrupoles (red), sextupoles (yellow), septa (green) and the betatron core (blue)	80

4.3	Comparison of relative errors ($\frac{\Delta X}{X}$) in tracking of the X-coordinate three codes. Full diagram in Appendix A.	82
4.4	Comparisons of extracted betatron core distribution and spill.	86
4.5	Extracted beam distribution in phase-space using MedAustron betatron core methods for literature comparisons	88
4.6	Extracted beam distribution in phase-space from published MedAustron betatron core simulations to compare with Fig. 4.5	88
5.1	Example of FFT resolution with turn number	93
5.2	Scrolling tune example of NAFF resolution	94
5.3	BTF tune measurements changing with sextupole strengths	96
5.4	Beam isocentre and FFT spectra per excitation frequency	98
5.5	Plot of BTF tune magnitude response and phase varying as a function of tune, chromaticity and emittance.	99
5.6	Histogram of single-particle tune calculated by NAFF compared for two driven excitation frequencies.	100
5.7	Comparison of three-particles tune, position and phase-space.	101
6.1	Schematic of slow extraction from the PS to the East Area. Key components marked including quadrupoles (cyan), sextupoles (yellow), octupoles (orange) and septa (blue).	106
6.2	Simulation of one-turn of the PS during extraction. Colourbar represents tune proximity to resonance (red = 6.333).	110
6.3	BCT signal showing number of particles within the PS ring used to calculate trapping ratio as difference between average initial intensity (white bar) and final intensity (white dot)	111
6.4	Measurement of trapping ratio for each octupole strength as a function of sex- tupole strength (low=blue, high=brown)	112
6.5	Plotting datapoints in octupole-sextupole parameter space with colormap as the trapping ratio (cyan=high final current, black=low final current)	113
6.6	Contour plot showing trapping ratio at 24 GeV for measurement (left) and sim- ulation (right). (Black = stable, cyan = lost). Includes their comparison (middle) at 75% trapping.	113

6.7	Contour plot showing trapping ratio at 2 GeV for measurement (left) and simulation (right). Includes their comparison (middle) at 45% trapping.	115
6.8	Horizontal beam distribution with and without octupole components	118
6.9	East22 Results:BLM23, BLM57 and sum BLMs as a function of ODN strength. Color represents is XSE strength.	120
6.10	East22 XSEC measured intensity as a function of ODN strength. Colourmap shows XSE sextupole strength (red=lower, blue=higher).	121
6.11	Phase-space simulations for changing BSW23 strength	123
6.12	Measured losses at SEH23 and SMH41 septa as a function of BSW23 strength. . .	124
6.13	East23 Results: BLM23, BLM57 and sum BLMs as a function of ODN strength with (solid) and without (dashed) QH.PFW shift. Colormap is XSE strength. . .	125
6.14	Localised and temporal effects of octupoles on ring BLMs	126
6.15	BTV57 signal in X and Y with and without octupoles	127
6.16	Measurement profiles of BTV61D from ODN strength	128
7.1	Betatron core spill histogram and beam intensity as a function of turn number for two initial beam emittances.	132
7.2	Plot of Eq. 7.6 for given variables, and kick given in tracking simulations	134
7.3	RF-KO spill histogram and beam intensity as a function of turn number for three initial beam emittances.	135
7.4	Betatron core (green) and (blue) RF-KO extracted beam distributions in phase-space at the electrostatic septum	136
7.5	Phase-space (left) and tune-amplitude (right) distributions for the beam, showing the extraction of a single particle across 25-turns.	137
7.6	RF-KO FLASH spill histogram and beam intensity as a function of turn number, equivalent to 100 ms.	138
7.7	Schematic of the HeLICS lattice with dipoles (blue), quadrupoles (yellow), sextupoles (red) and labels of the resonant sextupole (SXH) and septa (ESE, MSE). .	139
7.8	Twiss parameters across the HeLICS lattice, showing beta, alpha and dispersion in X and Y planes. Calculated with MADX.	141
7.9	Separatrix and extracted beam distribution the two septa for a -3.5 mrad kick . .	144

7.10	Separatrix trajectory of the X-position throughout HeLICS. Final two turns (red, blue) of the particles before their kick at the ES (green).	145
7.11	Extracted particle trajectory throughout septa (zoom of Fig. 7.10)	145
7.12	Tune-amplitude particle distributions representing tune spread as a function of chromaticity and tune proximity	146
7.13	Strength variation of the resonant sextupole (blue) and quadrupoles (red) for a linear ramp (dots), an inverse Gaussian ramp (solid) and for a burst-like extraction distribution (dashed).	147
7.14	Spill response for linear quadrupole-driven ramp.	148
7.15	Spill response for inverse-Gaussian quadrupole-driven ramp.	149
7.16	Schematic of PID controller for RF-KO exciter	150
7.17	Output from RF-KO controller	151
7.18	RF-KO extracted spill, intensity and RF-KO kick	152
7.19	Spill response for inverse-Gaussian quadrupole-driven burst extraction	153
7.20	Output from RF-KO controller in burst mode	155
7.21	Spill, intensity and RF-KO kick for burst extraction	156
7.22	Dose and std of each burst for quadrupole-driven and RF-KO extraction	157
8.1	Top-down view of the LhARA spiral scaling FFA design in X-Y with parameters of Tab. 8.1 . Red lines show injection (dashed) and extraction (solid) orbit. Pictured is the added resonant sextupole (blue) and electrostatic septum (black).	165
8.2	Range of working points in horizontal-vertical tune space as a function of spiral angle and k-index gradient in zgoubi.	166
8.3	Set values of tune and multipole strength (quadrupole to decupole) for a given value of k-index at the extraction energy in zgoubi	167
8.4	Beta and dispersion across the FFA lattice in MADX for an on-axis beam at $Q_x = 3.3$, $R_0 = 3.47704$	171
8.5	Representation of the separatrices span when measured at one ES vs one ES in each cell in MADX	171
8.6	Percentage of the beam survival transversely. Blue curve only monitors at one ES. Red curve monitors at each cell. Black dashed line represents chosen ES field region.	172

8.7	Extraction with RF-KO in phase space and tune-amplitude in zgoubi.	173
A.1	Difference between δ_p and p_t representation of momentum. Difference in the approximation of $\delta_p = p_t/\beta$	189
A.2	1-Turn grid track comparing XSuite & PTC	191
A.3	1-Turn grid track comparing XSuite & maptrack	192
A.4	1-Turn grid track comparing PTC & maptrack	193
B.1	Separatrix and extracted beam distribution the two septa for $Q_x = 2.6$	194
B.2	Separatrix trajectory of the X-position throughout HeLICS for $Q_x = 2.6$. Final two turns (red, light red) of the particles before their kick at the ES (blue).	195
B.3	Comparison of the initial tune distribution prior to simulation, and the resulting spill after a linear quadrupole-driven ramp.	195
B.4	Analytical expression of horizontal detuning $\alpha_x x$ for three different machine extraction settings as function of horizontal tune tending towards the $1/3$ resonance [39]	197
B.5	Tune calculation of single-particles with a initial X-spread over 1024 turns. Compare for the 2.3 (blue) and 2.6 (green) settings, at natural (solid) and low (dashed) chromaticity.	198
B.6	Working Points and tune distribution for 2.6 (green) and 2.3 (blue) lattices	199
B.7	Output from the RF-KO controller for burst extraction at half-setpoint	201
C.1	Screenshot of the QMeter application showing the measurement of debunched beam	203
C.2	Changing beam energy via radial loop for chromaticity measurements	204
C.3	Screenshot of the QMeter application showing the measurement of non-linear chromaticity for 20 data points per momentum.	204
C.4	BCT trapping ratio as a function of ONO strength at 2 GeV (no XSE).	206
C.5	Two datapoints within the simulated trapping triangle, showing their phase-space distribution for octupole trapping and inverse-trapping.	206
C.6	Contour plot showing trapping ratio at 24 GeV for simulations above resonance ramping down (left) and below resonance ramping up (right).	207

C.7	Sum of ring BLMs as a function of ODN strength comparing East22 (solid) vs East23 (dashed) cycle loss relations at nominal sextupole strength (orange) and increased sextupole strength (cyan).	208
C.8	Defined currents for each PFW windings in <i>East_T8_22</i> (red) and <i>East_T8_23</i> (blue) cycles. Difference between the two (black) shown.	209
C.9	Measurement of PS non-linear chromaticity as a function of time in <i>East_T8_22</i> (left) and <i>East_T8_23</i> (right)	210
C.10	Calculated PS k_3 focusing (red) and defocusing (blue) strength from the non-linear chromaticity as matched to MADX (dashed line) in <i>East_T8_22</i> (left) and <i>East_T8_23</i> (right)	211
C.11	<i>East_T8_23</i> non-linear chromaticity with corrected PFW currents	211
C.12	Sum of ring BLMs as a function of ODN strength comparing <i>East_T8_22</i> (solid line), <i>East_T8_23</i> (dashed line), corrected <i>East_T8_23</i> (dotted line), and <i>East_T8_22</i> cycle applied in 2023. Compared at nominal sextupole strength (orange) and increased sextupole strength (blue).	212
C.13	BLM23 signal as a function of octupole strength in simulation (left) and measurement (right) as a function of sextupole strength (red = low, blue = high). . . .	212

List of Tables

1.1	Four options of synchrotron extraction for FLASH delivery	31
1.2	Dose Rate given NIMMS synchrotron frequency	35
1.3	NIMMS ion species, target intensities and irradiation field size and volume	35
3.1	Summary of Slow Extraction R&D as published for each facility	66
4.1	Chromaticity benchmark of simulation codes with β_{rel}	83
6.1	MD measurement parameters for cycles at two energies	114
6.2	Septa simulation parameters	117

7.1	HeLICS facility parameters	140
7.2	NIMMS slow extraction parameters	142
7.3	Septa designs from J. BORBURGH	143
7.4	UHDR burst statistics comparison	156
8.1	Parameters of the LhARA FFA	165
B.1	RF-KO parameters used in Ch. 7	200

Nomenclature

Accelerator constants

α_n	Twiss alpha
β_n	Betatron frequency
$\Delta p/p$	Momentum spread
δp	Longitudinal momentum
ΔQ	Tune distance
ϵ	Modified tune distance
\mathcal{H}	Hamiltonian
μ_n	Phase advance
ϕ	Separatrix angle
ρ	Bending radius
σ_n	RMS beam size
ε	Physical emittance
ε_n	Normalised emittance
ε_p	Single particle emittance
A_p	Single particle amplitude
B	Magnetic field strength
$B\rho$	Beam rigidity
C	Circumference
D'	Angular dispersion
D	Dispersion

dQ	Chromaticity
f_{rev}	Revolution frequency
I	Current
J	Action
k_n	Multipole Strength
L	Magnetic length
p_0	Reference momentum
Q_x	Horizontal tune
Q_y	Vertical tune
S	Normalised sextupole strength
s	Synchrotron position
S_{oct}	Normalised octupole strength
t	Longitudinal position
x'	Horizontal canonical momentum
x	Horizontal position
X_{ES}	ES septum foil position
y'	Vertical canonical momentum
y	Vertical position

Acronyms

ADTS	Amplitude-Dependent Tune Shift
AM	Amplitude Modulation

BTF Beam Transfer Function

ES Electrostatic Septum

FFA Fixed-Field Accelerator

FFT Fast Fourier Transform

FM Frequency Modulation

MEE Multi-Energy Extraction

MS Magnetic Septum

MTI Multi-Turn Injection

PID Proportional Integral Derivative

RF Radiofrequency

RF-KO Radiofrequency Knock-Out

UHDR Ultra-High Dose Rate

Facilities

HeLICS Helium Light Ion Compact Synchrotron

HIT Heidelberg Ion-Beam Therapy Center

LhARA Laser-hybrid Accelerator for Radiobiological Applications

NIMMS Next Ion Medical Machine Study

PIMMS Proton Ion Medical Machine Study

PS CERN Proton Synchrotron

SPS CERN Super Proton Synchrotron

PS Hardware

BCT Beam Current Transformers

BLM Beam Loss Monitors

BSW Slow Bumpers

ODN Octupole

ONO Octupole

PFW Pole-Face Windings

QSE Quadrupole Slow Extraction

XSE seXtupole Slow Extraction

Physics constants

β_{rel} Relativistic beta

γ_{rel} Relativistic gamma

A Atomic mass

c_0 Speed of light in a vacuum

F Force

I Current

m_0 Mass energy

m_e Electron mass

m_p Proton mass

q Particle charge

T Kinetic energy

v Velocity

Z Proton number

z Charge number

Thesis Overview

Ch. 1 provides an explanation of hadron therapy which motivates the need for slow extraction to provide active scanning over a tumour volume. In particular, it introduces the concept of FLASH therapy, how to produce ultra-high dose rates from proton synchrotrons, and noted that the definition of dose rates and the mechanism behind FLASH is uncertain. This chapter identifies a need for high intensity, fast timescale flexible beams so that such parameters can be further studied. It concluded by defining NIMMS, the Next Ion Medical Machine Study, as a clinical treatment and research facility to study such fundamental radiobiological questions.

It is challenging to provide these needs from a synchrotron, as introduced by **Ch. 2**. Linear and non-linear accelerator dynamics are put into the context of slow extraction. The analytical tools required to design the slow extraction schematic are delivered, and the limits of this analytical description is considered.

Slow extraction is an active area of research since its first application in the 1960s. **Tab. 3.1** in **Ch. 3** displays an overview of all of the latest slow extraction R&D performed at ion synchrotrons, and which of these NIMMS synchrotrons would benefit from.

The foundation of this thesis lies on three key simulation tools, outlined in the flowchart of **Fig. 4.1** in **Ch. 4**. These codes are described and benchmarked for the PIMMS lattice under three test environments: 4D tracking, tunes & chromaticities and resulting beam from betatron core extraction.

It is important to understand the tune dynamics of the beam, which **Ch. 5** explores by discussing the methods and limits of this in simulations. These methods are applied to the Heidelberg Ion-Beam Therapy (HIT) synchrotron to study the tune spectrum under BTF-like frequency excitation.

For measurement and hands-on experience, machine development studies at the CERN Proton Synchrotron were performed. As demonstrated in **Ch. 6**, octupoles were applied in a range of slow extraction environments - at high strengths to observe trapping formations, and at fine-tuned low strengths to minimize the losses at the septa.

The core of this thesis is **Ch. 7** which explores two NIMMS synchrotrons: the PIMMS-like normal-conducting carbon synchrotron, and the triangular normal-conducting helium synchrotron (HeLICS). Both apply momentum-based and RF-KO extraction with different optimisation methods to explore the dependencies of high emittance, faster extraction rates and burst extraction for ultra-high dose rate, FLASH-compatible beams.

Ch. 8 explores future R&D for slow extraction. A brief discussion considers how superconducting AG-CCT magnets may affect the slow extraction procedure. The options to extract a beam suitable for proton radiography is brainstormed. Extraction options from a fixed-field accelerator for a future radiobiological facility are considered. Two working points are studied, compatible with and without an additional resonant sexupole.

Ch. 9 concludes the thesis, then identifies each original contribution, the extent to which these findings are true, and the recommended next steps.



Hadron Therapy

The use of accelerators in hadron therapy has been considered for almost as long as the accelerators themselves. The first treatment - the 1954 irradiation by John Lawrence [1] - was a single fraction dose of a 340 MeV proton beam targeted at a pituitary gland. The machine in question was an 184-inch cyclotron designed by his brother Earnest Lawrence, built just 8 years prior. In comparison, the first conventional radiotherapy treatment with a LINAC was one year prior, in 1953 at Hammersmith Hospital, London [2].

This prompts the question: why does global access to hadron therapy remain so sparse, if it was developed alongside conventional radiotherapy? In the year 2000 there were only 10 proton therapy centres worldwide [3]. From the time of writing, this has now increased to 131 [3], but hadron therapy treatments still only account for $\approx 1.5\%$ of all radiotherapy treatments [4]. Increasing understanding and accessibility of hadron therapy is the core of the motivation for **NIMMS: The Next Ion Medical Machine Study**. The philosophy of this study is to develop technologies for future machines that are not just for patient treatment - which a commercial accelerator can deliver - but also to provide for radiobiological research which can investigate much-needed answers to the effects of hadrons on human tissue.

The demand for such a facility has increased dramatically since 2014, which was the first proposed application of high dose rates to cause the FLASH effect [5]. Given the growing interest in research on this topic, it is essential that NIMMS technologies are compatible with the intensity and timescales required to deliver FLASH ultra-high

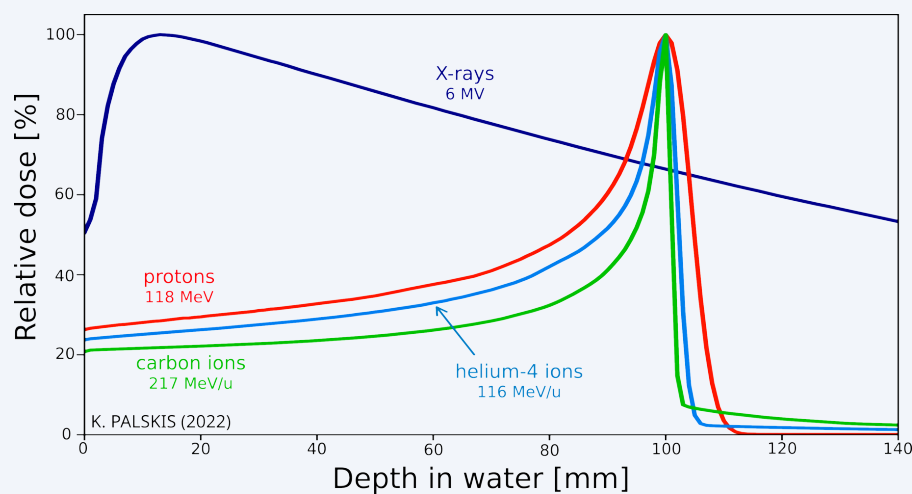
dose rates (UHDR). For synchrotrons, this is only possible with the advanced extraction methods represented in this thesis.

This chapter will provide a coherent background on the topic of hadron therapy and FLASH. Primarily, it will detail the benefits of hadron therapy from a simplified physicists perspective, attempt to divulge some biological perspectives of FLASH, and then summarise the historical and present statuses of hadron therapy facilities in Europe. Then it will emphasize the need for a dedicated research beam to answer unsolved questions in radiobiology, in particular those required for FLASH treatments. Through this, it will motivate the reasoning for the upgrades for the Next Ion Medical Machine, and future synchrotron-based hadron therapy centres.

1.1 Radiobiological Motivation: A Physicist's Approach

Hadron therapy refers to radiotherapy treatment of cancerous tumours using protons and ions. It is also referred to as advanced particle therapy, light ion therapy, heavy ion therapy, or via the specific particle used. Protons, helium-4 (2+) ions and carbon-12 (6+) ions are the three main particles that will be considered throughout this thesis. As the accelerator research within this thesis is performed with the application of hadron therapy in mind, the requirements for the output of the accelerator are driven by radiobiological effects. These radiobiological effects should be understood sufficiently to acknowledge how they affect the extraction process.

Figure 1.1.: Dose deposition of 4 species of radiation throughout water, modelled in Geant4 (K. PAŁSKIS [6]). Normalised to maximal dose.



The benefits of hadrons in treatment emerges from their interaction with matter. Through processes such as electron elastic scattering, multiple Coulomb scattering and nuclear fragmentation, energy is lost which slows the hadron and increases its interaction rate [7]. The sum of these effects causes a low energy deposition at the entrance, which culminates into a **maximum deposition peak, referred to as the Bragg peak**. This behaviour, represented in **Fig. 1.1**, is the key to the success of hadron therapy. These results were simulated in Geant4 by K. PALSKIS, assuming a uniform water medium - used due to its similarity to the density of human tissue.

Contrary to x-rays (dark blue), which passes radiation through the body, hadrons such as protons (red) can provide targeted dose to the desired depth. The benefit of this method is that it limits unnecessary dosage to surrounding healthy tissue. This peak can be superimposed to provide a shaped dosage distribution longitudinally, which is referred to as a Spread-Out Bragg Peak (SOBP). This is particularly beneficial to reduce risk of secondary tumours, necessary for pediatric cases, and for tumours in sensitive regions including head and neck.

Dose in radiobiology is defined in Grays (Gy), which is defined as the absorption of one joule of radiation per kilogram of matter (J kg^{-1}), typically normalised for water. The description of dose D is represented in **Eq. 1.1** [8], as a function of flux of particles N in area A , $\frac{dN}{dA}$, with a stopping power of $\frac{dE}{dx}$ through a material of density ρ . The full description of stopping power $\frac{dE}{dx}$ is expressed in **Eq. 1.2**.

$$D = \frac{1}{\rho} \left(\frac{dN}{dA} \right) \left(\frac{dE}{dx} \right) \quad (1.1)$$

A fraction of proton therapy will typically deliver an order of 1×10^9 particles between one to thirty seconds, aiming to be equivalent to 2Gy. Dose delivered is a physical parameter, however the biological response of the tumour cells depends strongly on their micro-environment. Environmental parameters such as cell type, tissue densities, intrinsic radio-sensitivity, temperature, pressure, oxygen concentration, and the type of particle used, all affect the amount of received damage [9]. For this reason, relative biological effectiveness (RBE) is used as a parameter that describes the effect of the radiation on the tumour. RBE is defined as the ratio of dose from an x-ray compared to dose of another particle that produces the same biological effect [10].

Since 2022 over 300,000 patients have been treated with protons, and 50,000 patients with carbon ions. They have been trialled for a wide range of conditions, mostly commonly those involving pediatric cases, glioblastomas, the central nervous system, and head and neck tumours [3].

1.2 Current Status of Hadron Therapy

As of writing, there are 131 operational clinical hadron therapy facilities. 32 more are under construction [3]. In order for ion species to be of sufficient energy to reach the tumour depth up to 30 cm, high energies are needed, therefore each of these facilities relies on a particle accelerator.

An accelerator is a machine for accelerating charged particles to high energies using electric and magnetic fields. There are three primary kinds of accelerators, LINACS, cyclotrons and synchrotrons:

LINACs (LINear ACcelerators) use straight alternating fields and work best for light particles and low energies. Electron LINACs are employed for most conventional radiotherapy treatments. Their use in hadron therapy is currently under extensive research [11].

Cyclotrons are circles of two magnet halves, which switch sign with frequency equal to the beam revolution. They work best for protons at medium energies, where their circumference is still reasonable. As mentioned in the introduction, cyclotrons were used for the first hadron therapy treatment and today there remains a large existing commercial market for cyclotrons. Of the existing hadron therapy facilities, 63 % (82 total) are cyclotron/synchrocyclotron-based. These cyclotrons benefit from a relatively small machine footprint of ≈ 5 m diameter, quick adjustable intensity [12] and continuous extracted beam. Cyclotrons are disadvantaged by having low extraction efficiency (≈ 40 -80 % depending on type), high radioactivity from these losses and the ability to only extract the maximum energy. Therefore to reduce the energy of the delivered dose, degraders are required, which scatter the beam prior to delivery, causing loss of beam intensity, reduced beam quality and further activation. Active work is ongoing to momentum cool the beam for varying energy extraction [13]. Presently cyclotrons are only able to accelerate protons, although the first IBA C400 carbon-ion cyclotron is under construction at Caen [14].

Synchrotrons are rings of many magnets, and work well for any particle species and are often

used to go up to the highest energies for research. 32 % of hadron therapy facilities use synchrotrons (42 total). They are able to extract any energy from injection to maximum, and do so with high efficiency ($\approx 90\text{-}99\%$ depending on facility).

Extraction from a synchrotron is challenging due to the high repetition rate of the beam, and its short bunches. For this reason, a dedicated extraction method is applied to be suitable for hadron therapy, known as slow extraction. **Slow extraction is a method which gradually removes a few particles from the beam each turn - over millions of turns - to create a smooth and continuous beam over seconds or minutes.** This is beneficial for the beam delivery techniques described in [Sec. 1.3](#), and is sufficient time for the dose profile of the beam to be properly calibrated with quality assurance methods. Slow extraction from the perspective of accelerator physics is described in [Sec. 2.3](#).

1.2.1 Ion Therapy

Synchrotrons have the advantage of accepting carbon ions in the same accelerator as protons, yet only 14 facilities in the world offer carbon treatment. Europe presently has four such facilities [3]. Two of these have emerged from the 1998 Proton-Ion Medical Machine Study (PIMMS) [15], formed as a collaboration via CERN (see [Ch. 3](#) and [Ch. 4](#)). This study resulted in the construction of two facilities: CNAO in Pavia, Italy [16], and MedAustron in Wiener Neustadt, Austria [17]. From GSI two further facilities were established in Germany, HIT in Heidelberg [18] and MIT in Marburg [19].

Synchrotron facilities are large, where typically proton-only synchrotrons have a radius of $\approx 10\text{ m}$ and carbon-and-proton synchrotrons require a larger radius of $\approx 25\text{ m}$ circumference.

Compared to the proton distribution in [Fig. 1.1](#), the dose delivered by carbon (green) ions features lower scattering at the entrance of the medium, lower lateral scattering, and a sharper peak. Carbon ions experience nuclear fragmentation after the peak, which accounts for the fragmentation tail. Analytically, this behaviour is represented by the Bethe-Bloch equation, in [Eq. 1.2](#) [7]. dE/dx represents the amount of energy transferred per unit path length. This value is referred to as the Linear Energy Transfer (LET) in $\text{keV}/\mu\text{m}$, and overall is proportional to the effective charge (Z) of the ion squared, divided by its relativistic velocity (β_{rel}) squared. As carbon is a heavier ion with a lower charge state, the LET at the SOBP has a higher range of $4\text{-}40\text{ keV}/\mu\text{m}$ compared to protons with $1\text{-}4\text{ keV}/\mu\text{m}$.

$$-\frac{dE}{dx} = KZ^2 \frac{Z}{A} \frac{1}{\beta_{\text{rel}}^2} \left[\frac{1}{2} \ln \frac{2m_e c^2 \beta^2 \gamma^2 T_{\text{max}}}{I^2} - \beta_{\text{rel}}^2 - \frac{\delta}{2} \right] \quad (1.2)$$

The higher LET from carbon results in an increased RBE of 1.3-3 compared to protons of ≈ 1.1 . Generally, ionising radiation converts water in the environment to radicals at a rate proportional to the amount of oxygen in the cell. The presence of oxygen thereby indirectly increases the damage to the DNA, referred to as oxygen enhancement ratio (OER). Consequentially, the benefit of carbon ions is that they can directly increase damage to the DNA, with reduced dependency on the oxygen levels of the cell. This is beneficial for the treatment of hypoxic tumours, which are otherwise radio-resistant.

Helium Ions

At the time of writing, only proton and carbon ions have been clinically approved for treatment. As each ion has different radiobiological effects, each must be treated as a different medicine, with the relevant trials applied.

The properties of helium ions are situated in-between proton and carbon. Within [Fig. 1.1](#) (light blue), helium ions feature a similar lower entry dose, lateral scattering and sharp peak of carbon ions, but with much reduced nuclear fragmentation post-peak.

The research interest in helium ions as used for treatment is growing, as facilities are anticipating clinical trials to begin [20].

MedAustron has begun commissioning the transfer of helium ions from the source to MEBT [21]. CNAO has added an AISHa source [22] for helium, lithium, oxygen and iron. HIT has already completed commissioning and have published their first patient treated with helium [23].

Helium has an almost identical Z/A ratio compared to carbon, and its lower nucleon number means lower energy required to reach the same depth compared to carbon. Other facilities are considering using a mixed carbon-helium beam, where the helium exits the body for use in imaging [24].

1.3 Beam Delivery

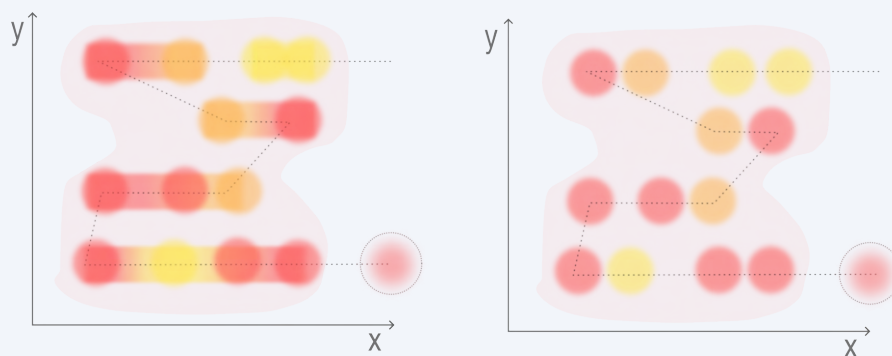
Radiotherapy treatment depends on the method by which the beam is extracted from the machine, and by which dose is delivered to the tumour. This applies even more to hadron therapy,

with its characteristic longitudinal profile.

The tumour is assumed to be a 3D object with order-of-magnitude 1 L volume, of a given depth within the body. Treatment plans are created by medical physicists which indicate the dosage required to each region of the tumour, in accordance to the intent of the oncologist. Based on these conditions, there are a series of methods which can deliver the dosage required by the treatment plan.

- **Passive beam scattering** is one of the first methods of dose delivery. The beam is enlarged across the whole tumour region and is shaped by a patient compensator to correct for size and depth [25].
- **Active scanning** scans the beam across the transverse plane via a series of focusing and bending magnets. There are a number of ways to apply this process.
 - In terms of transverse profile, **raster scanning** applies the beam continuously throughout the plane whereas **spot scanning** will apply the dose individually per voxel (volume pixel). **Fig. 1.2** shows a visual schematic between the two. For synchrotrons, slow extraction is necessary to obtain the continuous beam for raster scanning.
 - In terms of intensity profile, **single field** uniform dose applies only one uniform field from each direction. **Intensity modulation** varies the dose per region, either by reducing the speed of the raster scanning, or providing multiple shots, which targets dose to specific regions [26].

Figure 1.2.: Schematic comparing transverse raster scanning (left) and spot scanning (right) with variable intensity (yellow to red)



Delivery Standards

There are a series of requirements that proton and ion therapy facilities must uphold to ensure reliability and treatment safety standards (TSS) [26]. Announcing these parameters here provides an order of magnitude of what is expected, such that the reader can compare with results throughout the thesis. Within a beam, the variation in delivered energy must be $\pm 0.1\%$ - easier to achieve in synchrotrons than cyclotrons. The dose position must have a placement accuracy of ± 1 mm and ± 1 mrad. For conventional dose rates, it is expected that $2 \text{ Gy min}^{-1} \text{ L}^{-1}$ should reasonably be delivered to a cubic region of 10 cm^3 for any depth, in a recommended time of at least 1 min. The maximum field size that should be able to be irradiated is 40 cm^2 . The 1σ spot size of the beam should be less than 4-8 mm. The dose accuracy should be $\pm 2.5\%$ measured to a resolution of ± 1 cGy. For cyclotrons, the beam should be considered roughly Gaussian, although it may be circular or elliptical. This is not the case for synchrotrons slow extracted beam, with its characteristic rectangular phase-space, so it is permissible to have overlaps between adjacent spots for homogeneous doses.

1.3.1 FLASH Therapy

The **FLASH effect is a radiobiological effect where ultra-high dose rates (UHDR) of radiation have been observed to reduce toxicity damage to healthy tissue but preserve damage to tumour tissue**. Since the discovery that it could be used as a clinical modality in 2014 [5], FLASH has sparked a lot of research interest across its related interdisciplinary fields. There are targeted efforts to categorise the range of parameters where the FLASH effect occurs, and to build machines and facilities capable of reaching these parameters. These efforts largely focus on electron radiotherapy - the use of the FLASH effect in hadron therapy is in development.

The standard cited definition of FLASH in the original paper is to have a mean dose rate of at least 40 Gy s^{-1} [5]. This is in comparison to convention dose rates of less than 0.03 Gy s^{-1} . To irradiate a 1 L of tumour with a total dose of 2 Gy at the minimum FLASH rate of 40 Gy s^{-1} , a treatment time of 50 ms would be necessary. Many other publications cite that a maximum total dose of 8-10 Gy is a further necessary condition. With that said, the FLASH effect cannot be predicted mathematically in this way, as there are a range of further parameters that affect the likelihood of FLASH, in particular how the beam is applied, and the kind of tumour, tis-

sue, organ or environment it is applied to. For this reason, when referring to the extraction time and intensity that is FLASH-compatible, this thesis refers to it as UHDR extraction. It is essential that the solutions offered by this thesis are flexible enough that extraction can adapt to the evolving understanding of this topic.

What is dose rate?

The important quoted parameter for FLASH is dose rate - however pencil beam scanning with intensity modulation has uneven distribution of dose over time. In this scenario, how can dose rate be defined when each voxel receives different doses at different rates? A comparative study (*Deffet & Hamaide, 2023 [27]*) emphasises how different calculated dose rates can be for the same irradiation.

The conventional definition, dividing total dose by delivery time, is known as average dose rate. Average dose rate does not consider the temporal structure during the delivery, and does not consider non-irradiated spots. Alternative rates factor in the individual dose rate for each voxel - and a series of statistical methods can be applied, depending on the assumed threshold of each voxel.

Due to the low certainty of our understanding of the FLASH mechanism, the most suitable calculation of dose rate cannot yet be determined. To define a meaningful rate, experimental methods and biological data are essential, as the FLASH effect is not theoretically predicted. This requires availability of pencil scanning hadron beams which can provide a range of intensities and scanning rates.

FLASH with ions

FLASH trials have been performed experimentally with a range of particle species. Primarily electrons [5] are used, although studies have also been performed with photons (x-rays) [28], protons [29], helium ions [30] and carbon ions [31]. The primary difference between electron/photon radiotherapy and hadron therapy is the longitudinal Bragg Peak distribution, which is a further complication to FLASH delivery. It is not obvious whether the benefits of a Bragg peak are compatible with the benefits of FLASH. Even if the dose in the peak is FLASH-compatible, the dose given in the entryway is lower, and if it is not in the FLASH-compatible domain, is not likely to have these protective effects. To have FLASH-compatible UHDR in the entryway, 8-10 Gy in this region would be needed, and the overall intensity throughout

Table 1.1.: Four options of synchrotron extraction for FLASH delivery

	Raster Scanning	Spot Scanning
Bragg Peak	Continuous Spill Energy Varying	Burst Spill Energy Varying
Shoot Through	Continuous Spill Energy Constant	Burst Spill Energy Constant

the longitudinal distribution would have to be increased accordingly - which places further demands on the available intensity the machine can deliver.

The alternative to not having a SOBP for longitudinal dose delivery is to treat the proton similar to an electron or photon and only take the 'entryway dosage' across the whole tumour, where the Bragg peak would exit outside of the body. This is referred to as shoot-through, and was the dose delivery method that was applied for the first hadron therapy clinical trial - FAST01 [29], with single field dosage. To do so, much higher proton energies are necessary, at least 220 MeV.

With these newfound intensities and rates that provide protective effects, a new regime of safety standards will need to be determined. This is especially crucial because failure to provide the FLASH effect will result in excessive dose delivered to healthy tissue compared to conventional hadron therapy. Intensity thresholds, dosimetry, monitors and interlocks will all have to be adapted at higher intensities and higher timescales. When considering extraction limits on intensity and timescale, it is important to also realise that whatever solutions are implemented must also be consistent with the associated safety limits.

FLASH Synchrotron Extraction

From the perspective of slow extraction, introduced in [Ch. 2](#), what are the takeaway points in terms of UHDR. Given the range of ways one can deliver dose at $\geq 40 \text{ Gy s}^{-1}$, one should consider which of these are relevant to synchrotrons.

Tab. 1.1 displays four quadrants with two transverse methods of delivery and two longitudinal methods. It is assumed for all four that a uniform dose will be applied throughout. Both spot scanning and raster scanning will deliver the same dose rate, but the distinction is whether that dose is given as a continuous spill to be scanned uniformly, or whether it will be concentrated into bursts, with a $\leq 1 \text{ ms}$ gap between voxel irradiations. Raster scanning is limited by the

uniformity of the continuous beam within the delivery time. It would have to be a square beam with reduced variation, to avoid fluctuations about the safe dose rate. Spot scanning is limited by the uniformity of each burst. The machine would have to have good reproducibility of intensity, with limited shot-to-shot variation. However the distribution of each burst would not necessarily need to have a uniform, or a square function. A Gaussian-distributed intensity could be suitable, which is not the case for raster scanning.

For dose delivery via shoot-through, there is no depth dependency with energy, so the beam should be accelerated to the maximum energy possible in the synchrotron. For dose delivery via Bragg peak, a variation in energy is needed to irradiate the tumour in depth. It is often quoted that the conventional energy layer spacing is 3 mm, meaning that 1 L of tumour would need to be irradiated within 3 ms [32]. For this energy rate to emerge from the accelerator, the beam would most likely have to be injected, accelerated and extracted in this time frame. There are no current schemes which are able to perform this quickly. Multi-Energy Extraction (described in [Ch. 3](#)) occurs on a ≈ 100 ms time frame, and existing Rapid Cycling Synchrotrons are on a similar order of magnitude at ≈ 50 Hz. There are ongoing ideas of having an accelerating or decelerating RF cavity or RFQ (Radiofrequency Quadrupole) in the extraction line to provide this energy range per beam. Whilst this would result in bunching of the extracted beam, as mentioned above, this would not necessarily be a problem for spot scanning.

To combine the best attributes of the hadron therapy Bragg Peak to FLASH dose deliver, a recent idea known as FLASH stitching is emerging [33]. This would apply conventional intensity-modulated hadron therapy dose in the core of the tumour, and then include UHDR FLASH treatment to the fringes of the tumour near critical organs at risk, for optimal target coverage with the available intensity. The current extraction options suggested for applying FLASH is briefly described in [Sec. 3.3.7](#).

1.4 Treatment from NIMMS

This chapter has reviewed the physics behind hadron therapy, the radiobiological effects it causes, the present state of hadron therapy facilities, and the concept of FLASH with respect to hadrons. These concepts are crucial to know in the context of slow extraction, as it affects the form of beam that is being provided to the patient and it constrains the designs of the synchrotrons. Much like the PIMMS study of 1998, slow extraction is one of the first research

topic being covered with respect to the NIMMS synchrotron. To have a facility that is being designed patient-first, the output of the facility must closely follow the parameters that the machine must meet. This concluding section will analyse what questions remains of hadron therapy, the ability for NIMMS to provide FLASH-compatible beams, and what NIMMS as a facility aims to provide.

Producing the slow extraction designs for NIMMS ions therapy synchrotrons is the primary goal of the 3-year doctoral programme. As NIMMS is a technology development toolbox and not a specific accelerator project, this means that flexible extraction options should be considered. There are three current synchrotron designs, and multiple extraction designs in consideration. The first option is a normal conducting synchrotron for the SEEIIST Association (South East Europe International Institute for Sustainable Technologies) [34], for protons and carbon ions, which is based on the design of PIMMS, but with some crucial upgrades. The second option is a compact superconducting synchrotron designed of Compacted Cosine-Theta (CCT) magnets [35]; magnet modelling and R&D is required before this lattice design can be solidified for slow extraction (see [Ch. 8](#)). The third option is a compact 30 m normal-conducting synchrotron for the CERN Baltic Group, for only protons and helium ions [6]. All three potential facilities will be for both clinical treatment and radiobiological research, and hope to also include the necessary targetry for radio-isotope production.

As a clinical facility, NIMMS will need to provide conventional slow extraction beams that are suitable for continuous and uniform 1-30 s spills for pencil beam raster scanning. As a priority the extraction should be optimised for a good quality spill with reduced ripples. As a research facility, it would be beneficial for NIMMS to provide additional intensities, time scales and ion species for current areas of research that have a high demand for such beams. These demands cause large waiting list for the existing medical facilities that have beamlines available for experiments. It is essential that as a flexible research facility, this synchrotron can provide the radiobiological demands for faster dose delivery timescales as per the requirements of FLASH treatment; currently estimated to require treatment faster than at least 100 ms [32].

1.4.1 Open Questions in Hadron Therapy

This chapter opened by questioning why ion therapy treatment remains so sparse in comparison to the 15 400 conventional photon and electron radiotherapy units [36]. Whilst the core

reasons are multi-layered and historical, they can be boiled down to three points: firstly, ion accelerators are large, expensive and complicated. Secondly, hadron therapy is complicated. Thirdly, it takes time to transition to new technologies and methods. Tackling these problems head on requires an extensive R&D programme in compact proton and ion accelerator technology, and without disruptive changes, will require many generations of iterative innovation to fix.

As mentioned, the lack of available clinically viable ion beams to test is limiting the research that needs to be performed to gain evidence and improve confidence in new clinical methods of hadron therapy treatment. This is especially true for helium, as many dedicated trials performed with carbon in Japan since 1994 and HIT since 2009 [9]. The effect of different ions at a cellular and microbiological level is necessary, as is the case for in-vivo and human trials.

The discovery of the FLASH effect opened up further questions about our understanding of the effects of radiation on biological systems. Especially the case for the relation between ion beam therapy and FLASH. Lots of research required to stretch the limits of hardware, not just for extraction limitations, but also for safety constraints. This is especially true for Bragg peak delivered FLASH, if there are proposals to put 8-10 Gy into healthy tissue.

FLASH for NIMMS

FROM ACTIVE DISCUSSION WITH K. PAŁSKIS

Given the specifications of NIMMS machines, what can be expected in terms of the limits of the beam to deliver UHDRs? As it is not clear how this will be performed in treatment plans, baseline calculations can inform us of the average rough dose rate that can be provided.

Tab. 1.2 expresses dose rate as a function of extraction time (in ms and as turn number) and total dose delivered. This is calculated for the revolution frequency $f_{\text{rev}} = 4.8 \text{ MHz}$ equivalent to 8.2×10^{10} helium ions of $T = 220 \text{ MeV/u}$ for a 35 m circumference synchrotron (see **Sec. 7.2**). This provides a guideline for how many turns are necessary to extract a particular dose to meet a given dose rate, i.e. the target 40 Gy s^{-1} would not be reached if a 8 or 10 Gy dose was delivered in 500 ms, but this target is safely reached for extraction within 100 ms. Active discussions are contemplating if one can fast extract over one turn, equivalent to 0.0002 ms. This option would be the easiest technically for the synchrotron, but come with complications for the receiving end of the safety systems and dosimetry.

Table 1.2.: Resulting Dose Rate (DR) of a 8 Gy or 10 Gy beam for a given irradiation time. Converted to number of synchrotron turns assuming a NIMMS frequency of $f_{\text{rev}} = 4.8 \text{ MHz}$ (see [Sec. 7.2](#))

Time [ms]	Turns	DR(8 Gy)	DR(10 Gy)
500	2 400 000	16 Gy s^{-1}	20 Gy s^{-1}
100	480 000	80 Gy s^{-1}	100 Gy s^{-1}
62	300 000	129 Gy s^{-1}	161 Gy s^{-1}
10	48 000	800 Gy s^{-1}	1000 Gy s^{-1}
0.0002	1	$2.4 \times 10^7 \text{ Gy s}^{-1}$	$3.0 \times 10^7 \text{ Gy s}^{-1}$

Table 1.3.: NIMMS ion species, their target intensities and their resulting maximum irradiation field size and volume [K. PAŁSKIS]

		Proton	Proton	Helium	Carbon
Intensity		2.6×10^{11}	2.6×10^{11}	8.2×10^{10}	2×10^{10}
Energy		125 MeV	218 MeV	220 MeV/u	400 MeV/u
Max Field [cm]	Shoot 8 Gy	-	5.32	5.72	6.54
	Shoot 10 Gy	-	4.76	5.12	5.85
	SOBP 8 Gy	6.98	6.46	6.61	7.29
	SOBP 10 Gy	6.24	5.78	5.92	6.52
Volume [l]	SOBP 8 Gy	0.34	0.27	0.29	0.39
	SOBP 10 Gy	0.24	0.19	0.20	0.27

As indicated, FLASH is limited by dose *rate*. Facilities which are intensity limited could provide the necessary dose rate, but would do so at a small volume. As one large aim of NIMMS is to store increasing intensity for the purposes of multi-energy extraction (see [Sec. 3.3.4](#)) and FLASH. As an initial approximations of the FLASH-radiation volume that could be delivered, [Tab. 1.3](#) compares the expected energy, intensity and therefore field size and volume for each proposed species in NIMMS. This includes the use of protons for shoot-through delivery, and three species for Bragg-peak delivery, protons, helium ions and carbon ions. This is because the baseline energy for protons 125 MeV is not sufficient for shoot-through treatment, which requires an energy of at least 218 MeV. With the target intensities listed, it should be possible to get 5-7 cm maximum field sizes for all species. For perspective, a field of 0.25 L is equivalent to a $5 \times 5 \times 5 \text{ cm}^3$ volume.

Summary

The following benefits of NIMMS have been addressed.

- There is a need to continue to widen access to hadron therapy. NIMMS encourages this through the development of compact accelerator technologies.
- There is demand for a flexible, multi-ion, multi-time scale research facility for radiobiology. Many existing clinical facilities have limited beam time to dedicate to fundamental questions of how radiation interacts biologically. By intending to be both a research and treatment facility, NIMMS increases availability to experimental time with said beams.
- There is increasing interest to study FLASH with protons and ions. For covering large volumes, the limiting factor is the intensity. Many facilities can provide hadron FLASH at mm³ volumes, but NIMMS intends to deliver clinically viable cm³ volumes.
- Extraction is at the core of providing these developments, by stretching the limits of intensity, extraction rate and beam structure.
- The fundamental design of the synchrotron is shaped by the needs of slow extraction. It is a process which requires multiple components integrated across the whole machine. For this reason, the extraction is considered synchronously with the baseline machine designs.

For one final note, it is written in Jolly & Owen (2020) *"Even more so than with cyclotrons, new technological advances will be required in order to realise FLASH delivery with synchrotrons."* [32] With that said, let us continue to explore some of these technological advances, as they pertain to beam extraction.

Bibliography

- [1] J. H. Lawrence. "Proton irradiation of the pituitary". In: *Cancer* 10.4 (1957), pp. 795–798. DOI: [https://doi.org/10.1002/1097-0142\(195707/08\)10:4<795::AID-CNCR2820100426>3.0.CO;2-B](https://doi.org/10.1002/1097-0142(195707/08)10:4<795::AID-CNCR2820100426>3.0.CO;2-B).
- [2] D. I. Thwaites and J. B. Tuohy. "Back to the future: the history and development of the clinical linear accelerator". In: *Physics in Medicine & Biology* 51.13 (June 2006), R343. DOI: 10.1088/0031-9155/51/13/R20.
- [3] Administrator. *PTCOG - Facilities in Operation* — [ptcog.site](https://ptcog.site/index.php/facilities-in-operation-public). <https://ptcog.site/index.php/facilities-in-operation-public>. [Accessed 19-02-2024].

- [4] N. G. Burnet et al. “Estimating the percentage of patients who might benefit from proton beam therapy instead of X-ray radiotherapy”. In: *British Journal of Radiology* 95.1133 (Mar. 2022), p. 20211175. ISSN: 0007-1285. DOI: 10.1259/bjr.20211175.
- [5] V. Favaudon, L. Caplier et al. “Ultrahigh dose-rate FLASH irradiation increases the differential response between normal and tumor tissue in mice”. In: *Science Translational Medicine* 6.245 (2014), 245ra93–245ra93. DOI: 10.1126/scitranslmed.3008973.
- [6] M. Vretenar et al. “A Compact Synchrotron for Advanced Cancer Therapy with Helium and Proton Beams”. In: *Proc. IPAC’22* (Bangkok, Thailand). International Particle Accelerator Conference 13. JACoW Publishing, Geneva, Switzerland, July 2022, pp. 811–814. ISBN: 978-3-95-450227-1. DOI: 10.18429/JACoW-IPAC2022-TU0ZGD2.
- [7] Particle Data Group and P. A. Zyla. “Review of Particle Physics”. In: *Progress of Theoretical and Experimental Physics* 2020.8 (Aug. 2020), p. 083C01. ISSN: 2050-3911. DOI: 10.1093/ptep/ptaa104.
- [8] H. Paganetti. *Proton Therapy Physics*. Series in Medical Physics and Biomedical Engineering. CRC Press, 2016. ISBN: 9781439836453. URL: <https://books.google.fr/books?id=IGPRBQAAQBAJ>.
- [9] W. Tinganelli and M. Durante. “Carbon Ion Radiobiology”. In: *Cancers* 12.10 (2020). ISSN: 2072-6694. DOI: 10.3390/cancers12103022.
- [10] J. Overgaard B. S. Sørensen and N. Bassler. “In vitro RBE-LET dependence for multiple particle types”. In: *Acta Oncologica* 50.6 (2011). PMID: 21767171, pp. 757–762. DOI: 10.3109/0284186X.2011.582518.
- [11] A. Degiovanni and U. Amaldi. “Proton and Carbon Linacs for Hadron Therapy”. In: (2014), FRIOB02. URL: <https://cds.cern.ch/record/2062622>.
- [12] J. M. Schippers. “Cyclotrons for Particle Therapy”. In: (2017). 11 pages, Presented at the CAS- CERN Accelerator School on Accelerators for Medical Application, pp. 165–175. DOI: 10.23730/CYRSP-2017-001.165. arXiv: 1804.08541.
- [13] V. Maradia et al. “Demonstration of momentum cooling to enhance the potential of cancer treatment with proton therapy”. In: *Nature Physics* (July 2023). DOI: 10.1038/s41567-023-02115-2.
- [14] Y. Jongen et al. “Current Status of the IBA C400 Cyclotron Project for Hadron Therapy”. In: *Conf. Proc. C 0806233* (2008). Ed. by Ivan Andrian and Christine Petit-Jean-Genaz, TUPP120.
- [15] L. Badano et al. *Proton-Ion Medical Machine Study (PIMMS)*, 1. 1999.
- [16] Giuseppe Venchi. “The CNAO facility: operation and maintenance”. In: *Health and Technology* (Apr. 2024). ISSN: 2190-7196. DOI: 10.1007/s12553-024-00851-w.
- [17] Mauro T. F. Pivi. “The MedAustron particle therapy accelerator facility”. In: *Health and Technology* (Apr. 2024). ISSN: 2190-7196. DOI: 10.1007/s12553-024-00840-z.
- [18] C. Kleffner et al. “The Heidelberg Ion Therapy (HIT) Accelerator Coming into Operation”. In: *AIP Conference Proceedings*. AIP, 2009. DOI: 10.1063/1.3120065.
- [19] Uwe Scheeler et al. “Recommissioning of the Marburg Ion-beam Therapy Centre (MIT) Accelerator Facility”. In: May 2016.
- [20] A. Mairani, S. Mein et al. “Roadmap: helium ion therapy”. In: *Physics in Medicine & Biology* 67.15 (Aug. 2022), 15TR02. DOI: 10.1088/1361-6560/ac65d3.
- [21] N Gambino, M Kausel et al. “First injector commissioning results with helium beam at MedAustron Ion Therapy Center”. In: *Journal of Physics: Conference Series* 2244.1 (Apr. 2022), p. 012109. ISSN: 1742-6596. DOI: 10.1088/1742-6596/2244/1/012109.
- [22] G. Castro et al. “The AISHa ion source at INFN-LNS”. In: *Journal of Physics: Conference Series* 2244.1 (Apr. 2022), p. 012025. DOI: 10.1088/1742-6596/2244/1/012025.

- [23] T. Tessonnier, S. Ecker et al. "Commissioning of Helium Ion Therapy and the First Patient Treatment With Active Beam Delivery". In: *International Journal of Radiation Oncology*Biology*Physics* 116.4 (July 2023), pp. 935–948. ISSN: 0360-3016. DOI: 10.1016/j.ijrobp.2023.01.015.
- [24] L. Volz et al. "Experimental exploration of a mixed helium/carbon beam for online treatment monitoring in carbon ion beam therapy". In: *Physics in Medicine & Biology* 65.5 (Feb. 2020), p. 055002. DOI: 10.1088/1361-6560/ab6e52.
- [25] H. Youngyih. "Current status of proton therapy techniques for lung cancer". In: *Radiat Oncol J* 37.4 (2019), pp. 232–248. DOI: 10.3857/roj.2019.00633.
- [26] C-M Charlie Ma, T. Lomax et al. *Proton and Carbon Ion Therapy*. Vol. 40. Boca Raton: CRC Press, Nov. 2012. ISBN: 9780429192906. DOI: 10.1118/1.4802213.
- [27] S. Deffet, V. Hamaide and E. Sterpin. "Definition of dose rate for FLASH pencil-beam scanning proton therapy: A comparative study". In: *Medical Physics* 50.9 (2023), pp. 5784–5792. DOI: <https://doi.org/10.1002/mp.16607>.
- [28] Pierre Montay-Gruel, Audrey Bouchet et al. "X-rays can trigger the FLASH effect: Ultra-high dose-rate synchrotron light source prevents normal brain injury after whole brain irradiation in mice". In: *Radiotherapy and Oncology* 129.3 (2018), pp. 582–588. ISSN: 0167-8140. DOI: <https://doi.org/10.1016/j.radonc.2018.08.016>.
- [29] E.C. Daugherty, A.E. Mascia et al. "FAST-01: Results of the First-in-Human Study of Proton FLASH Radiotherapy". In: *International Journal of Radiation Oncology*Biology*Physics* 114.3, Supplement (2022). ASTRO Annual 2022 Meeting, S4. ISSN: 0360-3016. DOI: <https://doi.org/10.1016/j.ijrobp.2022.07.2325>.
- [30] Thomas Tessonnier, Stewart Mein et al. "FLASH Dose Rate Helium Ion Beams: First In Vitro Investigations". In: *International Journal of Radiation Oncology*Biology*Physics* 111.4 (2021), pp. 1011–1022. ISSN: 0360-3016. DOI: <https://doi.org/10.1016/j.ijrobp.2021.07.1703>.
- [31] W. Tinganelli et al. "Ultra-High Dose Rate (FLASH) Carbon Ion Irradiation: Dosimetry and First Cell Experiments". In: *International Journal of Radiation Oncology*Biology*Physics* 112.4 (2022), pp. 1012–1022. ISSN: 0360-3016. DOI: <https://doi.org/10.1016/j.ijrobp.2021.11.020>.
- [32] S. Jolly et al. "Technical challenges for FLASH proton therapy". In: *Physica Medica* 78 (2020), pp. 71–82. ISSN: 1120-1797. DOI: <https://doi.org/10.1016/j.ejmp.2020.08.005>.
- [33] João Lourenço. *A novel treatment planning method for proton FLASH radiotherapy: Combining FLASH with VMAT*. FRPT: FLASH Radiotherapy and Particle Therapy, Toronto 2023. 2023.
- [34] S. Damjanovic et al. "A novel facility for cancer therapy and biomedical research with heavy ions for the South East European International Institute for Sustainable Technologies". In: *JACoW IPAC2021* (2021), MOPAB414. 4 p. DOI: 10.18429/JACoW-IPAC2021-MOPAB414.
- [35] E. Benedetto et al. *A Carbon-Ion Superconducting Gantry and a Synchrotron Based on Canted Cosine Theta Magnets*. Submitted to Nuclear Instruments and Methods in Physics Research A. 2021. arXiv: 2105.04205 [physics.med-ph]. URL: <https://arxiv.org/abs/2105.04205>.
- [36] *The IAEA Directory of Radiotherapy Centres (DIRAC)*. <https://dirac.iaea.org/>. [Accessed 04-03-2024].

2

Accelerator Theory for Slow Extraction

Accelerators are complicated machines, possess many overlapping effects, and require dedicated study to understand the dynamics of a beam throughout the accelerator. **Ch. 1** established the complications of hadron therapy, and the various methods via which a beam should be delivered. This chapter will explain why such extraction is complicated to perform and design, to fulfil the requirements for necessary slow extraction efficiency. Before this can be explained, however, the basics of accelerator physics should be introduced. **Sec. 2.1** defines fundamental linear concepts assumed throughout the thesis. **Sec. 2.2** selects nonlinear dynamics concepts which are required for the purposes of slow extraction. **Sec. 2.3** explains some slow extraction specific equations and concepts. Finally we conclude by discussing the limits of the equations and approximations taken in this chapter.

Beginner-friendly Slow Extraction

Slow extraction, also referred to as resonant extraction, is a technique in accelerator physics to continuously remove beam from a synchrotron. In a synchrotron, beams of particles revolve roughly a million times a second (MHz frequencies). Conversely, hadron therapy treatment conventionally uses second-long spills, as explained by the needs of [Ch. 1](#). It is a challenge to transform a bunched MHz signal to a uniform and continuous Hz signal without ripples of frequency within this signal. To perform this transformation, the accelerator purposefully makes the beam unstable, and then uniformly controls this instability. This instability is created by putting the beam under resonance conditions: when the frequency of the particles are in sync with the frequency of the resonance, they increase in amplitude. A septum magnet is used to kick the particles that exceed a particular amplitude. The rate of particles becoming resonant can be controlled, which defines the rate of extraction. To understand these concepts further, explanations of accelerator dynamics are essential.

2.1 Linear Beam Dynamics

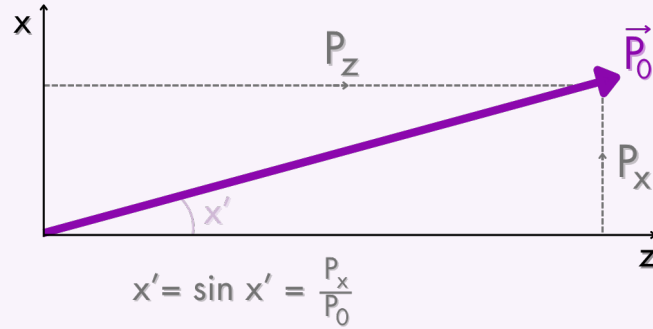
The ability for humanity to create and control intense densities of charged matter is an inspiring achievement. This is most notable whilst operating an accelerator or visiting the scale of engineering required within a facility. Reading and writing theory, however, has a sense of removal from the scenario which can dishearten those who are less mathematically enthused. This is especially the case for slow extraction, which is a topic with layers of understanding which may not ever be fully conquered. Despite this, extraction has the biggest impact, with direct effects on the application of the accelerator. With that said, let us investigate to as much detail as necessary to explain the phenomena explored in the results of the thesis.

2.1.1 The Beam

A beam is a collection of charged particles. The position and momentum of these particles are expressed with respect to the reference orbit of the beam. A complete picture of the beam in a synchrotron is expressed by three coordinates of position (x, y, z) and three coordinates of canonical momentum (p_x, p_y, p_z) . x, y are the horizontal and vertical transverse planes. It is convention to define the horizontal angular deviation from the reference momentum as $x' =$

$p_x/p_0, y' = p_y/p_0$, demonstrated visually in **Fig. 2.1**. As this angle is small, one can apply the small angle approximation where $\sin x' \approx x'$, in units of radians. As position and angle are coupled, dynamics are typically expressed in horizontal or vertical phase-space which is the plane of x vs x' or y vs y' . This thesis focuses on dynamics in the horizontal plane, and it is assumed to be decoupled from the vertical plane. All equations listed as a function of x in the horizontal plane also apply for the vertical plane.

Figure 2.1.: Schematic of particle momentum vector in (x, z) plane. Defines angle x' as per the transverse & longitudinal canonical momentum (P_x, P_z)



The distribution of an ideal particle beam will often take Gaussian-like distributions in the four transverse coordinates. As such, defining the total particle beam distribution $\sigma(x, x', y, y')$ often considers the 1-sigma envelope of a Gaussian beam in each plane $(\sigma_x, \sigma_{x'}, \sigma_y, \sigma_{y'})$. Other distributions are considered depending on the context, such as QGaussians, waterbag, uniform etc.

The size of a particle beam is proportional to the square-root of emittance ($\sigma_x \propto \varepsilon_x$). Emittance can be considered the multi-dimensional area that the beam occupies in position and momentum. For example, one can define the horizontal emittance $\varepsilon_x(x, x')$, the 4D transverse emittance $\varepsilon_{4D}(x, x', y, y')$, or the total 6D emittance $\varepsilon_{6D}(x, x', y, y', t, p_z)$. Physical emittance is calculated as the area of an ellipse, but absorbs the constant of π into the units - i.e. **Eq. 2.1** [37] would be expressed in units of $\pi \cdot \text{mm mrad}$.

$$\varepsilon_x = \frac{1}{\pi} \iint \sigma(x, x') dx dx' = \sqrt{\sigma_x^2 \sigma_{p_x}^2 - (\sigma_{x, p_x})^2} \quad (2.1)$$

A similar technique is used to calculate single particle emittance ε_p , which is shown in **Eq. 2.2**-

Eq. 2.5. Single particle emittance is the area enclosed by the oscillations of a single particle in phase-space, which also typically forms an ellipse. Here N_T is the number of turns T for the particle to complete one full oscillation, and x_0, x'_0 are the beam center-of-mass coordinates.

$$\sigma_{xx} = \frac{1}{N_T} \sum^T (x_T - x_0)^2 \quad (2.2)$$

$$\sigma_{x'x'} = \frac{1}{N_T} \sum^T (x'_T - x'_0)^2 \quad (2.3)$$

$$\sigma_{xx'} = \frac{1}{N_T} \sum^T (x_T - x_0)(x'_T - x'_0) \quad (2.4)$$

$$\varepsilon_p = \sqrt{\sigma_{xx} \times \sigma_{x'x'} - \sigma_{xx'}^2} \quad (2.5)$$

In accelerators the beam approaches relativistic speeds and this must be considered in its kinematics. In hadron therapy, particle energies are often lower than the mass energy per nucleon m_0 [MeV], so we refer to the kinetic energy T which is expressed in **Eq. 2.6** in megaelectronvolts per atomic mass unit [MeV/u] - meaning one must multiply by atomic number A to calculate Total Energy E . The relativistic factors (**Eq. 2.7, Eq. 2.8**) have a large effect on the beam dynamics, for example, the revolution frequency (**Eq. 2.9**) referred to in this thesis is defined by particle velocity $v = c\beta_{\text{rel}}$ divided by circumference C .

$$E = A(T + m_0) \quad (2.6)$$

$$\gamma_{\text{rel}} = \frac{E}{m_0} \quad (2.7)$$

$$\beta_{\text{rel}} = \sqrt{1 - \gamma_{\text{rel}}^{-2}} \quad (2.8)$$

$$f_{\text{rev}} = \frac{c\beta_{\text{rel}}}{C} \quad (2.9)$$

In addition, the size of the beam reduces as the beam is accelerated, and single particle normalised emittance $\varepsilon_{p,n}$ is defined to reflect this, multiplying physical emittance from **Eq. 2.5**, by the relativistic factor of $\beta_{\text{rel}}\gamma_{\text{rel}}$. This is used calculate single particle amplitude A_p as per **Eq. 2.10**. Single particle amplitude is the horizontal displacement of a particle in phase-space relative to its core (x_0, x'_0) , and will be used in later sections.

$$\varepsilon_{n,p} = \varepsilon_p \beta_{\text{rel}} \gamma_{\text{rel}} \quad (2.10)$$

$$A_p = \sqrt{\frac{\varepsilon_{n,p}}{\pi}} \quad (2.11)$$

Ion beams have additional considerations beyond single-charge beams, which emerges from their mass and their charge. The charge-to-mass ratio Z/A affects the particle's interaction with electromagnetic forces. The difficulty in bending the beam is expressed as the beam rigidity ($B\rho$), expressed in [Eq. 2.13](#). It is derived by equating the Lorentz force with the centripetal force as per [Eq. 2.12](#), then converting units into [GeV] and elementary force. In addition, the mass of heavier ion species also affects their momentum, where a carbon ion would require more energy to accelerate to the same speed compared to a helium ion, despite them having the same Z/A ratio.

$$F = q \cdot (v \times B) = \frac{mv^2}{\rho} \quad (2.12)$$

$$B\rho = \frac{mv}{q} \approx 0.33 \frac{p [\text{GeV c}^{-1}]}{q [\text{e}]} \quad (2.13)$$

Particle beams are not monoenergetic, and have a spread in momentum. The percentage spread in momentum with respect to the reference momentum is represented by the value $\frac{\Delta p}{p_0}$. The distribution of particles throughout this spread is conventionally modelled as a Gaussian. For a Gaussian, this spread is equivalent to the 1σ distribution where $\Delta p = \sqrt{\frac{1}{N} \sum (p_t - p_0)^2}$. Here p_t is the momentum of a single particle.

For the purposes of slow extraction, the momentum distribution is often prepared in such a way as to induce a uniform momentum spread. For a uniform distribution, Δp constrains the upper and lower bounds of the momentum spread around p_0 . Particles with different momentum will experience a different bending radius, as a result of [Eq. 2.13](#). The change in transverse positions of the particles from this momentum difference is referred to as dispersion (D_x, D_y) and angular dispersion (D'_x, D'_y). This correlation is given by [Eq. 2.14](#) - [Eq. 2.15](#), for any given value of $\frac{\delta p}{p}$ in distribution of $\frac{\Delta p}{p}$.

$$x = x_0 + D_x \frac{\delta p}{p}, \quad x' = x'_0 + D'_x \frac{\delta p}{p} \quad (2.14)$$

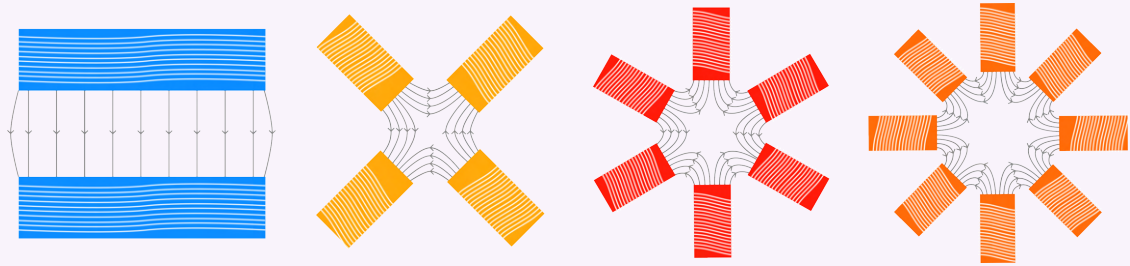
$$y = y_0 + D_y \frac{\delta p}{p}, \quad y' = y'_0 + D'_y \frac{\delta p}{p} \quad (2.15)$$

Particle beams of the same charge repel one another when they increase in proximity. This effect is known as space-charge. At small energies, the momentum in the longitudinal direction is reduced and the space-charge becomes more significant. At high relativistic speeds, this effect becomes negligible. Space charge is significant at low energies and high intensities, so becomes relevant for FLASH hadron therapy energies.

2.1.2 The Magnets

Synchrotron rings are composed of a series of magnets. The most common of these are dipoles and quadrupoles. **Dipoles** are made of two poles which provide a uniform field to bend the beam horizontally or vertically. **Quadrupoles** are made of four poles, and create a field which starts from 0 in the centre and increases with amplitude. This is used to focus the beam either horizontally or vertically, and defocus in the other plane. Higher-order magnets (sextupoles and octupoles) are introduced in [Sec. 2.2.3](#).

Figure 2.2.: Schematics of the four magnets types used in this thesis and their field lines: dipoles (blue), quadrupoles (yellow), sextupoles (red) and octupoles (orange).



These are often in the form of electromagnets, meaning they have a current I [A] which flows through the copper windings around the iron magnet poles and creates a magnetic field B [T]. A diagram of these magnets and their field-lines are represented in [Fig. 2.2](#). The strength coefficient of the magnet is referred to in [Eq. 2.16](#) as $k_n L$, where L is the length of the magnet and n is the magnet order ($0 = \text{dipole}$, $1 = \text{quadrupole}$ etc). The strength of the field B_n is

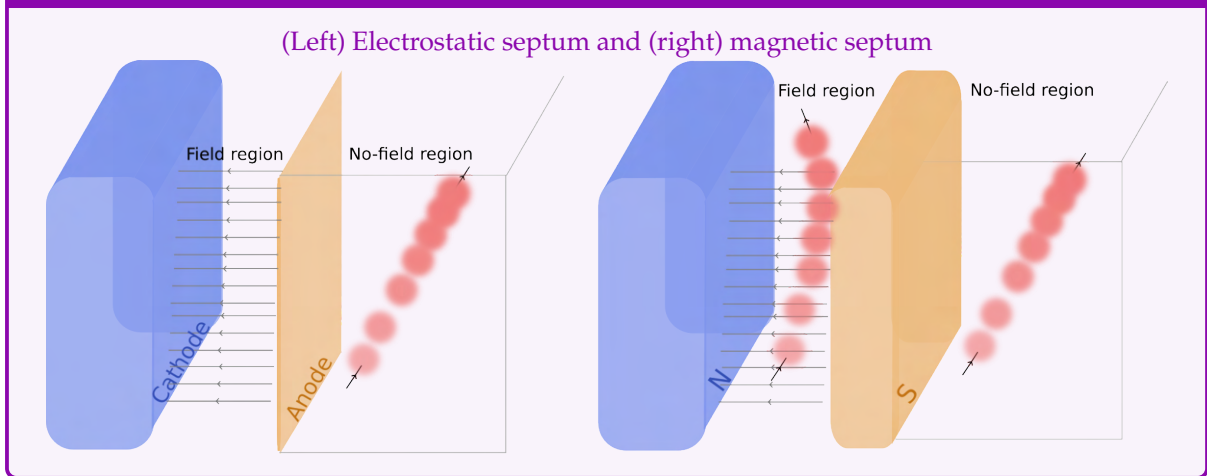
evaluated in the x -plane perpendicular to the closed orbit direction of motion.

$$k_n = \frac{1}{(B\rho)} \frac{d^n B}{dx^n} \quad (2.16)$$

Accelerator size is often limited by the strength of the dipole magnets, which defines the amount the particle can bend. To reduce the size of accelerators, often one has to use superconducting dipoles to reach higher field sizes. To reduce the number of individual magnets installed in the accelerator, one can include multiple combined magnets within the dipole. There are additional elements found throughout an accelerator: This includes RF cavities for acceleration and septa to split field and non-field regions.

Septum magnets normally fall into two categories: Electrostatic Septa (ES) and Magnetic Septa (MS). ES are formed of a thin-foil anode, and a thicker cathode, and apply a voltage across the two to form the field region. The thin foil is beneficial to reduce the interactions with the beam. MS are dipole-like magnets, but with a thinner pole to avoid beam losses. The ES provides a small kick (≈ 1 mrad) to ensure the beam is steered into the field region of the MS without hitting its pole, and the MS provides a larger kick (≈ 100 mrad) for the beam to be extracted from the machine. For higher energy synchrotrons, multiple MS may be required. Diagrams of both septa and their field lines are represented in **Fig. 2.3**.

Figure 2.3.: Schematics of the two septum types used in this thesis and their field lines. Blue and orange represent opposite polarities, and red circles represents the beam trajectory.

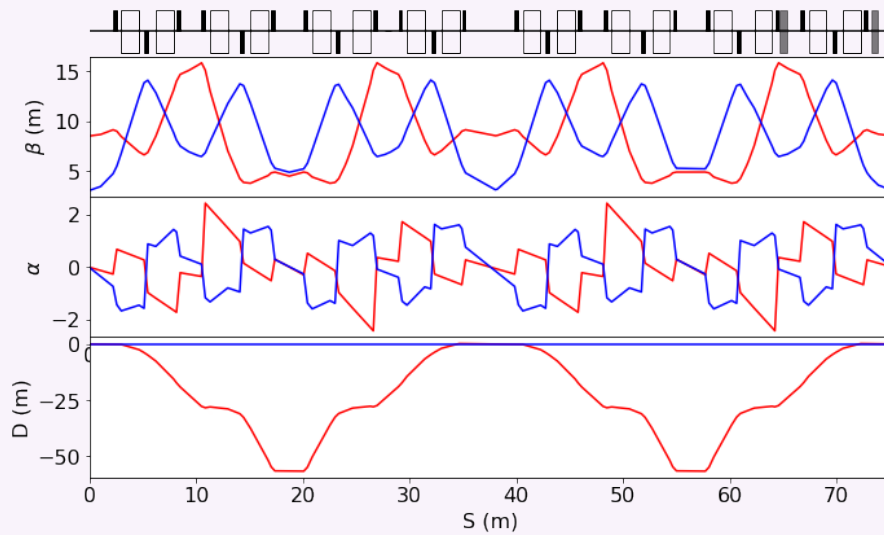


2.1.3 The Accelerator

These magnets are arranged in a closed loop which is referred to as a lattice. An example of a lattice can be seen in the top row of **Fig. 2.4**, which displays a series of 16 dipole magnets (transparent squares), 16 focusing quadrupoles (top lines) and 8 defocusing quads (bottom lines). As the particles orbit in a closed loop, the longitudinal component is no longer referred to as z , but as a position s along the ring of circumference C . This creates a transition from 3D cartesian coordinates to curvilinear coordinates, where the particles coordinates are defined relative to the on-orbit trajectory. Through your favourite transverse dynamics textbook chapter, one can

Figure 2.4.: Lattice and optics of PIMMS in horizontal (red) and vertical (blue) [15]

(1) Lattice overview as dipoles (white), quadrupoles (black) and septa (grey). Throughout synchrotron as a function of length S (2) Twiss beta oscillation (3) Twiss alpha and (4) dispersion.



derive and solve the linear equations of motion for the trajectory of the beam ([38] Section 7.2). The solution is an elliptical motion in phase-space via three parameters - known as the Twiss parameters. α defines the orientation of the ellipse, β defines the size in x, y and γ defines the size in x', y' . The Twiss parameters are related such that $\beta\gamma - \alpha^2 = 1$. As the quadrupoles focus the beam in one plane, β decreases, and α changes with respect to the rate of change of β . These values change periodically as a function of s , shown in **Fig. 2.4** (top) as quadrupoles oscillate β as a function of s , and α (middle) changes with rate of change of β . The change in D_x is shown as **Fig. 2.4** (bottom). Between any two points in the ring, the relative phase advance

μ is equivalent to the number of oscillations between those points, therefore can be expressed as $\mu_x = \int \frac{1}{\beta} ds$. Physically, phase advance corresponds to the rotation of the particles in phase-space. As the size and rotation of the beam is dependent on the Twiss parameters at the point in the circumference, where $x_{rms} = \sqrt{\varepsilon_{rms}\beta}$ and $x'_{rms} = \sqrt{\varepsilon_{rms}\gamma}$, the beam can be normalised with respect to these parameters. Normalised coordinate transformations are performed via Eq. 2.17 - Eq. 2.18, and should also factor in coordinate shift due to dispersion.

$$x_N = x / \sqrt{\beta} \quad (2.17)$$

$$x'_N = (\beta x' + \alpha x) / \sqrt{\beta} \quad (2.18)$$

Particles at large amplitudes are likely to hit the pipe wall and magnet materials in the accelerator and become lost. This limit is known as the physical aperture.

2.2 Non-Linear Beam Dynamics

2.2.1 Tune and Resonances

As beams revolve around the ring, they oscillate around the reference orbit in horizontal and vertical directions. The number of oscillations per turn is known as tune. Tune is a unitless measurement as it is the frequency of oscillations divided by the revolution frequency of the beam. Tune is composed of an integer component Q_{int} and a fractional component q where $Q = Q_{int} + q$. As quadrupoles control the number of oscillations per turn, they can be matched to provide particular tunes.

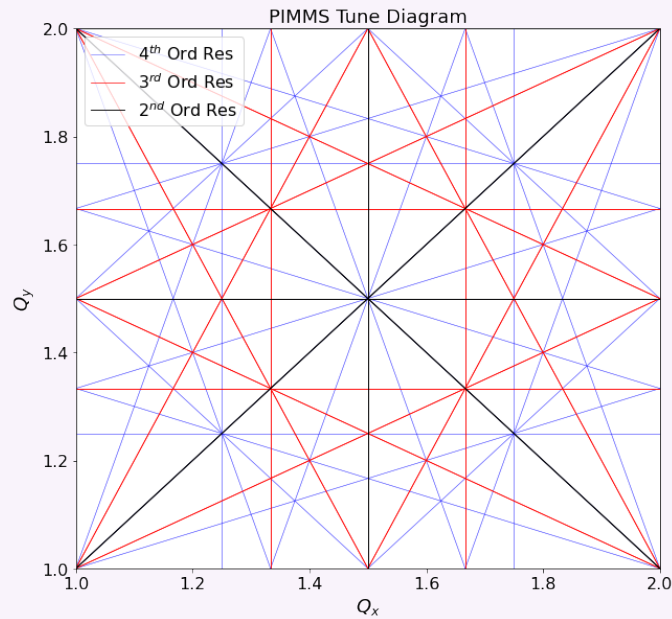
Due to the circular nature of a synchrotron, resonances occur when the tune of the beam is close to integer fractions of the revolution frequency. When resonant, particles experience perturbations, increase in amplitude and are lost on the apertures of the synchrotron. Systematic resonances are often caused by the field imperfection of magnets. Errors in the dipole fields drive first-order resonances at integer tunes, $q = 0, 1$ and errors in the quadrupole fields drive second-order resonances at such as $q = 0.5$. For higher-order resonances, sextupole errors drive third-order resonances at $q = 0.\dot{3}$, $0.\dot{6}$ and octupole errors drive fourth-order resonances at $q = 0.25, 0.75$. This trend goes up to infinite orders, although the strength of each order decreases by $\frac{1}{n!}$.

The general description of the resonance condition as applied to both horizontal and vertical plane is expressed in [Eq. 2.19](#) [38]. Here the fractional tunes are q_x and q_y , the order of the resonance is represented as N , and l, m, n are integers where $|l| + |m| = N$. This provides not only the resonances limited to one plane, but the coupled resonances between q_x and q_y .

$$lq_x + mq_y = nN \quad (2.19)$$

When plotted for $N \leq 4$, the corresponding resonance diagram for an integer resonance of $Q_{\text{int}} = 1$, such as the PIMMS machine, is represented in [Fig. 2.5](#). The 1st resonance is the boundaries of the figure, the 2nd resonances are displayed in black, the 3rd resonances in red, and the 4th resonances in blue. A particle beam can be represented as a spread on this diagram, and if their behaviour is within any of these lines, those particles are at risk of becoming resonant, increasing in amplitude and being lost.

Figure 2.5.: Diagram of resonance lines and their orders in horizontal & vertical tune space for the PIMMS lattice.



Each resonance line of order n is not an infinitesimal line in tune, but each has a stopband width of [Eq. 2.20](#), which is dependent on action J defined as [Eq. 2.21](#) [38]. The expected value of action is equivalent to emittance, both of which are proportional to the amplitude A of the particle squared. For a third order resonance, this can be rearranged and expressed as

Eq. 2.22 [15]. Larger sextupole strengths S create larger resonant bandwidths.

$$\Delta Q_{\text{stopband}} \propto n J^{n/2-1} \quad (2.20)$$

$$\langle J \rangle = \varepsilon = \langle A^2 \rangle \pi \quad (2.21)$$

$$A_{p,\text{stopband}} = \sqrt{48\pi\sqrt{3}} \left| \frac{\Delta Q_x}{S} \right| \quad (2.22)$$

Invariant amplitude can be calculated via single particle emittance as per **Eq. 2.5**. A more simplified interpretation of amplitude as per PIMMS Vol. 1 expresses it as $A_p = \sqrt{x^2 + x'^2}$, which is non-invariant and assumes perfectly on-orbit beams. The expression of amplitude-tune space in the context of slow extraction is referred to as the Steinbach diagram which is a useful interpretation to observe the tune and amplitude of the stable circulating particle beam with proximity to the resonance. For more detailed derivation and description of the resonance behaviour, Weidemann Ch. 16 Resonance is recommended [38].

2.2.2 Chromaticity

Much like how camera lenses focus red and blue light differently via chromatic aberration, the same occurs with quadrupoles magnets, as the focal point changes with particle energy. Chromaticity is expressed as a single number which correlates the tune deviation with respect to momentum spread - expressed in **Eq. 2.23**. An alternative terminology that is used is normalised chromaticity ξ_x , **Eq. 2.24**, which divides the chromaticity by tune. The convention used in this thesis always refers to dQ .

$$dQ_n = \frac{\Delta Q_n}{\Delta p/p} \quad (2.23)$$

$$\xi_n = \frac{1}{Q_n} \frac{\Delta Q_n}{\Delta p/p} \quad (2.24)$$

2.2.3 Higher order magnets

Sextupoles are magnets of 6 poles which provide a higher order focusing field when further from the closed orbit. This changes focusing as a function of particle position off-axis, so when the beam is in a region of dispersion - where momentum is correlated with position - the

machine's chromaticity is affected. Focusing sextupoles in high β_x positions primarily affect horizontal chromaticity, and defocusing sextupoles primarily affect vertical chromaticity. As mentioned, sextupoles affect driving terms of third orders, so multiple sextupoles are grouped in families of specific phase advance throughout the synchrotron to reduce these terms. The way they are applied in this thesis is primarily to excite the horizontal $q_x = 0.3$ tune, and to shape the resonant stopband width of Eq. 2.22. The quantification of a sextupole's strength is defined as normalised strength S , which is expressed in Eq. 2.25. With multiple sextupoles throughout the synchrotron, a 'virtual' sextupole can be established, which has an effective strength of Eq. 2.26, and an effective position at a phase of Eq. 2.27 [15]. For future uses, if the accelerator has more than one sextupole, it is assumed that $S = S_{\text{virt}}$.

$$S = \frac{1}{2}\beta_x^{3/2}k_2L \quad (2.25)$$

$$S_{\text{virt}} = \sqrt{\left[\sum_i S_i \cos(3\mu_{x,i})\right]^2 + \left[\sum_i S_i \sin(3\mu_{x,i})\right]^2} \quad (2.26)$$

$$\mu_{x,\text{virt}} = \frac{1}{3} \arctan \left(\frac{\sum_i S_i \sin(3\mu_{x,i})}{\sum_i S_i \cos(3\mu_{x,i})} \right) \quad (2.27)$$

Octupoles are the next stage of higher order magnets, made of 8 poles with a normalised strength of Eq. 2.28. Octupoles are used as a correction for chromaticity changing as a function of momentum. Consequentially, particles tunes are affected as a function of amplitude, called Amplitude Dependent Tune Shift (ADTS).

$$S_{\text{oct}} = \frac{1}{6}\beta_x^2k_3L \quad (2.28)$$

To calculate the ADTS from a single octupole, S. Y. Lee ([39] Section 7.3) defines the horizontal amplitude detuning α_{xx} in Eq. 2.29. For sextupoles, as presented in Eq. 2.30, the ADTS is a second-order effect which only emerges from the summation over all combinations of sextupole pairs, where the indices i, j connotes any given sextupole pair.

$$\alpha_{xx} = \frac{3}{8\pi} \oint S_{oct} ds \quad (2.29)$$

$$\alpha_{xx} = \frac{1}{16\pi} \sum_{ij} S_i S_j \left[\frac{\cos 3(\pi q_x - |\mu_{x,ij}|)}{\sin 3\pi q_x} + 3 \frac{\cos(\pi q_x - |\mu_{x,ij}|)}{\sin \pi q_x} \right] \quad (2.30)$$

2.2.4 Hamiltonians

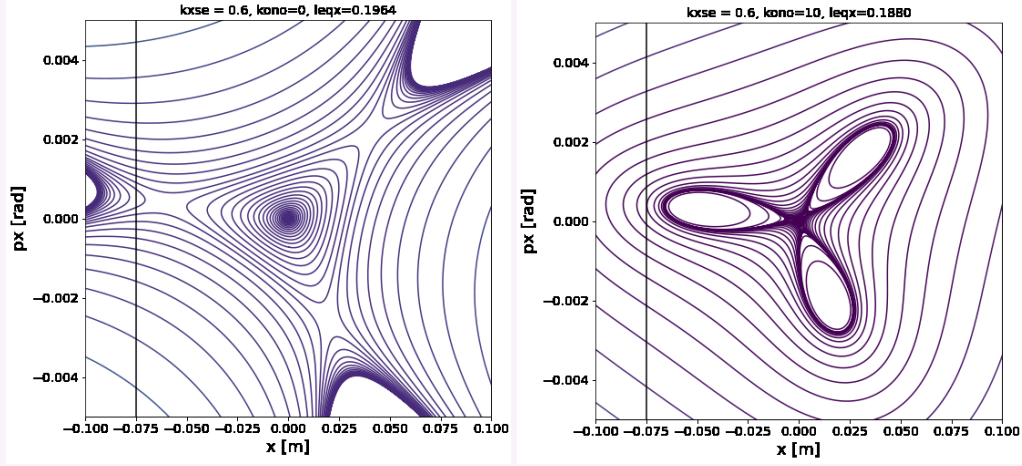
Hamiltonians are analytical tools used to describe the dynamic motion of a system in terms of its total energy and momenta. Hamiltonians are frequently applied to accelerator systems to understand linear and non-linear resonance effects in normalised phase-space. This approach can be derived from the general Hamiltonian from an accelerator, and predict the dynamical behaviour of the beam, e.g. the Kobayashi-Hamiltonian \mathcal{H}_S defined in [Eq. 2.31](#), is the resonant Hamiltonian that describes the machine at a tune distance from a driven third-order resonance [15]. The modified tune distance ϵ is defined as $\epsilon = 6\pi\delta Q$, where $\delta Q = Q_x - Q_{\text{res}}$, equivalent to the difference between the machine tune and the resonance.

$$\mathcal{H}_S = \frac{\epsilon}{2}(x_n^2 + x_n'^2) - \frac{S}{4}(3x_n x_n'^2 - x_n^3) \quad (2.31)$$

$$\mathcal{H}_{\text{Oct}} = \mathcal{H}_S + \frac{9}{32} S_{\text{oct}} (x_n^2 + x_n'^2)^2 \quad (2.32)$$

The Hamiltonian in unnormalised horizontal phase-space can be observed in [Fig. 2.6](#) (left), showing a phase-space orientation calculated at the electrostatic septum of the CERN proton synchrotron. The triangular stable area decreases as ϵ tends towards zero. Outside of this area, three boundaries between stable and unstable motion form, known as separatrices. The corresponding gif shows the Hamiltonian change as a function of quadrupole strength, as the tune approaches the resonance. When the tune is exactly on-resonance there is no stable area left of the beam. On the other side of the resonance, the stable triangle orientation is inverted 180° . With the addition of octupoles, Hamiltonian expansion of [Eq. 2.32](#) introduces an amplitude-dependent curvature to the separatrices, until a critical point of $\frac{S_{\text{oct}}}{S^2} \epsilon = 1/8$ [40]. Beyond this, three stable fixed-points form at $\text{Amp} = \frac{1}{3S_{\text{oct}}/S^2}$, corresponding to three islands around the initial stable triangle. This is observed in [Fig. 2.6](#) (right), with $k_3 = -10$ and S_{oct} corresponding to -25.5 .

Figure 2.6.: Contour plot of the Kobayashi-Hamiltonian equation in horizontal phase-space with (right) and without (left) octupoles



Available as a gif at

<https://gitlab.com/accelrtaylor/phdthesisx/-/tree/main/animations>

Parameters which are conserved with respect to the Hamiltonian are defined as invariant, which includes emittance ε and action J . Simulation codes are referred to as symplectic when the Hamiltonian structure is preserved. This conservation is violated when energy is added to or lost from the system, such as through synchrotron radiation, beam cooling or transverse exciters - however these effects are typically negligible in hadron synchrotrons.

2.3 Slow Extraction Theory

The above sections do not represent a complete overview of accelerator physics, but a selection of the concepts that are most important for the slow extraction topics raised throughout this thesis.

There are five main requirements that the synchrotron must fulfil for the correct resonance conditions to perform efficient slow extraction:

1. The horizontal tune is matched near the **third-order resonance**. After the acceleration of the beam, quadrupoles are matched to a stable tune close to the fractional tune of $\frac{1}{3}$.
2. A strong **resonant-driving sextupole** to drive the resonance, as per [Eq. 2.22](#). In an ideal scenario, the sextupole should be in a zero-dispersion region of the lattice to provide only

the resonance driving term, without any disruption to the chromaticity of the machine.

3. The **Electrostatic Septum (ES)** provides a small transverse kicks to separate the high-amplitude particles from the stable beam and to diverge them towards the MS. It has a thin anode foil on the order of 100 μm which is offset by X_{ES} from the closed orbit, and provides a field between this and the larger cathode. **The spread of particles within the field region of the ES is often called the bar-of-charge** due to its rectangular distribution in phase-space.
4. The **Magnetic Septum (MS)** provides a larger transverse kick to divert the beam towards the extraction line. The field is caused by a magnet pole on the order of $\approx\text{cm}$, hence the need for the ES to steer around this material. Due to this large geometry of material within the beamline, many particle losses during extraction are incident on the MS. The rate of particles extracted as a function of time is referred to as the **spill**. Spill shape (or macro-spill) refers to the uniformity of the spill, and spill ripple (or micro-spill) refers to the frequency of variation within the shape.
5. To create longer spills, the beam cannot be extracted at the same time, but must be gradually introduced to the resonant region. An **excitation option** is required to transfer particles in stable orbits towards the unstable motion beyond the separatrix.

2.3.1 Spiral Step

Once a particle is outside of the stable triangle in phase-space, its motion tends towards the three separatrices displayed in **Fig. 2.6** (left). Outside of the triangle, the particle oscillates exactly at a third-integer fractional tune, therefore at a given position every turn it appears that it jumps from one separatrix to the other. Comparing every three turns, from initial x_0, x'_0 , the unstable particle increases in position and angle via **Eq. 2.33** and **Eq. 2.34** respectively, until it reaches beyond the position of the ES foil X_{ES} [15]. The increase in position with turn number is referred to as the **spiral step** (Δx), and the increase in angle is referred to as **spiral kick** ($\Delta x'$). A larger sextupole strength S provides larger spirals, and therefore larger extracted beams. In addition it depends on the modified tune distance ϵ .

The final spiral step and spiral kick prior to extraction ($\Delta x_{\text{max}}, \Delta x'_{\text{max}}$) defined in **Eq. 2.35** and **Eq. 2.36**, is the most significant as it defines the dimensional spread of the extracted beam.

This is dependant on ϕ , which is the relative angle between the separatrix and the ES foil in phase-space, relative to the horizontal plane.

$$\Delta x = \epsilon x'_0 + \frac{3}{2} S x_0 x'_0 \quad (2.33)$$

$$\Delta x' = -\epsilon x_0 + \frac{3}{4} S (x_0^2 - x'^2_0) \quad (2.34)$$

$$\Delta x_{\max} = \frac{3}{4} S \frac{1}{\cos \phi} X_{\text{ES}}^2 \quad (2.35)$$

$$\Delta x'_{\max} = \frac{3}{4} S \frac{\tan \phi}{\cos \phi} X_{\text{ES}}^2 \quad (2.36)$$

2.3.2 Phase Advances

In the initial design stages of a synchrotron, the key components in slow extraction require specific positioning for optimal efficiency. The angle ϕ describes on the orientation of the separatrices at the resonant-driving sextupole, and the relative phase advance $\Delta\mu_{x,\text{XR} \rightarrow \text{ES}}$ between the resonant-driving sextupole (or virtual sextupole $\mu_{x,\text{virt}}$) and the ES. For a positive X_{ES} , ϕ should be $45^\circ \pm 15^\circ$ from the horizontal, to ensure that extraction is performed with only one separatrix facing the ES foil in phase-space [15]. For a negative X_{ES} the angle should be negative, to maximise the effect of a negative $\delta x'$ kick from the ES field. To obtain this necessary angle of ϕ , the position of the virtual sextupole strength should be chosen carefully with respect to the ES. There is no ideal value of $\Delta\mu_{x,\text{XR} \rightarrow \text{ES}}$ as it depends on the orientation of the separatrix at the resonant-driving sextupole. As the beam distribution has threefold rotational symmetry, solutions for $\Delta\mu_{x,\text{XR} \rightarrow \text{ES}}$ have a $\pm n \cdot 120^\circ$ degree of freedom.

Once the particles have received a kick from the ES, it is imperative that the same particle is oriented within the field region of the MS. Ideally, to fit within the limited magnetic field region and reduce losses, the long bar-of-charge should rotated in phase-space to be situated vertically. Therefore a relative phase advance of $\Delta\mu_{x,\text{ES} \rightarrow \text{MS}} = 90^\circ + n \cdot 180^\circ$ is necessary for that same separatrix to be correctly oriented towards the aperture of the MS. This process is significant for the needs of [Sec. 7.2.2](#).

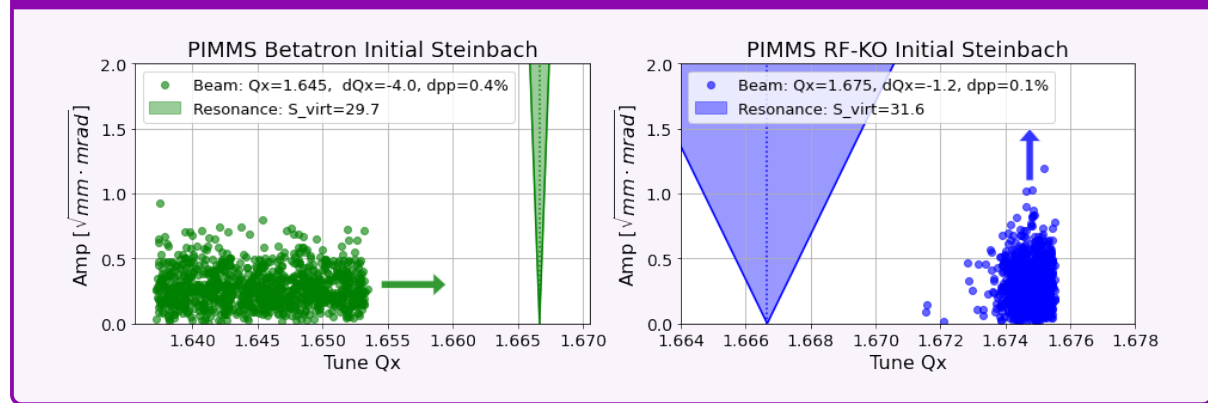
2.3.3 Excitation Methods

The above considerations are only specified during the design and commissioning phases to establish the extraction optics of the synchrotron. The art of slow extraction comes from the method and rate by which the particles are introduced to the resonance. The extraction rate, spill shape and spill ripple is dependent on the excitation components used.

Excitation can be separated into two categories: tune-dependent and amplitude-dependent effects. To understand both of these, we return to the concept of the Steinbach diagram. Tune-dependent excitation horizontally shifts the distribution of the beam towards the resonance, and amplitude-dependent excitation vertically shifts the distribution of a beam which is close to the resonance.

There are three main methods within tune-dependent excitation: Firstly one could adjust the

Figure 2.7.: Tune-amplitude diagram of a beam near a driven third-order resonance for betatron core (left) and RF-KO (right) extraction



tune of the machine directly, such as in **quadrupole-driven** extraction. Secondly one could alter the particles momentum, which changes the tune linearly with chromaticity, i.e. by using a **betatron core** - an element with a large coil around an iron core. Thirdly one could alter the momentum via **RF bucket** dynamics or similar.

For amplitude-dependent excitation, horizontal transverse excitations are necessary, which conventionally uses parallel plate kickers at radiofrequency frequencies, referred to as **RF-KO (radiofrequency knock-out)** extraction. Fig. 2.7 demonstrates two plots for the initial conditions of betatron core and RF-KO excitation as compared to the unstable region due to the resonant-driving sextupole. These were produced by calculating the tune for 1000 particles over 2048 turns from the method in Ch. 5, and calculating the individual amplitudes from

the single-particle emittance of [Eq. 2.5](#). The triangular stopband width was calculated from [Eq. 2.22](#).

Each excitation method has their own pros and cons. Betatron core requires a large momentum spread for a large tune spread, which introduces large dispersion and angular spread in extracted beam, so often requires the Hardt Condition, explained in [Sec. 2.3.5](#). For quadrupole driven extraction, changing quadrupole strength affects the optics, so will introduce a large spread in extracted beam. It is also possible to increase the sextupole strength to excite the stable beam, but this would increase the spiral step of the extracted particles, so would have to be in conjunction with a linear shift moving the beam further from the septum foil. RF-KO is more challenging to optimise compared to the other two, as unlike betatron and quadrupole-driven extraction, a linear rate of kick does not correspond to uniform spill (see [Sec. 7.1.2](#)).

[Ch. 3](#) introduces the excitation methods that each major facility uses.

2.3.4 Spill

As mentioned, spill refers to the rate of particles extracted as a function of time. The aim in slow extraction is to provide as smooth a spill as possible. Smoothness is an relative term, therefore the minimum useful timeframe must be defined, which is dependant on the needs of the application.

To quantify this numerically, a term is devised known as the spill duty factor. Spill duty factor is expressed in [Eq. 2.37](#). Here the total spill time is expressed as T_s , and the number of extracted particles N can be quantified across a small step in time t . More conventionally this is expressed in terms of the average extracted particles per interval $\langle N \rangle$.

$$\mathcal{F} = \frac{\langle N \rangle^2}{\langle N^2 \rangle} = \frac{\left[\int_0^{T_s} \frac{dN}{dt} dt \right]^2}{T_s \left[\int_0^{T_s} \left(\frac{dN}{dt} \right)^2 dt \right]} \quad (2.37)$$

The issue with defining duty factor is when time interval t becomes small. In this scenario, the expected particle count per interval is low, and therefore the probability of extracting the expected number of particles within this timescale becomes dominated by statistical noise. This is defined as the Poisson limit, where the probability of extracting N particles for an

expectation of μ particles becomes $P(N) = \frac{1}{N!} \mu^N e^{-\mu}$. As the distribution tends towards the Poisson limit, the variance tends towards the mean, where $\sigma^2 = \mu$.

For example, for a synchrotron with a beam of 1×10^8 particles and an extraction time of 1 s, a spill monitor with a 1 MHz readout time would expect 100 particles per interval. This would have a standard deviation of $\sigma = \sqrt{100} = 10$, and therefore would have a statistical noise of 10 %. The maximum duty factor F possible in this scenario is $\frac{\langle N \rangle}{1 + \langle N \rangle} = \frac{100}{101} = 0.99$.

2.3.5 Hardt Condition

As mentioned, beams with a significant momentum spread $\frac{\Delta p}{p}$ experience broader separatrices due to the horizontal dispersion at ES. This affects the size of the extracted beam distribution in phase-space and if excessive, could reduce downstream transmission in the extraction line. To optimise the extraction efficiency, a condition has been established using chromaticity as a free parameter to minimize the spread due to dispersion at the ES. [Eq. 2.38](#) applies separatrix angle $\phi = \phi_{XR} - \Delta\mu_{x,XR \rightarrow ES}$, where ϕ_{XR} is the orientation of the separatrix at the resonant-driving sextupole [15]. As S is often constrained by the required spiral step, one can adjust the dQ_x of the machine to match the horizontal dispersion and angular dispersion.

$$D_{x,ES} \cos(\phi) + D'_{x,ES} \sin(\phi) = -\frac{4\pi}{S} dQ_x \quad (2.38)$$

This condition, known as the Hardt Condition, is significant for betatron core extraction, as a large $\frac{\Delta p}{p}$ is often required to provide the tune spread needed for long spills. For RF-KO extraction, small momentum and tune spreads are desirable, so chromaticity is typically kept small, rather than optimised for the Hardt condition. The Hardt Condition is inapplicable for quadrupole driven, as the spread in bar-of-charge is also due to a change in optics, not just due to dispersion. When ES, MS and resonant-driving sextupole are in zero-dispersion regions, the Hardt Condition requires an achromatic transfer between magnets, or zero chromaticity in the machine.

For the above reasons, in this thesis the Hardt Condition is only significant for betatron core extraction from the PIMMS lattice, where the optimal chromaticity is calculated to be $dQ_x = -4.041$.

2.4 Conclusion

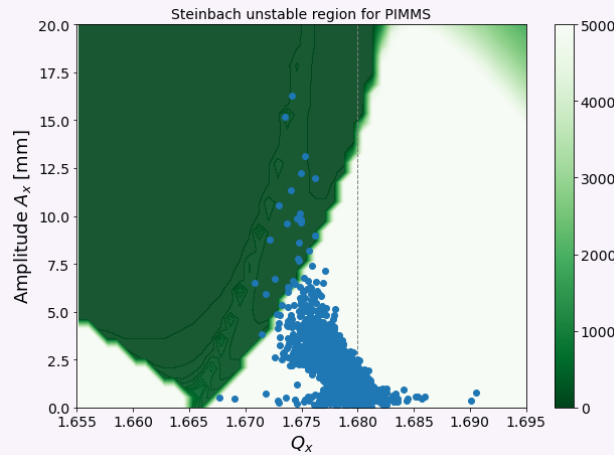
2.4.1 Exceptions

During the investigations performed in [Ch. 5- Ch. 8](#), there are scenarios where the prevailing theories are insufficient to describe the dynamics occurring in the system. For this reason, there is a limit at which the terminology described above, begins to break down.

In particular, this occurs when describing tunes with a close proximity to the resonance. In these regions, particles are likely to experience amplitude-detuning effects which cause shifts in tune towards the resonance. This change in frequency in itself is a component within the tune, as a higher order effect. In a more extreme case, as analysed in [Ch. 5](#), the beam near the resonance is being perturbed by a strong oscillator at a single frequency. In these conditions, linear descriptions of tune are no longer helpful.

The approximation for particle tune as a square-shaped stack is appropriate for large tune spread, as emergent effects are contained within the tails. For small tune spreads, as explored in [Sec. 7.2](#), these approximations begin to break down.

Figure 2.8.: Contour plot of a grid of tracked particles in δp - A . Colourbar represents the turn where the particle is lost from 0 to 5000, where white is more stable, and green is less stable



When it comes to the resonance, the stopband width is not always fully linear, but also factors in amplitude detuning effects, and is also asymmetrical. One example of this is in the PIMMS lattice, where a grid of particles can be tracked in momentum and position, to observe the

limits in tune-amplitude space. **Fig. 2.8** represents this concept, by tracking a grid of coordinates, representing regions of stability (white) and instability (green) as a function of the turn number when the particle is lost. This figure was created using the tracking tools of **Ch. 4**. Superimposed in blue is a particle beam distribution which is experiencing RF-KO extraction in the same simulation. An additional consideration is that this figure is produced by converting momentum δp into tune via a linear correlation with chromaticity. With non-negligible non-linear chromatic terms, this assumption is not correct.

2.4.2 Theory Discussion

To conclude, an understanding of transverse beam dynamics and some specific knowledge of non-linear dynamics is required to describe the effect of slow extraction. A description of the beam coordinates, emittance and relativistic effects was considered. An overview of the magnets, up to octupoles, and septum geometry is described. The transverse linear and non-linear dynamics of an accelerator was described, with a focus on resonances, chromaticity and amplitude detuning. Whilst longitudinal dynamics effects are also significant to slow extraction, theoretical understanding of this has not been applied for the projects explored in this thesis.

Slow extraction effect is complex, with many overlapping components and specifications required throughout the synchrotron. The relevant equations were listed - many of which will be referred to throughout the thesis, in particular the description of the Hamiltonian at the third-order resonance. Detail is given to slow extraction phase-advance set-up, the different excitation options, and resulting effects on spill quality.

In many capacities, there is a limitation to the understanding that theory can provide, particularly with overlapping dynamic effects in very close proximity to the third order resonance. For this reason, in absence of an available operational synchrotron which match the hadron therapy requirements of **Ch. 1**, simulations are the predominant investigative tool within this thesis.

Bibliography

- [15] L. Badano et al. *Proton-Ion Medical Machine Study (PIMMS)*, 1. 1999.

- [37] Giulia Russo. “Precise tune determination and split beam emittance reconstruction at the CERN PS synchrotron”. Presented 14 Mar 2022. Frankfurt U., 2022. URL: <https://cds.cern.ch/record/2862526>.
- [38] H. Wiedemann. *Particle accelerator physics: Third edition*. Jan. 2007, pp. 1–948. ISBN: 978-3-540-49043-2. DOI: 10.1007/978-3-540-49045-6.
- [39] S. Y. Lee. *Accelerator physics; 3rd ed.* Singapore: World Scientific, 2012. URL: <https://cds.cern.ch/record/1425444>.
- [40] M. A. Fraser, B. Goddard et al. “Demonstration of slow extraction loss reduction with the application of octupoles at the CERN Super Proton Synchrotron”. In: *Phys. Rev. Accel. Beams* 22 (12 Dec. 2019), p. 123501. DOI: 10.1103/PhysRevAccelBeams.22.123501.

*Your great new idea?
Forgotten papers wrote it,
sixty years ago.*

3

Review and Current Status of Slow Extraction

The needs of the NIMMS machine, and the theoretical principles of how to get there have been addressed in **Ch. 1** & **Ch. 2**. Now we can discuss recent breakthrough research that has been developed over the years across many slow extraction facilities. Learning about the current status of this research contextualises the contributions to slow extraction that this thesis provides.

Sec. 3.2 describes a brief history of facilities that provide slow extraction beams, grouped by trends of extraction design choices. **Sec. 3.3** lists valuable developments in beam dynamics R&D, and which facilities have published these developments. Finally, **Sec. 3.4** emphasizes how NIMMS contributes to the field and which of these technologies are expected to be integrated into the NIMMS baseline design.

3.1 Introduction

Within the field of accelerator physics and beam dynamics, slow extraction holds a specific research community. Its complex non-linear dynamics and specific experimental requirements means that it is often not the primary form of extraction unless there is a dedicated demand for slow, continuous spills. This demand is typically for medical or material irradiation applications, and also some high energy experiments. Subsequently, progress in this field is initially tailored for the needs of each facility, but is often highly transferable. This transferability means that it is easy to identify trends between facilities, which prompts active discussion on topics which connect said facilities. Researchers often discuss via the ICFA¹ mini-workshop on slow extraction workshop, the annual IPAC² conference, and IFAST-REX³ meetings. The first two are general accelerator topics, whereas iFAST-REX has specific focuses on spill measurement devices, RF-KO signal generation and simulation tools. These regular discussions provide insightful knowledge of the state-of-the-art developments. From these discussions, one can note that whilst there are many ways to produce a slow extracted beam, there are common trends on how this is performed. This chapter will identify and elaborate on the trends and recent developments which are relevant for the NIMMS study.

3.2 Historical

Slow extraction was first conceptualised for synchrotrons in 1960, by Hammer and Laslett. Their technique was adapted from extraction commonly used in synchrocyclotrons, applied to an Alternating-Gradient (AG) synchrotron [41]. This approach used either integer or second-order resonances, resulting in a faster but less stable extraction compared to the modernly used third order resonance. At the same time, Hereward applied resonant extraction to the CERN Proton Synchrotron (PS) [42] in 1961, which was used at a horizontal tune of 6, and gave a beam spill time of ≈ 150 ms [43] to the PS South Hall [44]. Later, in 1965 this was moved to the East Area, using a tune of 6.25.

¹International Committee for Future Accelerators

²International Particle Accelerator Conference

³Innovation Fostering in Accelerator Technology and Science - WP5.3 Resonant EXtraction

3.2.1 With Quadrupole-driven Extraction

It was not until 1971 that the decision was made to move to the third-order resonance for extraction to the PS East and West areas. The quadrupole-driven third-order resonance was referred to at the time as SQuaRE (Semi-QUAdrupole Resonant Extraction) [45]. The horizontal tune was ramped linearly from 6.25 to about 6.36. Even back then, the extraction was performed with a coasting beam to reduce the dependence on the RF radial loop and revolution frequency ripples. Many innovative slow extraction methods were first explored on the PS during this era, often published as brief technical notes [46].

The SPS began operation in 17 June 1976. Continuing from the PS, the SPS was able to extract at integer and half resonances, but operationally prioritised the third-order [47]. Like the PS, particles were brought into resonance by changing the current of the main-magnet quadrupoles to go towards the North Area, where it is still sent operationally to this day.

For the early emergence of slow extraction, it made sense to move particles into resonance via quadrupole tune-ramping, as that was the experimental method available at the time. Quadrupole-driven extraction is still used, particularly for high-energy machines which only use resonant extraction as the secondary way of extracting, i.e. PS, SPS, J-PARC, GSI. As mentioned in [Sec. 2.3.3](#), quadrupole-driven extraction is not considered ideal, as it changes the optics (and therefore dispersion) of the machine as a function of time. The resulting extracted beam has a wide angular spread, as the separatrices move as a function of momentum.

3.2.2 With Betatron Core

Beam requirements change when one enters the domain of clinical applications. Throughout second-long spills, a very stable extraction is essential. In particular, it is an advantage to keep lattice and resonant conditions constant and instead extract by moving the beam into the resonance [48]. As discussed in [Sec. 2.3.3](#), a betatron core is a large coil with an iron core, which is able to adjust the momentum of the beam with time, to induce it into the resonance. This option is beneficial as it produces a smoother spill than via quadrupoles and, safety-wise, will not send accidental beam spikes from tune slippage.

Prior to 1998, CERN hosted the PIMMS design study [15], a collaboration between the TERA foundation, MED-Austron and Onkologie-2000. A major motivation of the study was to solve

beam dynamics challenges to ensure stable slow extraction as the primary operational extraction method. The conclusions of this are presented in PIMMS Volume 1, and the outcome was the creation of CNAO and MedAustron facilities, as mentioned in **Ch. 1**.

Since commissioning and operation, these two facilities continue research into slow extraction R&D, included in **Sec. 3.3**.

3.2.3 With RF-KO

Whilst RF-KO has been discussed as a technique for the PS since 1961 [49], it was not actively involved in hadron therapy extraction until it was re-discovered in 1992 [50]. The 1992 paper considered simulations performed on the second-order resonance, so the technique was verified experimentally on the TARN II ion cooling ring at the third-order resonance with success. It has since become the baseline extraction method of HIMAC [51] (Heavy Ion Medical Accelerator in Chiba).

The major benefit of RF-KO for HIMAC is that the separatrices remain constant throughout extraction, and the beam can be rapidly switched on and off within a time frame less than the breathing period of the patient [52]. In addition, the transverse excitation signal is very adaptable, so the AM (amplitude modulation) and FM (frequency modulation) can be adjusted in accordance with the needs of the extraction.

The success of the RF-KO extraction method in a clinical setting encouraged the design choice of the Heidelberg Ion-Beam Therapy Center (HIT) extraction. In collaboration with GSI, this facility was built in 2008 and provides proton, helium, carbon, and oxygen beams for Heidelberg University Hospital. RF-KO excitation is the baseline design option, and is performed with an intensity-feedback system [53].

3.3 Recent Developments

As mentioned, slow extraction technology is highly transferable between facilities. Given the numerous synchrotrons mentioned in **Sec. 3.2**, it makes sense to compare the recent developments, rather than analyse each synchrotron separately. A comprehensive overview of the extraction R&D technologies, along with their published evidence, is collected in **Tab. 3.1**. A selection of facilities that relate to NIMMS are shown in the top row. The subsequent three rows shows the most common beam excitation methods. The final 8 rows show recent devel-

opments and advanced extraction additions on top of these baselines. This table is complete to the author’s best knowledge as of the Slow Extraction Workshop 2024. A citation does not necessarily mean that this technology is used operationally, but that a study has been performed and published that explores that technology. Whilst there is continuous development in slow extraction instrumentation and hardware, this chapter focuses on developments in beam dynamics.

Table 3.1.: Summary of Slow Extraction R&D as published for each facility. \circ represents NIMMS synchrotron considerations. \checkmark represents unpublished work, through personal correspondence

	MA	CNAO	HIT	HIMAC	PS	SPS	GSi	J-PARC	NIMMS
Quad-Driven	[54]				[55]	[47]	[56]	[57]	\circ
Betatron Core	[58]	[59]							
RF-KO	[60]	[61]	[62]	[52]	[63]		[64]		\circ
COSE	[54]				[65]	[66]			
Quad + RF-KO					[67]		\checkmark	[68]	
Adv. RF-KO signals			[69]	\checkmark			\checkmark		\circ
Empty-Bucket	[70]	[71]			[72]	[73]			
Burst Extraction	[74]				[75]				\circ
MEE	[76]	\checkmark	[77]	[78]					\circ
Octupole Folding					[Ch.6]	[40]			
Crystal Channelling						[79]			
Helium	[21]	\checkmark	[23]	\checkmark					\circ
FLASH	[80]		[31]	\checkmark					\circ

3.3.1 COSE

Constant-Optics Slow Extraction (COSE) is a method to solve the moving optics problem caused from quadrupole-driven extraction [66]. A common way to solve this is to ramp the B-field of the dipole magnets operationally. As the strengths of all magnets in the machine is dependent on the magnetic rigidity $B\rho$ (Eq. 2.16), this allows for a way to move the tune of the machine whilst keeping the optics constant. Similar techniques are applied under different names, but as referred to as COSE, this method has been applied operationally to the PS, SPS and MedAustron. It is traditionally difficult to perform in simulations, as it requires the dynamic adjustment of every magnet in the synchrotron. Likewise, this is mainly effective operationally with flexible and interconnected control systems such as LSA (see Sec. 6.1.2).

3.3.2 Advanced RF-KO

The flexibility of RF-KO and its attributed excitation signal allows for advanced techniques which are custom suited to the facility. This includes feedback systems, feed-forward systems, and spill ripple reduction methods. Whilst there are infinite ways to adapt the RF-KO system, two developments are mentioned here in particular.

Quadrupole-driven with RF-KO

As discussed, a disadvantage of quadrupole-driven excitation is that the ripple is dominated by the current frequency of the tune-ramping quadrupoles. Facilities - including J-PARC and PS - have combined the benefits of both RF-KO and quadrupole-driven extraction. This is especially beneficial for high-energy facilities that may not have sufficient transverse exciter voltage to extract the entire spill uniformly. J-PARC explored this in 2010, applying both longitudinal noise and transverse noise [68]. The PS in 2023 converted the QMeter application into providing a transverse excitation to an RF-KO exciter, and now uses this by default in the operational cycle to improve the quality of the COSE-like excitation [67].

FM Signals

Beam Transfer Function (BTF) investigations at HIT and GSI revealed fundamental behaviours of a beam undergoing RF-KO excitation [62]. The tune distribution of the beam does not represent a Gaussian, but instead a splitting into two coherent motions. This realisation changes how FM can be implemented in RF-KO, to cover the realistic frequency dynamics of the particles. A dedicated part of the single-particle tune dynamics of this research was performed as part of this thesis, shown in [Sec. 5](#). The ideal scenario is to improve the quality of the spill until it hits the Poisson limit - i.e. the inherent statistical noise. A common signal which is beneficial is random binary phase shift key (RBPSK) which is a sinusoidal signal which is randomly flipped 180° in phase [69]. This implements a broad spectrum with strong sidebands.

Another recent concept, called noise++, applies a broadband random signal, with a few targeted sharp peaks of a single frequency. It is specifically created for the purposes of slow extraction to reduce ripples whilst avoiding adding additional ripples artificially [69].

3.3.3 Empty-Bucket Channelling

The use of longitudinal buckets to affect the momentum shift of particles has been discussed via the PS since 1981 [46]. **Empty bucket channelling** was proposed as part of the PIMMS slow extraction development [81]. In this technique, a coasting beam is set up at flat-top in the synchrotron. A series of RF buckets are produced by turning the cavity on, but ensuring that the coasting beam is outside of these buckets. Then either the beam or the buckets are moved such that the beam dynamically shifts between the buckets, which produces a rapid change of momentum into a resonance compared to betatron core momentum changes. It has been explored at MedAustron, CNAO, PS and SPS due to its potential benefits in mitigation of spill ripple. The latest summary of updates in Empty Bucket R&D at CERN is presented in [82].

Burst extraction is a form of longitudinal slow extraction where rapid RF phase displacement allows for short and intense bursts of beam. It has the benefit of providing multiple bursts throughout the cycle by a series of sweeps through the beam. This means the same number of particles can be extracted in the same period of time, but with flux constrained into smaller bursts. This technique allows for fast extraction rates, dependent only on the flexibility of the RF-cavity ramping rate. This method was tested in simulations for the PS and MedAustron, and experimentally tested at MedAustron. At the SPS, this technique is being developed for the application of ENUBET, to provide short and intense pulses for neutrino physics experiments [83].

Burst extraction has particular interest in this thesis, as it has strong applications in producing beams for FLASH. The exact specifications of this technique as it pertain to NIMMS will be discussed in [Sec. 7.2.4](#).

3.3.4 Multi-Energy Extraction

Throughout this thesis, the importance of having high intensity is referred to a number of times. The foremost reason being that large intensity is often required to deliver high dose rates - for FLASH. However, this is also essential for a synchrotron that offers **Multi-Energy Extraction** (MEE).

MEE aims to reduce long patient beam delivery times. As most synchrotrons extract using a different cycles for each energy level, there is often a waiting time of around 2 s. This is because every cycle must have time for the magnet currents to fully ramp [84] up to flat-top and down

to zero, to avoid issues of hysteresis. An alternative is to have multiple energy operation with extended flat-tops. This was first demonstrated by HIMAC in 2010 [78]. There they provide 100-200 ms of continuous beam spill for each energy level. This technique was then adopted at HIT from 2017. MedAustron has validated the feasibility of MEE at their synchrotron via both RF-KO extraction and COSE extraction [74]. The majority of the challenge for MEE comes from the control systems implementation, rather than a beam dynamics challenge.

In order to combine multiple cycles into one, it is necessary to increase the number of injected protons by the same factor. For example, 10 flat-tops of different energies requires a tenfold increase in initial intensity. Obtaining these larger scales of intensity is challenging in synchrotrons. This is because of space-charge, which is especially prevalent at low energies during injection. To overcome this, **Multi-Turn Injection** (MTI) cumulatively adds to the circulating beam each turn by ‘painting’ across the transverse phase-space. This injection method was conceptualised in 1965, for the purposes of the PSB [85], and since then has been incorporated in some form into all of the mentioned facilities of **Tab. 3.1**. Because of the low intensity of the carbon ion sources and low transmission in the injector linac, present intensities are still low even with usage of MTI [86].

3.3.5 Octupole Folding

Incorporating higher-order nonlinear effects adds additional control over the shape of the slow extraction phase-space. In particular, the amplitude-dependent detuning effect from octupole magnets affects separatrix orientation at high amplitudes. This versatility is beneficial to optimise beam distribution to the geometry of the extraction septum. This technique was first applied operationally at the SPS [40] in 2019 to provide an extraction efficiency improvement of 40%. A detailed study of this effect, and its first application to the PS, is written in **Ch. 6**.

3.3.6 Crystal Channelling

A paradigm shift in beam control methods occurred when it was discovered that electrostatic forces between crystal atomic planes steers charged particle beams. The symmetry of a perfectly aligned crystal forms potential wells between which particles can move through [87]. Furthermore, this technique works best with thin-layers of material, as it reduces the likelihood of scattering. As the effect is independent of energy, it has strong benefits at the LHC,

where the 7 TeV beam can be steered with mrad of bending from mm of silicon crystal, rather than metres of dipole magnets. For this reason, the main current application in literature is for collimation effects [88].

A major limitation of this method is its bending efficiency, with 10-20% of the beam successfully transmitted, the rest either passed through, scattered or volume reflected. To make the best use of crystals, multi-pass mechanisms provide multiple opportunities for any given particle to be channelled, increasing its efficiency to 70-80% [89]. This unlocks opportunities for creative ways to incorporate crystals as part of the extraction process.

In the SPS this was explored via crystal shadowing, to channel extracted particles into the septum field and avoid the septum anode [89]. It has also been combined with octupole folding to reduce losses further, up to $4\times$. As a similar concept, many slow extraction facilities incorporate passive diffusers to pre-scatter the beam prior to the ES to localise losses away from the septum.

Considering that medical machines are typically low-energy, on the ≈ 100 MeV scale, it is important to verify that the channelling effect still applies in this domain. In theory, the physics of crystal channelling is the same for a broad range of energies, from keV to TeV [90]. In practise, as beam energy lowers, there is a linear reduction with the crystal size, which is beneficial as it reduces the number of scattering opportunities for any given particle. On the other hand, smaller crystals may increase the risk of de-channelling, resulting in a particle which does not gain the full angular kick, and may be lost on accelerator aperture. Whilst crystal channelling has been studied experimentally for high-energy fast extracted protons [91], and simulations have been achieved for low-energy slow extracted protons [92], there have been no simulations or experimental investigations to the channelling efficiencies of low-energy carbon ions within slow-extraction. This topic is a novel field and, if successful, would have some very interesting implications on the compactness of the extraction process of synchrotrons.

3.3.7 FLASH

Whilst there are plenty of synchrotrons that provide sub-second extraction rates for their experimental facilities, only a few have been explicitly published for the intention of FLASH. HIT performed FLASH with carbon ions for continuous spill RF-KO [31] (RF-KO defined in [Sec. 2.3](#)), MedAustron with pulsed RF-KO extraction and burst phase-displacement extraction [80], and HITACHI proton synchrotrons with an RF method [93]. Many are adapting

existing hardware to fulfil the FLASH conditions, optimising the existing intensities available from the ion sources.

3.4 Slow Extraction R&D at NIMMS

Each aforementioned facility and machine provides a new environment and application to enable novel innovations and R&D to emerge. In relation to the broader slow extraction community, NIMMS has a unique appeal as the machine is in the early design stage. When starting from scratch, slow extraction innovation can be inherent in the design without machine constraints. Furthermore, as NIMMS is intended for both radiobiological research and treatment, it has a focus on the range of beam parameters it can provide, instead of only baseline clinical needs. As a facility, NIMMS will not only incorporate existing **state-of-the art research**, but will expand on this, to contribute to the research community.

The circles of **Tab. 3.1** list the expected extraction technologies that reasonably would be part of the final design. On top of this, additional concepts have been explored as part of this thesis, including betatron core and octupole folding.

To provide a summary of **what NIMMS can learn from literature**:

In terms of baseline extraction design, NIMMS will be using **RF-KO** extraction. Using **quadrupoles** to ramp through the resonance will also be possible. The exciter of the RF-KO will be intended such that custom-frequency signals can be transmitted to match the **two-peak frequency** distribution of the beam. The limits of RF-KO for FLASH-like extraction will be tested, but it is likely that **burst extraction** is essential for microsecond spill timescales. **Multi-Energy Extraction** will be a baseline requirement of the dose-delivery method of NIMMS - and with MTI over ten turns to increase machine intensity. The lattice will be designed to handle the higher emittance that results from this large number of MTI turns. In combination with methods that provide faster extraction regimes, this high intensity gives it the ability to perform **FLASH-like** doses for large volumes of area. And both **helium ion** treatment and **FLASH** dose timescales will be offered as the radiobiological output.

The simulations exploring and confirming these options are studied in **Ch. 7**.

Bibliography

- [15] L. Badano et al. *Proton-Ion Medical Machine Study (PIMMS)*, 1. 1999.
- [21] N Gambino, M Kausel et al. "First injector commissioning results with helium beam at MedAustron Ion Therapy Center". In: *Journal of Physics: Conference Series* 2244.1 (Apr. 2022), p. 012109. ISSN: 1742-6596. DOI: 10.1088/1742-6596/2244/1/012109.
- [23] T. Tessonnier, S. Ecker et al. "Commissioning of Helium Ion Therapy and the First Patient Treatment With Active Beam Delivery". In: *International Journal of Radiation Oncology*Biophysics* 116.4 (July 2023), pp. 935–948. ISSN: 0360-3016. DOI: 10.1016/j.ijrobp.2023.01.015.
- [31] W. Tinganelli et al. "Ultra-High Dose Rate (FLASH) Carbon Ion Irradiation: Dosimetry and First Cell Experiments". In: *International Journal of Radiation Oncology*Biophysics* 112.4 (2022), pp. 1012–1022. ISSN: 0360-3016. DOI: <https://doi.org/10.1016/j.ijrobp.2021.11.020>.
- [40] M. A. Fraser, B. Goddard et al. "Demonstration of slow extraction loss reduction with the application of octupoles at the CERN Super Proton Synchrotron". In: *Phys. Rev. Accel. Beams* 22 (12 Dec. 2019), p. 123501. DOI: 10.1103/PhysRevAccelBeams.22.123501.
- [41] C. L. Hammer and L. Jackson Laslett. "Resonant Beam Extraction from an A. G. Synchrotron". In: *Review of Scientific Instruments* 32.2 (1961), pp. 144–149. DOI: 10.1063/1.1717299.
- [42] H G Hereward. *The possibility of resonant extraction from the C.P.S.* Tech. rep. Geneva: CERN, 1961. URL: <https://cds.cern.ch/record/297121>.
- [43] H. G. Hereward. "The Cps Resonant Extraction System". In: (1963). URL: <https://cds.cern.ch/record/2065209>.
- [44] Y. Baconnier, O. Barbalat and D. Dekkers. *Status of studies on the CPS slow extraction.* Tech. rep. Geneva: CERN, 1969. URL: <https://cds.cern.ch/record/2831263>.
- [45] J-P. Burnet, C. Carli et al. *Fifty years of the CERN Proton Synchrotron: Volume 1.* CERN Yellow Reports: Monographs. Geneva: CERN, 2011. DOI: 10.5170/CERN-2011-004.
- [46] R. Cappi and C. Steinbach. "Low frequency duty factor improvement for the CERN PS slow extraction using rf phase displacement techniques". In: *IEEE Trans. Nucl. Sci.* 28 (1981), pp. 2806–2808. DOI: 10.1109/TNS.1981.4331919.
- [47] Y. Baconnier et al. "Extraction from the CERN SPS". In: *IEEE Trans. Nucl. Sci.* 24 (1977), pp. 1434–1436. DOI: 10.1109/TNS.1977.4328969.
- [48] L Badano and S Rossi. *Characteristics of a betatron core for extraction in a proton-ion medical synchrotron.* Tech. rep. Geneva: CERN, 1997. URL: <https://cds.cern.ch/record/327305>.
- [49] M. Geiger. *Partial beam knock-out: Note on some preliminary experimental results.* Tech. rep. Geneva: CERN, 1961. URL: <https://cds.cern.ch/record/2831782>.
- [50] K. Hiramoto and M. Nishi. "Resonant beam extraction scheme with constant separator". In: *Nuclear Instruments and Methods in Physics Research Section A: Accelerators, Spectrometers, Detectors and Associated Equipment* 322.2 (1992), pp. 154–160. ISSN: 0168-9002. DOI: [https://doi.org/10.1016/0168-9002\(92\)90023-W](https://doi.org/10.1016/0168-9002(92)90023-W).
- [51] A. Itano, M. Kanazawa and K. Sato. *HIMAC synchrotron.* Japan: Research Center for Nuclear Physics, Osaka Univ, 1990. URL: http://inis.iaea.org/search/search.aspx?orig_q=RN:22016454.
- [52] K. Noda et al. "Slow beam extraction by a transverse RF field with AM and FM". In: *Nuclear Instruments and Methods in Physics Research Section A: Accelerators, Spectromet-*

- ers, *Detectors and Associated Equipment* 374.2 (1996), pp. 269–277. ISSN: 0168-9002. DOI: [https://doi.org/10.1016/0168-9002\(96\)00096-4](https://doi.org/10.1016/0168-9002(96)00096-4).
- [53] C. Schömers. “Entwicklung einer dynamischen Intensitätsregelung für das Heidelberger Ionenstrahl-Therapiesynchrotron”. PhD thesis. 2013.
 - [54] P. A. Arrutia Sota, P. Burrows et al. “Implementation of a Tune Sweep Slow Extraction with Constant Optics at MedAustron”. In: *JACoW IPAC 2022* (2022), pp. 1715–1717. DOI: 10.18429/JACoW-IPAC2022-WEP0ST015. URL: <https://cds.cern.ch/record/2845862>.
 - [55] C. Steinbach, H. Stucki and M. Thivent. “The new slow extraction system of the CERN PS”. In: (1993). URL: <https://cds.cern.ch/record/251171>.
 - [56] J. Yang et al. “Improvement of Spill Quality for Slowly Extracted Ions at GSI-SIS18 via Transverse Emittance Exchange”. In: *Proc. IPAC’22* (Bangkok, Thailand). International Particle Accelerator Conference 13. JACoW Publishing, Geneva, Switzerland, July 2022, pp. 2093–2095. ISBN: 978-3-95-450227-1. DOI: 10.18429/JACoW-IPAC2022-WEP0TK021.
 - [57] M. Tomizawa et al. “Performance of Resonant Slow Extraction from J-PARC Main Ring”. In: *Proc. IPAC’12* (New Orleans, LA, USA, May 2012). JACoW Publishing, Geneva, Switzerland, 2012, pp. 481–483. URL: <https://jacow.org/IPAC2012/papers/MOPPD051.pdf>.
 - [58] M. Pullia, E. Bressi et al. “Betatron Core Driven Slow Extraction at CNAO and MedAustron”. en. In: *Proceedings of the 7th Int. Particle Accelerator Conf. IPAC2016* (2016), Korea. DOI: 10.18429/JACoW-IPAC2016-TUPMR037.
 - [59] L. Falbo, E. Bressi et al. “Betatron Core Slow Extraction at CNAO”. In: *9th International Particle Accelerator Conference*. June 2018. DOI: 10.18429/JACoW-IPAC2018-TUZGBF3.
 - [60] F. Kühnle. “Design study of radio frequency knockout slow extraction for the MedAustron synchrotron”. en. In: (2020). DOI: 10.34726/HSS.2020.77640.
 - [61] S. Savazzi, E. Bressi et al. “Implementation of RF-KO Extraction at CNAO”. In: *10th International Particle Accelerator Conference*. 2019, THPMP010. DOI: 10.18429/JACoW-IPAC2019-THPMP010.
 - [62] E. C. Cortés García. “Investigation of RF signals for the slow extraction at HIT’s medical synchrotron”. en. MA thesis. Darmstadt: Technische Universität, 2022, ix, 105 Seiten. DOI: <https://doi.org/10.26083/tuprints-00020811>.
 - [63] T. Bass and Y. Dutheil. “A Comparative Analysis of Simulations and Experimental Outcomes: Slow Extraction Driven by RF Transverse Excitation at the CERN Proton Synchrotron”. Presented 2023. Royal Holloway, University of London, 2023. URL: <https://cds.cern.ch/record/2884477>.
 - [64] M. Kirk, D. Ondreka and P. Spiller. “SIS-18 RF Knock-Out Optimization Studies”. In: *4th International Particle Accelerator Conference*. 2013, MOPFI007.
 - [65] M. Fraser, E. Johnson et al. “Production of slow extracted beams for CERN’s East Area at the Proton Synchrotron”. en. In: (2023). DOI: 10.18429/JACoW-IPAC2023-MOPA099.
 - [66] V. Kain, F. M. Velotti et al. “Resonant slow extraction with constant optics for improved separatrix control at the extraction septum”. In: *Physical Review Accelerators and Beams* 22.10 (Oct. 2019). DOI: 10.1103/physrevaccelbeams.22.101001.
 - [67] T. Bass, P. Arrutia Sota et al. “Benchmarking simulations of slow extraction driven by RF transverse excitation at the CERN Proton Synchrotron”. en. In: (2023). DOI: 10.18429/JACoW-IPAC2023-TUPM116.
 - [68] A. Schnase et al. “Application of Digital Narrow Band Noise to J-PARC Main Ring”. In: *Proc. IPAC’10* (Kyoto, Japan, May 2010). JACoW Publishing, Geneva, Switzerland, pp. 1446–1448. URL: <http://accelconf.web.cern.ch/IPAC10/papers/TUPEA051.pdf>.

- [69] P. Niedermayer, C. Cortés et al. “Investigation of micro spill in RF KO extraction using tailored excitation signals”. In: May 2023. DOI: 10.18429/JACoW-IPAC2023-TUPM094.
- [70] A. De Franco, T. Böhlen et al. “Upgrade Study of the MedAustron Ion Beam Center”. en. In: *Proceedings of the 8th Int. Particle Accelerator Conf. IPAC2017* (2017), Denmark. DOI: 10.18429/JACoW-IPAC2017-THPVA074.
- [71] L. Falbo, E. Bressi and C. Priano. “Empty Sweeping Bucket for Slow Extraction”. In: *9th International Particle Accelerator Conference*. June 2018. DOI: 10.18429/JACoW-IPAC2018-TUPAF010.
- [72] P. A. Arrutia Sota et al. “Implementation of RF Channeling at the CERN PS for Spill Quality Improvements”. In: *JACoW IPAC 2022* (2022), pp. 2114–2117. DOI: 10.18429/JACoW-IPAC2022-WEPOTK028.
- [73] P. A. Arrutia Sota et al. “RF techniques for spill quality improvement in the SPS”. In: *Proc. IPAC’23* (Venice, Italy). International Particle Accelerator Conference 14. JACoW Publishing, Geneva, Switzerland, Sept. 2023, pp. 319–322. ISBN: 978-3-95-450231-8.
- [74] F. Kuehteubl et al. “Investigating alternative extraction methods at MedAustron”. In: *Proc. IPAC’23* (Venice, Italy). International Particle Accelerator Conference 14. JACoW Publishing, Geneva, Switzerland, Sept. 2023, pp. 2419–2422. ISBN: 978-3-95-450231-8.
- [75] P. A. Arrutia Sota, P. N. Burrows et al. “Millisecond burst extractions from synchrotrons using RF phase displacement acceleration. Millisecond burst extractions from synchrotrons using RF phase displacement acceleration”. In: *Nucl. Instrum. Methods Phys. Res., A* 1039 (2022), p. 167007. DOI: 10.1016/j.nima.2022.167007. arXiv: 2205.13433.
- [76] A. De Franco et al. “Slow Extraction Optimization at the MedAustron Ion Therapy Center: Implementation of Front End Acceleration and RF Knock Out”. In: *Proc. IPAC’18* (Vancouver, Canada, Apr.-May 2018). JACoW Publishing, Geneva, Switzerland, pp. 453–456. DOI: 10.18429/JACoW-IPAC2018-MOPML025.
- [77] C. Schoemers et al. “First Tests of a Re-accelerated Beam at Heidelberg Ion-Beam Therapy Centre (HIT)”. In: *Proc. IPAC’17* (Copenhagen, Denmark, May 2017). JACoW Publishing, Geneva, Switzerland, pp. 4647–4649. DOI: 10.18429/JACoW-IPAC2017-THPVA083.
- [78] Y. Iwata, T. Kadowaki et al. “Multiple-energy operation with extended flattops at HIMAC”. In: *Nuclear Instruments and Methods in Physics Research Section A: Accelerators, Spectrometers, Detectors and Associated Equipment* 624.1 (2010), pp. 33–38. ISSN: 0168-9002. DOI: <https://doi.org/10.1016/j.nima.2010.09.016>.
- [79] M. Fraser, F. Addesa et al. “Experimental Results of Crystal-Assisted Slow Extraction at the SPS”. en. In: *Proceedings of the 8th Int. Particle Accelerator Conf. IPAC2017* (2017), Denmark. DOI: 10.18429/JACoW-IPAC2017-MOPIK048.
- [80] S. Waid et al. *Pulsed RF Knock-Out Extraction: A Potential Enabler for FLASH Hadrontherapy in the Bragg Peak*. 2023. arXiv: 2311.08960 [physics.med-ph].
- [81] M. Crescenti. *RF empty bucket channelling combined with a betatron core to improve slow extraction in medical synchrotrons*. Tech. rep. Geneva: CERN, 1998. URL: <https://cds.cern.ch/record/346139>.
- [82] P. A. Arrutia Sota. “Advanced RF techniques for CERN’s future slow-extracted beams”. PhD Thesis. Keble College, University of Oxford, 2024.
- [83] F. Acerbi, G. Ballerini et al. *The ENUBET project*. Tech. rep. Geneva: CERN, 2018. URL: <https://cds.cern.ch/record/2645532>.
- [84] E. Benedetto et al. “Comparison of Accelerator Designs for an Ion Therapy and Research Facility”. In: (2020). URL: <https://cds.cern.ch/record/2748083>.

- [85] W. Hardt. “A Slow Cycling Injection Method for Intensity Improvement of the CERN-PS (Twin Accelerator Ring Transfer Scheme)”. In: (1966). URL: <https://cds.cern.ch/record/2058472>.
- [86] U. Amaldi et al. “South East European International Institute for Sustainable Technologies (SEEIIST)”. In: *Frontiers in Physics* 8 (2021). ISSN: 2296-424X. DOI: 10.3389/fphy.2020.567466.
- [87] V. M. Biryukov, Yu. A. Chesnokov and V. I. Kotov. *Crystal channeling and its application at high-energy accelerators*. 1997. ISBN: 978-3-642-08238-2.
- [88] R. W. Assmann, S. Redaelli and Walter Scandale. “Optics study for a possible crystal-based collimation system for the LHC”. In: (2006). revised version submitted on 2006-09-15 14:33:57. URL: <https://cds.cern.ch/record/972334>.
- [89] F. M. Velotti et al. “Septum shadowing by means of a bent crystal to reduce slow extraction beam loss”. In: *Phys. Rev. Accel. Beams* 22 (9 Sept. 2019), p. 093502. DOI: 10.1103/PhysRevAccelBeams.22.093502.
- [90] M. B. H. Breese. “Beam bending using graded composition strained layers”. In: *Nuclear Instruments and Methods in Physics Research Section B: Beam Interactions with Materials and Atoms* 132.3 (1997), pp. 540–547. ISSN: 0168-583X. DOI: [https://doi.org/10.1016/S0168-583X\(97\)00455-2](https://doi.org/10.1016/S0168-583X(97)00455-2).
- [91] W. Scandale et al. “The UA9 setup for the double-crystal experiment in CERN-SPS”. In: *Nuclear Instruments and Methods in Physics Research Section A: Accelerators, Spectrometers, Detectors and Associated Equipment* 975 (2020), p. 164175. ISSN: 0168-9002. DOI: <https://doi.org/10.1016/j.nima.2020.164175>.
- [92] S. Bellucci and V. M. Biryukov. “Possibility of crystal extraction and collimation in the sub-GeV range”. In: *Phys. Rev. ST Accel. Beams* 10 (2007). DOI: 10.1103/PhysRevSTAB.10.013501.
- [93] Lingshu Yin et al. “Feasibility of Synchrotron-Based Ultra-High Dose Rate (UHDR) Proton Irradiation with Pencil Beam Scanning for FLASH Research”. In: *Cancers* 16.1 (2024). ISSN: 2072-6694. DOI: 10.3390/cancers16010221. URL: <https://www.mdpi.com/2072-6694/16/1/221>.

4

Simulation Models & Reproducibility

Simulations models are the core research methodology of this thesis. As the majority of projects within the thesis consider future facilities, an obvious concern is prompted: How can we ensure the reliability of the results from these models without physical versions to take measurement comparisons from?

This chapter takes care to demonstrate clear robustness and validity between machines simulated, and simulation codes used. As a standard machine to benchmark to, slow extraction from the PIMMS synchrotron is modelled.

This machine is chosen as it is widely studied in published literature, including operationally, and shares many similar needs and parameters to NIMMS. **Ch. 2** introduced the equations of beam dynamics, and from that, **Ch. 4** can now address how these equations are applied in simulation models.

Sec. 4.1 discusses the three main codes I use throughout the thesis, including where and why they are used. In **Sec. 4.2**, I perform three benchmarks tests of increasing complexity for each simulation code. Finally in **Sec. 4.2.4**, I compare two examples of extraction results from published literature to betatron core extraction results.

Only once slow extraction models are proven to work reliably for an established case can they be applied in successive chapters to research new optics and extraction designs.

4.1 Introduction to Accelerator Simulations

To understand accelerators, simulation models of the beam dynamics throughout magnets and elements are produced. Typically this incorporates the dynamics introduced in **Ch. 2** into functions that alter the 6D coordinates of a generated array of particles.

In practice, there are many ways to incorporate theoretical dynamics into simulations. The detail of the theoretical model depends on the complexity and precision of the job. For this thesis, I applied three main simulation models. Each one provides different computational methods which apply to particular use cases. **Fig. 4.1** shows a flowchart of the research projects referred throughout the thesis, and the code which is best suited for the purpose of that research.

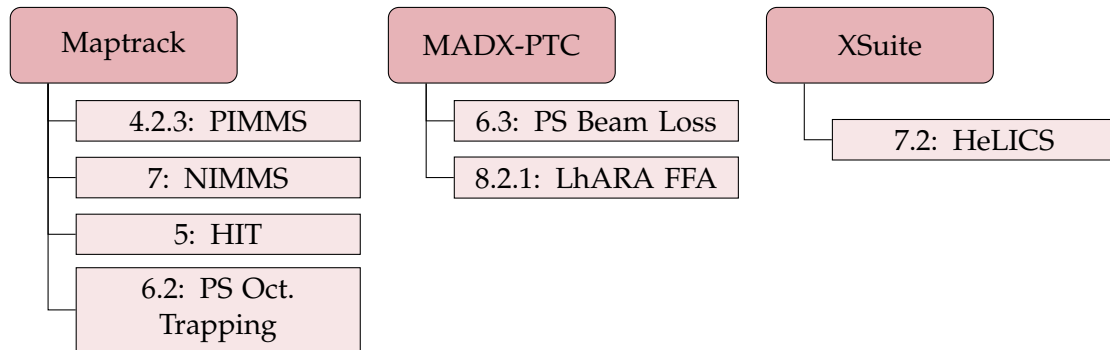


Figure 4.1.: The simulation tool used for each project, referenced by section number.

To summarise, I used **MAD-X** to represent the optics of the accelerator lattice and track with MADX-PTC; **maptrack** to track through slices of one-turn maps with functions between these slices; and **Xsuite** to simulate the latest flexible lattices.

All three are used in python, either written directly or with python bindings installed. Because of this common language, the tools written for slow-extraction processes and post-tracking analysis are largely transferable between each code. Despite these similarities, each one must be tested and benchmarked to trust and verify the simulated results.

4.1.1 MADX & PTC

MAD-X (Methodical Accelerator Design) [94] is the *de facto* scripting language at CERN to describe particle accelerators and optimise beam optics. It is written in C/C++ and Fortran. Primarily I coded via jupyter notebooks and cpymad - a cython binding to MADX .

Use Case: MADX is used for all accelerators within this thesis. For each project, a MADX

sequence file lists the series and order of accelerator elements. This *.seq* file is used to calculate, visualise and optimise synchrotron optics, and to match e.g. tune and chromaticity. In this thesis, MADX is not used for tracking as it can only track thin element approximations. Instead PTC (Polymorphic Tracking Code) [95] exists within MADX as a library. PTC is a symplectic kick code based on map formalism of a given precision [96]. It has a high degree of control over higher-order effects, and has options to use exact Hamiltonian calculations. MADX-PTC Track is ideal when constant conditions are necessary. In particular, MADX-PTC was used with PS separatrix folding with octupoles, as the beam was modelled to be exactly on resonance.

Example: The setup for MADX-PTC in **Lst. A.1** is the default used in simulations. Here, a single on-orbit particle is tracked for 100 turns, and is observed at the start element and the ES marker. The MADX-PTC manual [97] (Chapter 36) contains the definition of all terms.

4.1.2 Maptrack

Maptrack [98] is a python module which converts a MADX sequence into a one-turn transfer map via PTC. This transfer map is used as a single transformation to convert the 6D coordinates of the particles. The order of the map determines the precision of the tracking. This is an efficient way to compress large accelerator lattices into a few crucial components. Slicing the single-turn map at sections along the ring allows freedom in-between these map segments, where I wrote extraction elements as python functions to transform the beam.

Use Case: Maptrack was used initially for simulations of octupole island formation in the PS, as it could include quadrupole ramping through the resonance, and quick changes of octupole and sextupole strengths. The relatively larger complexity of the PS was ideal for maptrack, as the main units between extraction elements could be absorbed within the map slices. As I developed the tools initially to compare with PS MDs, it was convenient to later adapt them for the PIMMS lattice. The subsequent upgrades from PIMMS to the NIMMS normal-conducting carbon synchrotron followed in maptrack. The freedom maptrack provided was essential for this early stage of simulation development to create and test all the necessary tools for slow extraction, i.e. betatron core, RF-KO excitation and septa aperture regions.

Example: A dedicated NIMMS note [99] describes how I adapted maptrack to suit slow extraction simulation conditions. This note includes examples of memory-handling, parallelisation and simulation speed were added to reach larger particle statistics and turn number. Maptrack uses the same flags as in **Lst. A.1**, but with an additional map order. Order 4 is the minimum

that should be used with octupole magnets. Order 5 and 6 provide additional accuracy especially at large amplitudes of the separatrices.

Disadvantages: Despite including dynamic python functions, the maps themselves are static, meaning that any change in chromaticity or tune requires a new map. This is time consuming for large lattices and results in complete flexibility within one set of accelerator settings, but low flexibility between accelerator settings. This is not ideal for an accelerator with an evolving lattice, such as the Helium Synchrotron. A further downside is that when the beam is not on-orbit, the map segments introduce an offset, which has to be considered when feeding the beam through custom elements. Should this element change this bump, such as a quadrupole, this effect may not be reflected within the map segment. Compared to PTC Track, maptrack is non-symplectic.

4.1.3 Xsuite

XSuite is a simulation tool for accelerator beam dynamics formatted as a series of python packages. It began development in March 2021 and slowly expanded its features and user-base in the following years. The strength of Xsuite is in its flexibility, due to its pythonic structure with elements transferred to C. This lightweight structure allows itself to run via multi-threaded CPU and GPU for fast simulation times. Furthermore the difficulties of C-development are avoided as memory handling remains in python.

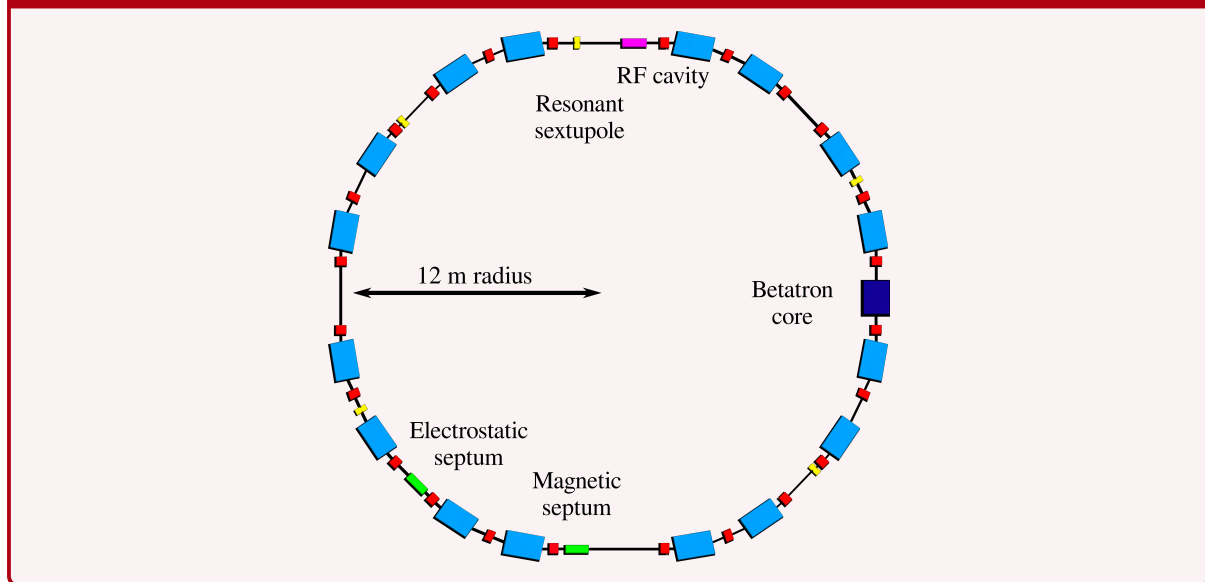
Use Case: As a new simulation code, Xsuite was not adopted as part of my simulation workflow until 2023 when some key Xtrack features were developed. In particular tracking for thick-element was needed, especially for ions with different mass and charge ratios. Xsuite suits dynamic simulations with elements that change with time, such as quadrupole strengths, needed for a quadrupole-driven excitation. This similarity with maptrack made the transfer from maptrack to Xsuite user friendly. Despite this, other elements were missing in Xsuite, especially septum models and betatron core momentum sweeps. In order to fully benchmark with maptrack, I wrote custom functions for these elements in C, and tested them in the python environment. Xsuite was used primarily for the simulations of the Helium Synchrotron. The synchrotron is an evolving design, with regular updates to septa positioning and lattice structure, and the madx import into Xsuite makes these evolutions effortless. An important stipulation is in the modelling of small synchrotrons in XSuite. The large bending angle results in multipole expansions which are different to that typically required for the modelling of the

LHC (which is what the code is intended for). This in particular is significant for small accelerators with large k_1 components in their combined function dipoles. A tracking integrator was implemented in XSuite bend elements to slice the multipole coefficients along the bend, according to a number of Yoshida integrator slices [100]. This has the benefit of larger accuracy in the second-order chromaticity when benchmarked to PTC. It has the downside of slowing down tracking time for small machines, unless this multipole factor is set explicitly to 1.

Example: The Xsuite notebooks for the helium synchrotron are recorded in the gitlab repository alongside this thesis, with the custom elements in *xtraction_helpers.py*.

4.2 PIMMS Benchmarks

Figure 4.2.: Schematic of the PIMMS synchrotron showing dipoles (cyan), quadrupoles (red), sextupoles (yellow), septa (green) and the betatron core (blue)



Simulations require a well-understood accelerator to provide a standard by which models can be benchmarked between each simulation code. From conception, PIMMS was designed for the purposes of optimal slow extraction, so it makes sense to use it to develop the simulation tools required to perform slow extraction.

Fig. 4.2 is a outline schematic of the PIMMS lattice - it is 75 m in circumference composed of two superperiods, each with 8 dipoles, 12 quadrupoles and two sextupoles. The quadrupoles are split into three families, two focusing and one defocusing, to be matched to suit three conditions: horizontal tune, vertical tune and horizontal dispersion. There are three families of

sextupoles to match for horizontal chromaticity and vertical chromaticity, and to control the extraction resonance. **Sec. 4.2.3** will elaborate how these mentioned extraction components are implemented in each code.

Three benchmark tests are performed via this lattice, to compare the behaviour of MADX-PTC, maptrack and Xsuite. First the 4D coordinate drift after 1 turn of tracking is compared. Then the differences in Twiss calculations of horizontal and vertical chromaticity. Finally the extracted distribution from a complete betatron core simulation - just for maptrack and XSuite. Once consistency is established between codes, benchmarking is applied to results from literature.

4.2.1 Tracking

Before considering extraction effects, tracking must show standard behaviour between codes. This is typically performed by launching a grid of particles under stable conditions. In this instance, stable means a constant tune far from excited resonances.

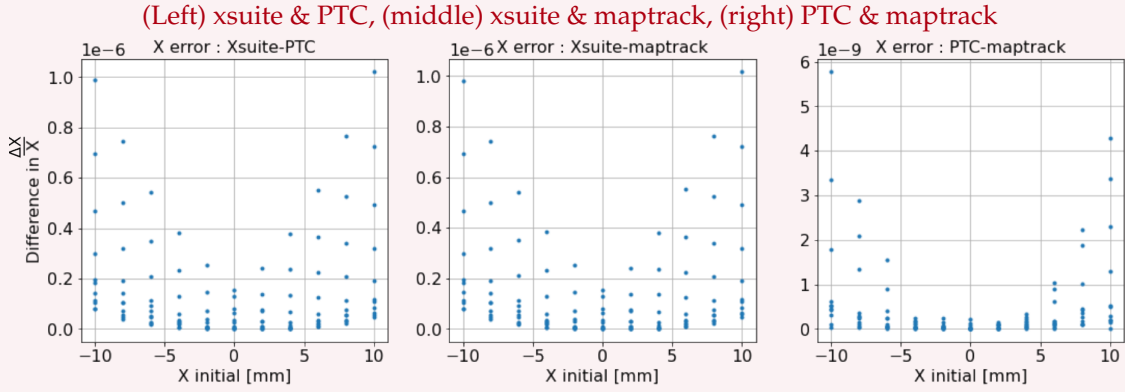
Each plane is independent so three simulations are run: firstly with a grid in only $x - px$ coordinates, secondly with a grid in $y - yp$, and finally in $x - pt$. This is because the momentum coordinate is tracked differently between codes (See **Sec. A.1**), so that momentum dependent errors do not affect other coordinates. No RF cavity is included in any simulations, so only the 4D transverse coordinates and the longitudinal momentum component is considered, without any longitudinal position.

The grid is chosen based on the range of the ideal injected Gaussian beam used in PIMMS. 112 particles are selected for each simulation with a range of, i.e. $-10\text{ mm} - 10\text{ mm}$ in X. The simulation begins at the injection point, and the beam is tracked until the ES. This is so it is consistent with all simulations in this report, which also typically inject the beam at $S=0\text{ m}$ and focuses on the dynamics at the ES.

In Appendix A, the particle grids tracking results from MADX-PTC, maptrack and XSuite are plotted in **Fig. A.2**, **Fig. A.3**, **Fig. A.4**. This includes the sum difference in each coordinate compared between simulation codes. A summary plot of these three results is represented in **Fig. 4.3**. This Figure shows the difference in only the x-coordinate between XSuite and PTC, between XSuite and maptrack and between maptrack and PTC.

This result is significant as it shows the reliability of simulation codes often assumes an

Figure 4.3.: Comparison of relative errors ($\frac{\Delta X}{X}$) in tracking of the X-coordinate three codes. Full diagram in Appendix A.



on-orbit particles, and that errors in tracking increasing amplitude. This could become considerable over millions of turns, especially as separatrix dynamics typically occurs at high amplitudes from the beam centre. In addition, there is a difference in scale between comparing maximum relative difference between PTC and maptrack (6×10^{-9}) and when comparing these with XSuite (1×10^{-6}). This result is expected, as PTC and maptrack in this example are using the same map and the flags, but at a different order and with three slices in maptrack.

The next step would be to repeat with sextupoles, as it is the non-linear element that is often different between tracking codes. As the difference in position and momentum as a function of sextupole strength is defined as the chromaticity, we can instead benchmark the chromaticity value between codes.

4.2.2 Tune and Chromaticity

For the aforementioned codes, a Twiss calculation was performed to benchmark the horizontal and vertical tune ($Q_{x,y}$) and chromaticity ($dQ_{x,y}$). Other than Maptrack, these codes have the option of considering the lattice as a series of thick-lens magnets of length L , or as thin-lens magnets sliced n_s times each with length $\frac{n_s}{L}$. For comparative purposes, thick tracking and thin tracking was performed, with the latter using a TEAPOT algorithm [101] of 100 slices. A table of these calculations is presented in **Tab. 4.1**.

For all cases, the tune for PIMMS was in agreement to 5 decimal places, with values of $Q_x = 1.64500$ and $Q_y = 1.72000$. Despite this, chromaticity has some different behaviours between

codes:

- Firstly, for the default beam ($\beta_{rel} = 1$), there is a difference between the thick-lens tracking ($dQ_x = -2.06292$) and the thin-lens tracking ($dQ_x = -2.86777$). This has a 40 % larger relative offset than the thick-lens tracking, and an increased number of slices does not converge to the chromaticity of the thick-lens tracking. This implies it is a function of the slicing itself.
- Secondly, when looking at an ion beam, for example C^{6+} at 400 MeV/u, the relativistic beta in the simulation changes. In this case, $\beta_{rel} = 0.7145$ [102]. The reason for this in MADX can be found in Appendix A, **Sec. A.1**. This relativistic factor does not change the chromatic calculation of XSuite or PTC (thin). For this reason, the value for chromaticity increases by 71.45 % for MAD-X and PTC, so that ($dQ_x = -2.88719$), whereas for xsuite it remains at ($dQ_x = -2.06292$). Then in addition there are differences in values for thick and thin lens tracking for the ion beam.

To conclude, for MADX and PTC Twiss (thick), chromaticity in both planes are divided by β_{rel} . Whilst this may not have any effect directly on the tracking, it is important to consider when interpreting values of dispersion or chromaticity from MADX and PTC Twiss calculations.

Table 4.1.: Chromaticity benchmark of simulation codes with β_{rel} .

	default beam		C^{6+} 400 MeV/u	
	dQx	dQy	dQx	dQy
MADX (thick)	-2.06292	-0.59123	-2.88719	-0.82746
PTC Twiss (thick)	-2.06292	-0.59123	-2.88719	-0.82746
XSuite (thick)	-2.06282	-0.59130	-2.06282	-0.59130
Maptrack	-2.06292	-0.59123	-2.06990	-0.59323
MADX (thin)	-2.86777	-0.51807	-2.88719	-0.82746
XSuite (thin)	-2.86777	-0.51807	-2.86777	-0.51807
PTC Twiss (thin)	-2.86777	-0.51807	-2.86777	-0.51807

4.2.3 Betatron Core Simulations

Methods

Betatron core extraction is the default extraction option for PIMMS, and is relatively simple to implement, therefore it is beneficial as a technique to benchmark a full extraction simula-

tion. This extraction method is sensitive to tune, chromaticity, momentum and 6D phase-space tracking, so cohesion when benchmarking confirms that all these effects apply together. The techniques used to simulate slow extraction are necessarily different between each codes. The approach to the simulation method depends heavily on how the simulation is run, and how accessible the set of particle data is. This especially pertains to the extraction septa and chosen extraction method.

In **MADX-PTC**, the particles cannot be accessed until results are written to a *.onetxt* file. For ease of access, this is converted to a pandas dataframe post-tracking. Results can then be filtered by e.g. particle ID, turn number or element S-position. A slow alternative is to rerun *ptc_create_universe* code in a loop and input the results from the previous turn.

The **septum** could be added via an aperture limit, but this cannot consider complex ES geometry. Instead septa effects are calculated in post-processing, which includes measuring losses at the thin anode foil, at the thick cathode and applying kicks in the field-region. The first instance of any given particle exceeding the septum limit X_{ES} is recorded, and each subsequent turn after that is dropped from the dataframe.

Betatron core methods are difficult to model in MADX-PTC, as it is challenging to alter the momentum of the particles, aside from rebuilding the simulation each turn. Rebuilding is an inefficient use of time, and so betatron core simulations are not run in MADX-PTC in this thesis.

In **maptrack**, I coded my own method to save and handle data after each map transformation [99]. This method involves two files: one containing stable particles measured at the septum every turn, *ES.npy* ($6 \times N_{\text{particles}} \times N_{\text{turns}}$), and one containing information when particles were lost, *Extr.npy* ($7 \times N_{\text{particles}}$, the 7th coordinate being turn number). To save time and memory when writing and loading results, I used python memory maps, known as memmaps. The **septum** is modelled with a series of masked numpy arrays based on the X-coordinate, which is what assigns particles to *Extr.npy*. With additional complexity, masks can differentiate between the anode, cathode and field region.

Betatron Core is modelled by a simple thin-lens function at the position of the betatron core element. It adds a constant momentum kick to the 6th coordinate of every stable particle every turn.

Xsuite has pre-defined particle and monitor objects. Monitor objects allows the user to define where in the ring the particles are saved, how many particles and how often they are monitored. The resulting data sets are treated as arrays, but have built-in array-like filtering. They can be saved and loaded via .json files.

I wrote additional functions to serve as the **septum**. These use the *LocalParticle_get_x* function to assign the constraint, and *LocalParticle_set_state* function to assign a negative flag to lost particles. More complicated geometries are easily adapted, including those that provide kicks to particles in the field region, and include both anode and cathode apertures.

The **Betatron Core** function I created is similar, but uses the *LocalParticle_update_delta* function, which would have additional effects on the longitudinal plane, if relevant.

Results

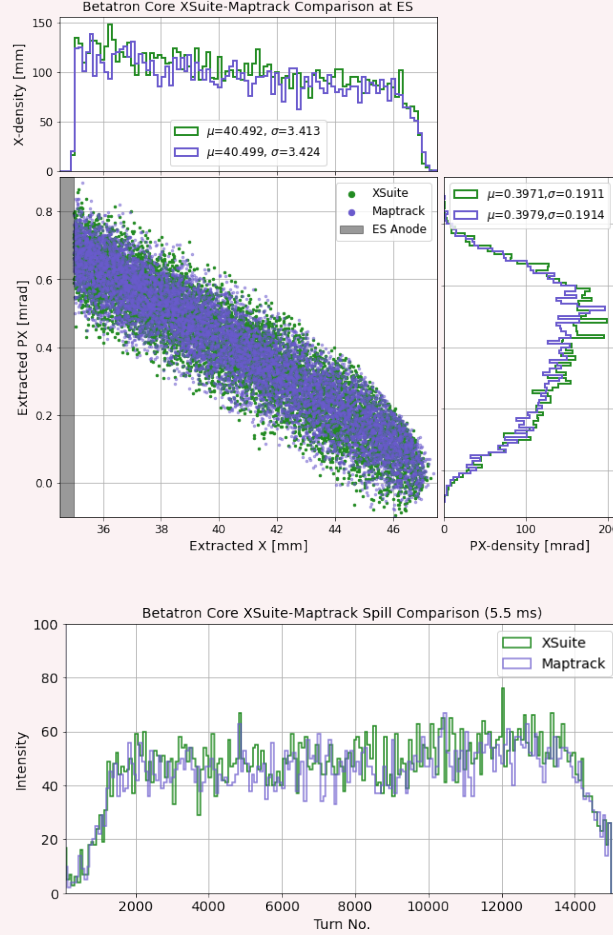
Betatron core simulations were launched for maptrack and Xsuite. This simulation tracks 15 000 turns and 10 000 particles. I assumed operational conditions for a 400 MeV/u C⁶⁺ beam, with a momentum spread of $\Delta p/p = 0.4\%$ and an RMS normalised emittance of $\varepsilon = 0.75\pi\text{mm.mrad}$ [102]. The chromaticity required to fulfil the Hardt Condition (**Sec. 2.3.5**) is calculated to be $dQ_x = -4.041$. The tune spread resulting from the chromaticity and momentum spread requires a stable initial tune of $Q_x = 1.645$, to avoid any initial extraction. The quadrupoles and sextupoles of the PIMMS MADX .seq file are matched to meet these conditions. Dispersion was matched to be zero in the straight-sections, for the resonant sextupole. The resonant sextupole used the MedAustron operational strength of $K_2 = 8.65$. In maptrack, a 4th order PTC map was generated from the MADX sequence file at these settings. An initial Gaussian beam was created with the Twiss conditions at injection, and this distribution was saved for both maptrack and XSuite. In maptrack the beam was iteratively passed through three maps: the elements between injection and the betatron core, between the betatron core and electrostatic septum, and between electrostatic septum and injection. In XSuite, the MADX sequence was imported as thick lens models. The betatron function, septum function and ES monitor were subsequently added to the line.

The distribution of extracted particles in horizontal phase-space at the ES (known as the bar-of-charge) was compared for both maptrack (purple) and XSuite (green). **Fig. 4.4** displays the bar-of-charge for a 12 mm spiral step. Maptrack and XSuite are in good agreement in both

Figure 4.4.: Comparisons of extracted betatron core distribution and spill.

(Top) Overlay of xsuite (green) and maptrack (purple) tracking comparing extracted beam distribution in phase-space. Histograms show density distributions in x and x' . (Bottom)

Extracted spill of beam as a function of turn number.



planes of the extracted beam. The mean and standard deviations were calculated for the X and PX distributions, and agree to four significant figures (shown in the legends of **Fig. 4.4**). An attempt was made to compare for each individual particle ID, as they had the same initial conditions, but there is little dependency between the initial position and the final position at extraction, so large variation was displayed.

Spill was also observed as a function of time, shown in **Fig. 4.4** (bottom). For the purposes of benchmarking, a spill time of 5.5 ms was simulated, showing excellent agreement. With a revolution frequency of 2.84 MHz, this is equivalent to 15 000.

4.2.4 Comparison with Literature

The CNAO and MedAustron lattices deviate subtly from the initial PIMMS designs. For MedAustron in particular, the dipoles bend with a negative angle - i.e. whilst the elements are in the same order as PIMMS, the accelerator is mirrored and the beams bend in the anti-clockwise rather than clockwise. Consequentially, the dispersion is represented as negative, meaning the Hardt Condition applies in the negative axis. As a result, the ES is also notated to have a negative X_{ES} . In addition, hardware and systems decisions cause subtle differences in magnet sizes, strengths and positions - particularly the sextupoles. This means using the same MADX magnet strengths as those listed in literature will give different tunes and chromaticities. Comparisons are more agreeable if instead the PIMMS lattice is matched to the literature-given tune and chromaticity values ($Q_x = 1.6, dQ_x = -4.041$).

Two masters theses relating to MedAustron perform betatron core simulations with the MedAustron lattice with the same tune, chromaticity and momentum shift: Feldbauer [103] (2011) and Kuehteubl [104] (2020). The simulations in these theses both run with 1000 particles over 150,000 turns, and observe the phase-space distribution of the beam at the ES. The 2011 results were performed with WinAgile and Track-It! and the 2020 results were in MADX. I performed an XSuite simulation to judge compatibility to this literature. Here, dipoles are set to negative strength and the ES position is moved to $X_{ES} = -0.0035$ mm. PIMMS sextupole magnets are 0.2 m long and MedAustrons are 0.26 m, so the K_2 of 8.65 is adjusted to $8.65 \times \frac{0.26}{0.2} = 11.245$. The subtle adjustments in positioning of the resonant sextupole and ES in MedAustron result in a different phase-advance between the two elements which is equivalent to $\mu_x = 0.0186\pi$. The phase-advance differences causes a rotation at the beam-centre origin of around 3.3° . To offset this difference, the resonant sextupole XRr is positioned 0.93 m forwards. In accordance with Table 4.8 of Feldbauer, the horizontal tune is set exactly on resonance and the beam is set off-momentum by $\frac{\Delta p}{p} = 3.3 \times 10^{-3}$. This gives different results compared to having an on-momentum with an off-resonance tune (as in [Sec. 4.2.3](#)), due to dispersion effects in both horizontal planes. The resonant sextupole ramps up to full strength for 2000 turns, then the betatron core turns on at an acceleration of 5×10^{-8} 200 turns later.

The resulting extracted beam of [Fig. 4.5](#), can be directly compared to the literature results of Kuehteubl [104] (left) and Feldbauer [103] (right) shown within [Fig. 4.6](#). The three distribu-

Figure 4.5.: Extracted beam distribution in phase-space using MedAustron betatron core methods for literature comparisons

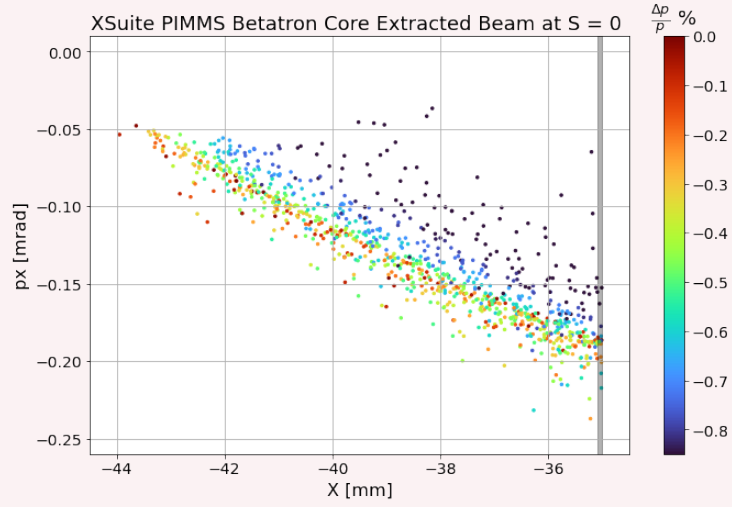
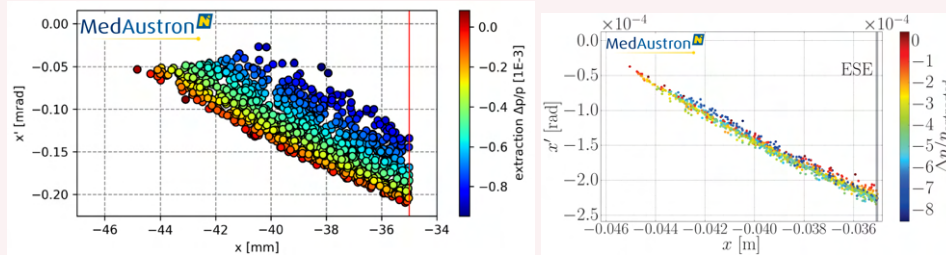


Figure 4.6.: Extracted beam distribution in phase-space from published MedAustron betatron core simulations to compare with Fig. 4.5

(Left) F. Kuehteubl (2020) [104] published with permission from the author.

(Right) G. Feldbauer (2011) [103].



tions have an agreeable spiral step, all emerging from beyond the anode wire at -35 mm and stretching 9 mm for XSuite and Kuehteubl and 10 mm for Feldbauer. The explainable 1 mm stems from the difference in chromatic sextupoles strength and length, which are not strictly adjusted like the XRR is, but still contribute to the virtual sextupole strength. The spread in px depends strongly on the orientation of the separatrices at the ES and is in agreement of being between -0.20 mrad and -0.05 mrad. The width of the distribution emerges from the closeness of the machine chromaticity matching the value required to fulfil the Hardt Condition, and visually looks similar for XSuite and Feldbauer.

It is reasonable to conclude that the simulation models produced in this thesis when applied to the PIMMS lattice, compares well with extraction models of the MedAustron synchrotron.

4.3 Simulation Discussion

Simulations are the backbone of any modern physics PhD. In this thesis, they are not just used to predict experimental results, but also to guide the design choices to be made for the extraction methods. Throughout this process, ensuring reproducibility and consistency between simulation codes was demonstrated for cohesiveness between projects.

First, comparisons ensured that stable single-turn tracking is comparable between the three main codes to a difference of 10^{-6} . This tracking occurred in five of the six particle coordinates (x, px, y, py, pt) and identified the impact from the way pt is handled between codes (Appendix A). Secondly, Twiss functions were calculated for each code to ensure that tune and chromaticity were treated the same. Relativistic and non-relativistic beams were compared, which is essential when using high-energy accelerator tools for comparatively low-energy applications. As a result of the difference in pt and δ_p , a noticeable factor of β_{rel} is observed in the chromaticity for MADX and PTC twiss functions.

Finally, these effects were combined into a complete betatron core simulation, performed for XSuite and maptrack, which gives good agreement in the phase-space bar-of-charge, and in spill as a function of turn number. With PIMMS being a conceptual design, and MedAustron a fully-installed machine, there are differences between the two lattices. In order to make fair comparisons between the two, simulations were repeated in XSuite with minor adjustments. Overall, there is demonstrable security that the models created for the purpose of NIMMS slow extraction design have good agreement and reproducibility with existing literature of existing clinical hadron therapy facilities.

Notes for future studies: The slow extraction simulation tools that will be passed on for future studies will be in XSuite.

Bibliography

- [94] H. Grote and F. Schmidt. "MAD-X: An Upgrade from MAD8". In: (2003). URL: <http://cds.cern.ch/record/618496>.
- [95] P. K. Skowronski, F. Schmidt and E. Forest. "Advances in MAD X using PTC". In: *Conf. Proc. C 070625* (2007). Ed. by C. Petit-Jean-Genaz, p. 3381. DOI: 10.1109/PAC.2007.4440432.

- [96] F. Schmidt, E. Forest and E. McIntosh. *Introduction to the polymorphic tracking code: Fibre bundles, polymorphic Taylor types and Exact tracking*. Tech. rep. Geneva: CERN, 2002. URL: <http://cds.cern.ch/record/573082>.
- [97] L. Deniau et al. “The MAD-X Program (Methodical Accelerator Design) User’s Reference Manual”. In: (Feb. 2022). URL: <https://madx.web.cern.ch/madx/releases/last-rel/madxguide.pdf>.
- [98] F. M. Velotti. *maptrack*. <https://gitlab.cern.ch/abt-optics-and-code-repository/simulation-codes/maptrack>.
- [99] R. Taylor et al. “Flexible beam dynamics simulations for slow extraction with Maptrack”. In: (2024). URL: <https://cds.cern.ch/record/2889951>.
- [100] H. Yoshida. “Construction of higher order symplectic integrators”. In: *Physics Letters A* 150.5 (1990), pp. 262–268. ISSN: 0375-9601. DOI: [https://doi.org/10.1016/0375-9601\(90\)90092-3](https://doi.org/10.1016/0375-9601(90)90092-3).
- [101] L. C. Schachinger and R. Talman. “TEAPOT: a thin element accelerator program for optics and tracking”. In: *Part. Accel.* 22 (1987), p. 35. URL: <https://cds.cern.ch/record/165372>.
- [102] P. J. Bryant, L. Badano et al. *Proton-Ion Medical Machine Study (PIMMS)*, 2. Tech. rep. 2000. URL: <https://cds.cern.ch/record/449577>.
- [103] G. Feldbauer. “Extraction methods for the MedAustron Synchrotron”. Available at <https://repositum.tuwien.at/handle/20.500.12708/14810>. Master Thesis. MedAustron, Austria: Technische Universität Wien, May 2011.
- [104] F. Kühleubl. “Design study of radio frequency knockout slow extraction for the MedAustron synchrotron”. en. In: (2020). DOI: 10.34726/HSS.2020.77640. URL: <https://repositum.tuwien.at/handle/20.500.12708/1297>.

*The path to measure
good tune is through the method
that you did not use.*

5

Dynamic Tune Analysis

As hinted at in [Ch. 2](#), particle beams near unstable resonances are complicated to model. The likelihood of extraction depends on the particle's frequency relative to the resonance. Without a dedicated model of the frequency of particles, it is difficult to track and predict the rate at which these particles are extracted. Such models are essential to ensure good spill smoothness.

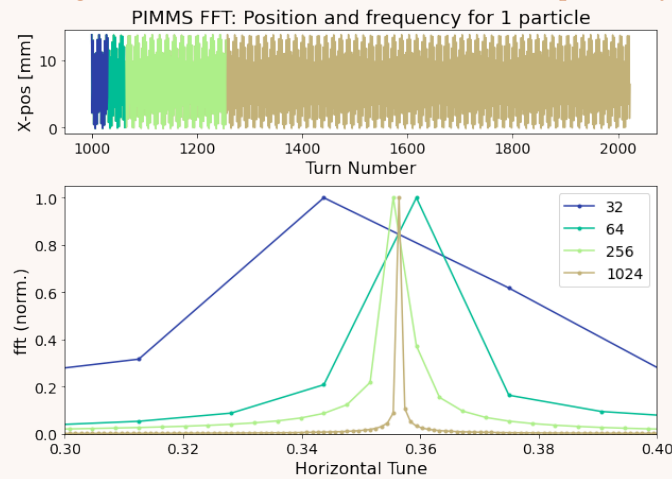
This chapter introduces the methods used in the thesis to measure tune dynamics throughout simulations. The methods are established via [Sec. 5.1](#) and an in-depth case-study is analysed in [Sec. 5.2](#), based on the HIT synchrotron . The HIT synchrotron uses RF-KO to extract their particles. Particles under RF-KO behave similarly to a BTF measurement, used to calculate the tune of the beam. The simulations in [Sec. 5.2.2](#) onwards explores multi-particle and single-particle tune effects under the BTF, as compared to measurements.

5.1 Introduction to Frequency Analysis

As introduced in [Ch. 2](#), tune is defined by the horizontal or vertical oscillation frequency of particles in one turn of a machine. It is possible to measure the fractional portion of tune by taking multiple measurements of particle position. A fast-Fourier transform (FFT) applied on these position measurements over a period of time can analyse the frequency spectrum of the particle. Whilst the frequency spectrum of one particle can have many components to it, the highest frequency response is conventionally taken as the fractional component of the tune in this time frame. The integer components should be added to this fractional value. FFTs are

Figure 5.1.: Example of FFT resolution with turn number

(Top) Particle horizontal position as a function of turn number, selected for 32, 64, 256 and 1024 turns. (Bottom) Resulting resolution of FFT distribution shows dependency with turn number.



limited by the amount of samples of turn-based position measurements, which corresponds to the data points in the spectrum, i.e. higher resolution in frequency requires more points in measurements. This is described by the Nyquist-Shannon theorem, the consequence of which says that for a given sampling freq frequency values of up to $f_{\text{Samp}}/2$ can be extracted from the signal. [Fig. 5.1](#) samples the position as a function of time for a range of window sizes. As used by numpy, the algorithm works best in powers of 2 and the FFT spectrum equally spaces samples between 0 and 0.5, therefore it should be identified whether it is a $1/3$ or $2/3$ fractional tune. It is clear that in this example, 32 samples is insufficient to cover the exact region of the particle's tune, and implies a larger tune spread. Higher samples provide higher resolution of the frequency. Operationally, the oscillations of a beam due to tune are often too subtle to be

measured directly, so an alternative is to give the beam a strong single kick and pick up the resulting damped oscillations. The specifics of this in measurement can be seen in [Sec. C.1](#).

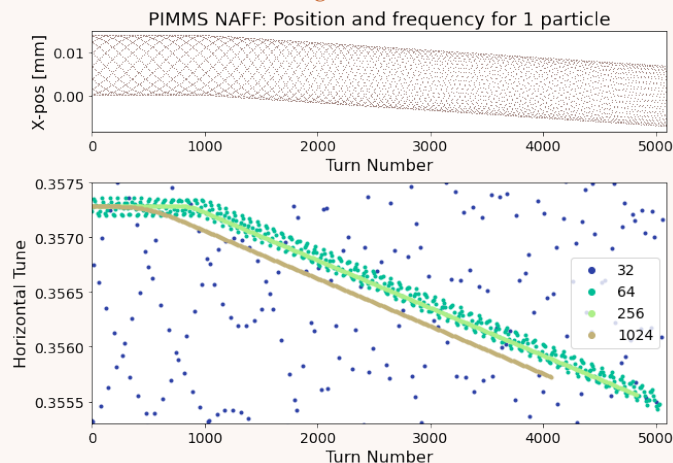
5.1.1 NAFF

NAFF (Numerical Analysis of Fundamental Frequencies) is an FFT-based analysis package [105]. NAFF allows for faster and more accurate frequency calculations than FFTs. To avoid the strong dependency on number of data points, NAFF performs a convolution via a Hann window [106]. It then identifies the largest frequency in the FFT spectrum and performs further refinement and interpolations [107]. The signal harmonic, fractional tune and amplitude (real and complex) are returned. Due to the interpolation performed, the data works best in multiples of 6. The analytical limit on precision that a NAFF calculation can make increases as an order of $\frac{1}{N^4}$. This is an improvement in comparison with FFT calculations which increase as an order of $\frac{1}{N}$. NAFF can be improved with a higher number of monitors M such that the precision increases with an order of $\frac{M}{(MN)^4}$ [108].

For FFT-based methods, only one value of tune can be acquired for a set of positions as a function of time. To analyse a dynamic tune system, such as during slow extraction, the tune has to be calculated as a function of time. For this method, a scrolling window is implemented. A

Figure 5.2.: Scrolling tune example of NAFF resolution

(Top) Particle horizontal position during betatron core extraction. (Bottom) Resulting resolution of NAFF calculations for a scrolling window of 32, 64, 256 and 1024 turns.



set of turn-based data is analysed of a given window-size, then gradually stepped forwards.

Fig. 5.2 represents this for an exaggerated betatron core transform on one particle, for the PIMMS lattice. As the momenta is increased linearly by 5×10^{-6} per turn, its position changes linearly as a function of dispersion at the monitor, and its tune changes linearly as a function of machine chromaticity. Smaller turn numbers give larger uncertainty in tune and larger oscillations in tune. As the scrolling-window is an average as a function of time, larger windows will have a phase offset. By combining tune calculations with the particle's amplitude, it can be incorporated into a dynamic Steinbach diagram. This concept will be explored further in **Ch. 7**.

5.2 HIT Studies

THIS SUBSECTION WAS PERFORMED IN COLLABORATION WITH C. CORTES AND P. NIEDERMAYER
As introduced in **Ch. 1** and **Ch. 3**, Heidelberg Ion Therapy (HIT) is a synchrotron based hadron therapy treatment facility. In 2021 an interesting measurement was performed, which observed that the tune spectrum of a beam does not behave as expected [62], and forms an additional distribution towards the resonance.

5.2.1 Measurements

Measurements at HIT were initially performed for a 124.25 MeV/u carbon beam of 7×10^8 particles. The operational cycle used unbunched extraction conditions without use of the RF-KO exciter. The nominal resonant sextupole strength applied a strength of 0.98 m^{-2} .

The tune was measured via the Beam Transfer Function (BTF). In both RF-KO and BTF measurements, the beam is transversely excited at frequencies near to the beam tune. In RF-KO this is at large amplitudes to promote beam instability, whereas in BTF this is swept across beam frequencies at smaller amplitudes. When the BTF driven frequency matches the particle frequency it acts as a driven harmonic oscillations. Schottky parallel plates are then used as a non-invasive diagnostic tool to measure the statistical fluctuations of a current. Due to their similarities, this method is a good model for what is occurring to the beam during RF-KO.

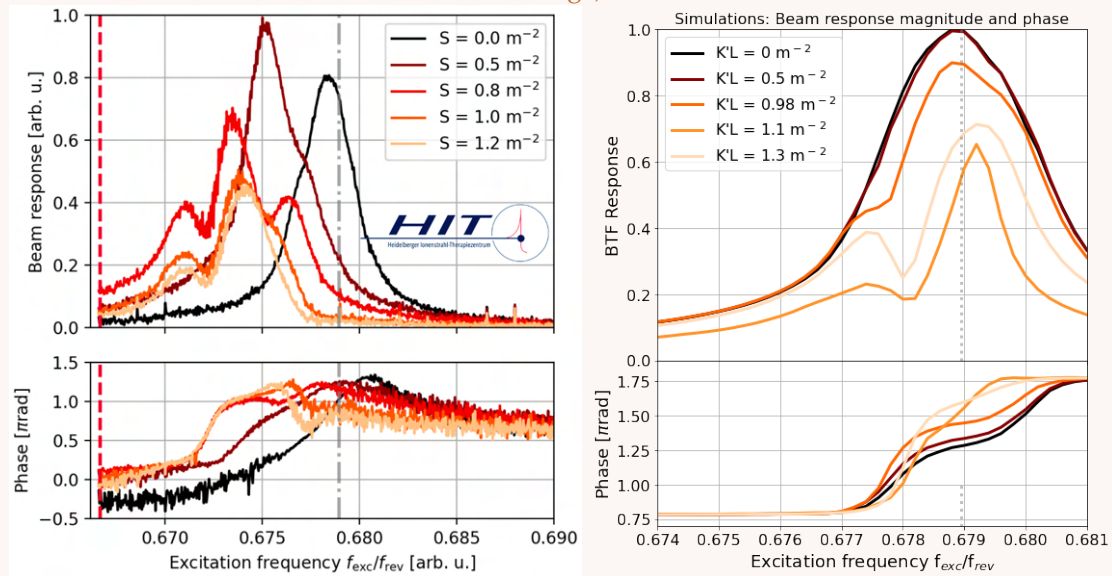
The Network Analyser produces a fast tune sweep in steps of 1.5 ms. The analyser compares amplitude and phase difference of the initial driven signal to the received Schottky signal. This amplitude difference gives the tune response as a function of frequency. In measurements, this was performed at the ≈ 10 th harmonic to receive a stable signal. The received signal depends

strongly on the Network Analyzer settings, i.e. whether the frequency is ramped up or ramped down, and the amplitude (dB) the signal is generated at.

When performed initially in 2021 by C. Cortes ([62] Fig. 3.3), it was found that beam tune was not a Gaussian but forms two peaks, depending on sextupole S . The tune distribution of the beam is important to understand for RF-KO extraction, as the excitation frequency directly affects the extracted spill duty factor (described in [Sec. 2.3.4](#)). This study was used to engineer unique frequency-amplitude spectrum and increase spill duty factor to over 90% for protons and carbon [62].

Figure 5.3.: BTF tune measurements changing with sextupole strengths

HIT measurements (left C. Cortes) and simulations (right R. Taylor) in beam resonance magnitude and phase difference. Colourmap shows sextupole strength (low = black, high = orange).



In order to study why this distribution forms in this manner, further measurements were taken collaboratively in March and May 2022. With permission from C. Cortes, [Fig. 5.3](#) (left) shows his original results from end of 2021. Initially, with no resonant sextupole strength, the tune distribution is a Gaussian almost centred on the machine tune. Increasing K_2L causes subtle tune deformations at $0.5 m^{-2}$, and two-peaks from the nominal settings of $1.0 m^{-2}$ onwards. The smaller secondary peaks are seen in the direction towards the resonance. These results were produced from single shots of the accelerator, which has high shot-to-shot variation. The most recent results are presented in [109].

Simulations are another tool to aid understanding of the origin of this phenomena. They also allow for a variety of parameters to be varied systematically, and can observe this for both whole-beam dynamics, [Sec. 5.2.2](#), and single-particle dynamics, [Sec. 5.2.3](#), as a function of time.

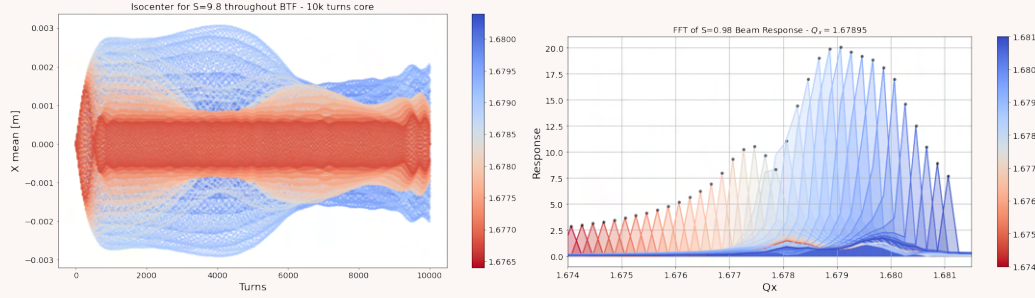
5.2.2 Whole-Beam Simulations

Maptrack was used for simulations to reproduce the tune splitting observed in measurements. The setup for the simulation applied a seven step process:

1. First a static map was generated of the MADX lattice of HIT for extraction optics. It is important to note that the MADX lattice was generated on-orbit, whereas the machine has a non-negligible closed orbit offset.
2. To match experimental conditions, an initial beam distribution of 50,000 particles was produced. This distribution was initially tracked for 10,000 turns to allow it to stabilise near the resonance of a given sextupole strength k_2L .
3. Once a stable initial distribution was produced, an excitation signal was introduced to model the network analyser. Every turn, the x' angle of the particles was changed according to a sine function with a given frequency of f_q . This signal was given with large excitation strength of 2 mrad, equivalent to ≈ 2 dB of amplitude in measurement. Each frequency setting was tracked for a further 10,000 turns. With a revolution frequency of 2.17 MHz, this corresponds to 4.6 ms.
4. This process was repeated whilst increasing f_q in across 40 small steps to model the BTF. Unlike the BTF, this process was repeated from the initial stable beam rather than from the previous step of f_q . This was to avoid cumulative beam loss from the previous frequencies. The effect of cumulative beam loss was observed in similarly performed simulations [109].
5. To compare with experiments, the beam is measured as a whole, and the isocentre of the beam is calculated as a function of time. [Fig. 5.4](#) (left) shows the oscillation of the isocentre for each frequency f_q , where lower-to-higher frequencies f_q are represented by the red-to-blue colourmap.
6. From there, the tune response can be calculated via FFTs, as represented by [Fig. 5.4](#) (right), with the same colourmap. The benefit of this approach from simulation data

Figure 5.4.: Beam isocentre and FFT spectra per excitation frequency

(Left) Mean beam position as a function of turn number, and resulting and FFT spectra.
(Right) Colourmap shows driven excitation frequency (low = red, high = blue).



is that it can check for multiple frequency responses in the spectrum.

Alternatively, using the BTF method, the magnitude A and phase ϕ , calculated as a ratio of input signal S_1 and isocentre S_2 , the calculations for which are shown in Lst. 5.1.

Listing 5.1: BTF Magnitude & Phase Difference

```

1     sin = np.sin(2*np.pi*f*t)
2     cos = np.cos(2*np.pi*f*t)
3     C1 = np.trapz(s1*cos) + 1j*np.trapz(s1*sin)
4     C2 = np.trapz(s2*cos) + 1j*np.trapz(s2*sin)
5     A = np.abs(C2)/np.abs(C1)
6     phi =
        (np.angle(C1)-np.angle(C2)+np.pi)%(2*np.pi)-np.pi

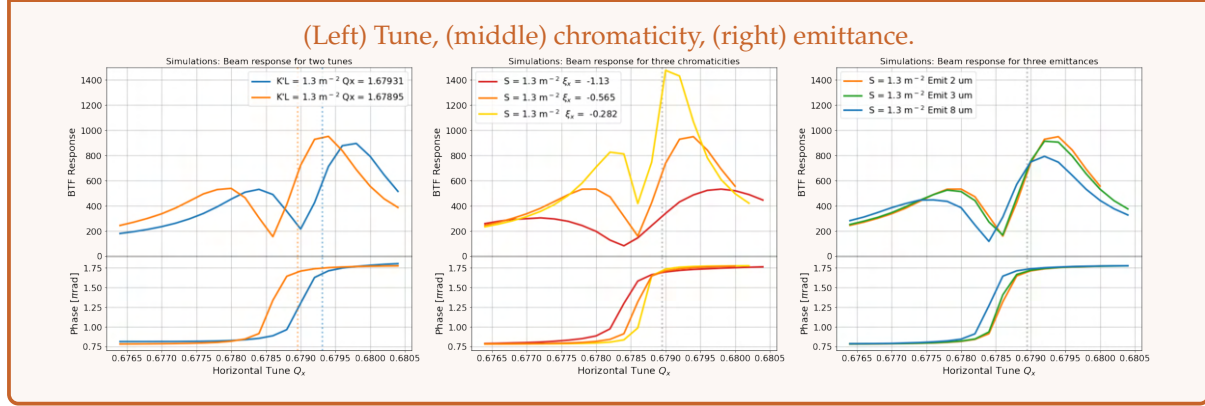
```

7. Finally, to compare to published measurements [109], this procedure was repeated for a range of sextupole strengths.

The results of the simulation can be seen in **Fig. 5.3** (right). Like the experimental results, the beam response has been normalised to 1, with the larger responses from the Gaussian-like peaks. Due to simulation time restraints, 40 excitation frequencies were investigated between $q_f = 0.674$ and $q_f = 0.681$, compared to the 701 data point resolution of the Network Analyser. Increasing sextupole strength increases the tune depletion until two peaks are formed. From this perspective, it is clear to see that the formation of the two-peaks happens within the Gaussian spread of the original distribution. Unlike measurements, simulations are not experiencing an offset which decreases towards the resonance with sextupole strength. This

is due to radial-loop in the machine causing a tune offset of the beam towards the resonance. As there are no longitudinal effects in the simulation or closed orbit offsets, this is difficult to represent.

Figure 5.5.: Plot of BTF tune magnitude response and phase varying as a function of tune, chromaticity and emittance.

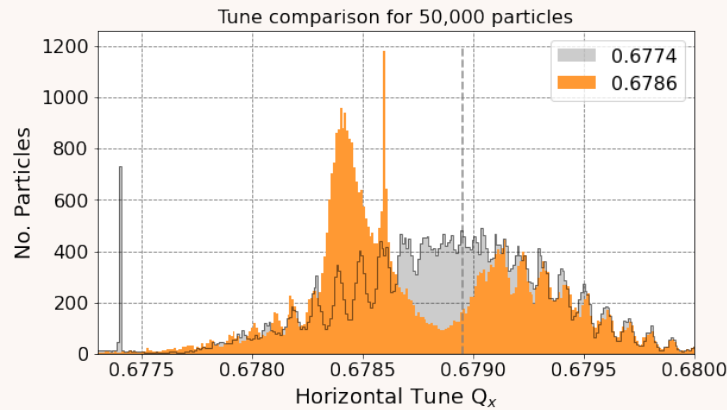


This process is repeated in Fig. 5.5 for different tune, chromaticity and emittance values, to understand their dependencies. Moving the tune towards the resonance will shift the distribution and heighten the amplitude response, which emphasizes that the resonance is causing this effect. Chromaticity has the most substantial effect on the distribution, as it widens the tune distribution therefore increases or lowers the amplitude response. Emittance amplifies the scale of the detuning by a small amount. Whilst tune and chromaticity are well defined operationally, there is no means to measure emittance in the machine, but in simulations it is otherwise assumed to be $1\pi\text{mm mrad}$.

5.2.3 Single-Particle Dynamics

For the above set of simulations, the individual particle traces were saved to compare their response to BTF measurements. For this set of simulations, a resonant sextupole strength of $k_2L = 1.3$ was chosen to emphasize the effects. NAFF was used to calculate tune of all 50,000 particles individually, over a given window. Calculating the tune over the whole 10,000 turns showed dramatic features in the tune spectrum. This is demonstrated in Fig. 5.6, which shows two tune distributions at different excitation frequencies. The first, in grey, has an excited frequency of $q_f = 0.6774$. This frequency, where a couple of particles are being driven at in a sharp peak, is far from the machine tune of $q_x = 0.6789$, and therefore has no effect on the Gaussian spread of the beam. The second, in orange, has an excited frequency of $q_f = 0.6786$, shown by

Figure 5.6.: Histogram of single-particle tune calculated by NAFF compared for two driven excitation frequencies.



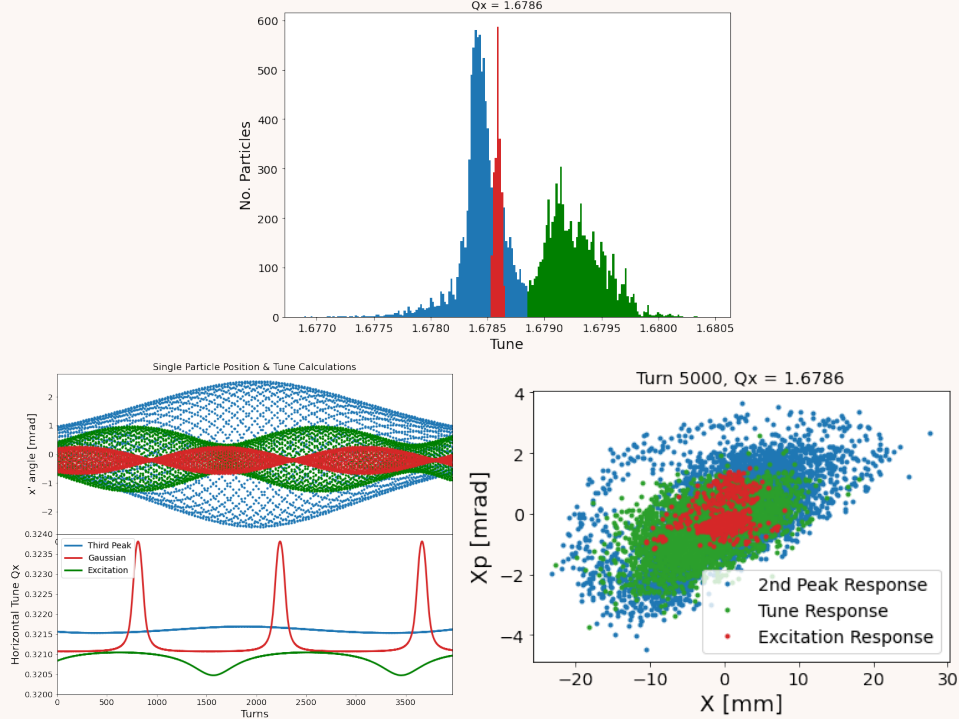
the sharp orange peak. Instead of a Gaussian, a region of tune is being depleted, causing a higher secondary peak.

Another feature of this figure is a small characteristic frequency ripple across the tune spread which is identical in both Gaussian peaks. This suggests the ripple is independent of the frequency excitation of the BTF, and is likely to be caused by sidebands of the excited sine wave. When analysed, this frequency was demonstrated to be at 230 Hz.

To take a look at some individual particles within this distribution of $f_q = 0.6786$, **Fig. 5.7** (left) identifies tune behaviour into three regions: the usual Gaussian tune response (green), the sharp excitation frequency peak (red) and the new peak due to the formation of the depletion region (blue). **Fig. 5.7** (centre) shows three particles, one taken from each region. The top plot shows their position, and the bottom plot shows a scrolling window of the tune covering 256 turns. All three particles feature regular position and tune beating. When looking at the average tune across the whole time, we see the dominant clusters of tunes that the particles are beating between. When looking at smaller time samples, we see the periodicity between the two tunes. This beating effect is more extreme when frequencies are being excited at the beam tune. The particles which were initialised in a stable state have a frequency corresponding to the machine tune - now that they are transversely responding to an external excitation frequency, the concept of linear tune breaks down, and it does not make sense to use a single value to describe both responses. From the raw position data, for a system like this, both the amplitude and the frequency of the particles are regularly changing as a function of time.

Figure 5.7.: Comparison of three-particles tune, position and phase-space.

(Top) Histogram of single particle tune split into three regions of behavior. (Left) Horizontal position and scrolling tune as a function of turn number for three particles within these regions. (Right) Phase-space distribution of particles within these three regions for a given turn number.



Gif available at

https://gitlab.com/accelrtaylor/phdthesisx/-/blob/main/animations/Ch5_HIT_1.mp4

Fig. 5.7 (right) demonstrates how these dynamics affects the phase-space distribution of the beam, for a single turn after 5000 turns of excitation. This distribution as a function of time is made clearer in the linked animation, where the phase-space has been normalised by dispersion, and the difference in distribution with coherent and peaked tunes changes with time. This correlation matters as the Schottky pickup is weighted by high amplitude particles, and is less affected by the dynamics at the core of the beam.

As whole-beam models have rough agreement with measurements, it is important that single-particle and whole-beam models also converge. This is to ensure that the validity of the single-particle model. The HIT BTF specifically picks out low bandwidths of 70-100 Hz, to filter for the excited peak. As a first attempt to extract the double-peak effect from simple particle tune dynamics, a gif is shown at <https://gitlab.com/accelrtaylor/phdthesisx/-/blob/main/>

[animations/Ch5_HIT_2.gif](#). It displays a NAFF-made histogram for the full 5,000 turns for each f_q excitation. A black line traces the highest amplitude peak within the low bandwidth. The low number of excitation frequencies makes this a low-resolution trace, however it implies a double-peak distribution similar to that seen in [Fig. 5.3](#).

Alternatives to NAFF

In this study, a system of varying amplitude and varying frequency is being sampled across a period of time. This is inefficient to calculate an immediate value of tune. The most optimal way at handling NAFF is to calculate the period of beating, and ensure that the window size covers a few periods of this. Otherwise FFT-based tune calculations run the risk of small windows capturing local minima/maxima at high uncertainties, or large windows averaging over and simplifying a series of overlapping effects.

Unlike measurements, simulations can have complete knowledge of particles throughout the system. For example, an instantaneous tune could instead be calculated by measuring phase-advance differences across a couple of turns. Alternatively, the FFT spectrum of individual particles could be checked for multiple response peaks in the spectrum. Future studies could benefit from investigating and comparing these methods.

5.2.4 HIT Discussion

Following a series of measurements at HIT, the set of maptrack simulations fulfilled two goals. Firstly they were able to verify that the two-peak response was not just an effect limited to measurements, but as a phenomenon is repeatable in simulations. Secondly, simulations elaborated on the current understanding of this effect, and help towards phenomenological explanations. They identified additional consequences of this effect on single-particle phase-space dynamics which would not have been observable through direct measurements.

To summarise, frequency measurements of a beam experiencing strong transverse excitations when near the third-order resonance produces a characteristic tune depletion, resulting in the appearance of two or three peaks. Numerical analysis of the system is proving challenging, hence the need for flexible and dynamic simulations to model this system. BTF signals were reproduced in simulations by exciting a beam through a range of frequencies. Both whole-particle isocentre analysis and single particle NAFF analysis provided further insight into this

effect. Useful insight into tune beating and behaviour was produced, and single-particle tune models produced good convergence into the whole-beam effects. The research concludes that the tune splitting of the BTF signal is the cumulative result of many particles under a system driven by two frequencies: the tune of the particle set by the machine, and the frequency of the driven signal from the Network Analyser.

As published by C. Cortes, this effect is beneficial to understand, as it was used to engineer a new HIT RF-KO signal which improved spill duty factor to over 90% for protons and to 95% for carbon [62]. Due to the complications of highly non-linear systems near resonances with strong perturbations, the collaboration has yet to develop a theoretical explanation which derives and accurately predicts the origins of this effect.

To conclude, this project was a unique opportunity to deep-dive into a theoretically difficult system. It encouraged the development of advanced simulation tools, which are highly transferable to the other chapters involving simulations and transverse excitation at resonant conditions.

Bibliography

- [62] E. C. Cortés García. “Investigation of RF signals for the slow extraction at HIT’s medical synchrotron”. en. MA thesis. Darmstadt: Technische Universität, 2022, ix, 105 Seiten. DOI: <https://doi.org/10.26083/tuprints-00020811>.
- [105] N. Karastathis. *A Python module that implements the Numerical Analysis of Fundamental Frequencies*. <https://github.com/nkarast/PyNAFF>.
- [106] *NumPy v1.26 Manual* — [numpy.org](https://numpy.org/doc/stable/reference/generated/numpy.hanning.html). <https://numpy.org/doc/stable/reference/generated/numpy.hanning.html>. [Accessed 19-12-2023].
- [107] P. Zisopoulos F. Asvesta N. Karastathis. *PyNAFF: A Tool for Numerical Analysis of Fundamental Frequencies*. 2019.
- [108] Claudia Carollo. “Dynamic tune measurement methods during slow extraction”. In: (2023). URL: <https://cds.cern.ch/record/2879826>.
- [109] R. Taylor E.C. Cortes Garcia P. Niedermayer. “Interpretation of the horizontal beam response near the third integer resonance”. 2024.

*Wish we could go back
to how it was, but now we're
too close to the wire.*

Haken (Carousel)

6

Measurements of slow extraction with octupoles

Slow extraction is an inherently non-linear process, which makes it highly sensitive to higher order effects. This chapter evaluates the effects of octupoles on a machine near the driven third-order resonance. Compared to [Ch. 7](#), which primarily looks at simulations for future designs, this chapter explores the slow extraction process on an existing machine. CERN Proton Synchrotron was used as the basis for these machine development studies. In [Sec. 6.2](#), octupole trapping results are demonstrated via simulations and measurement at 24 GeV and 2 GeV. These results provide a basis for the octupole model of the PS and explore the limits of the combined multipole effects. [Sec. 6.3](#) presents octupole folding as a method of shaping extracted phase-space to optimise the field-region of the ES. With cycles in both 2022 and 2023, the effects on tune-ramping, sextupole strength and extraction bumps are explored. It concludes with octupoles being beneficial to limit localises losses in the septum regions.

Whilst octupoles are not often explicitly present in hadron therapy synchrotrons, the amplitude-detuning effects of octupoles are a second-order effect of sextupoles, and future compact designs using combined magnets may unintentionally end up with such effects. It would be beneficial for these effects to be constrained such that they improve the extraction efficiency, rather than degrade it.

6.1 Background

THE WORK PERFORMED IN THIS CHAPTER WAS IN COLLABORATION WITH M.A. FRASER, P. ARRUTIA SOTA, E. JOHNSON AND M. DELRIEUX

Applying higher order nonlinear magnets to manipulate beam density is a common technique employed during synchrotron extraction. In 2019, the SPS Losses & Activation Working Group (SLAWG) applied octupoles during slow extraction at the SPS and demonstrated over 40% reduction in beam loss [40] from the ring. Via the mechanisms explained in [Sec. 2.2.4](#), this technique applied a bending effect to the high-amplitude separatrices of the slow-extraction phase-space. The strength of the amplitude-detuning distributes the extracted bar-of-charge with the aim of matching to the geometrical constraints of the extraction septa. With a successful demonstration of this effect at the SPS, the path is clear to perform the same procedure on the CERN Proton Synchrotron (PS). A dedicated study is required, as the PS is an older machine with its own unique geometric and non-linear components. Within the context of this thesis, this is an excellent opportunity to develop realistic simulation models, validated through matches to experimental data. In addition, the accessibility of the PS in terms of physical proximity and available beam time provides valuable freedom to this study.

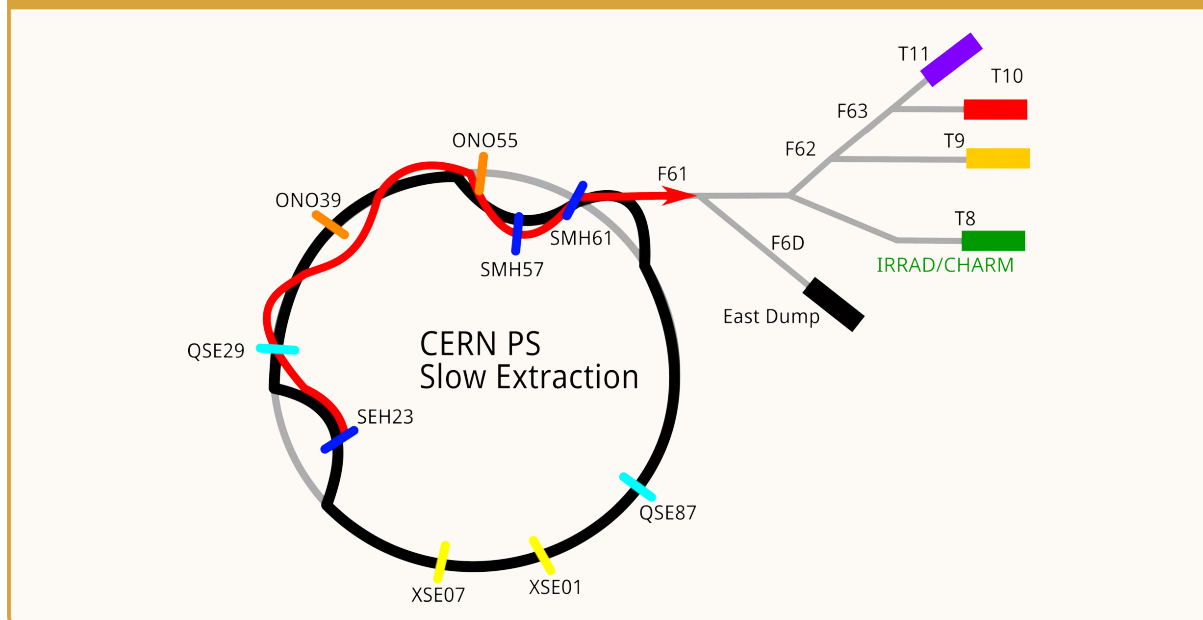
6.1.1 Proton Synchrotron

The Proton Synchrotron (PS) is a 100m radius, 628.3m circumference synchrotron, with a design energy of 26 GeV [45]. Built in 1959, it is the first example of an alternating-gradient synchrotron, with strong focusing of the particle beams. This is achieved via 100 combined-function magnets called Main Units (MU). These MUs combine dipole fields, focusing quadrupole components, and extra Pole-Faced Windings (PFW) around focusing and defocusing poles to provide higher order effects (see [Sec. C.3](#)). The segments of the PS are labelled from 01 to 100, with each one having a MU and a straight section for instrumentation and additional magnets. Components in each straight-section are numbered accordingly.

For extraction to the East Area, [Fig. 6.1](#) shows the elements used when beam is sent to the transfer F61 line. The machine tune is brought near the third-order resonance with the two QSE (Quadrupole Slow Extraction) quadrupoles (29, 87 in cyan). This resonance is excited by the three XSE (Sextupole Slow Extraction) sextupoles (01A, 01B, 07 in yellow). The tune of

the machine ramps through the resonance via the B-field, which controls the logical k_n of all magnets in a COSE-like manner (see [Sec. 3.3.1](#)). Extraction rate is fine-tuned via a high-order QH (Horizontal Tune) knob from the PFWs. The electrostatic septum SEH23 is offset via an extraction bump, and is negatively oriented. The kick from SEH23 provides an oscillating orbit which enters the field region of the first magnetic septum SMH57, which leads to the second magnetic septum SMH61 to provide a stronger kick through a gap in a MU to the F61 transfer line. The final beam is either extracted and dumped on the East Dump, or internally on the PS dump. If used operationally, it would be sent to the experimental facilities, from T8 - T11. When performing experiments with octupoles, two chains are available: the 8 ODN magnets

Figure 6.1.: Schematic of slow extraction from the PS to the East Area. Key components marked including quadrupoles (cyan), sextupoles (yellow), octupoles (orange) and septa (blue).



installed in the machine for non-linear control, and 2 ONO magnets (39, 55 in orange) installed in 2007 for the purposes of island formation and manipulation. The two octupole magnet families have lengths of 0.22 m and 0.5 m respectively.

6.1.2 Methodology

Machine Development (MD) studies are performed in the CERN Control Room (CCC). Each MD user has their own cycle which consists of a database of settings sent to the machine. The PS supercycle is made up of a series of smaller cycles, each taking 1.2 s for injection, accelera-

tion (ramp-up), flat-top, and ramp-down. This includes beam sent to the Antimatter Decelerator, East Area, the SPS and the neutron time-of-flight experiment. The MD used primarily in this study is referred to as MD5744. It is a low-intensity East T8 beam which is programmed to go to either the PS internal dump or the East dump.

Below is an overview of the tools, instrumentation and considerations referred to within this chapter to set up MD cycles. Some additional considerations are in Appendix C - [Sec. C.1](#).

Control and LSA

Control of the machine is performed via a series of GUIs and webtools where settings can be changed and edited for each Working Group of parameters. In this MD, the most important is LSA (LHC Software Architecture), where trims of the strengths of the magnets (in k or kL) are converted into a current and sent to the power converter for each magnet set. This way, custom signals can be sent to the apparatus, as long as they do not exceed the maximum current strength or ramp rate. This provides complete freedom of adjustments that can be made to the machine during extraction.

RF Bunching

The acceleration during ramp-up is performed by the RF cavity at the 8th harmonic, which bunches the beam into RF-buckets. In the East operational cycles, the beam is shared with nTOF. As nTOF requires a short-pulse length, the RF dynamics during acceleration introduces a phase-rotation to suit this pulse, then a further rotation is performed to increase to a larger momentum spread as needed for the East Area.

Slow extraction, is usually performed with unbunched (or coasting) beams to allow for continuous spill with no strong frequency relating to the revolution frequency. Group 2 of the RF Phase Voltage is used to inhibit the RF after 950 ms, with extraction starting after 1200 ms. Most instrumentation in the ring will require a bunched beam. This means that with a fully coasting beam in extraction conditions, it can be difficult to measure most properties of the beam. However, turning the RF cavities on to perform these measurements may not be comparable with the coasting option; the radial-loop within the PS has a dramatic effect on most optics, especially with strong amplitude-detuning, when octupoles are involved. The tune in the machine is now able to measure an unbunched beam via the method in Appendix [Sec. C.1](#)

Intensity and losses instrumentation

The most important instrumentation considered in this chapter are those that measure stable beam intensity, beam losses, and extracted beam intensity. The ring BCTs measure the intensity of the beam in the ring, calibrated to the number of injected particles. In this study, they are used to check the stability of the beam and to observe a rough uniform rate of extraction via a linear intensity decrease. The decrease in BCT signal is a sum of extracted beam and lost beam. In an ideal situation for MD5744, there would be constant intensity from 0-1200 ms, then a linear decrease throughout extraction until beam dump at 1600 ms. Any other signals suggest beam losses through other resonances, or failed transmission.

There are 100 ring BLMs to measure the losses throughout each straight-section of the PS. They are acquired as a function of time, but are not calibrated to any particular unit. In particular they are used to observe the total beam loss and losses on the three septa regions.

The F61 XSEC in the East Area extraction line is a Secondary Emission Chamber, used as a measure of extracted beam. XSEC23 is positioned before the switcher magnet going to the East Dump. From 2022 to 2023, a calibration difference of x20 was observed within this device. Consequentially, the XSEC is only used for relative comparisons, between measurements taken in the same year.

There is one additional instrumentation used later in the study which is the Beam TV (BTV). The BTV is a destructive measurement that allows for imaging of the beam. A screen is lowered into the beampipe, and when the beam interacts with the screen, a camera takes a photo of the resulting light emitted. There is a BTV at section 57 (BTV57), after the magnetic septum, which takes a photo of the extracted beam. In addition there are a series of BTV screens in the East Area extraction line, including at the East Dump (BTV61D). As these are destructive measurements, they hinder the beam quality for the other users of the East Area, and therefore should be used sparingly.

pyJAPC

To automatically get and set parameters to acquire results, pyJAPC (Java API for Parameter Control) scripting tools were applied in interactive jupyter notebooks. These scripts use the acc-py environment [110], sourced locally from the CCC computers. The scripts used are incorporated into the octutrap git repository [111].

For any parameter not manually measured during the MD slot, it can be acquired later via Timber, the CERN Accelerator Logging Service web application [112]. The *scan.ipynb* notebook was used in Sec. 6.2, for the beam trapping MD and could provide automated parameter setting. In Sec. 6.3, when dealing with beam loss, it is important to not needlessly dump radiation onto sensitive components. There, the setting of parameters is performed manually via LSA, and measured with the *monitor.ipynb* notebook found in the octutrap repository.

6.2 Octupole Trapping

Eq. 2.32 and Fig. 2.6 demonstrate how adding an octupole provides a bending effect to the slow extraction Kobayashi-Hamiltonian creating two distinct regions, the stable triangular core of the beam, and three islands of particles oscillating around stable fixed points. Whilst it is difficult to directly observe these islands in the machine, it is possible to observe the boundary between slow extraction and complete stability of the beam, by measuring the intensity within the machine with the BCT. By comparing with simulations, we can then visualise the processes that are occurring. This provides a good model of the sextupole and octupole dynamics in the machine, which is crucial for Sec. 6.3.

This MD is performed with the 2 ONO octupoles as they are stronger and more localised. Due to the large size of the islands the beam must be on-orbit to avoid hitting aperture limits, therefore the Slow Closed Bumpers (BSW23, BSW57) are turned off.

6.2.1 24 GeV: Simulations and Measurements

The simulation process was first understood by modelling the PS in Maptrack, chosen for its flexibility in making custom elements for the tune-ramping quadrupoles used in this experiment. A 6th order map was made from the East Slow Extraction scenario of acc-models-ps[113]. Map slices were made at the following elements: **START, XSE01.A, XSE01.B, XSE07, SEH23, QSE29, ONO39, ONO55, SMH57, QSE87**

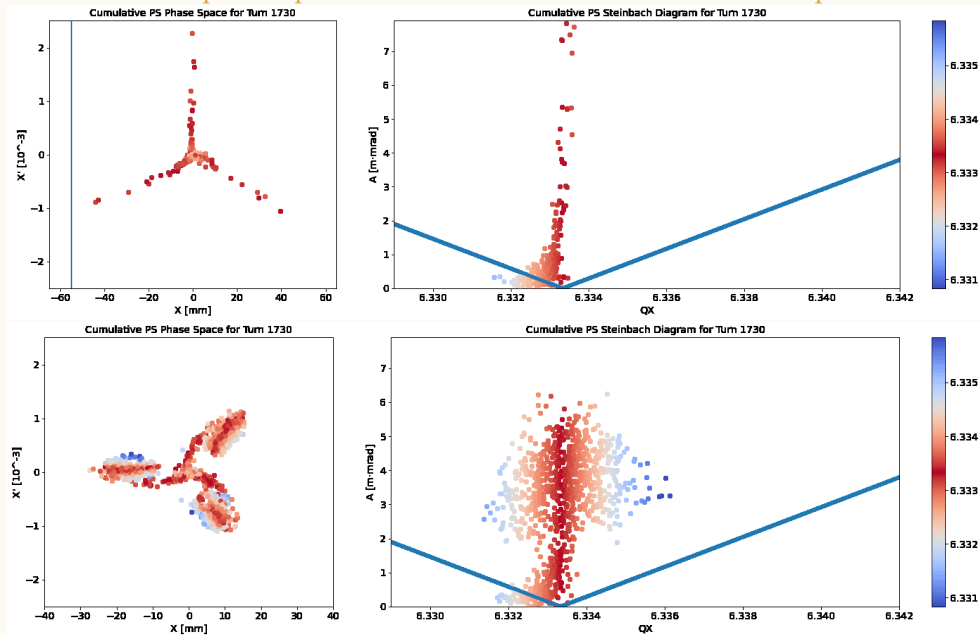
Start is used to generate an initial Gaussian beam with initial settings. QSE, XSE, and ODN are all modelled from their thick-lens transformation matrix. This allows for the quadrupole to be ramped dynamically through the resonance, and for the sextupoles and octupoles to be changed in-loop between each simulation with the same map.

The SEH23 septum is used as a counter for extraction, removing any particles that exceed the

aperture limit of -55 mm. This is later matched to the Timber acquired value of -72.95 mm $+ 50$ μ m. The SMH57 septum is used to check the orientation of the extracted beam at its entry. For a full extraction simulation, the particles at SEH23 would also need to be kicked and tracked to SMH57 and SMH61.

Figure 6.2.: Simulation of one-turn of the PS during extraction. Colourbar represents tune proximity to resonance (red = 6.333).

(Top) Nominal simulation without octupoles. (Bottom) simulation with high ONO octupole strength. (Left) Phase-space in $x - x'$, marking septum aperture X_{ES} as a thin blue line. (Right) tune-amplitude plot with thick blue line as the resonance stopband.



Available as a gif at

gitlab.com/acclrtaylor/phdthesisx/blob/main/animations/Ch7_PS_Extraction.gif

To understand the dynamics of this process, a simulation of 1000 particles is launched, which ramps into the resonance with QSE quadrupoles. **Fig. 6.2** shows this exact scenario twice, at the same turn number, with and without an arbitrarily high ONO strength $k_3 = -100$ m $^{-3}$. The colourmap indicates the tune of the particles, calculated from pyNAFF, described in **Sec. 5.1.1**. Note the stable regions in blue, compared to on-resonance in red, and how the measured tune of the particles in the islands remains distributed around 6.333, even after the stack of the beam has been pushed past that.

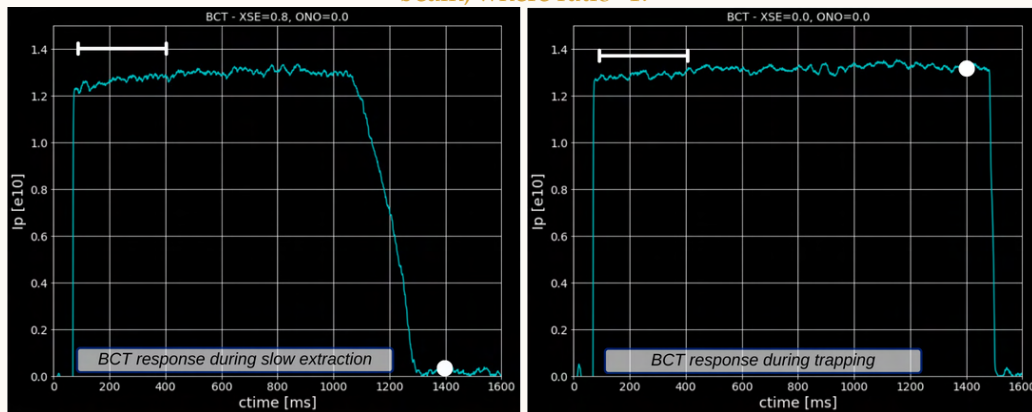
In measurements, there are two ways to measure island trapping. The first is to directly recon-

struct the beam phase-space, which requires a series of position measurements with a known phase-rotation between them. Whilst possible, this is difficult to perform at low intensities. The second is to calculate the stability of the beam in parameter space of sextupoles and octupoles. This is a five-step process to perform in measurements:

1. Firstly, the BCT can be used to measure the current as a function of time. Using the ratio of initial and final current, a *trapping ratio* can be determined. The recorded BCT signal for this process is expressed in Fig. 6.3. Where the ratio is 1 (Fig. 6.3, right), no particles are lost during the cycle, and therefore the beam is stable. Where the ratio is 0 (Fig. 6.3, left), all particles are lost throughout the cycle, and therefore the beam has undergone slow extraction, or is unstable. Anything in-between is where the beam is partially lost, i.e. if the islands have partially hit the septum anode.

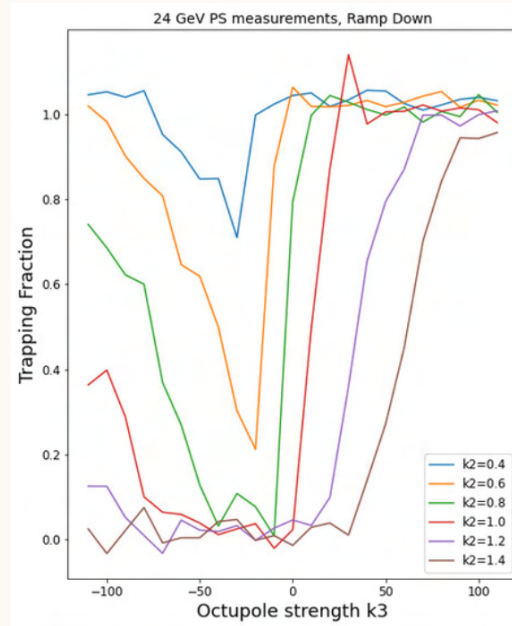
Figure 6.3.: BCT signal showing number of particles within the PS ring used to calculate trapping ratio as difference between average initial intensity (white bar) and final intensity (white dot)

(Left) Signal for complete extraction where ratio=0, (right) signal for a stable or trapped beam, where ratio=1.



2. Secondly, the octupole strength can be changed with each shot, to observe how the stability of the beam varies. A pyJapc script automatically sets values of strength to the XSE/K and ONO/K variables and the recording of intensity from the BCT was automatically acquired for each data point. Fig. 6.4 shows that high absolute octupole strength results in higher trapping ratio (stability), and that there is a minimum around $k_3 = 25 \text{ m}^{-3}$ where the final beam current is lowest, and that this minimum is wider for larger sextupole strengths.

Figure 6.4.: Measurement of trapping ratio for each octupole strength as a function of sextupole strength (low=blue, high=brown)



3. Thirdly, the data points in **Fig. 6.4** can be represented as a point in parameter-space between sextupole and octupole strengths. This outlines the regions where slow extraction occurs, regions where trapping occurs, and then regions in-between. **Fig. 6.5** plots this information, representing the cyan circles as regions of stable beam where the trapping ratio = 1, and the black circles as regions of unstable beam, where the trapping ratio = 0.
4. Finally these datapoints can be turned into a contour plot to clearly define the regions within sextupole-octupole parameter space. **Fig. 6.6** (left) shows the resulting measurement. Simulations were performed where each simulation at a different sextupole and octupole setting was combined together to create the same plot in **Fig. 6.6** (right). As contour plot requires a large number of data points, a large number of simulations needed to be performed, so for this example each one is only made from tracking 200 particles. This low number means that statistical fluctuations are significant.
5. The benefit of this perspective is that it allows the effect of octupoles in the synchrotron to be represented as a single triangle. **Fig. 6.6** (middle) compares the measurement and simulation trapping triangles. Whilst the low statistics in simulations explains some of

Figure 6.5.: Plotting datapoints in octupole-sextupole parameter space with colormap as the trapping ratio (cyan=high final current, black=low final current)

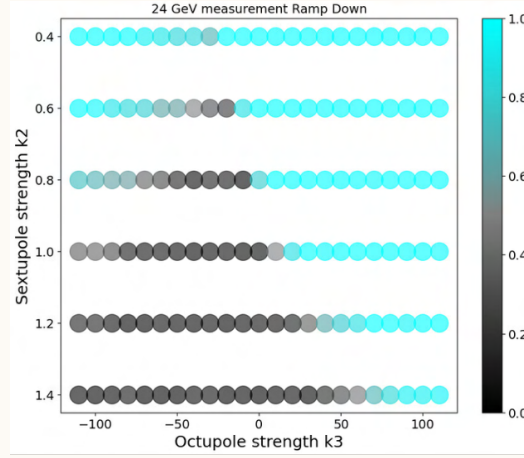
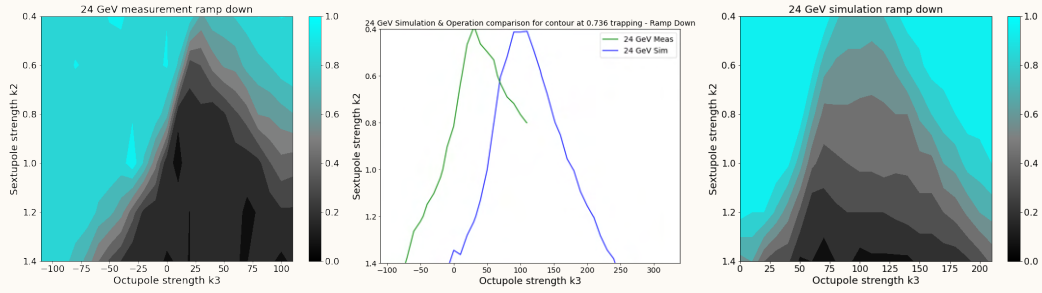


Figure 6.6.: Contour plot showing trapping ratio at 24 GeV for measurement (left) and simulation (right). (Black = stable, cyan = lost). Includes their comparison (middle) at 75% trapping.



the distinctions between simulations and measurements, the process of comparing simulations and measurements identified some key discrepancies in the machine. A polarity difference between the software and hardware current was identified, along with a calibration difference of length $L=0.5$ between the set ONO/KL value in LSA and the converted current. Both of these were corrected. Whilst the triangles constraining the trapping region have a similar width, they have a significant offset by $k_3 = 30$, which suggests a difference in the inherent octupolar strength in the machine between simulations and measurements. This difference was identified to be due to the PFWs.

Tab. 6.1 shows the parameters that were set for this measurement at 24 GeV, which were the same as those used in the simulation.

Table 6.1.: MD measurement parameters for cycles at two energies

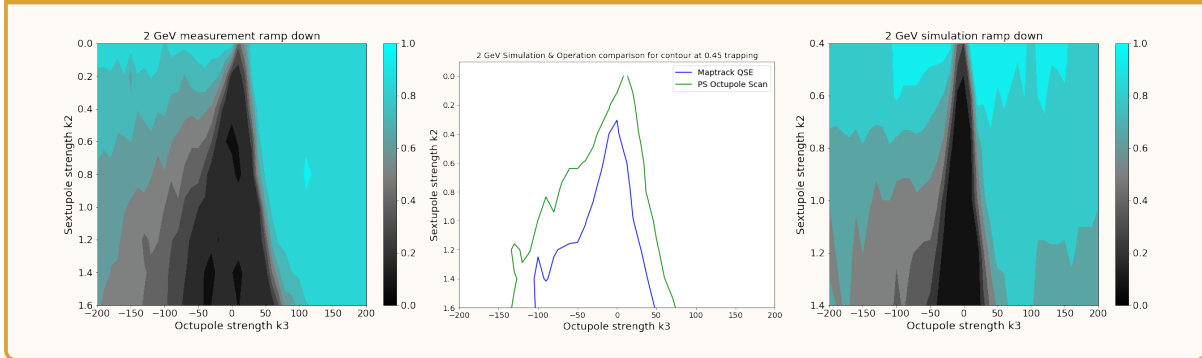
Param.	24 GeV	2 GeV
Q_x	$6.35 \rightarrow 6.333$	$6.35 \rightarrow 6.333$
Q_y	6.23	6.399
$\epsilon_x [\pi\text{mm}\cdot\text{mrad}]$	1.0	1.0
$\frac{\Delta p}{p} [\%]$	0.0324	0.266
$n_{\text{particles}} [10^9]$	6	1.5
$t_{\text{dump}} [\text{ms}]$	1600	1600
LEQ $k_1 [\text{m}^{-1}]$	0	$0.1977 \rightarrow 0.1644$
QSE $k_1 [\text{m}^{-1}]$	$0.118 \rightarrow 0.102$	0
XSE $k_2 [\text{m}^{-2}]$	$0.4 - 1.4$	$0 - 1.6$
ONO $k_3 [\text{m}^{-3}]$	$-55 - 55$	$-100 - 100$
Aper. [m]	-0.075	-0.075

6.2.2 2 GeV: Simulations and Measurements

To experimentally verify if the PFWs are responsible for the offset in the octupole trapping triangles, a new cycle was produced at the energy of 2 GeV, i.e. at injection energy, which does not involve the PFWs, as there is no acceleration. At this energy, the Low Energy Quadrupoles (LEQs) were used in place of the QSE quadrupole in both simulations and in measurement. In measurements, significant drops in intensity were observed, even at nominal settings with no extraction, shown in Appendix C, [Fig. C.4](#). The working theory for this is because of the larger space-charge, enhanced by the excited 4th-order resonances once octupoles were added. Previous studies performed at 1.4 GeV in 2003 have studied the space-charge under this same system, and confirmed space-charge as a factor of amplitude-detuning and cause of beam loss [114]. For further explanation of how octupole tune-spread behaves in the PS under space-charge, please see F. ASVESTA 2020 ([115] Figures 5.47 - 5.51). To minimize this effect, new working points in tune were explored. Vertical working points were limited in order for Q_x to remain close to the $Q_x = 6.3$ resonance. To mitigate the effect of this distribution, the background losses as per XSE = 0, ODN = 0 was subtracted from each datapoint.

The process for 2 GeV was repeated in both simulation and measurement. [Fig. 6.7](#) shows the characteristic triangular region with a 0 trapping ratio, but now experiences a larger fringe-region of partial losses, due to this space-charge affect disrupting the stability of the islands. Most importantly however, they are both centred on zero, giving strong evidence that the offset due to octupole strength is from the residual k3 strength of the PFWs.

Figure 6.7.: Contour plot showing trapping ratio at 2 GeV for measurement (left) and simulation (right). Includes their comparison (middle) at 45% trapping.



Discussion

The investigation of island formation with octupoles was important as a first experience into accelerator operation and machine development. Without the septa or aperture to consider, it was a relatively simple set-up, with identifying features. Despite this, the formation of islands is interesting, and simulation set up provided many questions along the way. Presently there is a growing interest in octupole island formation at the third-order resonance in combination with channelling crystals, for septum-less extraction.

Within this study, the largest curiosity along the way was the asymmetry in the triangular contour plots. There are two main variables that affect the polarity of the Hamiltonian of [Fig. 2.6](#). The first is the polarity of the octupole strength, and the second is the direction that one enters the resonance (i.e. the sign of ϵ). Having an incorrect combination results not in three distinct islands of trapping, but instead trapping around the non-linear Hamiltonian, where the three islands are depleted, and everywhere else is filled. Appendix C contains [Fig. C.5](#) which displays the phase-space of the beam at two polarities. This would explain why the side of the trapping triangle which has non-linear trapping experiences larger amplitudes and therefore more likely to have losses.

Overall, the measurements have a surprising similarity with simulations considering the inappropriately low statistics used in Maptrack. Should this study be repeated, the use of Xsuite would allow for faster simulation times and well-needed higher statistics. In addition, more caution should have been given to the inherent non-linear chromaticity of the system emerging from the PFWs. An attempt was made in simulations to match the MADX PFW components to

the non-linear chromaticity measured in QMeter, although the results gave worse agreement to measurements than the default MADX settings. There is also an incompatibility between the MADX calculated virtual octupole strength from the PFWs, and the actual octupole offset from either simulations or measurements, demonstrated and explained in Appendix C, [Sec. C.3](#).

6.3 Beam Extraction Efficiency

Losses in slow extraction commonly arise from particles scattered on the aperture limits of the extraction septa. The wire of electrostatic septum anodes are designed to be as thin as possible to limit interactions with the beam. This can be further minimized by increasing the spiral step ([Eq. 2.33](#)) of the extraction process via a higher sextupole strength, however this causes a larger rectangular bar-of-charge, and risks overlapping with the cathode aperture.

The optimum solution would be to increase the density of the beam within the septum such that a larger sextupole can reduce errors on the anode, and the curvature from the octupole can avoid the beam incident on the cathode.

Methodologically speaking, a similar approach as octupole trapping can be implemented. The major difference is that the strengths of the octupoles are fine-tuned to a specific region where the curvature applies within the field-region of the electrostatic septa. Fine-tuning downstream ensures this new distribution can navigate throughout the remaining magnetic septa into the extraction line.

Measuring an improvement of extraction efficiency means observing not just the intensity of the beam leaving the machine, but also counting the losses throughout the machine during extraction, and keeping track of where the losses are occurring. Typically, peaks in the BLM spectrum can be seen at sections 23, 57 and 61, where the three septa are positioned, but scattering of particles from the septa apertures also spreads the losses throughout neighbouring sections.

The octupoles used in this study will be the ODN-chain of octupoles, as they are more equally spread across the ring and have a lower strength, meaning a gentler and non-localised combined octupole effect. The 8 ODN magnets can be found in straight-sections 40, 50, 52A, 52B, 70A, 70B, 90, 100, and are controlled by the same set of power converters. Compared to [Sec. 6.2](#), the extraction bumps have been reintroduced via the BSW magnets, giving a closed orbit with high amplitudes, which enhances the effects of the octupoles. In addition the SEH23 was rein-

roduced to its optimal position.

A low intensity is used in this study, of 20E10. This is because it limits position damage to the SEH23 anode wire, and there is a limit to what intensity can be sent to the East Dump, of 30E10, and beam should not be sent to experimental areas whilst experiments are running. When sending beam to the East Dump, a negative magnetic field is applied across the switching dipole which causes bending hysteresis. This dampens the next positive magnetic field to experimental areas, causing an asymmetric mis-steer of their received beam. During MDs, this is solved by adding a two-period 'degauss' cycle between the east-dump and the next east cycle.

6.3.1 Simulation indications

Ch. 4 outlines MADX-PTC which is used here for simulation comparisons with extraction efficiency measurements. The numerous octupoles in the ODN chain, plus the off-momentum orbits due to the BSW extraction bumps makes this simulation challenging with Maptrack. Maptrack becomes slower and less efficient with more slicing, and orbit differences between each map and custom elements. When the simulations were needed, Xsuite was not yet fully released, leaving MADX-PTC as the main tool available.

Table 6.2.: Septa simulation parameters

		SEH23	SMH57	SMH61
Kick	mrاد	-0.3907	4.362	1.536
Anode Width	mm	0.1	4.0	25.0
Anode Pos	mm	-72.95	-76.1	73.0
Cathode Pos	mm	-88.05	-106.1	122.0

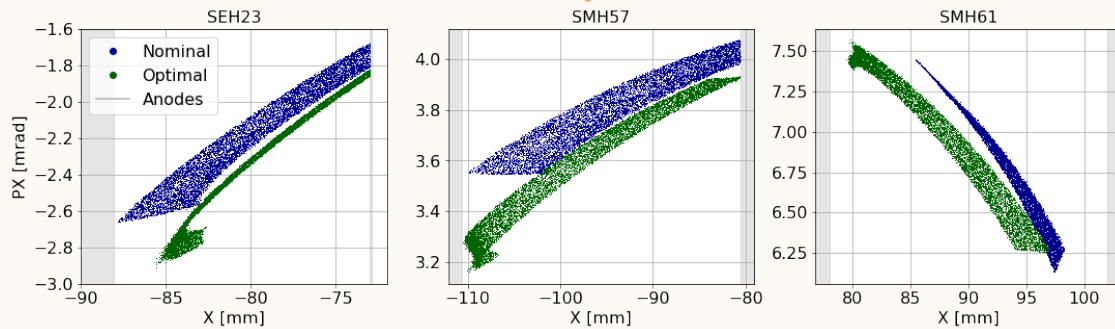
The East Slow Extraction scenario of acc-models-ps [113] was run within *ptc.track* with optics established exactly on resonance, to observe the standard behaviour of particles, assuming ideal conditions in the machine (e.g. Hardt condition). The simulation is run much like **Sec. 6.2.1**, except now advanced aperture models for the SEH23, SMH57 and SMH61 are generated. For MADX-PTC, these are made in analysis post-processing to selectively remove lost particles in the aperture regions of **Tab. 6.2**. The field throughout the septa can be included as part of the simulation, but the increase in computation time makes it incompatible to perform high-statistics simulations. Instead further MADX-PTC simulations are made to take the

SEH23 extracted distribution and apply kicks to SMH57 and SMH61, respectively. A further challenge of simulating this system is that the scattering from the septa gives downstream losses which are difficult to reproduce without extensive material modelling of the whole PS from sections 23 to 57 to 61.

Figure 6.8.: Horizontal beam distribution with and without octupole components

(Top) Phase-space of extracted beam for each septa with (green) and without (blue) octupoles.

(Left) At electrostatic septum, (middle) downstream at the first magnetic septum, (left) downstream at the final septum before extraction.



(Bottom) Histogram of x-distribution showing extracted beam density.

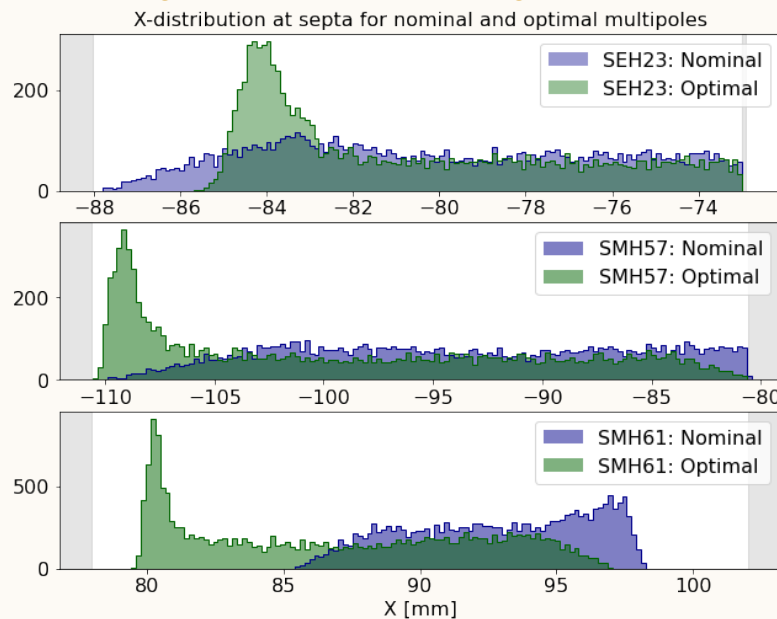


Fig. 6.8 shows the results of the simulation when observing the distribution of the beam for the nominal settings ($XSE=1.414$, $ODN=0$) and for a specifically chosen optimal setting ($XSE=1.836$, $ODN=-6.0$). It is clear to see the benefits of the octupole for not only curving the peak of the bar-of-charge away from the cathode, but also for providing a peak to the otherwise

uniform beam density, which can be steered away from the downstream aperture limits.

6.3.2 Measurements 2022

THE RESULTS OF THIS SUBSECTION HAVE BEEN PUBLISHED AS PART OF IPAC23 PROCEEDINGS [116].

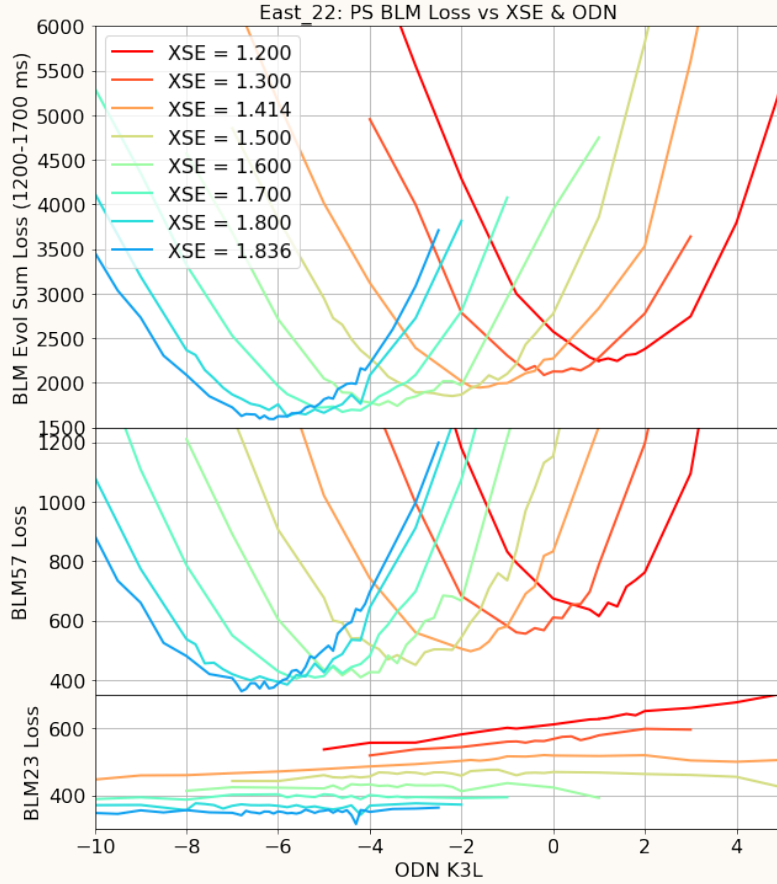
10.18429/JACoW-IPAC2023-MOPM071

Much like for [Sec. 6.2](#), the MD performed in autumn of 2022 involves a scan of changing sextupole and octupole strengths, although this time performed manually to ensure the losses in the ring were not at critical levels. An East.T8 cycle was used at 24 GeV, delivered to the East Dump, called *MD5744_East_T8_22*. Values for the BCT, BLM XSEC, and other variables were obtained for each parameter via *monitor.py*. The time-period over which the losses were acquired is important, because once the B-field ramps down, any beam not extracted is often lost on its way towards the PS internal dump. Losses are typically tracked from 1200 ms - 1700 ms, as this is the time period over which extraction occurs. Caution is necessary, as being too close to the resonance will give uncounted losses around 1150 ms, when the QSE starts ramping. In addition, an improvement in losses before 1700 ms will not translate to higher extracted intensity if they end up all lost at 1750 ms.

[Fig. 6.9](#) shows the results of the octupole and sextupole scan for three sets of BLM measurements:

- (Bottom) BLM23, representing the losses due to scattering from the SEH23 electrostatic septa. The losses on SEH23 have a strong dependency on sextupole strength (low=red, high-blue) and a slight linear dependency on the octupole setting. The dependency on the sextupole strength suggests that the majority of loss reduction is due to the increased spiral step, therefore more particles are avoiding the anode foil. The reduced dependency on octupole strength suggests that there are no significant losses from the cathode, and therefore curvature of the beam phase-space due to the octupoles is not significant.
- (Middle) BLM57, representing the losses due to scattering from the SMH57 magnetic septa. It is clear that the loss distribution is dominated by SMH57, which displays a strong parabolic distribution as a function of octupole strength. Each parabola has a minimum octupole value for each sextupole setting. The gap of the SMH57 septa is very small relative to the size of the beam, so the minima point corresponds to the ideal parameter settings that minimize both the scattering on the left and right poles.

Figure 6.9.: East22 Results:BLM23, BLM57 and sum BLMs as a function of ODN strength. Color represents is XSE strength.

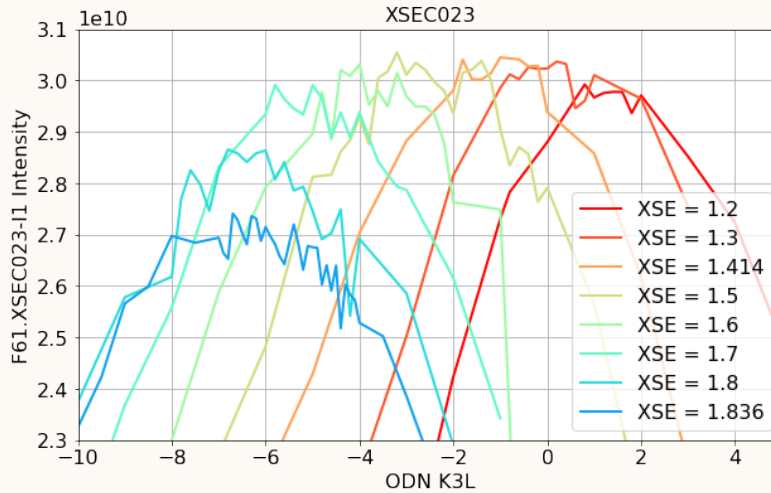


- (Top) Sum of the ring BLMs throughout the whole machine, which is dominated by the parabolic losses from the SMH57. At the center of each parabola, the resolution varies with shot-to-shot intensity fluctuations.

As the parabola for XSE $k_2=1.414$ (orange) does not have its minima at exactly ODN $k_3 = 0$, it suggests that a small negative ODN strength is beneficial to the losses on SEH57 and total ring losses.

Every result in Fig. 6.9 has the same quadrupole strength and ramping rate which is intended for the nominal settings of XSE=1.414. This means that there is an incomplete extraction rate in the BCT when one changes the octupole and sextupole settings. This can be observed in the XSEC of Fig. 6.10, showing that less beam is extracted at higher XSE. Instead one can calculate the ratio of beam lost to beam extracted, representing the extraction probability per proton.

Figure 6.10.: East22 XSEC measured intensity as a function of ODN strength. Col-ourmap shows XSE sextupole strength (red=lower, blue=higher).



The most optimal multipole setting has an extraction probability per proton improvement of 25% with respect to the nominal operational settings [116], however this is with incomplete extraction.

6.3.3 Measurements 2023

With a new year, the *East_T8_23* cycle introduced some configuration changes. These changes were set up during commissioning by operators to improve the losses for the nominal operational extraction to the East Areas. The largest effect was a steering algorithm ([Sec. C.3](#)) used to optimise SEH23 position, angle and voltage and SMHs angle and strength. This required the adjustment of the extraction bumps 23 and 57, and the QSE optics to help close this bump. The nominal XSE strength was changed to 1.393 instead of 1.414 to improve spiral step. Furthermore, changes in the acceleration ramping allowed for slightly longer extraction times, so all extraction components ramping occurs around 100 ms earlier. In addition the PFWs has been tweaked to keep the beam stable during acceleration, see [Sec. C.3](#).

Cumulatively, these changes give a subtle effect to the extraction of the beam, but initial investigations found a dramatic effect on the octupole-loss relation, compared to [Fig. 6.9](#). Instead larger XSE and ODN strengths gave a worse beam loss compared to nominal.

In light of these changes, the priority of this study is to include octupoles as an additional tool to reduce the losses in the ring. For this to be provided operationally, it is important to un-

derstand the consequences of the distorted extraction distribution, and how it changes with extraction magnet variables. Other than the multipoles, most predominate control comes from the strengths of the extraction bumps, which were kept constant throughout the previous year of study.

Extraction Bumps

When extraction bumps are activated, the closed-orbit of the beam is non-zero throughout the synchrotron. On top of this there are two predominant bumps in the optics. The first is BSW23, (Slow Closed Bumper at section 23) to adjust the proximity to the beam at SEH23. The second is BSW57 to do the same for SMH57.

As the most sensitive component is the anode-wire of SEH23, the priority in simulations and measurements is to understand and reduce this local loss in the BLM23. When exploring how BSW23 affects the septa, an interesting effect is found.

Simulations in MADX-PTC launch 10,000 on-resonance particles until a sufficient number of them are lost (≈ 200 turns). This is repeated for a range of BSW23 K values - limited by the constraints one can input into LSA. The phase-space as a function of the BSW23, and the corresponding losses on the septa wire and cathode are shown in [Fig. 6.11](#). The same colours are used for the same BSW23 strengths in both figures. The left-hand plot demonstrates how the BSW23 bump allows for the separatrix to have more room or less to bend within the same octupole strength.

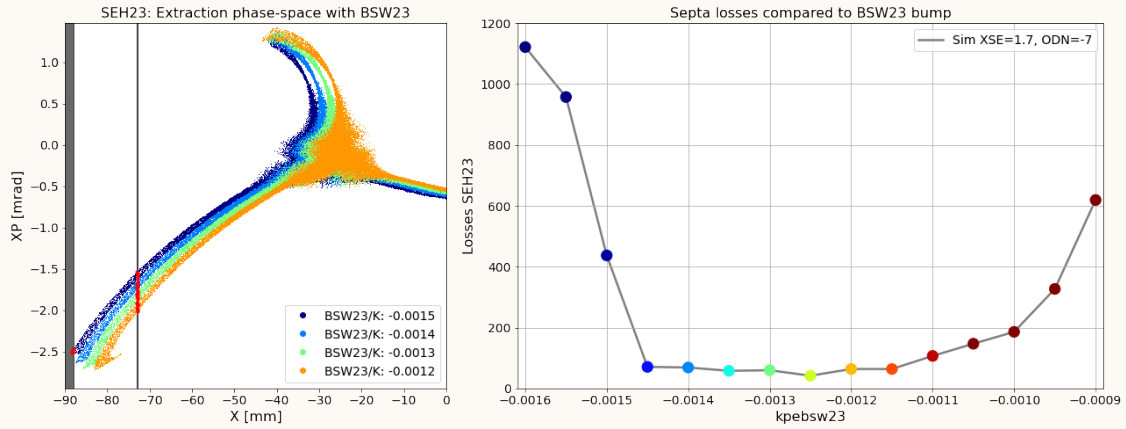
This plot informs us that a larger BSW bump will increase losses at the SEH23 cathode via larger spiral step. Likewise, a smaller BSW bump will increase losses at the anode from the beam folding back towards the wire. We can predict that the optimum BSW23 value will be the smallest possible value before the beam curves back onto the anode wire.

When explored in measurements, [Fig. 6.12](#) agrees with this distribution of having a clear flat-plateau of minimum losses, in-between two steep increases. The line in orange represents how the shape of this distribution changes with both the octupole and sextupole strength, as both of these affect the spiral step and curvature. An important realisation was that large spiral step has a consequence on losses downstream. The dashed lines in [Fig. 6.12](#) shows how small strengths of BSW23 causes dramatically increasing losses at the magnetic injection septum of BLM41. This strongly implies that optimising BSW23 for the SEH23 will not necessarily reduce

Figure 6.11.: Phase-space simulations for changing BSW23 strength

(Left) Simulated phase-space distribution with colormap showing change in BSW23 strength.

(Right) SEH23 losses as a function of BSW23 strength with same colourmap.



global losses.

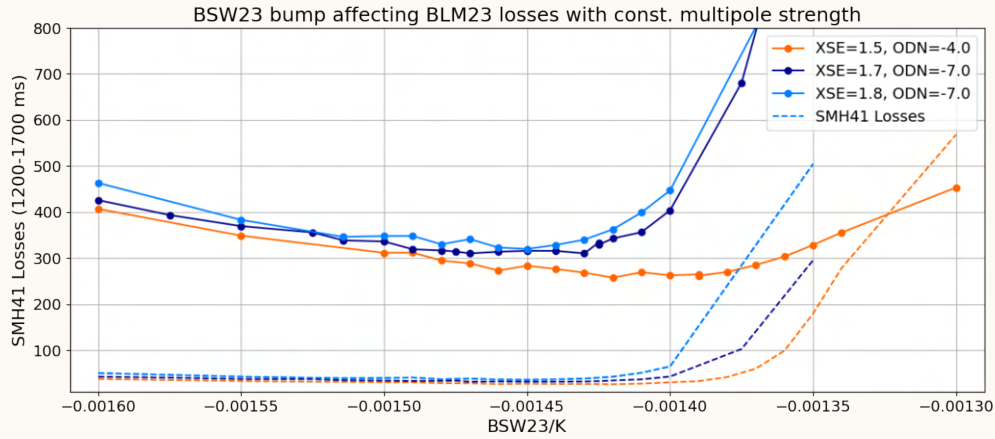
Final Results

It is clear from the previous investigations that there is a large range of parameters that affects extraction losses on the septa. Some are PPM (pulse-to-pulse modulation), meaning they can be different between each cycle, and some are non-PPM and affect every cycle. The PPM parameters commonly used are QSE or QH.PFW, XSE, ODN, BSW23, BSW57, SMH57, SMH61 and the DHZs (see [Sec. C.1](#)). On top of this, the SEH position, angle, voltage and SMH57 and SMH61 position and angle are adjustable but non-PPM. It would not make sense to find a complete set of these optimised parameters, as the MD5744 cycle uses low-intensity and it cannot be assumed that this would map directly to the operational cycles. Instead, it is worthwhile to identify the effect of octupole folding on the extracted beam distribution.

To identify this effect, first the default settings are taken to study the relation of octupole and beam losses. Then one at higher XSE and ODN is chosen, with the tune ramp rate adjusted with the QH.PFW to compensate for the change in resonance. Then a comparison is made between the nominal settings of the cycle, and this higher sextupole strength, adjusted tune and increased negative octupole strength from the ODN.

Fig. 6.13 represents the combined data-set for this process, where the solid lines are the default settings for East23 settings. To represent the changes from octupoles, a XSE of 1.7 was chosen,

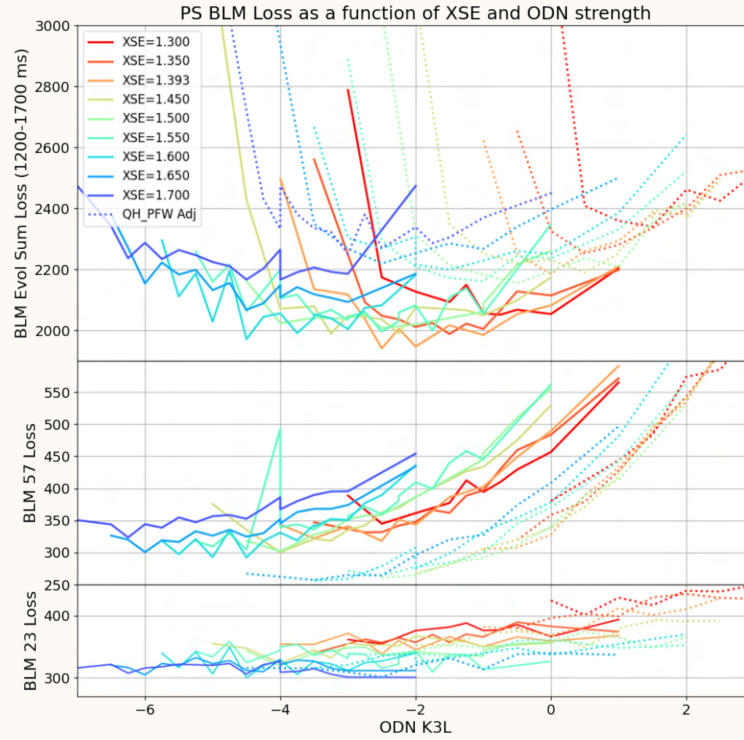
Figure 6.12.: Measured losses at SEH23 and SMH41 septa as a function of BSW23 strength.



which is the highest safest LSA setting that does not trip the magnet. To adjust to this higher XSE, and to maintain constant rate of extraction, the QH_PFW knob across 1150 ms - 1690 ms was adjusted from $[0.0075 \rightarrow 0.005]$ to $[0.012 \rightarrow 0.0095]$. Whilst it is possible to also change with the QSE, this would affect the optics of the extraction bump and therefore not preserve the loss relation. The dashed lines of Fig. 6.13 represent the octupole-loss relation for this new set of parameters. Whilst there are many more net losses across the ring, there is a dramatic reduction in the losses at the magnetic septum, and a small improvement in the electrostatic septum. It is possible to alter the parameter space to reduce these net losses to below nominal settings, but it often comes at the price of having increased septa losses. Then the losses were summed for each BLM from 1200 ms - 1700 ms. Fig. 6.14 shows the difference between the two scenarios. The negative relative losses means an improvement compared to nominal, and increased relative losses demonstrates regions with more losses as a result of the octupoles. The figure below compares the sum of all losses through a wider timescale, and it is clear that these benefits are lost after around 1720 ms, once extraction ends. Consequentially, despite a reduced loss measured at the septa during extraction, in this scenario it does not translate to an improved extraction intensity delivered to the East Area. To observe the resulting effect on the individual BLMs, acquisitions were taken for nominal (XSE=1.39, ODN=0) and with octupoles (XSE=1.7, ODN=-3) averaged over five shots.

To visually demonstrate the effect of octupoles, measurements were taken at the Beam-TV at 57 and on the East Dump. BTV57 is just after the magnetic septum, and has a retractable screen

Figure 6.13.: East23 Results: BLM23, BLM57 and sum BLMs as a function of ODN strength with (solid) and without (dashed) QH_PFW shift. Colormap is XSE strength.

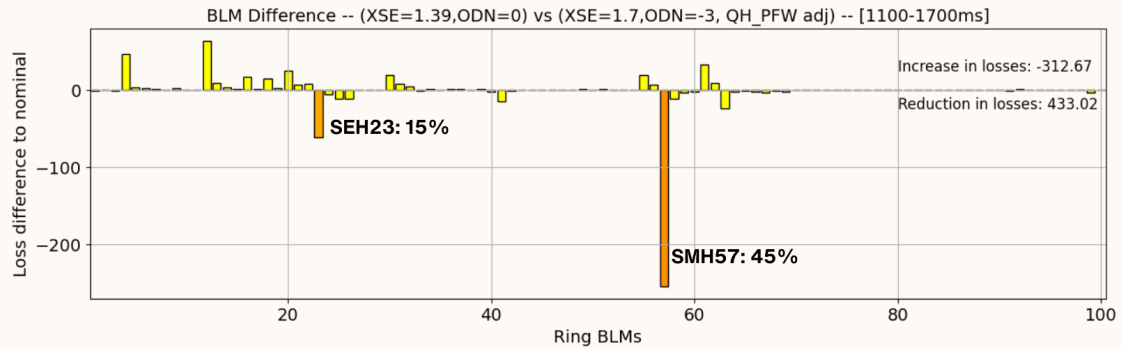


where images of the beam can be taken. **Fig. 6.15** shows the physical image of the beam in the nominal setting (blue) and with higher octupoles and sextupoles (green). The wider beam size due to increased sextupole and spiral step is clear. Furthermore it can be clearly seen that the density of the beam has shifted, creating a linear intensity distribution in X compared to nominal. With higher sextupole strengths this peak can be increased, however due to losses, it also showed a lower intensity on the BTV. Only two measurements could be taken, as the BTV at SMH57 is a destructive measurement which affects all other East cycles. The simulations were performed with 10 000 particles over 500 turns, exactly on resonance. The setup of the simulation is relatively simple, and the parameters of the MD can be matched, along with agreement in the bump and septa kick parameters. The clear difference in the behaviour can reasonably be attributed to the inherent octupole offset in the machine shown in **Fig. 6.6**. The changing k_3 component in the PFW changed between 2022 and 2023, and it is not trivial to derive this component from the PFW currents.

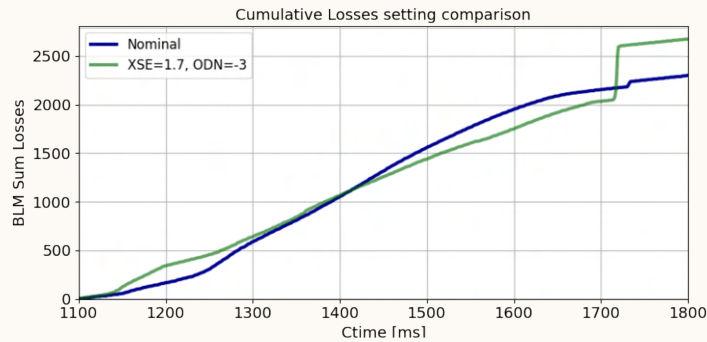
BTV61 measurements shown in **Fig. 6.16** provided more freedom of measurement as it is po-

Figure 6.14.: Localised and temporal effects of octupoles on ring BLMs

(Top) Difference in ring BLM signal with and without octupoles, showing local benefits and disadvantages.



(Bottom) Sum of ring BLM signal as a function of time with (green) and without (blue) octupoles.

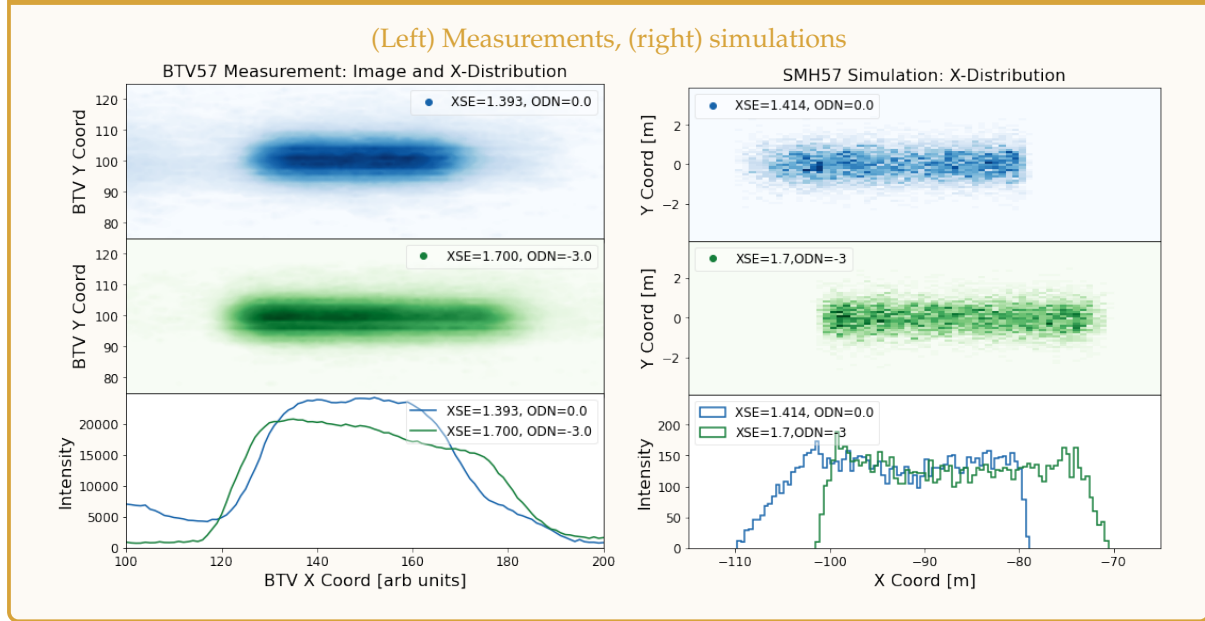


sitioned just before the dump, however the beam distribution is affected by the fringe fields of the exiting MU, and the F61 transfer line [116]. As a result, statistics are much lower at higher octupole strengths due to non-optimised steering in the transfer line. It is clear to see the smearing of the Gaussian-like initial distribution towards a linear-like distribution.

6.4 Chapter Approach & Conclusions

The conclusion of this chapter is that finely-tuned octupoles are beneficial in shifting the density of the extracted beam in phase-space. Whilst this works best with an increased sextupole strength to increase spiral step, this leads to a larger beam size which is harder to transfer downstream and to the F61 extraction line. The most beneficial way that this information can be implemented is the East cycle commissioning at the beginning of the year, when optimising the steering.

Figure 6.15.: BTV57 signal in X and Y with and without octupoles

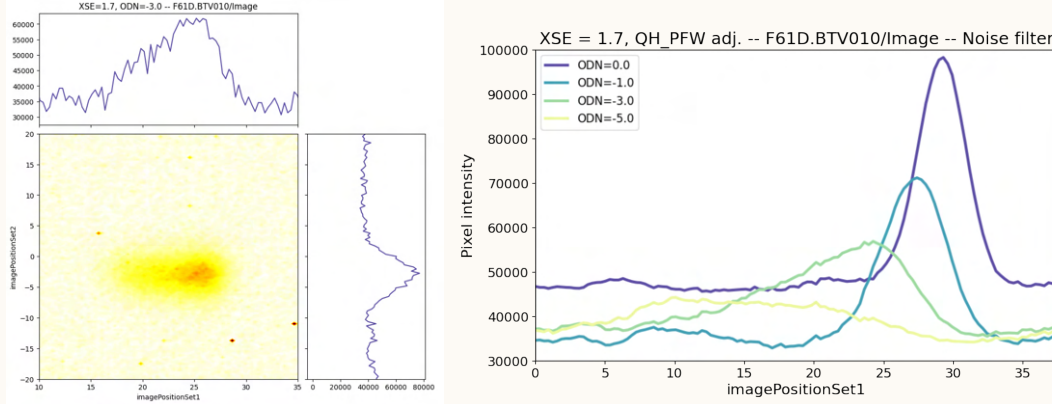


There are two options to applying octupoles during PS extraction. The first is to apply a small negative strength at nominal settings, which improves losses by a few percent at the SMH57 septa, and as a sum of all losses. The SEH23 has very low losses from the cathode, so changing octupoles does not reduce SEH23 losses. The effects are not significant, as the slight octupole inherent in the PS MUs is already beneficial to the extraction, but this has the benefit that it does not change the optics substantially.

The second option is to increasing both sextupole and octupole strength in the machine. As this will adjust the rate of extraction, the QH.PFW knob should be adjusted linearly to maintain a complete extraction. This will reduce losses on the SEH23 up to 15 %, as the spiral step has increased, and with sufficient octupole strength, significant losses on the SMH57 can be reduced, up to 45 %. However this setting produces a marginal increase in losses globally in the machine, especially at other tight apertures such as the injection septa. Consequentially, there is no improvement in extraction efficiency to the East Area. This is especially apparent on the XSEC61 and BTV61D monitors, as the F61 line was not optimised to steer this change in beam shape.

Figure 6.16.: Measurement profiles of BTV61D from ODN strength

(Left) Beam distribution in X-Y at BTV61D monitor. (Right) Noise-smoothed BTV61D X-distribution as a function of octupole strength.



PS Discussion

The work performed on the PS was a consistent backbone of the workflow of the PhD. The transfer of tools and knowledge from studying the comprehensive PS slow extraction models were useful for all other chapters of the thesis, and gave opportunities to be integrated into the CERN complex and accelerator community.

The initial trapping study demonstrates good agreement between simulations and measurement, but was not explored to high statistics. The extraction efficiency studies of 2022 provided very clear sextupole-octupole loss relations, as published in IPAC23 [116]. The consistency of these results was put into question when the East extraction cycle was reconfigured, primarily as the extraction bumps were altered. The same measurement provided a significant offset in terms of loss reduction (see Appendix [Fig. C.7](#)). For future reliability, the extraction efficiency studies of 2023 also analysed the sextupole-octupole losses as a function of the bump strength. A side study explored the octupolar component of the PFW strengths, and noted a change in non-linear chromaticity compared to previous years. The results of this study are listed in the Appendix, [Sec. C.3](#), however adjusting this had a net negative effect on losses.

Towards the end of the year, a steering optimisation algorithm was applied under various weightings, parameters and variable ranges. The algorithm was able to find minima in losses at the septa, but could not provide an increase in higher measured XSEC intensity compared to the nominal settings. A significant challenge in simulation predictions and simulation-

measurement comparisons is the inherent octupole component in the machine from MUs and PFWs. As the PFW currents are changed between years, between different cycles and during the East cycle, it is complicated to model the octupole component from the current. The process to do so is described in the appendix - where it is shown that in 2023, the non-linear chromaticity is increasing linearly throughout extraction, suggesting a continuous change of octupole strength. A true measure and control of this effect is essential for further investigation and optimisation of extraction with octupoles.

This chapter has aided the understanding of the extracted beam distribution and behaviour under sextupole and octupole strengths, and further investigations require optimisation and adaptation of the machine to account for this change in distribution.

Bibliography

- [40] M. A. Fraser, B. Goddard et al. "Demonstration of slow extraction loss reduction with the application of octupoles at the CERN Super Proton Synchrotron". In: *Phys. Rev. Accel. Beams* 22 (12 Dec. 2019), p. 123501. DOI: 10.1103/PhysRevAccelBeams.22.123501.
- [45] J-P. Burnet, C. Carli et al. *Fifty years of the CERN Proton Synchrotron: Volume 1*. CERN Yellow Reports: Monographs. Geneva: CERN, 2011. DOI: 10.5170/CERN-2011-004.
- [110] *acc-py*. <https://abpcomputing.web.cern.ch/guides/accpy/>.
- [111] P. A. Arrutia Sota and R. Taylor. *Octutrap*. <https://gitlab.cern.ch/parrutia/octutrap>. Scripts for Octupoles trapping studies for the PS. 2021.
- [112] *TIMBER: Accelerator Controls Wikis (BE/CSS)*. <https://wikis.cern.ch/display/TIMB/TIMBER+Home>. 2019.
- [113] A. Huschauer and R. De Maria. *Project Title*. <https://gitlab.cern.ch/acc-models/acc-models-ps/-/tree/2023/scenarios/east>. Official optics repository of the CERN Proton Synchrotron (official name PR). 2023.
- [114] G. Franchetti et al. "Space charge and octupole driven resonance trapping observed at the CERN proton synchrotron". In: *Phys. Rev. Spec. Top. Accel. Beams* 6.12 (2003), p. 124201. DOI: 10.1103/PhysRevSTAB.6.124201.
- [115] F. Asvesta. "Space charge and lattice driven resonances at the CERN injectors". Presented 16 Sep 2020. National Technical University of Athens, 2020. URL: <https://cds.cern.ch/record/2771289>.
- [116] R. Taylor et al. "Slow extraction with octupoles at CERN proton synchrotron to improve extraction efficiency". In: *Proc. IPAC'23 (Venice, Italy)*. International Particle Accelerator Conference 14. JACoW Publishing, Geneva, Switzerland, Sept. 2023, pp. 1144–1147. ISBN: 978-3-95-450231-8.

*I must confess that...
This extraction is taking
a great act of will.*

Tim Minchin
(I'll Take Lonely Tonight)



Extraction from NIMMS Synchrotrons

This chapter is the main heart of the thesis, where everything formerly mentioned is packaged together in the context of NIMMS synchrotrons [117, 118]. The baseline extraction designs for the machines are provided, and this process introduces several novel elements. The first is applying extraction methods to fit in very compact rings. The second is extracting higher intensity and higher emittance beams. The third and most significant is realising the temporal limits of extraction to produce beams at Ultra-High Dose Rates (UHDR).

Sec. 7.1 starts with a normal-conducting carbon synchrotron based on the PIMMS lattice [84], which is the most likely design choice for the SEEIIST initiative. The goal is to adapt this so that it matches the requirements needed for a NIMMS (Next Ion Medical Machine Study) design. To achieve this goal, the extraction method is first replaced with an RF-KO transverse exciter, then extraction is adapted to fit higher emittance beams, and finally reduce timescales to show a working example at FLASH-compatible rates.

Sec. 7.2 is the first study performed with the design for Helium Light Ion Compact Synchrotron (HeLICS). Two extraction schematics are considered, first at working point for 2.6 and then an alternative at 2.3. A RF-KO PID controller is developed to aid the extraction process. This method, and quadrupole-driven extraction are compared at UHDR timescales, for both continuous and burst spills.

7.1 From PIMMS to NIMMS: Upgrades for UHDRs

THE WORK IN THIS SECTION REFERS TO PUBLICATION 2023 J. PHYS.: CONF. SER. 2420 012101 [119]. From the specifications outlined in [Ch. 1](#), for a dose of 2 Gy to be delivered to a 1-litre tumour for ten stages of MEE, the synchrotron must store $1\text{--}2 \times 10^{10}$ carbon ions [84]. This intensity is $20\times$ higher than what current European hadron therapy synchrotrons can deliver. With an ion source of $600\text{ }\mu\text{A}$, a multi-turn injection method of 30 turns needs to be performed to achieve this higher intensity, assuming 50% injection efficiency. This method via MTI would consequently generate a horizontal, normalised rms emittance increase of $\varepsilon_{x_{\text{rms}}} < 6\pi \cdot \text{mm} \cdot \text{mrad}$ [119]. Slow-extraction studies must be performed to assess the feasibility of extracting a beam with these larger emittances and faster timescales.

The focus of this section is not the lattice used, but the techniques required, and should be applied to any NIMMS synchrotron option.

7.1.1 Betatron Core Extraction

Returning to the PIMMS betatron extraction in [Sec. 4.2.3](#), it is time to take our default extraction set-up and adapt it for NIMMS requirements. The work in this section was performed with Maptrack simulations of the PIMMS lattice much like [Ch. 4](#). The only major difference is that this simulation will displace the modified tune distance ϵ away from the resonance and have the momentum distribution of the beam centred at zero, rather than have the tune at exactly $Q_x = 1.6$ and use a non-zero momentum spread offset. This has little effect other than a horizontal offset of the beam due to dispersion.

Since adjustments were made to maptrack to enable parallelization and enhanced memory handling [99], the procedure can be repeated for more powerful simulations, featuring a realistic spill time of slow extraction.

The revolution frequency for 400 MeV/u C^{6+} ions for the 87 m circumference synchrotron is 2.8 MHz. This means that 1 s of beam spill is equivalent to 2.8×10^6 turns. A beam of 5,000 particles was generated at a Gaussian distribution for an emittance of $\varepsilon_{x_{\text{rms}}} = 1\pi \cdot \text{mm} \cdot \text{mrad}$. This beam used an initial uniform momentum spread of $\frac{\Delta p}{p} = 0.3\%$. With the horizontal tune at $Q_x = 1.645$, and the Hardt Condition chromaticity of -4.041 , the necessary momentum increase induced by the betatron core was -3.2×10^{-9} per turn.

Figure 7.1.: Betatron core spill histogram and beam intensity as a function of turn number for two initial beam emittances.

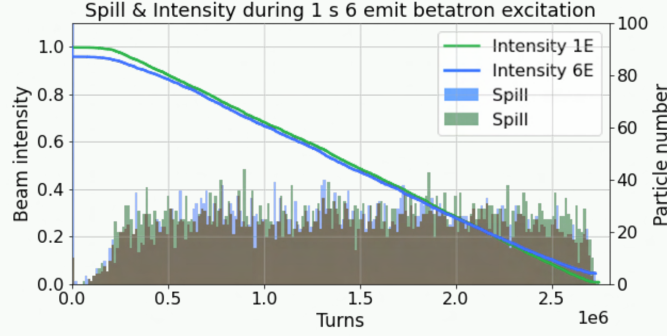


Fig. 7.1 compares this scenario for initial distributions of $\epsilon_{x_{rms}} = 1 \pi \cdot \text{mm} \cdot \text{mrad}$ normalised emittance and $\epsilon_{x_{rms}} = 6 \pi \cdot \text{mm} \cdot \text{mrad}$. The solid line shows the decreasing normalised intensity in the machine as a function of time. The number of extracted particles is represented as a histogram binned every 5 ms (14 000 turns). Given the low number of tracked particles, there is a low statistics with a mean of 30 particles per bin. There are strong tails at the start and end of the spill, which is expected for betatron core extraction, due to its initial tune-amplitude relation, and these tails are cut before delivery to the patient. Both emittances show near identical extraction rate and histogram distributions. The only significant difference is that at $6 \pi \cdot \text{mm} \cdot \text{mrad}$, a small fraction of the beam is lost at the simulation start. This slight loss can be easily fixed via the modified tune distance ϵ .

7.1.2 Radiofrequency Knock-out Extraction

The concept of RF-KO excitation is introduced in [Ch. 2](#) and its current usage at other facilities is discussed in [Ch. 3](#). RF-KO excitation is the default slow extraction option for NIMMS due to its flexibility and its compatibility with MEE.

Simulation examples of how RF-KO functions in the PIMMS machine, have been previously performed. Adaptations of RF-KO excitation for the PIMMS lattice exists via upgrades for MedAustron [60] and CNAO [61]. Instead, the goal for this section is to see how the conditions of the machine and its hardware must change due to increased emittance or extraction of UHDR.

To avoid reinventing the wheel, the same design and location for the CNAO RF-KO exciter

is chosen [61]. At CNAO the exciter is located in-between the injection septum and the first chromatic sextupole. It has a maximum voltage of 367 V, corresponding to a kick limit of 2.8 μrad for 250 MeV protons and a 1.0 μrad limit for 400 MeV/u carbon ions [61]. Eq. 7.1 [53] is used in simulations to convert the exciter voltage (V_p) into a kick (θ_k) to the particle's p_x (μrad). The kick strength of the beam depends on the properties of the beam [charge-mass ratio Z/A and relativistic particle velocity $\beta = v/c$] and properties of the exciter [length L and plate distance a]. In simulations this kick is provided to all particles equally each turn. Realistically, with a unbunched beam, the longitudinal component of the particles is significant, and the kick should be allocated as a function of time, rather than turn number. This has a non-negligible effect on the statistics, due to lagging particles.

$$\theta_k = \frac{Z}{A} \frac{e}{m_p} \frac{V_p}{a} \frac{L}{\beta^2 c^2} \quad (7.1)$$

$$\delta x' = \theta_k \cos(2\pi(q_x + \delta q_x)T) \quad (7.2)$$

The RF-KO signal from the exciter is made of two components: amplitude modulation (AM) and frequency modulation (FM). The ideal scenario is to provide a signal which is exactly the frequency of the particle, at exactly the amplitude required to remove it from its stable orbit. As it is famously impossible to know the exact momentum and position of any single particle, stochastic processes are applied across the whole beam to increase the statistical likelihood of extraction at the desired rate. A Gaussian range of frequencies at a bandwidth δq_x around fractional beam tune q_x is considered, to factor in the tune spread of particles.

An AM curve changes θ_x throughout extraction, which exponentially increases with time. The exponent e follows the increased density of particles towards the beam core, the function of which was developed for use at HIT [53], shown in Eq. 7.3. It has nine variable inputs: One for the maximum voltage of the RF-KO exciter, V_{RF} , four to control the time periods of each behaviour: T_{start} , T_{pre} , T_{main} , T_{end} , and four to control the amplitudes of each time period: A_{start} , A_{pre} , A_{main} , A_{end} , in units of volts. Without a feedback system, the only way to simulate a smooth and complete extraction would be to optimise the extraction rate ourselves. A visualisation of the kick limit defined by this function for a given set of parameters is in Fig. 7.2 (left) for 1 s of extraction. The right plot represents the same curvature, including the kick given each turn in-between the limits.

Eq. 7.3 - 7.6: Bathtub function for smooth spill - C. Schoemers [53]

$$V_{\text{main}} = (A_{\text{pre}} - A_{\text{main}} \frac{1}{e}) \exp(-t/2T_{\text{pre}}) + A_{\text{main}} \exp(t/T_{\text{main}} - 1) \quad (7.3)$$

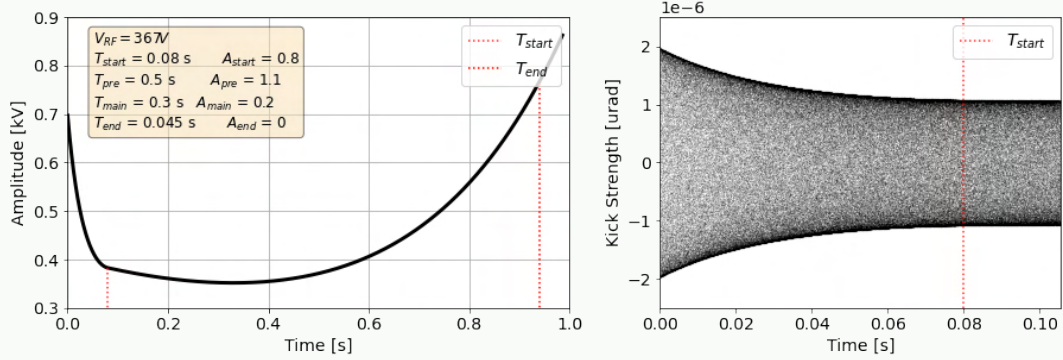
$$V_{\text{start}} = A_{\text{start}} \left(\exp((1-t/T_{\text{start}})^2 - 1) \right) \frac{1}{e-1}, \quad t \in [0, T_{\text{start}}] \quad (7.4)$$

$$V_{\text{end}} = A_{\text{end}} \left(\exp((1-t/T_{\text{end}})^2 - 1) \right) \frac{1}{e-1}, \quad t \in [T_{\text{end}}, T_{\text{max}}] \quad (7.5)$$

$$V_{\text{kick}} = V_{\text{RF}} \times (V_{\text{main}} + V_{\text{start}} + V_{\text{end}}) \quad (7.6)$$

Figure 7.2.: Plot of Eq. 7.6 for given variables, and kick given in tracking simulations

(Left) Voltage amplitude θ_k as a function of time over 1 s. (Right) Close-up of the kick $\delta x'$ signal for the first 10 ms



Implementation

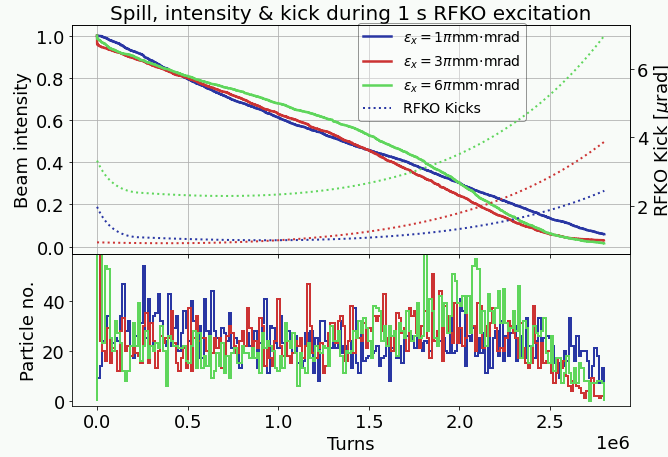
A few adjustments to the machine optics were necessary for the transition from betatron core to RF-KO extraction. Firstly, the strength of the sextupole was increased from $k_2L = 8.65$ to $k_2L = 12.5$. Secondly, the tune spread was reduced by both reducing the momentum spread to 0.1% and matching the chromaticity to -0.004 . Finally the beam tune was moved much closer to the resonance, from 1.645 to 1.675 such that the amplitude of the beam was just below the resonance.

Results

The emittance of the beam was increased to $\varepsilon_{x_{rms}} = 3\pi \cdot \text{mm} \cdot \text{mrad}$ and $\varepsilon_{y_{rms}} = 6\pi \cdot \text{mm} \cdot \text{mrad}$, and the corresponding RF-KO signals were compared. For each scenario, the optimal AM signal of Eq. 7.3 for a smooth macro-spill, was calculated manually. First the *start* and *main* variables were optimised at small turn numbers. For larger simulations across all turn

numbers, variables were ran in parallel to optimise the *end* variables.

Figure 7.3.: RF-KO spill histogram and beam intensity as a function of turn number for three initial beam emittances.



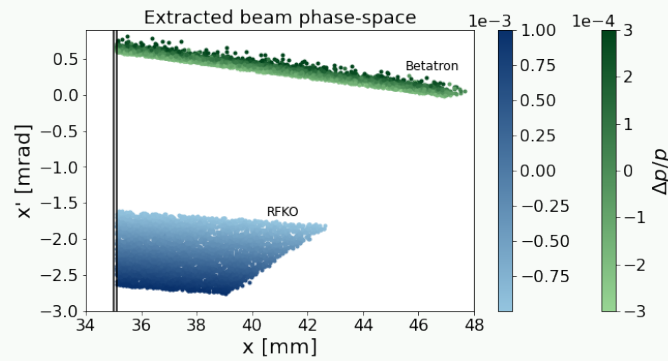
The results are compared in [Fig. 7.3](#). The default extraction for a $\varepsilon_{x_{rms}} = 1\pi \cdot \text{mm} \cdot \text{mrad}$ Gaussian beam of 5,000 particles is shown in dark blue. The intensity in the ring decreases linearly (solid line), and the AM limit of the RF-KO kick (dashed line) follows the [Eq. 7.3](#) exponent. The below plot shows the histogram of extracted particles with binning every 14 000 turns, equivalent to 5 ms. This gives an average number of particles per bin of 25 ± 5 as the statistical Poisson limit (see [Sec. 2.3.4](#)). The present variance is higher than this, suggesting that we are not yet limited by statistics. The distribution does not show the characteristic tails of betatron core, as the extraction starts immediately when the strong transverse excitation is applied.

When increasing the emittance to $\varepsilon_{x_{rms}} = 3\pi \cdot \text{mm} \cdot \text{mrad}$ (red), the higher amplitude particles are closer to the resonance. This means that little initial kick is required to bring the outermost particles to the resonance. Despite this, the particles have a wider amplitude spread, so a larger kick is required towards the end of extraction, particularly when the number of particles in the beam is lower, giving lower extraction statistics.

Finally, for the emittance of $\varepsilon_{x_{rms}} = 6\pi \cdot \text{mm} \cdot \text{mrad}$ (green), the beam amplitude overlaps with the resonance, and so immediately the particles are lost at the start of extraction. To avoid this, the tune of the initial beam is moved further to $Q_x = 1.68$, to ensure a stable beam at the start of the simulation. Given the further amplitude distance from the centre of the beam to the resonance, the minimum required kick is higher overall. The kick required towards the end of

the simulation increases as far as $\delta x' = 7 \mu\text{rad}$. The histogram of all three extraction rates is not perfectly uniform, and decreases towards the end of the simulation, as particle statistics drops. This would be aided by having a feedback loop or function optimiser (see [Sec. 7.2.3](#)).

Figure 7.4.: Betatron core (green) and (blue) RF-KO extracted beam distributions in phase-space at the electrostatic septum

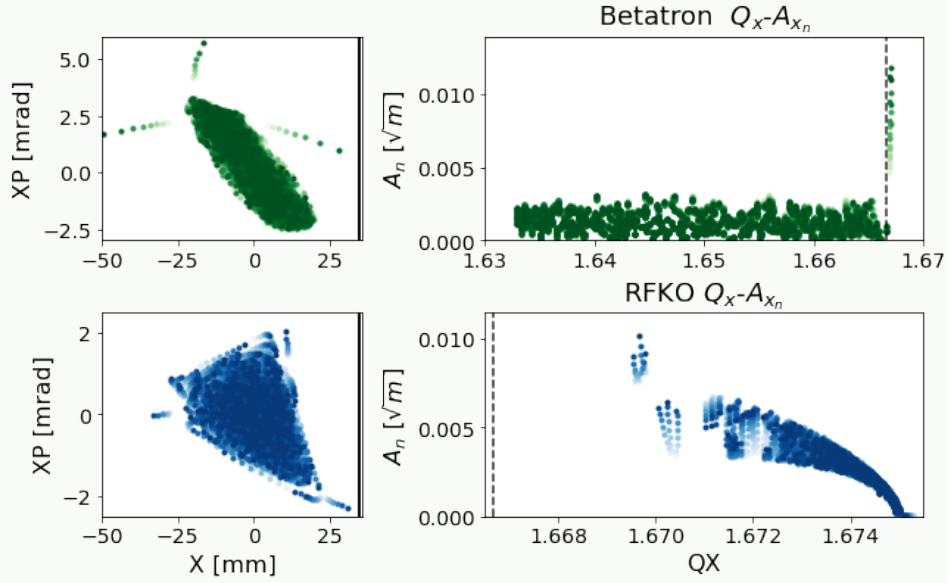


To compare the processes of RF-KO and betatron core in the same system, [Fig. 7.4](#) compares the $x - x'$ bar-of-charge of extracted particles at the position of the ES. As the RF-KO (blue) chromaticity does not satisfy the Hardt Condition, there is a wide spread in horizontal angle x' which is dependent on the initial momentum spread. The betatron core simulation (green) features a higher shift in x' position and has a wider spiral step, despite the lower sextupole strength. Both effects are because dispersion moves the centre of the stable beam further from the septum. This response is also represented in [Fig. 7.5](#), which represents phase-space (left) and tune-amplitude (right) diagrams for both betatron core (green, top) and RF-KO (blue, bottom).

The plots track the entire beam for ≈ 25 turns to follow the extraction of a single particle. The resonance relative to the beam tune is represented as a dashed line at the 1.6 resonance, although in reality it is represented as a triangular region with a stopband width. The long spread of the stable triangle (green) from dispersion is due to the $4\times$ larger momentum spread of the beam in betatron core extraction. Likewise one can see the large tune stack of the beam that behaves linearly, compared to the small tune stack in blue that features strong amplitude detuning in the direction towards the resonance.

Figure 7.5.: Phase-space (left) and tune-amplitude (right) distributions for the beam, showing the extraction of a single particle across 25-turns.

(Top, green) Betatron core, (bottom, blue) RF-KO. Turn number represented by the colourmap.

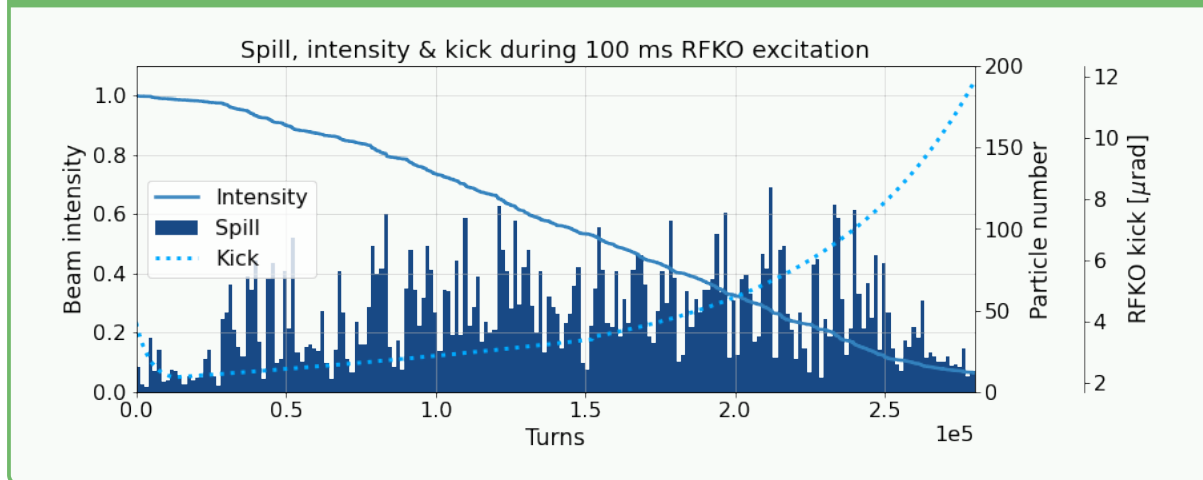


FLASH-compatible Timescales

To adapt the RF-KO slow extraction simulation for UHDR, the number of simulated turns was reduced to 280 000, equivalent to 100 ms, and the particle number was doubled to 10 000, due to increased simulation performance. This provides effectively a $20\times$ higher dose rate than the previous simulation. As before, the 9-parameter AM curve was optimised by hand to find a series of settings that provided a linear intensity decrease and uniform spill. The initial generated beam was the same as that for an emittance of $\varepsilon_{x_{rms}} = 1\pi \cdot \text{mm} \cdot \text{mrad}$. The tune and chromaticity settings of the machine remained unchanged. Fig. 7.6 shows the intensity (solid line), voltage kick (dashed line) and histogram for this scenario.

The results show a much higher variance in the extracted intensity per histogram bins of 1400 turns, equivalent to 0.5 ms. With 10 000 particles extracted, the expected number of particles per bin is 50 ± 7 . The variance shown in the histogram is much higher than this, suggesting we are presently limited by extraction method, not by statistics. This result reveals a challenge of RF-KO at UHDR: When the same number of particles needs to be extracted in a shorter timescale, it suggests that a larger exponential increase in the AM is required. Fig. 7.6 expresses this by showing that the AM limit goes as high as $12 \mu\text{rad}$. When converting this with Eq. 7.1,

Figure 7.6.: RF-KO FLASH spill histogram and beam intensity as a function of turn number, equivalent to 100 ms.



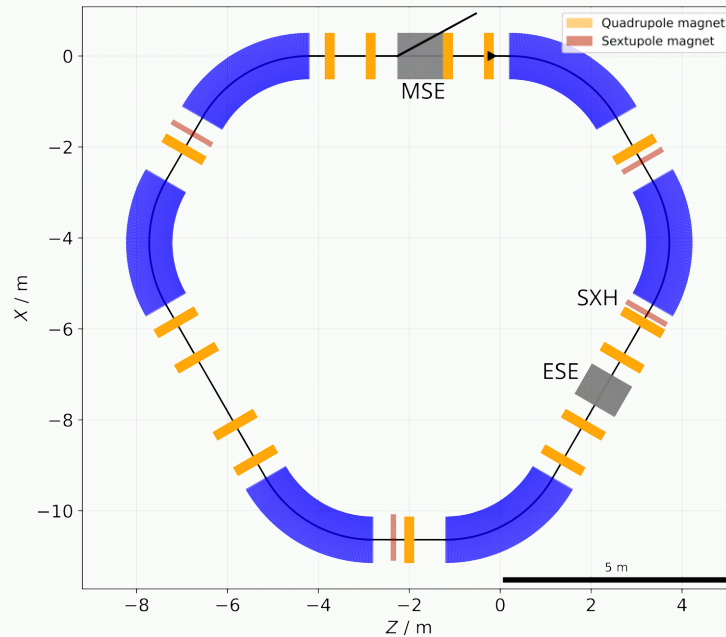
this value corresponds to a voltage of 4 kV. This is difficult to obtain with the available parallel plate hardware for a gap distance of 15 cm.

7.1.3 PIMMS to NIMMS Discussion

The results in this section emerged from the 2022 IPAC publication *Slow Extraction Modelling for NIMMS Hadron Therapy Synchrotrons*, published by IOP conference proceedings. The results remain valid for all NIMMS designs, and are not specifically tied to the PIMMS lattice that was used for the study.

This study estimates that higher emittance beams do not affect the extraction procedure for betatron core extraction but do for RF-KO extraction. As RF-KO is amplitude-driven, changes in emittance have a strong impact on both the lattice schematic and the strength of the kick delivered to the beam. When applying faster extraction rates for UHDR, it is found that the same system requires a higher exponential kick, suggesting a voltage strength as high as 4 kV. The PIMMS lattice benefits from a large amount of slow extraction R&D from both MedAustron and CNAO. For this reason, it makes sense to confirm that further investigations are possible with alternative synchrotron designs that NIMMS is actively designing.

Figure 7.7.: Schematic of the HeLICS lattice with dipoles (blue), quadrupoles (yellow), sextupoles (red) and labels of the resonant sextupole (SXH) and septa (ESE, MSE).



7.2 HeLICS: Helium Light-Ion Compact Synchrotron

The flagship project of NIMMS synchrotrons is HeLICS - the Helium Light Ion Compact Synchrotron. HeLICS was born from the drive to produce hadron therapy synchrotrons with smaller footprints. This ambition is constrained by the available fields in dipole magnets, which are required to bend a beam of a given energy per nucleon. Therefore, the options are either to increase the fields in the synchrotron - unlocking the NIMMS superconducting carbon synchrotron - or to use a particle of a lower nucleon number - directing us towards a normal-conducting helium machine. Coupled with the recent growing interest in helium ion therapy - discussed in [Sec. 1.2.1](#) - the initiation of this design comes at a fruitful research period.

This compact normal-conducting helium machine has no severe show-stoppers. All of the technology is available to be built now, with one exception: That is, of course, the FLASH extraction methods.

7.2.1 Baseline Design and Optics

The baseline design for HeLICS was first published in 2022 [6]. The whole proposed facility foresees a 2200 m² surface area schematic. This facility houses the injection line, synchrotron, two treatment rooms and an experimental room. The injection line also benefits a radioisotope production facility - the challenge of which comes from the targetry, isotope capture and radiation safety - so requires its own separate consideration.

The first optics for HeLICS was computed by E. BENEDETTO after February 2023 - published

Table 7.1.: HeLICS facility parameters

Circum.	35 m	Q _x	2.3
Inj. Current	2 mA	Q _y	1.075
Intensity	8.2×10^{10}	Nat. Q' _x	-2.803
Max. B-Field	1.65 T	Nat. Q' _y	-3.379
Beam Rigidity	4.5 T m	$\varepsilon_{n,x}$	3 π mm mrad
Inj. Energy	5 MeV/u	$\varepsilon_{n,y}$	1 π mm mrad
Max. Energy	220 MeV/u	$\frac{\Delta p}{p}$	0.5 %
Rev. Freq.	4.84 MHz	β_{rel}	0.54

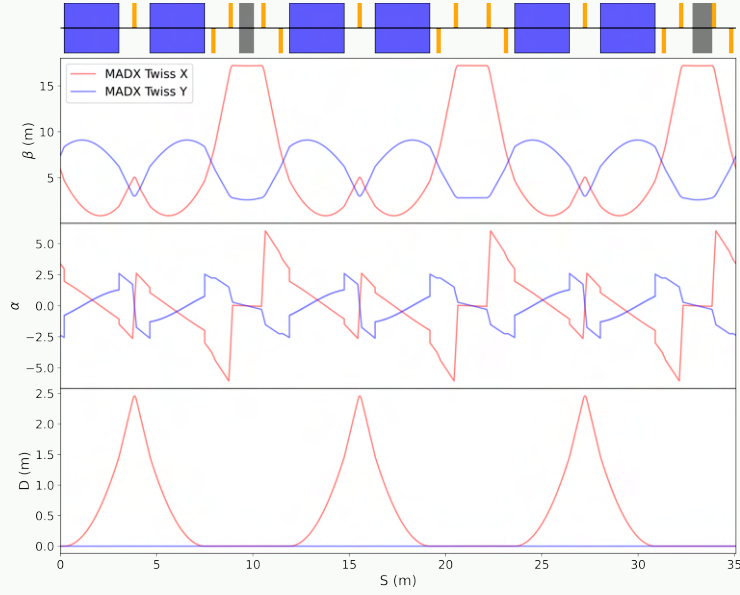
via the optics repository [120]. From there, the design was iterated and adapted by H. HUTTUNEN and F. ASVETA [121]. An xsuite-generated diagram [122] is displayed in **Fig. 7.7**. It is clear to see the three bending sections, made of two dipoles each, and the three main straight-sections between them.

Fig. 7.8 represents the beta, alpha and dispersion throughout the accelerator, starting at the entrance of a dipole. The beta horizontally peaks at the centre of each of the three straight sections, in-between the focusing quads. The alpha has a large variation, but tends towards zero within the straight sections. The dispersion peaks in the centre of each of the three dipole-bends, but is matched to be zero within the straight sections. The benefit of this zero-dispersion shall be discussed in **Sec. 7.2.2**.

Of the small 35 m circumference, almost exactly half of this is taken up by the 2.84 m long combined function dipoles. This means one must be efficient with the usage of space in the remainder of the straight-sections. The injection and extraction in particular requires long components.

The primary parameters of the synchrotron are in **Tab. 7.1**, which are the parameters assumed for this section.

Figure 7.8.: Twiss parameters across the HeLICS lattice, showing beta, alpha and dispersion in X and Y planes. Calculated with MADX.



7.2.2 Extraction Configuration

Sec. 2.3.2 provides an overview of the design choices necessary between slow extraction components. This section will elaborate on these choices made within the context of HeLICS. These choices consider the horizontal tune, the sextupole location and strength location, and the location and X-offsets of ES and MS.

Starting with the **horizontal tune**: the major choices are either the $2.\dot{3}$ resonance or the $2.\dot{6}$ resonance. The initial optics found an extraction solution using $Q_x = 2.\dot{6}$, however a further optics parameter study implied improved beta function when closer to $2.\dot{3}$. For this reason, this chapter will work assuming $Q_x = 2.\dot{3}$, but within Appendix C, an alternative configuration for the other working point is considered. When establishing the configuration, the tune is placed exactly on resonance. Later on, when simulations of complete excitation methods are performed, the distance from resonance will be adjusted according to the stable tune-spread for a given chromaticity and $\frac{\delta p}{p}$.

The **resonant sextupole**, (*sxh* - keyword for Sextupole for eXtraction, Horizontal) is positioned within the straight-section of zero dispersion. The lack of dispersion ensures that there is no correlation between position and momentum, and therefore the sextupole has little to no effect on the chromaticity of the machine.

Table 7.2.: NIMMS slow extraction parameters

SXH k_2	1.2 m^{-2}
S_{virt}	9.9
X_{MS}	85 mm
X_{ES}	-75 mm
Spiral step	12 mm

With the positioning of the *sxh* confirmed, the relative positions of the **electrostatic and magnetic septa** can be determined. The threefold superperiodicity and $Q_x 2.3$ means that every segment progresses the phase-advance by 280° . As introduced in **Ch. 2**, the ES should be orientated such that the separatrix is 45° from the horizontal and the MS should be $90^\circ + n \cdot 180^\circ$ with respect to the ES [15]. This is to ensure that the separatrix arm that receives a kick from the ES is the same one that enters the field-region of the MS. Despite this, HeLICS is compact and can only hold the septa and resonant sextupole in the longer straight-sections. With this in mind, some compromise is necessary to ensure that the separatrix orientation between elements is sufficient. The resonant sextupole is placed at $S = 7.77 \text{ m}$ and has a separatrix angle of $\alpha = 45^\circ$. As this is already the ideal orientation for the ES, there is a $0^\circ + n \cdot 120^\circ \pm 15^\circ$ safety margin on their relative phase advance. This is sufficient degree of freedom to position the ES in the same straight section, at 9.30 m, with a $\Delta\mu_x = -7.3^\circ$ compared to the sextupole, at a negative orientation. The MS is positioned in the next straight section at a positive orientation, with a $\Delta\mu_x = 200^\circ + 360^\circ$ phase compared to ES. This is not exactly at 90° ($+120^\circ + 360^\circ$), and instead is 10° off, therefore the extracted beam at the MS is not as rotated as would be ideal. In addition, the ES kick of -2.5 mrad is insufficient to reach the MS field region. However the orientation of the separatrices with respect to the MS is sufficient, and this set up is appropriate to perform the studies needed for this chapter. Additional adjustments of their relative positions are required once more accurate modelling and integration of the lattice is performed.

Once the lattice schematic is established, the spiral-step of the extraction should be optimised to achieve the desired bar-of-charge. As established in **Eq. 2.33**, the size of the extracted beam depends on the strength of the sextupole S_{virt} and the electrostatic septum limit X_{ES} . The parameters selected are expressed in **Tab. 7.2**. The aperture limits for both septa seem large, which is to maximize the kick for the extracted beam to reach the MS aperture limit. This relation is flexible, as long as the spiral step is constrained. Future constraints on beam pipe geometry can limit the parameter of X_{ES} , and SXH k_2 will need to be reduced accordingly.

Table 7.3.: Septa designs from J. BORBURGH

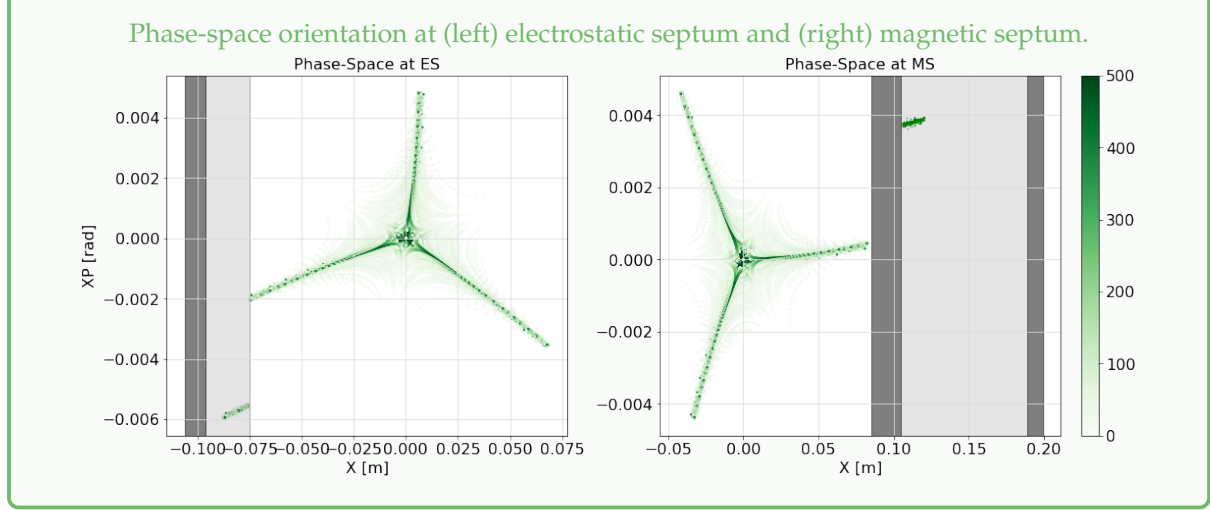
	ES	MS
Deflection angle [mrad]	2.5	100
Physical length [mm]	750	1000
Active length [mm]	550	910
Gap height [mm]	35	35
Gap width [mm]	21	84
Septum thickness [mm]	0.2	20

Simulations

The ideal scenario is simulated as a preliminary study to confirm the baseline extraction schematics. These simulations are performed in XSuite with low-emittance beams ($\epsilon_x=1 \pi\text{mm mrad}$) with no momentum-spread ($\frac{\Delta p}{p} = 0$), for a machine which is placed exactly on resonance ($Q_x = 2.3$) and with natural chromaticity. **Fig. 7.9** shows the results of this simple tracking, where the green colourmap is plotted as a function of turn number. When exactly on resonance, most of the beam is extracted by 500 turns. One can see the bar-of-charge within the ES field region, and the kicked beam which appears within the MS field region. Septa behaviour is created from a custom-written XSuite element class. Four variables are parsed to the element: anode position, anode width, cathode position and p_x kick. When the particle overlaps with the anode or cathode aperture, a -2 loss-flag is provided. When the particle overlaps with the septum field region, either the p_x kick is applied to the particle, or a -20 extraction loss flag is provided. An example of the element is in *xtraction_helpers.py* in the git repository.

To observe how the three separatrix arms behave longitudinally throughout the synchrotron, **Fig. 7.10** represents the beam in the final three turns before each individual particle is extracted. Near the third-order resonance, particles at maximum amplitude within the separatrix are in one of three positions: either between the green line (final turn), blue line (final turn - 1) or red line (final turn - 2). At 9.30 m, the ES gives a -3.5 mrad kick to the green beam which causes the track to diverge towards the MS at 32.84 m. The beam is tracked throughout both the ES and MS assuming a uniform kick increase every millimeter, as in **Fig. 7.11**. If necessary, it is possible to rotate both septa to maximize acceptance of the beam throughout their field.

Figure 7.9.: Separatrix and extracted beam distribution the two septa for a -3.5 mrad kick



With chromaticity

Within slow extraction, there are advantages in controlling the machine chromaticity. This free parameter allows the user to decide whether to prioritise low-chromaticity for reduced tune-spread, or optimised chromaticity to maximize Hardt Condition. Given that the three straight sections of HeLICS features zero-dispersion regions, the only remaining region to include chromatic sextupoles is between the combined-function dipoles. Three sextupoles are applied symmetrically, to counter out strong driving terms. In MADX and XSuite they are modelled as thin lens multipoles after the QB quadrupole.

As there is no dispersion in the straight-sections containing the electrostatic septum and resonant sextupole, the ideal chromaticity to fulfil the Hardt Condition of Eq. 2.38 defaults to zero. Hardt Condition is typically required for betatron core extraction due to the large momentum spread of the beam, however it is impossible to perform betatron core extraction when the machine chromaticity is zero. This is because changes in the momentum of the beam will not correspond to any meaningful increase in tune. In simulations the machine chromaticity is matched to a small, negative value close to zero. Should dispersion be applied to the three straight sections, the required Hardt Condition chromaticity as a function of said dispersion will change as a function of Eq. 2.38. Otherwise the natural machine chromaticity is kept to $dQ_{x,\text{nat}} = -3.4$.

Figure 7.10.: Separatrix trajectory of the X-position throughout HeLICS. Final two turns (red, blue) of the particles before their kick at the ES (green).

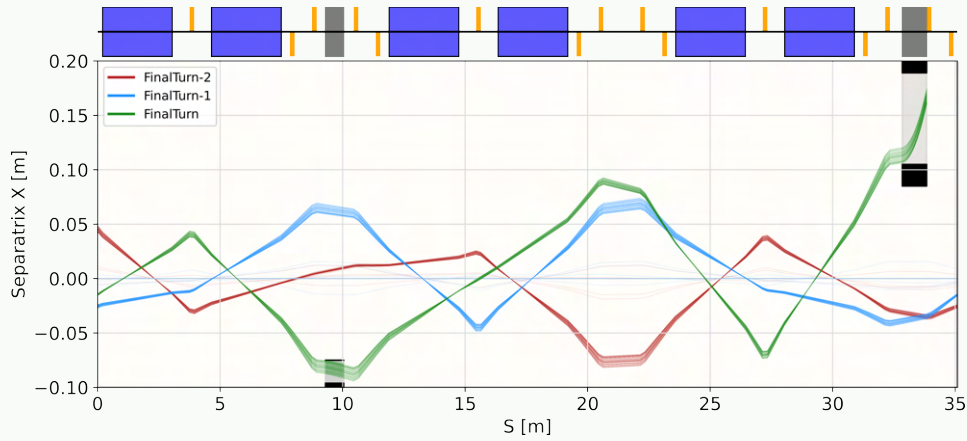
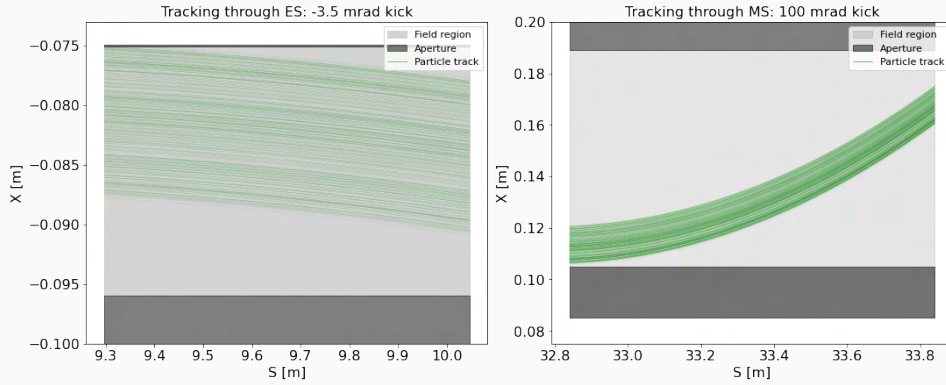


Figure 7.11.: Extracted particle trajectory throughout septa (zoom of Fig. 7.10)

X-S distribution through the (left) electrostatic septum and (right) magnetic septum.



7.2.3 Continuous UHDR for FLASH

Now that the ideal extraction schematic has been established, more realistic parameters can be re-introduced to the simulation. This will be for higher-emittance beams ($\varepsilon_x = 3 \pi \text{ mm mrad}$) with reasonable momentum-spread ($\frac{\Delta p}{p} = 0.1\%$), for a machine which is placed off resonance, such that the initial beam is stable ($Q_x = 2.295$). In such a scenario, an extraction method is necessary to transfer the particles from their stable orbit into a consistent slow extraction regime.

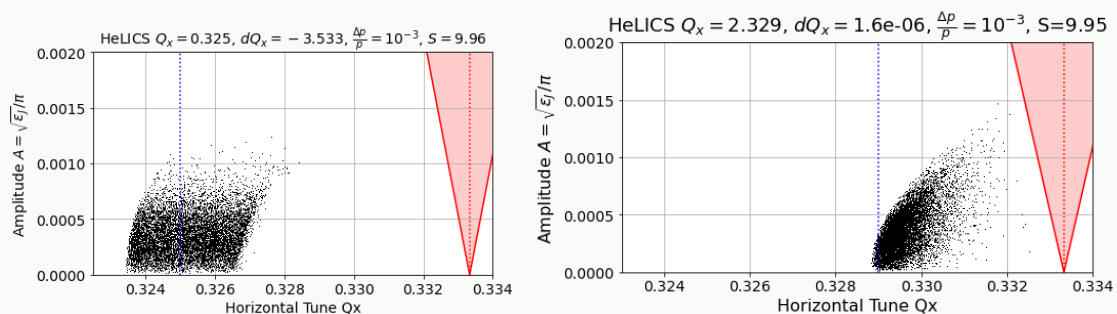
As emphasized in [Ch. 1](#), FLASH effects emerge from high intensity and fast timescale beams to deliver large dose rates. Such rates do not guarantee FLASH, but provide the domain with

which it has previously been observed. When designing the novel UHDR extraction methods of HeLICS, it is important to review the extraction methods used in conventional extraction and how the hardware must be adapted to suit the new high intensity rates. The methods can be split into two: tune-based and amplitude based.

- **Tune-based** extraction like betatron-core extraction and tune-ramping extraction are limited by the hardware that can provide the more rapid extraction rate. To reduce the time required to extract the entire distribution, the tune spread of such a beam should be as small as possible, and as close to the resonance stopband width as possible without extraction of the stable beam. An example is provided in **Fig. 7.12** (left) which shows a slight linear amplitude-tune correlation at the start and end of the stack, where the highest amplitude particles will be extracted first.
- **Amplitude-based** extraction like RF-KO is limited by the strength of the kick that can be provided by the hardware. As the amplitude modulation of the RF-KO extraction signal typically increases exponentially with time, reducing these timescales requires even higher exponents. The other limit relates to the time resolution provided by feedback systems required to regulate the intensity and spill of the extracted beam. Amplitude-based requires different initial optics, with a smaller tune spread and reduced tune distance. An example of the initial beam orientation is in **Fig. 7.12** (right), showing more dramatic amplitude-tune correlation such that very few particles are at the machine tune (dashed blue line).

Figure 7.12.: Tune-amplitude particle distributions representing tune spread as a function of chromaticity and tune proximity

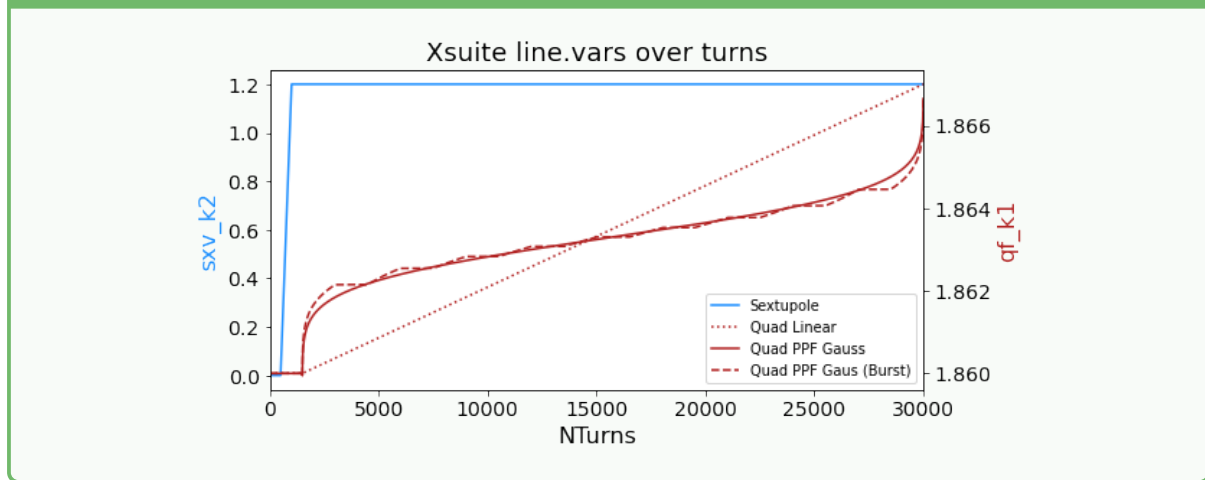
(Left) Larger chromaticity and tune far from resonance - in red, compared to (right) small chromaticity close to resonance.



Quadrupole-Driven extractions

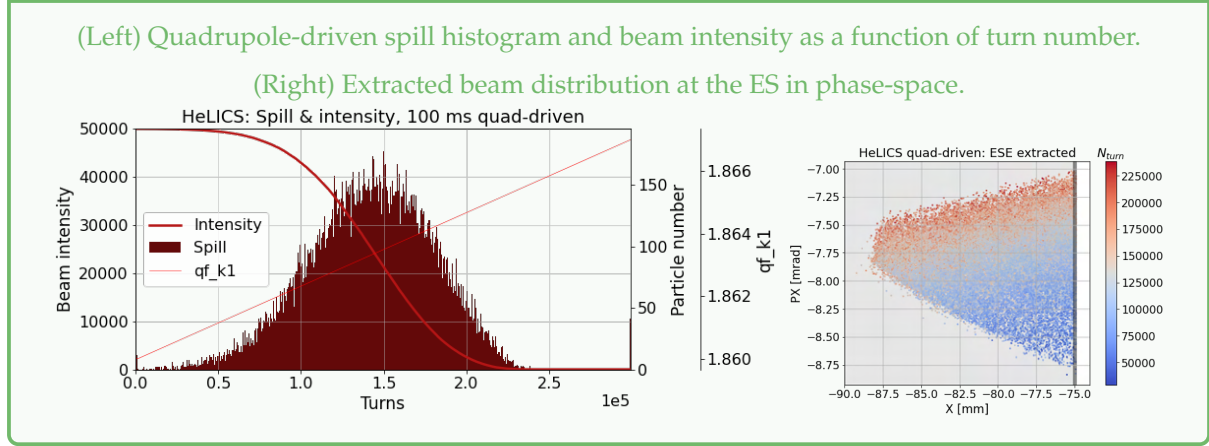
There are multiple options for tune-based extraction. **Betatron core** extraction would have been challenging as the Hardt Condition would not have been met, due to the zero dispersion at ES and SXH. **RF phase displacement** extraction is a form of tune-based extraction, however at this stage of the simulation, no reliable longitudinal model of the RF cavity existed, and as such, would not be realistic to the operational scenario. Therefore, **quadrupole-driven** extraction is applied for the purposes of demonstrating UHDR feasibility. To replicate exper-

Figure 7.13.: Strength variation of the resonant sextupole (blue) and quadrupoles (red) for a linear ramp (dots), an inverse Gaussian ramp (solid) and for a burst-like extraction distribution (dashed).



imental scenarios, the beam of 100 000 particles initialised for the injection Twiss parameters was tracked for a 500 turns to establish the phase-space. Then for 500 turns, the SXH sextupole ramps from 0 to its full strength, stable for a further 500 turns to establish the stable triangular distribution. Then the quadrupole ramping function was performed for 300 000 turns. Depending on the particle revolution frequency, this time period is equivalent to 60 ms of a 220 MeV/u helium ion, or 100 ms of a 45 MeV/u helium ion. This procedure for two different quadrupole ramping functions is displayed in **Fig. 7.13**. **Fig. 7.14** (left) represents the particles extracted per window of 300 turns, the drop in intensity in the machine (dark red), and the linear increase in quadrupole strength (light red - same as the dotted line in **Fig. 7.13**). **Fig. 7.14** (right) shows the x-px bar of charge distribution of extracted beam as a function of the time within which they were extracted. This is expressed rather than as a function of $\frac{\delta p}{p}$ momentum spread because there is no strong correlation in spread of $\frac{\delta p}{p}$, which is unexpected

Figure 7.14.: Spill response for linear quadrupole-driven ramp.



for a momentum-driven procedure.

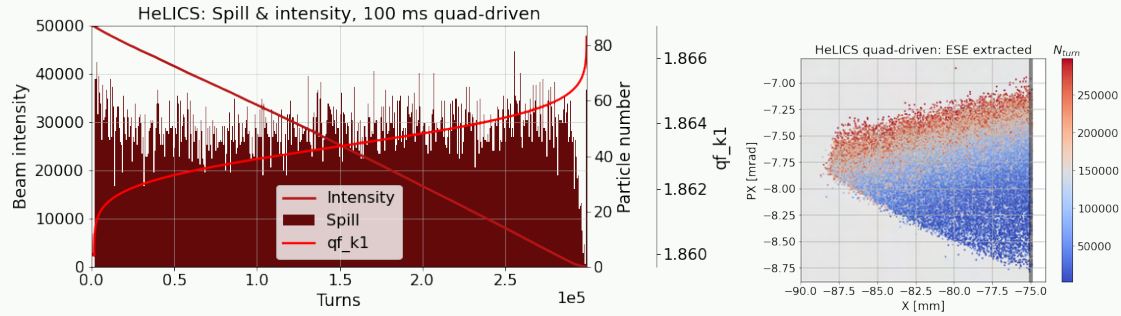
When looking at the histogram of beam spill, there is a very clear Gaussian distribution with time, which makes one wonder why the spill is non-uniform for a uniform momentum spread and a linear tune ramp. There are several established reasons which all contribute: Most significantly, the spread of the tune is small with respect to the slope of the resonance stopband width. This establishes that the extraction rate is linearly dependent to the amplitude-tune relation of the beam. The effect is exacerbated by any ADTS (amplitude-dependent tune shift) effects in the lattice, which tend to exponentially increase with proximity to the resonance (see [Sec. B.1.1](#)).

For a continuous 100 ms spill, it is important that a consistent intensity is provided across the scan, to ensure that a equally high dose rate is provided across the tumour plane. Given the highly-Gaussian distribution, the next logical step is to repeat the procedure but to provide the inverse of the non-linear intensity function of [Fig. 7.14](#) (left). The function matched closely with the probability point function (ppf) of a Gaussian, which was closely matched for a quad ramp central point of $k_1 = 1.8633 \text{ m}^{-1}$, and a sigma scale of $\sigma(k_1) = 0.0009 \text{ m}^{-1}$. The ppf function was provided after the ramping of the sextupole, as demonstrated by [Fig. 7.13](#) (solid red line).

The results are represented in [Fig. 7.15](#) and represent a much more linear decrease in intensity (red line) and a uniform spill histogram (dark red), with minimal fluctuations that would be appropriate for treatment. The size and distribution of the extracted bar-of-charge is identical, other than more particles at the start and end of the simulation time. When performing an FFT, no significant frequency spikes were detected in the response signal.

Figure 7.15.: Spill response for inverse-Gaussian quadrupole-driven ramp.

(Left) Quadrupole-driven spill histogram and beam intensity as a function of turn number.
(Right) Extracted beam distribution at the ES in phase-space.



The ramping function is equivalent to a shift in k_1 of 0.006 m^{-1} . Assuming maximum beam rigidity of 4.5 T m , this is equivalent to a $\Delta B_1 = 0.027 \text{ T m}$ throughout 100 ms . Even if the linear magnetic ramp rate of $0.27 \text{ T m}^{-1} \text{ s}^{-1}$ was feasible for quadrupoles, the Gaussian-ppf function starts and ends with rapid field changes, which are likely to reach hardware limits. Magnet ramp rates are usually defined by A s^{-1} , so a simple magnet design would have to be produced to model the expected current rate.

RF-KO Controller

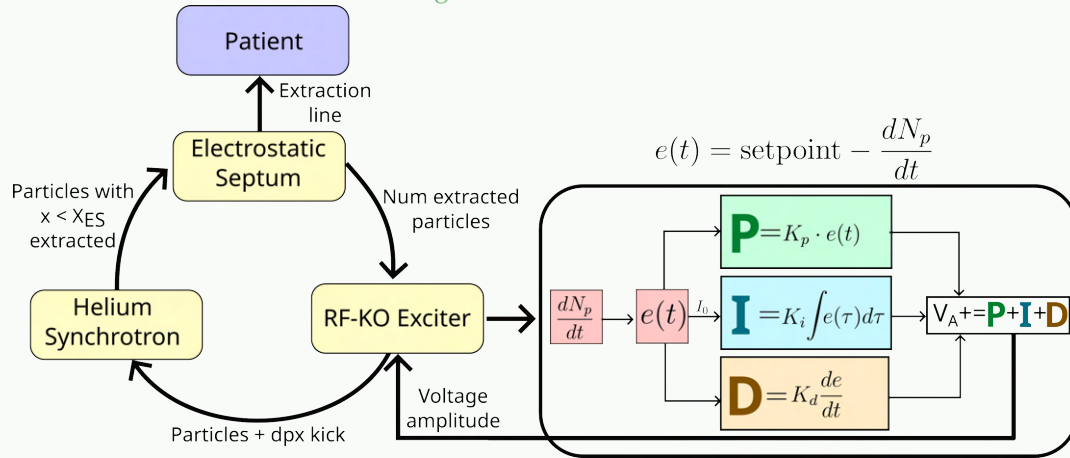
THE RESULTS OF THIS SECTION HAVE CONTRIBUTIONS FROM S. DETSI [123], SUPERVISED BY R. TAYLOR. The RF-KO simulations performed in [Sec. 7.1.2](#) concluded that shorter extraction timescales require higher transverse kicks. This conclusion was based on the amplitude-modulation signal from the function of [Eq. 7.3](#). This equation was a set, exponentially growing function, which may not necessarily be the most efficient AM kick to extract. In reality, facilities use feedback systems to control the transverse excitation provided to the beam. The introduction of a feedback controller would reduce the time needed to optimise the AM function via the technique of [Sec. 7.1.2](#).

For this reason, a PID-controller (Proportional Integral Derivative) controller was written and integrated as an element in XSuite [123]. A PID is an existing controller design widely used in control systems. For a given generated FM signal, the PID automatically adjusts the AM provided to the kick. The target of the PID is to change the voltage amplitude based on the number of extracted particles per window of turn. [Fig. 7.16](#) shows a schematic of the controller with relation to the HeLICS simulation setup. The **error** is calculated based on the difference

Figure 7.16.: Schematic of PID controller for RF-KO exciter

(Left) The relations between HeLICS components that are relevant for controlling spill quality.

(Right) A standard PID schematic relying on number of particles extracted that outputs the voltage of the RF-KO Exciter.



between the extracted particles per turn, and the defined setpoint rate. The P-controller varies the signal **Proportional** to the error via a manually set factor of K_p . The I-controller varies the signal considering all **Integrated** previous errors via a factor of K_i . The D-controller dampens rapid increases of error by calculating the **Derivative** changes of the error via a factor of K_d . Both the absolute values and the ratio between these three parameters depends on the needs of the system that the controller is correcting. PID controllers for RF-KO exist in simulations and in operation, and many dedicated studies are in place to apply the optimal voltage signal to enhance macro and micro spill structures [124].

For a detailed explanation of the PID controller set-up for HeLICS, please refer to [Sec. B.2](#) which also provides advice on hand-optimising the PID.

Between the limits of the voltage kick given by the controller, an FM signal is provided. This is defined by the user through any function that can be generated in python. The most common FM signals used by the slow extraction community are the following: Random white noise; a single-frequency sine wave at the machine tune; a broad-band signal of noise around a particular sine frequency; a periodic chirp of increasing frequency; random binary phase shift keyring (RBPSK) and Noise++ [125], defined in [Sec. 3.3.2](#).

When it comes to frequency-dominated systems like RF-KO, it is important to acknowledge that the FM component is crucial to improve extraction quality. Providing advanced FM sig-

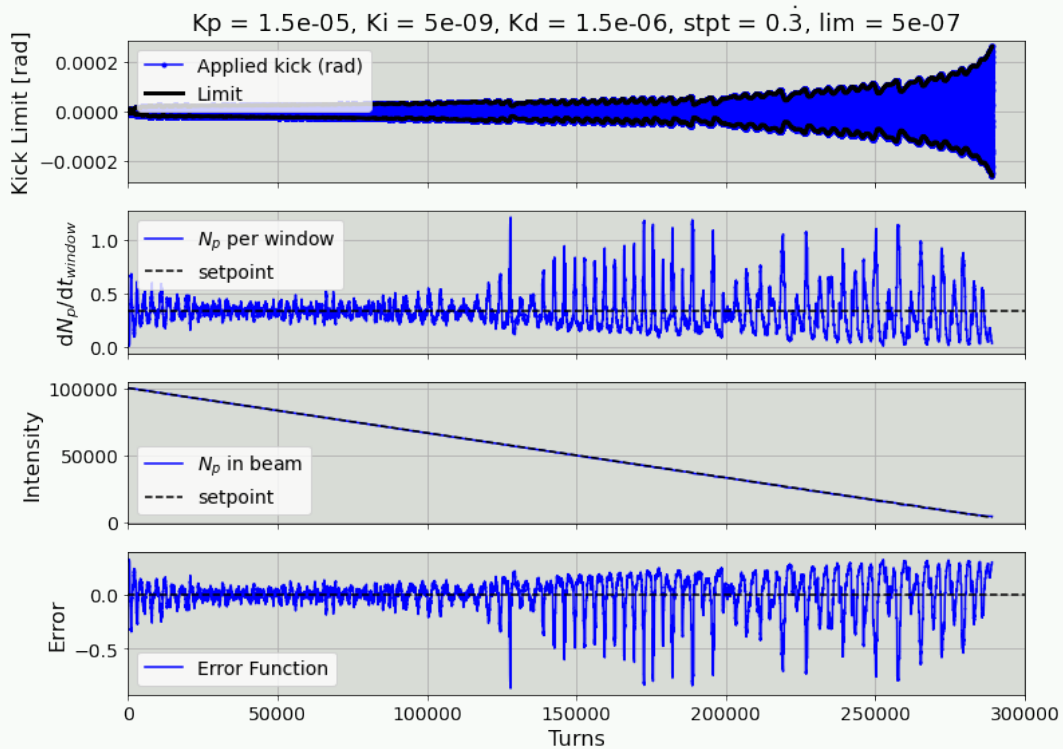
nals that closely match the true frequency distribution of the particles eases the ability to extract and therefore reduces the voltage necessary to kick the beam at a uniform rate. This was the conclusion of the investigations with HIT in [Ch. 5](#).

The RF-KO process was also simulated in XSuite for 100 000 particles over 300 000 turns. The controller was set up with the parameters as per [Tab. B.1](#), with the setpoint providing a rate of 0.3 particles per turn-interval.

The response of the PID controller for this simulation setup is expressed in [Fig. 7.17](#). From top to bottom, [Fig. 7.17](#) shows: the limit of the p_x kick (black) and the FM signal applied between these limits (blue); the average number of particles extracted per turn, oscillating around the setpoint of 0.3; the intensity count of particles in the machine decreasing linearly in accordance with the setpoint and the error between number of particles extracted and the setpoint.

Figure 7.17.: Output from RF-KO controller

As a function of turn number, (1) the kick provided to the beam in radian (2) the number of particles extracted per time window (3) the intensity reduction of the beam in the machine (4) the difference between the setpoint and the extracted particles.



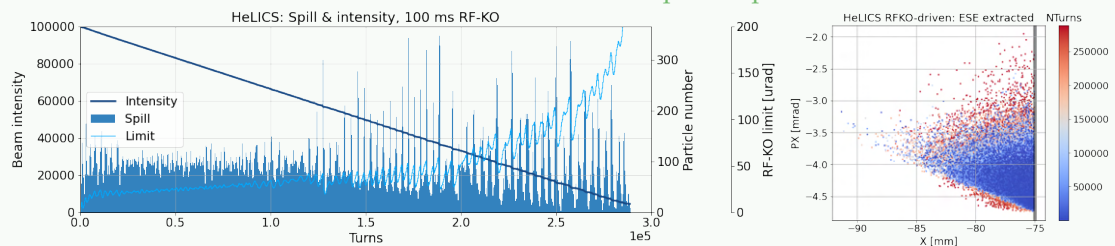
Given the long period of time to simulate, it is difficult to optimise to ensure good quality

of spill towards the end of the simulation. It is clear to see that the reduced intensity within the synchrotron clearly follows the setpoint, yet the number of particles extracted irregularly oscillates around the 0.3 extraction rate. The irregular oscillations around the setpoint suggests overshoots, which will emerge from a higher initial k_D parameter. The fact that increasing oscillations are growing typically implies an unstable system. Through correspondence, other researchers investigating RF-KO PID controller simulations also observed a decline in spill quality towards the end of in simulations, which is not observed operationally. It is assumed the cause of this is because as particle statistics is reducing in the tracked beam, statistically this will result in higher fluctuations. Should twice the number of particles be simulated, but with the same setpoint, it is reasonable to assume that these fluctuations would decrease, as suggested by Appendix Fig. B.7.

As a direct comparison to Fig. 7.15, Fig. 7.18 (right) shows the same spill response and response as a function of time, but for RF-KO. The extracted beam distribution has the same beam size, but a very different angular spread, with the beam being extracted at a different range of px , (-9 mrad to -7 mrad compared to -2 mm to -4.5 mm). In addition the particle distribution as a function of time is different, which will have effects on the beam distribution in the extraction line, and the delivery time of particular regions of the tumour.

Figure 7.18.: RF-KO extracted spill, intensity and RF-KO kick

(Left) RF-KO spill histogram and beam intensity as a function of turn number. (Right) Extracted beam distribution at the ES in phase-space.



7.2.4 Burst UHDR for FLASH

Compared to continuous UHDR for FLASH, burst extraction compresses the same dose into short discrete pulses. The large benefit of this is that, in principle, the dose could be delivered per spot, rather than scanned continuously, but the same dose rate is applied. This would

provide more accurate tracking of the dose per voxel. For burst extraction, it is likely that the distribution of each burst does not strictly require uniform intensity. What is more significant for treatment is that each burst has the same delivered intensity, with minimal fluctuations between shots.

For this investigation, a burst spill time of 15 000 turns is assumed, and equally 15 000 turns between bursts. This should cause 10 bursts in the extraction time of 300 000 turns.

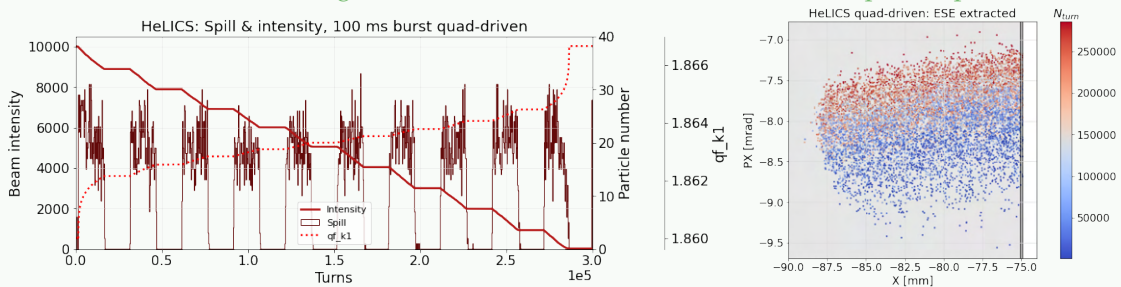
In this section, quadrupole and RF-KO burst extraction are simulated, and phase-displacement burst extraction (PDE) is discussed.

Burst quadrupole-driven extraction

Following from the results of [Sec. 7.2.3](#), the signal provided to the k_1 quadrupole strength as a function of time was adapted so that a plateau was established every 10 ms of the 100 ms extraction time. The corresponding signal can be seen as the dashed line following the Gaussian ppf function in [Fig. 7.13](#). The results are expressed in [Fig. 7.19](#) (left), which displays a characteristic burst extraction function, and step-like decrease in machine intensity as a function of time. The corresponding extracted particle signal of [Fig. 7.19](#) (right) shows the same distribution as in [Fig. 7.15](#) (right), but with more explicit banding as a function of time. As the intensity consistency per burst is important, [Tab. 7.5a](#) compares the mean and variation for each burst. As a proof of principle, it is possible to simulate quadrupole driven burst extrac-

Figure 7.19.: Spill response for inverse-Gaussian quadrupole-driven burst extraction

(Left) Quadrupole-driven spill histogram and beam intensity for burst extraction as a function of turn number. (Right) Extracted beam distribution at the ES in phase-space.



tion, to compare with alternative methods. Whether it is possible to perform in the machine is entirely dependent on hardware speed. Similar quadrupole burst extraction simulations have been performed for the SPS in preparation for the ENUBET neutrino experiment [75].

Operationally, quadrupole burst extraction is not a recommended extraction method. This is for the same reasons it is not applied for conventional slow extraction, due to the rapid changes in optics, corresponding large spread in p_x , and frequency peaks due to quadrupole power converter ripples. In addition, with regards to safety method, having constant quadrupole strength does not guarantee that extraction is paused. Aforementioned fluctuations in current ripple, or unexpected shifts in particle or machine tune would prompt the undesirable extraction of particles in-between bursts.

Burst RF-KO extraction

Burst extraction controller is more difficult to obtain in simulations compared to quadrupole driven. When initialising gaps every 15 000 turn, the controller is no longer following the setpoint, and therefore responds strongly once the burst spill begins. A demonstration of this is expressed in [Fig. 7.20](#). The controller parameters are the same from [Fig. 7.17](#). Considering the gaps between bursts, the setpoint is doubled, and then adapted to follow the desired burst trend. The controller is programmed to recall the limit from the previous burst. Despite this, the sharp increase in setpoint causes the controller to measure a large increase in error, responding with an increase in limit, causing a sharp peak to preface every burst. In particular the regular and frequent oscillations per burst indicate the K_p value should be lowered. Interestingly, the sharp peak at the start of RF-KO spills is a common feature observed in other facilities, including MedAustron and HIT. Despite this, the height of the initial response spike does have a large variation per spike. The numerical details of each burst is compared in [Sec. B.2.1](#), with the specifics in [Tab. 7.5b](#). A repeat of the simulation by extracting half of the statistics is in [Fig. B.7](#) and it is clear that the AM kick is consistent every burst with sufficient statistics. This confirms that the kick only tends exponentially when the particles in the machine reduces.

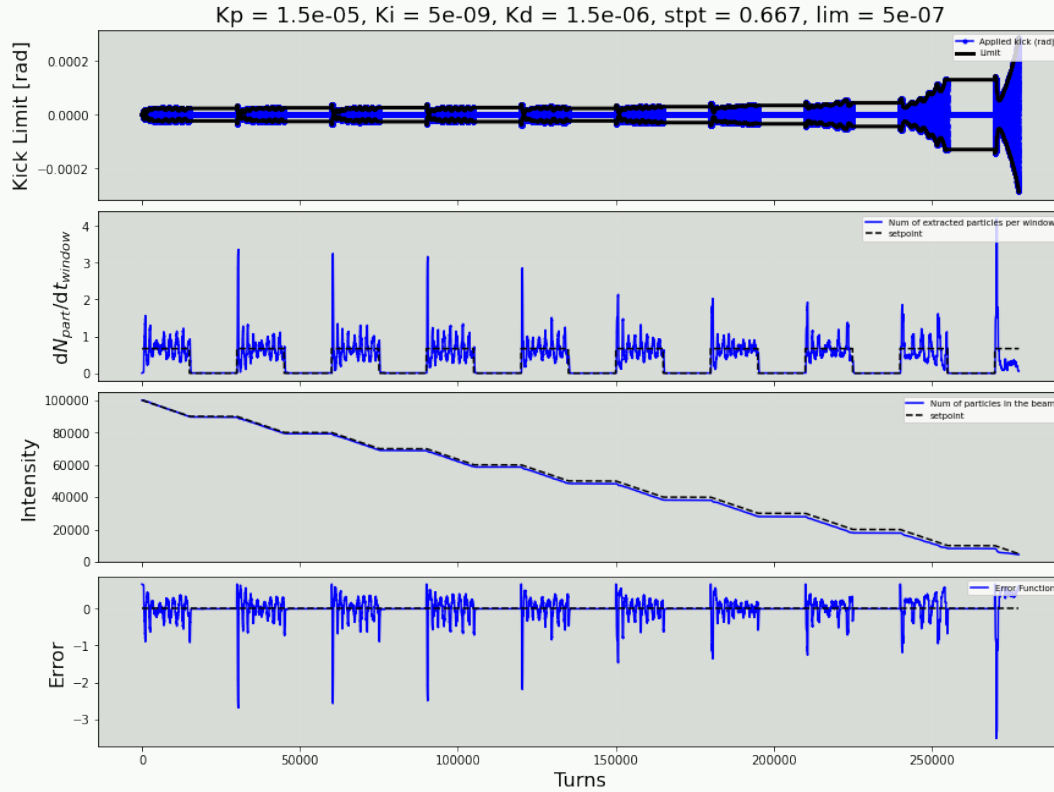
The particle spill per 300 turns is represented by the histogram (dark blue). It is clear to see the immediate response between the controller limit and the corresponding spill.

Burst UHDR Comparisons

[Tab. 7.4a](#) and [Tab. 7.4b](#) are compared, which provide the mean and standard deviation within each burst, and across all bursts. The binning for this scenario is 300 turns. The plot of each

Figure 7.20.: Output from RF-KO controller in burst mode

As a function of turn number, (1) the kick provided to the beam in radian (2) the number of particles extracted per time window (3) the intensity reduction of the beam in the machine (4) the difference between the setpoint and the extracted particles.



burst, its mean, standard deviation and sum dose can be seen in [Fig. 7.22](#).

Due to the low statistics towards the end of the spill, the final burst is not used in the calculation of the mean. The mean per burst is near identical for both methods (176 & 178), suggesting similar filling across the spill. The quadrupole-driven individual bursts of [Tab.7.4a](#) have half of the standard deviation compared to the RF-KO bursts (54 & 100), suggesting smoother spills within the burst. However the lack of automatic controller and the approximate use of Gaussian tune ramp in quadrupole-driven extraction results in three times higher standard deviation between bursts (606 & 210). As a result, only 1 out of 10 bursts are within 1 % of the mean dose, compared to 6 of the 10 bursts using RF-KO burst extraction with the controller. For this reason, even for quadrupole-driven burst extraction, controllers are recommended for ensuring minimal variation between shots, even if this comes at the expense of ripple within the burst.

Figure 7.21.: Spill, intensity and RF-KO kick for burst extraction

(Left) RF-KO spill histogram and beam intensity for burst extraction as a function of turn number. (Right) Extracted beam distribution at the ES in phase-space.

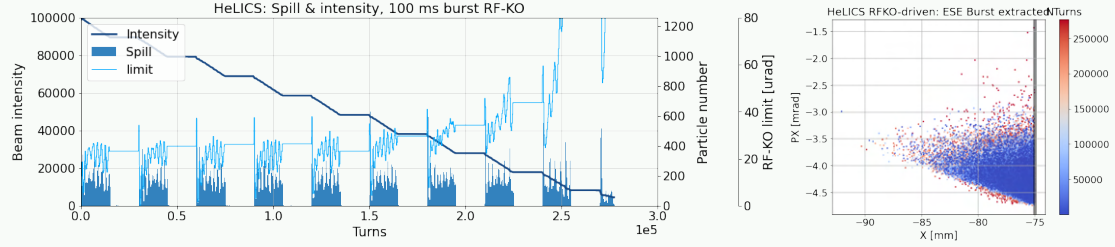


Table 7.4.: Burst statistics comparison: Particles per burst and % difference to mean particles per burst. Individual burst mean and std for particles per 300 turns. Total mean not inc. final burst

(a) Quadrupole-driven					(b) RF-KO				
Burst	Sum	% Diff	Mean	Std.	Burst	Sum	% Diff	Mean	Std.
1	11341	12.8 %	206	42	1	10378	1.8 %	172	88
2	9718	-3.3 %	176	37	2	10273	0.8 %	174	110
3	9386	-6.7 %	167	39	3	10387	1.9 %	167	109
4	9457	-5.9 %	168	39	4	10279	0.8 %	174	101
5	9632	-4.2 %	163	54	5	10249	0.5 %	183	92
6	9906	-1.5 %	165	57	6	10206	0.1 %	182	101
7	10023	-0.3 %	169	54	7	10235	0.4 %	179	94
8	10270	2.1 %	160	69	8	10095	-1.0 %	183	90
9	10756	7.0 %	176	63	9	9648	-5.4 %	172	114
10	9196	-8.5 %	176	52	10	3723	-63.5 %	132	234
Mean	10054±606		178±14	54	Mean	10194±210		176±5	100

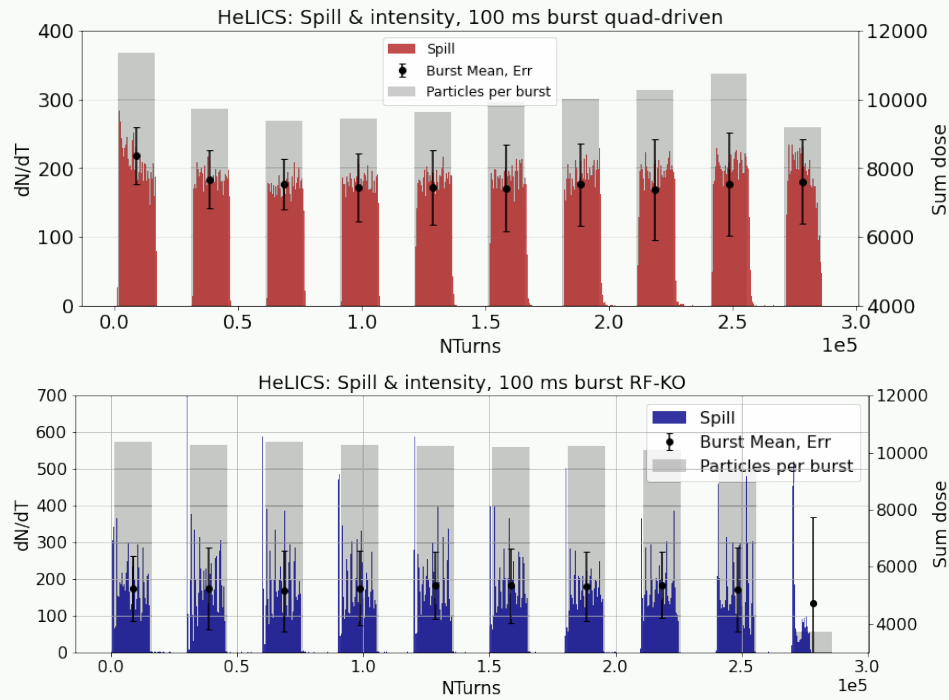
Burst RF Phase Displacement

RF phase displacement extraction (PDE) as a concept was mentioned in [Ch. 3](#) within the context of empty bucket channelling, but was not given a dedicated description with respect to NIMMS. As interest in burst extraction grows, the most common method of doing so in synchrotrons is with PDE. Whilst PDE experiences significant high ripples for long spills, it is ideal for burst extraction [75]. Depending on the time resolution of the RF cavity vs the RF-KO controller, it could provide a range of shorter bursts. Furthermore, it would be beneficial if such a method did not require any additional hardware in the already compact facilities.

For this reason, it is recommended for the next set of burst extraction simulations to provide a

Figure 7.22.: Dose and std of each burst for quadrupole-driven and RF-KO extraction

Results from **Tab. 7.5b** showing intensity per burst and spill quality within burst for (top) quadrupole-driven and (bottom) RF-KO extraction. Binned every 300 turns



test of RF phase displacement for the NIMMS synchrotrons. The concept of RF phase displacement, as described via PIMMS V1, is to sweep the longitudinal beam stack through the channels of an empty longitudinal bucket [15]. To provide a realistic simulation of this for HeLICS, a suitable RF cavity should be designed and incorporated into the lattice. Once inserted, longitudinal tracking should be performed in near-extraction conditions to ensure stability. This could be achieved for example in Xsuite with BLongD implementation [126]. Alternatively, simplified simulations, such as via a henon map, could be possible as explored in [75].

7.2.5 HeLICS Discussion

This chapter began by reproducing conventional extraction methods from existing synchrotron designs, and it concluded by simulating novel UHDR extraction methods from conceptual synchrotrons. The baseline design of NIMMS will use RF-KO excitation for conventional slow extraction, but decisions had yet to be made on how NIMMS would push the limits to achieve higher intensities and faster extraction rates from its synchrotrons.

When extracting higher intensity, higher emittance beams, few changes need to be made for tune-driven extraction methods such as betatron core or quadrupole driven extraction. For amplitude-driven extraction, the emittance is limited by the ceiling of the resonance stopband. When the emittance increases closer to the resonance, a reduced initial kick is required to initiate the extraction process, but a higher final kick is required. Past a particular emittance, the initial beam will no longer be stable, and should be moved to a larger tune distance. With upgrades towards a high voltage transverse exciter, this can be adapted for continuous beam for as short as 100 ms.

With increasing research, it is becoming clear that the tune distribution of a beam during RF-KO is not linear as it is for betatron or quadrupole driven extraction. The plots of [Fig. 7.5](#) shown in the 2022 slow extraction workshop was one of the first representations of how strong the detuning is in this regime. The realisation from this has been changing the understanding of the frequency of excitation that is applied to the beam ([Ch. 5](#)), and improving spill ripples across many facilities.

The most significant effect of increasing the beam intensity in a synchrotron is the space-charge. This would most be significant for injection and acceleration, but is less significant at the highest extraction energies. In particular because the beam is coasting prior to extraction, meaning a wider longitudinal beam spread. At HeLICS, the minimum extraction energy is 70 MeV/u. The effect of space charge in extracting beams of this energy range is likely to cause an increased tune distribution, meaning the beam must be further from the resonance, and that the frequency modulation spectrum of the RF-KO excitation must be broader.

Bibliography

- [6] M. Vretenar et al. "A Compact Synchrotron for Advanced Cancer Therapy with Helium and Proton Beams". In: *Proc. IPAC'22* (Bangkok, Thailand). International Particle Accelerator Conference 13. JACoW Publishing, Geneva, Switzerland, July 2022, pp. 811–814. ISBN: 978-3-95-450227-1. DOI: 10.18429/JACoW-IPAC2022-TU0ZGD2.
- [15] L. Badano et al. *Proton-Ion Medical Machine Study (PIMMS)*, 1. 1999.
- [53] C. Schömers. "Entwicklung einer dynamischen Intensitätsregelung für das Heidelberger Ionenstrahl-Therapiesynchrotron". PhD thesis. 2013.
- [60] F. Kühteubl. "Design study of radio frequency knockout slow extraction for the MedAus-tron synchrotron". en. In: (2020). DOI: 10.34726/HSS.2020.77640.

- [61] S. Savazzi, E. Bressi et al. “Implementation of RF-KO Extraction at CNAO”. In: *10th International Particle Accelerator Conference*. 2019, THPMP010. DOI: 10.18429/JACoW-IPAC2019-THPMP010.
- [75] P. A. Arrutia Sota, P. N. Burrows et al. “Millisecond burst extractions from synchrotrons using RF phase displacement acceleration. Millisecond burst extractions from synchrotrons using RF phase displacement acceleration”. In: *Nucl. Instrum. Methods Phys. Res., A* 1039 (2022), p. 167007. DOI: 10.1016/j.nima.2022.167007. arXiv: 2205.13433.
- [84] E. Benedetto et al. “Comparison of Accelerator Designs for an Ion Therapy and Research Facility”. In: (2020). URL: <https://cds.cern.ch/record/2748083>.
- [99] R. Taylor et al. “Flexible beam dynamics simulations for slow extraction with Maptrack”. In: (2024). URL: <https://cds.cern.ch/record/2889951>.
- [117] M. Vretenar et al. “The next ion medical machine study at CERN: Towards a next generation cancer research and therapy facility with ion beams”. In: *JACoW IPAC2021* (2021), MOPAB413. DOI: 10.18429/JACoW-IPAC2021-MOPAB413.
- [118] E. Benedetto and M. Vretenar. “Innovations in the Next Generation Medical Accelerators for Therapy with Ion Beams”. In: *Journal of Physics: Conference Series* 2687.9 (Jan. 2024), p. 092003. DOI: 10.1088/1742-6596/2687/9/092003.
- [119] R. Taylor et al. “Slow extraction modelling for NIMMS hadron therapy synchrotrons”. In: 2420.1 (Jan. 2023), p. 012101. DOI: 10.1088/1742-6596/2420/1/012101.
- [120] E. Benedetto et al. *Helium Synchrotron Optics Repository*. <https://gitlab.cern.ch/retaylor/hesync-optics-repository>. 2023.
- [121] F. Asvesta H. Huttunen et al. “Optics design of a compact helium synchrotron for advanced cancer therapy ” (Nashville, USA, June 2024). presented at IPAC’24, Nashville, USA, June 2024, unpublished.
- [122] P. Niedermayer. *Beamline Xplt 0.5.0 documentation — eltos.github.io*. <https://xsuite.github.io/xplt/>. 2023.
- [123] S. Detsi. “A Feedback Controller for the RFKO Method for Slow Extraction”. In: (2023). URL: <https://cds.cern.ch/record/2879791>.
- [124] A. Narayanan, K. J. Hazelwood et al. “Optimizing Mu2e Spill Regulation System Algorithms”. In: (Aug. 2021). DOI: 10.18429/JACoW-IPAC2021-THPAB243.
- [125] K. Noda, T. Furukawa et al. “Advanced RF-KO slow-extraction method for the reduction of spill ripple”. In: *Nuclear Instruments and Methods in Physics Research Section A: Accelerators, Spectrometers, Detectors and Associated Equipment* 492.1 (2002), pp. 253–263. ISSN: 0168-9002. DOI: [https://doi.org/10.1016/S0168-9002\(02\)01319-0](https://doi.org/10.1016/S0168-9002(02)01319-0).
- [126] CERN. *Beam Longitudinal Dynamics code BLoND*. <http://blond.web.cern.ch>.

*Cyclotron current,
And synchrotron extraction,
Both seem quite useful*

*If only there were
Some accelerator type
With both benefits*

Adam Steinberg

8

Future Technologies

The NIMMS toolbox offers a series of realistic and immediately available radiotherapy solutions. With the aim of compactness and affordability, the aforementioned synchrotron options of NIMMS are ideal to begin building within the next decade. Looking further afield, there are a wide range of developing accelerator technology options that ion therapy treatment may further benefit from.

Sec. 8.1 provides an overview of two newer technologies that NIMMS is developing, and how they affect the slow extraction process. First bent CCT superconducting dipoles for compact carbon synchrotrons and secondly low-current beam for proton tomography scans to provide imaging from all synchrotron types. These two concepts are in early stages of development, and it would not yet be possible to do complete slow extraction simulations and studies of each. Hopefully these intuitions can guide preliminary studies for those in the future.

Sec. 8.2 introduces the UK ITRF's Laser-hybrid Accelerator for Radiobiological Applications (LhARA). LhARA's baseline design for acceleration is a scaling Fixed Field Accelerator to preserve the laser-driven beam structure. This section presents the first simulations of slow extraction from a scaling FFA. The alternative accelerator option is explored, with extraction from a normal-conducting synchrotron.

8.1 Future R&D of NIMMS

8.1.1 Superconducting Medical Machine

In [Ch. 7](#), the two NIMMS normal conducting options were covered, along with their slow extraction schematics. The NIMMS superconducting carbon synchrotron is of a similar circumference and design to the normal-conducting helium synchrotron. The main difference is in the bending magnets. Instead of a conventional warm dipole, a superconducting alternating-gradient canted cosine-theta (AG-CCT) design with strong curvature will be implemented [35]. The design for a 430 MeV/u carbon ion synchrotron plans for 4 T magnets, a radius of curvature of 1.65 m and bending angle of 45° [127]. There are various challenges to modeling these magnets, particularly due to their non-linear fields. In a curved geometry, the concept of multipolar fields ($\frac{dB_n}{dx_n}$) begins to break down as the field does not neatly separate into quadrupole, sextupoles and nonlinear terms. In particular, these multipole coordinates increase at the longitudinal fringes of the magnet when further away from the good-field region at 60 cm (Fig. 3 of [127]). A large amount of work is going into modelling and tracking these magnets, including in MADX or XSuite.

It will be interesting to determine the direct impact of these multipole gradient effects on slow extraction. Any traces of sextupole strength across the accelerator would accumulate into a virtual sextupole of a particular phase-advance. This effect must be considered when placing any resonant and chromatic sextupoles in the design, especially as it could excite particular driving terms.

It is likely that a similar effect will occur in the transverse fringes of the CCT magnets. In this instance, the large-amplitude particles within the separatrices would experience increased sextupole and octupole components compared to on-orbit low amplitude particles. Left unchecked, this would affect the spiral step and separatrix curvature as a function of amplitude. Accurate simulations would be required to measure the full effect of this on the extracted beam. Once reliable AG-CCT magnets are incorporated into MADX or XSuite, the same simulation setup as [Ch. 4](#) can allow for simulation comparisons to begin. The sextupole component would likely cause larger final spiral step, therefore larger horizontal spreads in beam. Left uncorrected, this would require wider septa gaps which results in increased field strength and therefore power consumption. The octupole component, if the wrong polarity or strength, could cause

ADTS effects (see [Ch. B](#)), and in extreme cases result in island formation. If optimised properly, this component could be beneficial and bend the beam away from the septum cathode to reduce losses, via the same technique demonstrated in [Ch. 6](#).

The residual multipole component in the AG-CCT magnets is also affected by the material of superconductor used. For high-temperature superconductors, such as those in ReBCO, the thicker tape width of ≈ 4 mm affects the current flow throughout the tape, leading to higher multipole-strengths compared to conventional low-temperature superconductors. For this reason, it would be interesting to predict the virtual sextupole strength for the superconducting carbon synchrotron depending on the material used.

8.1.2 Proton Radiography

FROM DISCUSSION WITH K. PAŁSKIS

Preliminary investigations are determining if proton radiography is feasible from HeLICS. Proton radiography would be used to obtain 2D scans of the patient prior to treatment. This would be a useful as a patient position verification method for image guided therapy, available with very little additional technical cost on the side of the accelerator. To do so requires the beam to be transmitted through the patient towards the detector, so presently only protons can be accelerated to these transmission energies. Due to its lower lateral scattering, helium could be a more beneficial particle to use for radiography, but is less studied due to the higher energy acceleration needed, and reconstruction to remove fragmentation effects.

Operationally, this method requires a very low beam current - on the scale of a few pA - due to readout frequency limitations of currently available detector systems [128]. On average, the readout frequency is expected to be in the MHz range. The detector would work best under single particle tracking, meaning smooth spacial resolution without pile-up or deadtime. The timeframe would be on the scale of 10-100 s, meaning 1×10^7 - 1×10^8 particles would be needed to provide this current. From a synchrotron, it is reasonable to assume that the only way to provide this low current over a long timescale is via slow extraction. This prompts investigation to consider how slow one can slow extract, to obtain this low current.

The slow extraction mechanism to provide proton radiography would depend on the operational mode chosen for the synchrotron. Assuming it is feasible for NIMMS to inject a low

current to circulate in the machine, a slow quadrupole ramp for tune-driven extraction would be sufficient. However, it may be the case that NIMMS has to inject the full ion source output for one turn of the MTI, i.e. 10^9 protons. If so, only a fraction of the beam would need to be extracted. Having RF-KO extraction at a very low voltage would be able to extract just a few particles per turn, at the highest amplitudes. The rest of the unextracted beam would be later dumped. One could tailor the RF-KO voltage signal to specify the rate required for proton radiography.

The limit of RF-KO extraction, as a stochastic process, is that one would hit the Poisson limit of random noise for low-current applications (see [Sec. 2.3.4](#)). Having a resolution of one particle per μs , the Poisson extracted particle mean is equivalent to the variance where $\lambda = \sigma^2 = 1$, meaning the error margin is 100% of the mean. This means the spill would have high variance and its smoothness could not be fully ensured. It depends on the experimental needs of the radiography beam whether smoothness is as crucial as it is for hadron therapy. Given the low particle numbers required for a realistic simulation, this method would be relatively easy to track. The simulation methods developed in Xsuite are available to help with this.

8.2 Ion Therapy Research Facility

The Ion Therapy Research Facility (ITRF) is a proposed project from the UK. The flagship design for this facility is LhARA, the Laser-hybrid Accelerator for Radiobiological Applications. The latest laser technology will be used to generate an ion beam from a laser source via target-normal sheath acceleration [129]. After the ion source, the species and energy of ions are captured and focused via a series of Gabor plasma lenses [130]. This laser and capture section in Stage 1, will deliver 15 MeV proton beams and $\approx 5 \text{ MeV/u}$ ion beams to an in-vitro end station for cellular radiobiological studies.

LhARA's use as an in-vitro and in-vivo radiobiological facility necessitates that it has a different beam constraints than that of NIMMS, which must meet clinical standards. This relaxes a lot of constraints, in particular the energy specification of the beam, which does not need to reach the full 30 cm of depth. In addition, the LhARA beam will inevitably be different due to the properties of the laser-driven ion beam. The high spread of the beam from the laser will be contained by an energy capture segment, which is estimated to produce a high momentum spread of 2%, compared to the NIMMS estimate of 0.1%. The spot-size of the beam of LhARA

is expected to be uniform in distribution and to match the approximate size of the samples in the Stage 1 end-station, between 1-3 cm. This is contrary to the helium synchrotron injected beam which is predicted to be Gaussian in distribution with an RMS of at most 1 cm for a $5 \pi \text{mm} \cdot \text{mrad}$ emittance beam. Both the laser source of LhARA and the ECR (Electron Cyclotron Resonance) source of NIMMS expect to produce 10^9 ions per shot. For NIMMS, increased intensity is delivered by injecting 10 shots to the synchrotron via multi-energy extraction. For LhARA, increased intensity is delivered due to its high shot-rate, with the laser pulsing at 10 Hz.

LhARA FFA

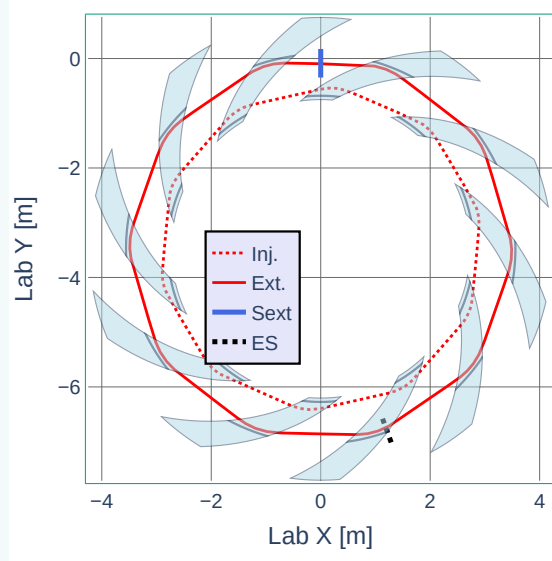
LhARA Stage 2 intends to reach higher energies for in-vivo irradiation. For this, a Fixed Field Accelerator (FFA) has been proposed. The FFA would reach up to 125 MeV for protons and 34 MeV/u for ions. FFAs are different to synchrotrons as their closed orbit changes as a function of energy. Initially the beam starts at a small radius, and as the beam is accelerated, it spirals outwards and experiences a higher gradient of field from the fixed magnets. An FFA is the most beneficial option in this scenario for multiple reasons: Firstly, the lack of ramping magnets during acceleration means that the 10 Hz signal can be preserved without the need for a rapid-cycling synchrotron (RCS). It also means that should a faster laser pulse be used, on the order of 100 Hz, the FFA continues to be compatible. Secondly, FFAs have the benefit of handling higher currents at lower energies without the space-charge emittance blow-up of synchrotrons, due to the FFA's rapid acceleration. Thirdly, as a spiral scaling design has been chosen based on the RACCAM magnets [131], this FFA has a particularly compact design to reduce the footprint of the accelerator.

The specifications of the initial FFA design for LhARA is shown in [Fig. 8.1](#), with parameters of [Tab. 8.1](#). This FFA is intended to operate as an energy multiplier, where the extracted beam energy E is varied by controlling the injection energy and the reference magnetic field B_0 is changed to match to this energy. Using the RACCAM design of magnets, the magnetic length is expected to be 0.7537 m. It is composed of 10 of these magnets symmetrically with a 0.34 packing factor, providing a total circumference of 21.853 m, with respect to the reference orbit r_0 .

Table 8.1.: Parameters of the LhARA FFA

Parameter	Value	Parameter	Value
E [MeV]	15 - 125	Packing Factor	0.34
B_0 [T]	1.4	r_0 [m]	3.47704
Magnet length [m]	0.7537	ε_x [$\pi\text{mm}\cdot\text{mrad}$]	0.41
gradient k	4.756	Spiral angle ζ	43.14°

Figure 8.1.: Top-down view of the LhARA spiral scaling FFA design in X-Y with parameters of Tab. 8.1. Red lines show injection (dashed) and extraction (solid) orbit. Pictured is the added resonant sextupole (blue) and electrostatic septum (black).



Plotted by A. Steinberg

8.2.1 Slow Extraction from Fixed Field Accelerators

THIS SECTION WAS PERFORMED WITH EQUAL CONTRIBUTION FROM A. STEINBERG. IT REFERS TO PUBLICATION 2024 J. PHYS.: CONF. SER. 2687 022022 [132]

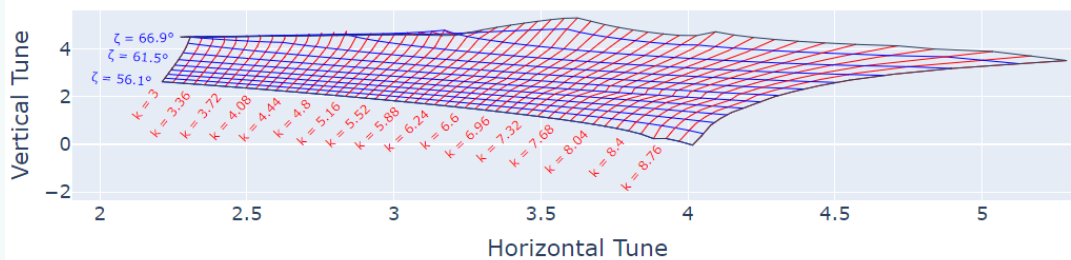
The aim of this study is to investigate methods to slow extract from a Fixed Field Accelerator, and first level tracking simulations to test these methods. Through this, one can determine limitations of FFAs which may prevent efficient slow extraction. Due to the high packing factor and periodicity, beam extraction often presents a challenge for FFAs. Decisions taken early in the design process, such as the working point, will remain fixed and will influence the extraction mechanisms. As such, beam delivery must be considered concurrently with the

initial optical design. Given that FFAs have similarities to both cyclotrons and synchrotrons, the difficulty of this study is to preserve these benefits without forcing the FFA to behave as a synchrotron to perform extraction.

FFA Theory & Slow Extraction

As mentioned, the magnet design for the LhARA FFA is based on the RACCAM spiral sector magnets. These magnets use a gap shaping method to change the k -index gradient between the poles of a dipole [131]. The magnet is curved with a spiral angle of ζ , which provides vertical edge-focusing to the accelerator. These two parameters have a large effect on the accelerator design. Once the magnet is built, these two variables are fixed. For the LhARA FFA, the relation between spiral angle, k -index, and the corresponding horizontal and vertical tune is demonstrated in **Fig. 8.2**. This figure is useful as a reference to know how to adjust the spiral angles for exploring different working points. It also represents the range of tunes that can be reached for reasonable angle geometries and k -index hardware.

Figure 8.2.: Range of working points in horizontal-vertical tune space as a function of spiral angle and k -index gradient in zgoubi.



Plotted by A. Steinberg

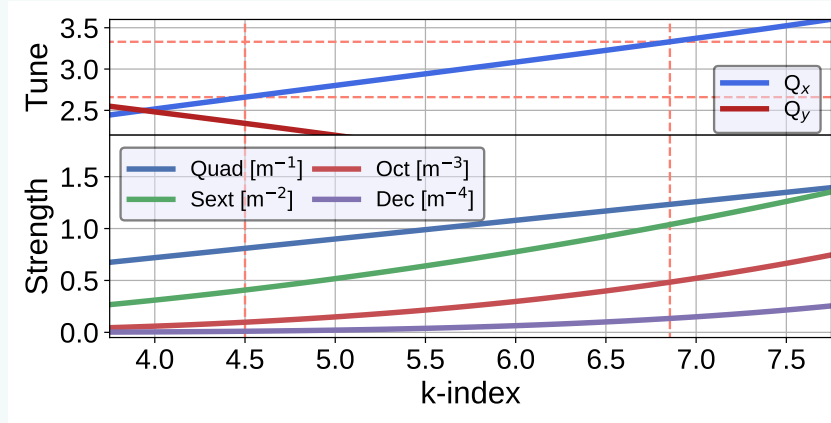
The law defining scaling FFAs is given by **Eq. 8.1**. B_0 is the reference field along reference radius r_0 . Form factor \mathcal{F} describes the magnet fringe and body fields.

$$B = B_0 \left(\frac{r}{r_0} \right)^k \mathcal{F} \left(\theta - \tan(\zeta) \ln \frac{r}{r_0} \right) \quad (8.1)$$

The magnetic multipole terms are determined by B_0 , r_0 , and k . In a Taylor expansion of **Eq. 8.1** [133] in orders of k , the first term determines the dipole field, the second is the quad-

rupole gradient, and so on for higher orders. **Fig. 8.3** represents how the relative multipole strengths are fixed as a function of k-index and therefore tune, for a particular spiral angle ($\zeta=57.0^\circ$). Multipoles at the 2.6 and 3.3 resonances are indicated by dashed orange lines. Varying any one multipole strength, i.e. introducing a sextupole strength, is not possible without breaking the scaling law. The scaling law ensures there is no tune relation with energy, i.e. no chromaticity.

Figure 8.3.: Set values of tune and multipole strength (quadrupole to decupole) for a given value of k-index at the extraction energy in zgoubi



Plotted by A. Steinberg

The approximations assumed for synchrotron-based slow extraction are no longer valid under this system. In particular for synchrotron dynamics, $\frac{d^2B}{dx^2}$ is typically defined as the field perpendicular to beam axis for a closed orbit solution. This is no longer the case for FFA dynamics, so an instantaneous direction of motion would need to be taken. In addition, sextupole strength will vary as a function of energy. The fundamental equations of **Ch. 2** would need to be revisited if one wants to acquire a 'realistic' approximation of virtual sextupole strength, and thereby obtain a comparable model of the slow extraction process and therefore the properties of the extracted beam.

As established in **Ch. 2.2.4**, the Kobayashi-Hamiltonian is a useful theoretical tool to describe the dynamics of the phase-space of the beam for a given accelerator system. Hamiltonians are derived via synchrotron dynamics, particularly for the coordinate transforms from action and phase to physical phase-space. FFAs differ as they feature a horizontal gradient which increases in orbit. As slow extraction causes particles to increase in amplitude, it is expected

that this gradient will most affect particles at these amplitudes. Due to the increased fields at these amplitudes, particles are likely to experience a higher or lower spiral step, depending on whether they are positive or negative with respect to the closed reference orbit. It is not obvious what gradient is necessary to begin to observe these distortions, and it is not obvious if this effect would cancel out due to the rotation of the separatrices throughout the accelerator. It is likely that any effect on the spiral step would be higher at stronger k gradients. Future studies should investigate if the Kobayashi-Hamiltonian of the FFA system under slow extraction conditions incorporates this gradient, and thereby predict how the dynamics will shape the phase-space of the beam.

Simulations

The LhARA FFA optics was first provided by J. PASTERNAK in the form of a MADX lattice. The preliminary geometry and optics investigations for the FFA were continued in MADX by R. TAYLOR. MADX is limiting for models of FFAs. First of all, the Lie algebra for PTC tracking takes small-angle approximations which are no longer valid for large deviations. This means that MADX may not capture edge focusing or defocusing effects at large edge angles. It also may not capture changes in orbital paths as a result of the FFA gradient, or change in k -strength. In addition, MADX represents FFA magnets as additional multipole strengths as applied to an S-bend. These additional multipoles go up to a maximum of octupole effects whereas FFA tracking simulations often need at least decupole (10-pole magnets) features to be accurate, as found by PAMELA simulation studies ([134] Fig. 14).

For more realistic FFA modelling, tracking was performed by A. STEINBERG in zgoubidoo (a Zgoubi python library). Zgoubi uses ray-tracing with numerical integration of equations of motion, initially created for the purposes of modelling mass spectrometers, and later adapted for accurate FFA modelling. Additional tracking functions benefited from the zgoubisnax simulation tools, showcased in [135]. Given that many of the results were conceptualised in MADX and finalised in Zgoubi, many of the final versions of plots are attributed to A. Steinberg.

To provide a proof of principle of slow extraction from FFAs, variables were simplified as much as possible, given the complexity of the system. Although the static magnetic fields make it possible to simultaneously transport multiple beams of different energies, LhARA currently

plans to operate with only one circulating beam per cycle. For this work, it is assumed that the closed orbit trajectory at extraction is energy-independent, and that the beam dynamics of lower energy orbits can be ignored. In particular, this study was performed for protons for only one energy (125 MeV). In addition, solutions were found for only the reference extraction orbit. This is significant as the Twiss changes as a function of the orbit for an FFA. Before full tracking simulations could begin, the closed orbit solution has to be calculated in zgoubi. This is an iterative process which means that whilst zgoubi ensures accuracy and relevance for FFA dynamics for a given orbit, it can take up to 10x longer than MADX simulations.

The most significant simplification is that the septa are represented as singular points, to avoid the geometric difficulties of the FFA's high packing factor.

Compared to the flexibility of maptrack and Xsuite, it is not obvious how to represent dynamic extraction excitation options in zgoubidoo. Three excitation options were considered:

- **RF-KO extraction:** RF-KO extraction is the simplest option, as it only changes the distribution of the beam, not the lattice itself. An RF-KO function was written where each turn, the p_x coordinate of the beam distribution in mrad is obtained, and an RF-KO kick is added, which changes as a function of turn number. This is simplified for transverse-excitation only as longitudinal effects of a coasting beam would be difficult for RF-KO modelling.
- **k -index ramping:** Whilst fixed-field magnets have fixed fields, if one had a series of individual coils within the shaped gap of the magnet, the gradient of the magnet could be altered as a function of time. Doing so would have the benefit of changing the horizontal tune, allowing for extraction via tune ramping. However, this would change the closed orbit of the beam, and also the vertical tune, potentially leading towards resonance lines. If not performed adiabatically, this would increase the emittance of the beam. k -index ramping simulations in zgoubidoo would need to be done with single-turn simulations, using new settings each turn with the ending coordinates of previous simulation equal to the new starting coordinates. It would be hard to observe how the tune varies with ramping k -index, as the offsets will be discontinuous. If the k -index and the B -field of the magnet is ramped simultaneously, this could prevent the closed orbit from moving. For example, the FETS FFA has a main coil for individual conductors which could be adapted for the LhARA FFA [136]. The emittance increase from non-adiabatic ramping may

be unintentionally beneficial, as may move particles into unstable orbits for extraction.

- **RF-phase displacement:** Like in [Sec. 7.2.4](#), RF-phase displacement is the most promising result operationally. In particular as one of the first RF-phase displacement studies published was with a spiral sector FFA via the MURA association [137]. Performing this simulation would require a detailed model of the RF-cavity within the LhARA FFA, which has not been completed yet. In addition, it would require exact models of longitudinal dynamics in a spiral scaling FFA, which itself requires a dedicated study. Furthermore, RF-phase ramping is ideal for burst-like extraction, but may be unstable for second-long slow extraction. This means its use depends on the exact time ranges that LhARA will need to provide to its users. In particular, the limits on spill flux should be defined by the LhARA facility. It does not have to provide clinical standards of signals, but should still give reliable beam to the experiments.

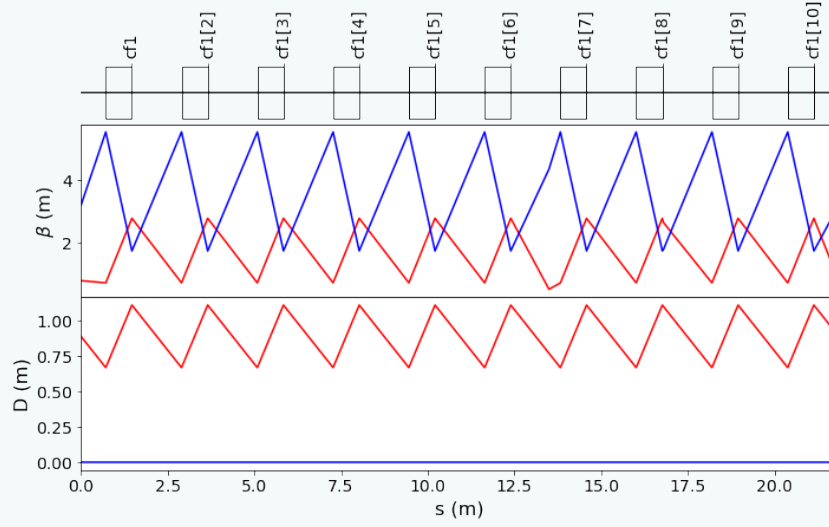
Due to time limitations, RF-KO was chosen to gain the final extraction result as it was the simplest to incorporate simulation-wise.

Working point 3.3

There are numerous disadvantages to adding a sextupole to a Fixed Field Accelerator. Most obviously, there is no dispersion-free region in a scaling FFA, by definition. This necessarily means that any added sextupole will introduce chromaticity into the accelerator and break the scaling law. Furthermore, an FFA features a wide horizontal beam pipe and no single closed orbit. This means that the addition of a singular multipole would have to be of an interesting geometry, likely perhaps focused on a particular extraction orbit. So, if it is indeed true that one should avoid adding a sextupole to the FFA, it therefore follows that the intrinsic sextupole strength within the FFA itself must be sufficient to produce slow extraction.

A series of horizontal resonances was selected to determine which ones were able to perform slow extraction whilst exactly on resonance. For the majority of working points, the beam was found to be stable despite having a horizontal tune exactly on resonance. The exception to this is for $Q_x = 3.\dot{3}$. The $10/3$ resonance is particularly strong as the FFA has a superperiodicity of 10, meaning each individual cell has a $1/3$ phase-advance. This creates a structural resonance within the accelerator. The phase-advance of FFAs is limiting, as the high symmetry and

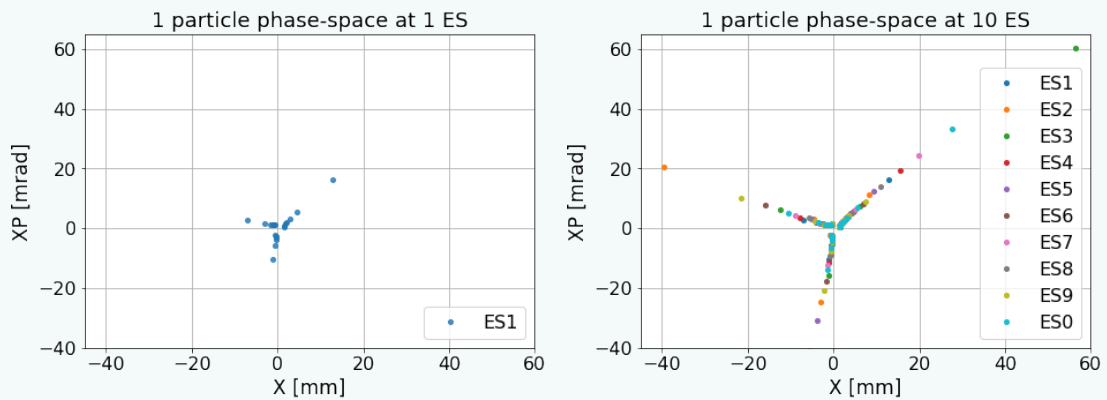
Figure 8.4.: Beta and dispersion across the FFA lattice in MADX for an on-axis beam at $Q_x = 3.3$, $R_0 = 3.47704$



super-periodicity means μ_x is identical at all equivalent points in each cell, making septum positioning difficult.

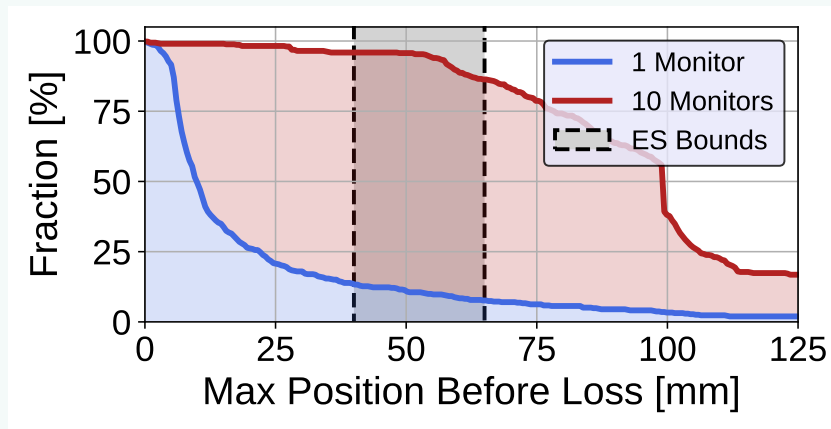
The LhARA design spiral angle of 48.7° was vertically unstable at this horizontal tune. This may be countered by increasing vertical focusing by optimising the fringe fields. Here, k and ζ were set to 6.678 and 59.876° respectively, with a 25 mm wide ES centred at 52.5 mm. To provide the required relative phase-advance explained in [Ch. 2](#), the electrostatic septum (ES) is centered between the 6th and 7th magnet (13.5 m) and the magnetic septum (MS) is centered between the 8th and 9th magnet (16.8 m). Typically with a third-order resonance, the particles

Figure 8.5.: Representation of the separatrices span when measured at one ES vs one ES in each cell in MADX



will experience a spiral step in amplitude once every three turns around the lattice. This particular tune now produces that step every three magnets. This causes particles to leave the machine ten times faster than expected, and forces the spiral step within one revolution to be larger than the reasonable width of the ES. Fig. 8.5 represents how this looks in phase-space, and how it is hard to resolve in simulations. With one monitor, the particle as a function of time looks as though it stops tracking before 20 mm. One gets the full picture by looking at a monitor in the same position symmetric across all 10 magnets. The consequence of this effect is illustrated in Fig. 8.6. It shows the maximum horizontal position of each particle before tracking fails. In a lattice with only one ES (blue), 90 % of all particles jump over the septum, and are lost elsewhere in the ring - i.e. there is only 10% extraction efficiency. This effect is unique only to the 3.3 resonance, specifically due to the tenfold symmetry of the FFA.

Figure 8.6.: Percentage of the beam survival transversely. Blue curve only monitors at one ES. Red curve monitors at each cell. Black dashed line represents chosen ES field region.



Plotted by A. Steinberg

It may be possible to use this self-exciting resonance in a lattice with a smaller spiral step, but it would require significant modifications to the FFA design. Instead, a new working point was chosen, requiring an excitation sextupole.

Working point 2.6

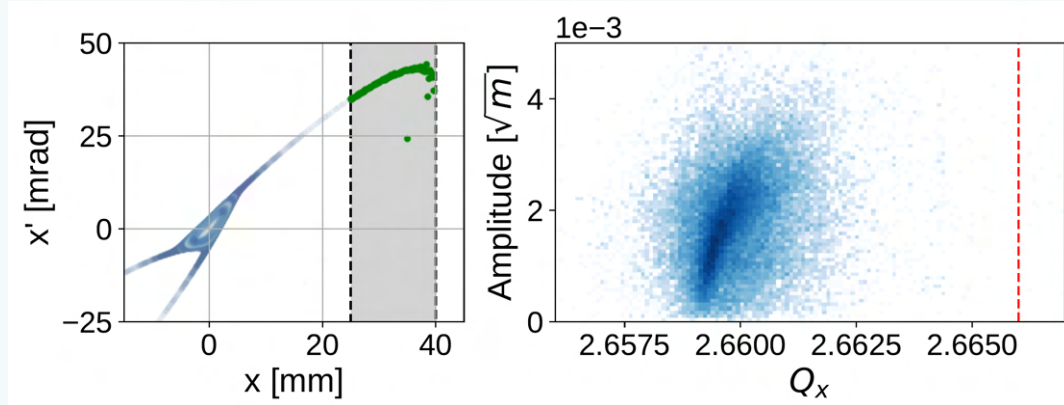
The FFA at the optical settings of 2.6 does not have a strong enough inherent sextupole component to drive the resonance. Therefore an additional sextupole must be added to the lattice to perform slow extraction. A thin-lens (1 mm) sextupole is added using the *make_multipole* func-

tion of zgoubisnax. This sextupole has a strength of 50 T m^{-2} , corresponding to $k_2 L = 29.99 \text{ m}^{-2}$. It is important to ensure that the angle of the sextupole is aligned so that it is perpendicular to the extraction orbit. It is not yet obvious how such a sextupole would be designed if it were to be installed in reality. As the sextupole will break the FFA scaling law, it will inevitably introduce a chromaticity to the beam. For this reason, the sextupole should only be switched on once the beam has finished accelerating, and is at the extraction orbit to minimise the effect.

As there is now a strong localised sextupole, the ES must be relocated to ensure the necessary relative phase-advance with respect to the septum. The majority of the phase-advance changes in the FFA occur in the fringe fields of the main magnets. For this reason, the only conditions where the phase advance was suitable was to position the ES within one of the magnets, still modelled as a single point. Neither of these conditions are ideal. The ES was angled to be perpendicular to the tangent from the centre of the lattice. The slow extraction spiral step is proportional to $\propto S \cdot X_{\text{ES}}^2$, so these variables must be chosen to control the extracted particle distribution, and to avoid losses on the ES electrodes. To optimise extraction efficiency with a reasonable extracted beam size, the ES anode foil was positioned at 32.5 mm with a field width of 15 mm. With the extraction schematic set up, the beam was then excited into the resonance

Figure 8.7.: Extraction with RF-KO in phase space and tune-amplitude in zgoubi.

(Left) Phase-space of all particles throughout all turns (white=earlier turn, blue=later turn), and extracted particle distribution (green) after the ES field region (grey). (Right) Density-based tune-amplitude plot with respect to the resonance line (red dashed).



Plotted by A. Steinberg

via a zero-length RF-KO exciter. The RF-KO excitation signal did not optimise the AM, instead using a simple sinusoidal excitation of constant $25 \mu\text{rad}$ amplitude and frequency $Q_x = 0.6590$

per turn. A bandwidth of $\Delta Q_x = 1.5 \times 10^{-3}/\text{turn}$ was applied to the angular component of the beam to cover the tune spread of the beam. Fig. 8.7 shows the cumulative phase-space distribution over 30 000 turns for 256 particles, and the tune shift towards the resonance at large amplitudes. The low statistics is because a large number of turns is required for RF-KO simulations, which took order of ≈ 8 hours via Zgoubi. On the left the ES field region is shown in grey with the extracted particle distribution in green. On the right the centre of the resonance is given by the dashed line. The beam is successfully extracted, although further statistics and optimisation of the excitation signal is recommended for analysis of extracted spill quality. It is clear to see the bend of the extracted beam. This is due to the octupolar k_3 component, the higher multipole effects in the FFA magnets and the many k_2 magnets with strong B-fields and small bends. This is a slight effect of unintended amplitude-detuning in the machine. In this instance it was reduced by having a closer X_{ES} . If this aperture limit was not possible in reality, it would be difficult to remove this effect, due to the scaling multipoles of the FFA.

FFA Discussion

As one of the first papers explicitly on extraction from a scaling FFA since 1960 [41], this study revealed a lot of follow-up questions and research areas that would be necessary before operational slow extraction can be tested on an FFA. In addition, a list of challenges that must be considered is provided in the below box, as well as a section focusing on new concepts that could be beneficial to explore and test.

This study tested the accelerator layout by adding the required components for slow extraction, and then using an excitation signal to extract the beam towards the ES field region. However, it was not able to characterise the quality of the spill or provide high statistics studies. It would be difficult to comment on the ability to get good quality spills via an FFA. Primarily, this will be dominated by the longitudinal effects which have yet to be incorporated into the FFA model.

Challenges

- FFAs have orbit changing as a function of energy. An ES will have a fixed position, and the sextupole will be designed for a particular orbit. It is best to choose an extraction orbit that the beam can be moved to, independent of energy. This choice

constrains the FFA in forcing it to act closer to a synchrotron.

- The ES will kick the high amplitude particles which will likely oscillate into strong spiral FFA fringe fields. It is unclear how the beam distribution will be warped prior to entering the MS.
- A horizontal gradient is likely to affect the spiral step of the separatrices increasing with k .
- Geometry limitations, limited space between magnets and limited phase rotation between magnets all affect realistic models of the extraction septa.
- Strong separatrix bending from FFA octupoles and higher order multipoles cause amplitude detuning which can not be easily amended. At low detuning this will shape the extracted bar-of-charge, and at high detuning it may prevent extraction altogether due to trapping or otherwise. This effect will be higher at higher k -index.

Conceptual Ideals

- Use a race-track design for more space for extraction elements. This may also break the scaling law, where the tune becomes correlated with energy - although this may be needed anyway with the addition of sextupoles.
- Investigate wider or stronger electrostatic septum using superconducting technologies (SuShi).
- Consider an open-iron sextupole to fit geometric constraints and only affect the extraction orbit.
- Alter machine chromaticity such that the tune approaches the resonance as the particle approaches extraction energy. The beam will tends towards triangular phase-space as its orbit increases towards extraction orbit.
- Any extraction solution should apply and preserve the unique features of the FFA as much as possible. Cyclotron extraction methods should also be explored.

Next Steps

In a theoretical sense, slow extraction as modelled in a synchrotron is not transferable to a highly non-linear environment such as the FFA. The present theoretical understanding should

be benchmarked with an ideal slow extraction scenario to identify if there is any significant discrepancy. If there is, it would be beneficial to develop models of the Hamiltonian dynamics in such a system.

Experimentally, it would be beneficial to test some of these principles at an existing FFA, whilst waiting for the LhARA FFA to be commissioned. One possible suggestion is to perform a machine development study e.g. adding a resonant sextupole at the KURNS facility [138]. Despite the set-up being different to the LhARA FFA, it could allow for investigation of other issues that simulations would not be able to identify, e.g. coupling between transverse and longitudinal planes.

More specifically with regards to LhARA, steps should be taken to get closer to the experimental programme. This includes more realistic geometric modelling of the FFA, including where and how the two septa magnets and RF-KO would be positioned. More difficult is how to add an external sextupole strength, and understand the consequences of the sextupole breaking the scaling of the FFA at flat-top.

The rapid acceleration of the nanosecond laser-driven ion beam via the FFA is ideal to create unique time structures for FLASH-compatible rates. The intensity of the laser-induced beam may restrict the volume that could be irradiated, however for the cellular studies that LhARA is planning, this may be suitable. If RF longitudinal bunch rotation is not sufficient to vary the timescale of the beam beyond nanoseconds, then a burst-like slow extraction option from the FFA could be necessary. The present research with LhARA on the topic of FLASH relates primarily to ion-acoustic imaging [139].

8.2.2 Synchrotron Option

The ITRF project has many high stakes R&D technology options. To consider conventional alternatives and to compare with the LhARA FFA design, a synchrotron design is under development [140]. The design is based on the NIMMS synchrotrons as part of a Framework Collaboration Agreement. To make it comparable with the LhARA design, the NIMMS helium synchrotron design has been adjusted to be comparable to the LhARA maximum energy of 125 MeV. The radiobiological limits of this energy, in particular for ions, is to be evaluated. The circumference is designed to be comparable to the LhARA FFA, at 21.3 m. It is designed to be compatible with conventional ion sources, like NIMMS, instead of being fitted after the

LhARA laser ion source.

This design will have similar challenges for extraction as that found for the NIMMS helium synchrotron. This particularly relates to its compact geometrical restrictions, due to its reduced size. Furthermore, its similar three-fold symmetry and strong bending magnets may experience similar non-linear difficulties once chromatic effects are introduced.

Bibliography

- [35] E. Benedetto et al. *A Carbon-Ion Superconducting Gantry and a Synchrotron Based on Canted Cosine Theta Magnets*. Submitted to Nuclear Instruments and Methods in Physics Research A. 2021. arXiv: 2105.04205 [physics.med-ph]. URL: <https://arxiv.org/abs/2105.04205>.
- [41] C. L. Hammer and L. Jackson Laslett. “Resonant Beam Extraction from an A. G. Synchrotron”. In: *Review of Scientific Instruments* 32.2 (1961), pp. 144–149. DOI: 10.1063/1.1717299.
- [127] E. Benedetto et al. “Strongly curved super-conducting magnets: beam optics modeling and field quality”. English. In: *Proc. IPAC’23* (Venice, Italy). IPAC’23 - 14th International Particle Accelerator Conference 14. JACoW Publishing, Geneva, Switzerland, May 2023, pp. 3379–3382. ISBN: 978-3-95450-231-8. DOI: 10.18429/JACoW-IPAC2023-WEPL115.
- [128] R. P. Johnson. “Review of medical radiography and tomography with proton beams”. In: *Reports on progress in physics* 81.1 (2017), p. 016701.
- [129] G. Aymar, T. Becker et al. “LhARA: The Laser-hybrid Accelerator for Radiobiological Applications”. In: *Frontiers in Physics* 8 (Sept. 2020). DOI: 10.3389/fphy.2020.567738.
- [130] T. S. Dascalu et al. “Second Beam Test and Numerical Investigation of the Imperial College Plasma (Gabor) Lens Prototype”. In: *Proc. IPAC’21* (Campinas, Brazil, May 2021). JACoW Publishing, Geneva, Switzerland, pp. 2943–2946. DOI: 10.18429/JACoW-IPAC2021-WEPA140.
- [131] F. Meot. “RACCAM: An example of spiral sector scaling FFA technology”. In: (Apr. 2019). DOI: 10.2172/1507116.
- [132] R. Taylor, A. F. Steinberg et al. “Slow Extraction Techniques from Fixed Field Accelerators”. In: *Journal of Physics: Conference Series* 2687.2 (Jan. 2024), p. 022022. DOI: 10.1088/1742-6596/2687/2/022022.
- [133] K. R. Symon et al. “Fixed-field alternating-gradient particle accelerators”. In: *Physical Review* 103.6 (1956), p. 1837.
- [134] K. J. Peach et al. “Conceptual design of a nonscaling fixed field alternating gradient accelerator for protons and carbon ions for charged particle therapy”. In: *Phys. Rev. ST Accel. Beams* 16 (3 Mar. 2013), p. 030101. DOI: 10.1103/PhysRevSTAB.16.030101.
- [135] A. Steinberg et al. “A novel large energy acceptance beamline for hadron therapy”. In: *Proc. IPAC’23* (Venice, Italy). International Particle Accelerator Conference 14. JACoW Publishing, Geneva, Switzerland, Sept. 2023, pp. 5004–5007. ISBN: 978-3-95-450231-8.
- [136] I. Rodriguez et al. “FFA magnet prototype for high intensity pulsed proton driver”. In: *Proc. IPAC’23* (Venice, Italy). International Particle Accelerator Conference 14. JACoW Publishing, Geneva, Switzerland, Sept. 2023, pp. 2261–2264. ISBN: 978-3-95-450231-8.

- [137] L. W. Jones et al. "Comparison of experimental results with the theory of radio frequency acceleration processes in FFAG accelerators". In: (Sept. 1994).
- [138] M. Tanigaki et al. "Present status of FFAG accelerators in KURRI for ADS study". In: *Proceedings of EPAC 2006*. Citeseer. 2006, p. 2367.
- [139] M. Maxouti et al. "Three-stage simulation for the development of an ion-acoustic dose-deposition mapping system for LhARA". In: *Proc. IPAC'23* (Venice, Italy). International Particle Accelerator Conference 14. JACoW Publishing, Geneva, Switzerland, Sept. 2023, pp. 4714–4717. ISBN: 978-3-95-450231-8.
- [140] M. Johnson. "ITRF WP3 Radiobiology Synchrotron Study" (Daresbury Laboratory, March 2023). <https://indico.stfc.ac.uk/event/722>.

9

Conclusions

A programme to establish slow extraction beams from yet-non-existent machines is a challenge of creativity. Situated between pure physics and engineering, but without existing engineering constraints, this study becomes a blue skies research project - applying fundamental beam dynamics driven by interest and curiosity. The aim of the work requested was to provide a design of the slow extraction procedure from NIMMS next-generation compact synchrotrons. In an exploratory manner, close to every method of slow extraction excitation was picked up and investigated in some capacity. Each of these investigations left a trail of further questioning, providing a wealth of future beam dynamics topics - each suitable for a potential masters or PhD project.

Sec. 9.1 presents the conclusions of the work performed, the impact of this thesis, and some next steps for future investigations. **Sec. 9.2** expresses the original research contribution of each chapter, with a commentary on the extent to which these findings are true, and the recommended next steps.

9.1 Discussion

To determine the best slow extraction method for NIMMS, many excitation methods were explored via simulation and literature review, with the conclusion that RF-KO is the best option for conventional slow extraction. This is confirmed for both a PIMMS-like lattice and the latest HeLICS lattice, where the extraction schematic was established for two working points. FLASH-compatible extraction with UHDR beams were explored at the HeLICS lattice for short continuous spills on the ≈ 60 ms timescale, and for 10 bursts of ≈ 3 ms timescale. To perform this in simulations via RF-KO extraction, a PID controller was developed. With a high voltage RF-KO exciter, it should be possible to use the same hardware for both conventional and UHDR extraction.

To extract the entire beam within one 100 ms spill via a sinusoidal excitation with Gaussian-noise from the PIMMS lattice, up to 4 kV of excitation is necessary. This is calculated for a 400 MeV C^{6+} beam. Additional studies of advanced-FM are recommended to lower the maximum kick strength further. High emittance beams will need to be further from the resonance for RF-KO extraction, so will also be in need of stronger excitation voltages. The benefit of NIMMS will be the higher intensity of protons and ions, capable of irradiating higher cm^3 volumes at FLASH-compatible UHDRs.

Beyond this, three side-projects were explored which all provided valuable insights to the field of slow extraction, and returned to benefit the core NIMMS work:

- Tune dynamics were frequently studied early in the PhD, which culminated in a dedicated chapter for this topic. Originally applied to understand how the PIMMS beam behaves in proximity to the resonance, [Ch. 5](#) analyses how one can reduce the number of turns required in the NAFF calculation to access behaviour with a resolution of 64-256 turns, changing as a function of time. Prior to this, it was common convention in slow extraction to use FFTs over thousands of turns. The application for this was crucial to analyse single-particle dynamics under strong transverse excitations at set frequencies. This was necessary to model a BTF measurement, and to explain the mechanism behind the double-peak tune formation at strong sextupole strengths near the third order resonance.

- The way to keep blue skies ambitions grounded is to test on physical machines - hence the benefit from studies at the CERN Proton Synchrotron, in [Ch. 6](#). Measuring the extracted current ratio as a function of sextupole-octupole strength at 2 GeV provided good agreement between simulation predictions and measurements, with some disturbance due to space-charge. At 24 GeV this study revealed a difference in the inherent octupole modelling of the PS PFWs.

When octupoles were applied to reduce losses throughout the PS, the octupole-loss relation was revealed to be a parabola which changes as a function of sextupole strength. Octupoles during slow extraction are beneficial to shape the distribution of the extracted beam. Additional steering and optimisation is required to transport this distribution to the experimental lines. The experience from amplitude detuning effects from octupoles helped to identify similar behaviour in the LhARA FFA and HeLICS

- Finally, looking towards high R&D hadron therapy options, Fixed-Field Accelerators help to preserve the time structures from laser-induced ion beams, but need slow extraction techniques if longer spills are requested. The first simulations of slow extraction from FFAs were performed, and found many further questions for additional exploration, represented in [Sec. 8.2.1](#).

[Sec. 9.2](#) emphasizes the original contributions of each research project.

Impact

The impact on society with respect to medicine is clear, not just for treatment but also for imaging via proton radiography. Beyond this, for the CERN Proton Synchrotron, improved extraction efficiency techniques would be beneficial for material irradiation tests of space components, detector components and for providing slow beams for high energy physics experiments. With regards to environment, smart extraction set-up choices can be used to minimize the strength of septa kicks, thereby reduce the power consumption of the septa magnets - one of the largest single uses of energy in a hadron therapy synchrotron [141].

As stated in [Ch. 3](#), the slow extraction R&D performed in this thesis is not specific to NIMMS, but is inherently transferable to any other slow extraction facility. Close collaboration with the wider slow extraction community throughout the years has expanded the exchange of ideas and impact of results.

Next Steps

Within this thesis, the majority of simulations and experiments focused on behaviour within the transverse planes. For future studies, consideration of longitudinal effects are crucial, especially with respect to the RF-KO signal - which has significant effects on the spill. Furthermore this will be necessary for simulations of PDE burst extraction, which HeLICS would benefit from.

Many questions arising from this thesis come from the limits of the knowledge of the FLASH effect. Identifying the relevant parameter-space of successful FLASH irradiations would help narrow down the specifications the beam must meet. Additional measurements, particularly on the topic of FLASH-compatible beams, would have brought additional insights to the operational limitations of FLASH.

With respect to NIMMS R&D, the clear next step is to explore the superconducting synchrotron option, once it is ready. In particular this relates to how multipole contributions from the unique magnetic fields will realistically accumulate in the machine, as this will cause further slow extraction challenges.

Hadron therapy synchrotrons perform slow extraction because they must match their output to the existing clinical standards, defined by the abilities of cyclotrons. With the the discovery of FLASH opening new dose rate domains, there are few reasons to stick to conventional solutions. The unique abilities of synchrotrons should be explored to its fullest in this endeavour. Through this, we can continue to adapt this technology from answering questions about the universe, to answering questions about the body, and how radiation affects it.

Much of this work will not stop with this thesis, but will continue to be relevant for both existing facilities upgrading their potential, and for new facilities incorporating these effects into their baseline designs. For those who continue these studies, I have a few questions and recommended directions.

The ability to irradiate UHDRs in depth with the spread-out Bragg peak requires rapid transition between energy levels (≈ 3 ms). Are there methods of slow extraction that can provide changes in energy at these timescales? How can we ensure the UHDR extracted beams match the limits of conventional hadron therapy dosimetry and safety recommendations? More significantly, what is the fluctuation in the machine per shot for continuous and burst UHDR, and how can these be reduced? And finally, what is preventing operational fast (single-turn) extrac-

tion for FLASH-compatible beams, and can this fast extraction also be performed in NIMMS synchrotrons? For these reasons, the next steps for NIMMS should prioritise integration from extraction to the patient, ensuring compatible safety and dosimetry standards.

9.2 Key Results

Contribution 5A: Simulations can replicate the double-peaked BTF tune spectrum.

A BTF spectrum with $S = 0$ displays a Gaussian tune distribution, and increasing S increases tune depletion in the spectrum increases, in agreement with measurement.

FFT transformations of the isocentre agrees with the BTF magnitude-phase calculation, and also show additional frequency responses in the spectrum.

Extent of study: Beam was simulated exactly on-orbit, whereas BPM signals suggest the operational beam is offset. Maptrack tracking time limited number of excited frequencies, reducing resolution and range. Each frequency was applied individually, rather than sweeping continuously, due to high cumulative losses.

Next steps: Further simulations performed in Xsuite, published in [109] which confirm results reported here, via a similar model.

Contribution 5B: Single-particle tunes can reproduce the multi-particle isocentre signal

NAFF single particle tunes showed characteristic distributions for each excitation frequency. Clear tune beating observed in Fig. 5.7, caused oscillations in tune depletion as a function of time. A low-bandwidth peak for each excitation frequency traces out a rough 2-peak signal.

Extent of study: A single value of tune does not accurately represent time-varying amplitude and frequency effects.

Next steps: Alternative calculations of accurate instantaneous tune calculated over <10 turns could provide beneficial.

Contribution 6A: Strong octupoles applied at slow extraction conditions in the PS will cause behaviour synonymous with island trapping.

Measurement and simulation have good agreement at 2 GeV (Fig. 6.7). At 24 GeV they experience similar distribution but with a significant displacement which is equivalent to $k_3 = 30 \text{ m}^{-3}$, due to the inherent PFW strengths (Fig. 6.6).

Original Contribution: Very few, if any, MDs have explored island formation at the third-

order resonance for the PS at maximum energy. At these energies, effects from space-charge are reduced, however the complexities of the machines inherent multipolar components become problematic.

Extent of study: Islands were not observed directly due to the low intensity in the machine. Ramping of the octupoles were non-adiabatic in producing the islands, so one cannot comment on the particle flow from the stable triangle to the islands. Simulation statistics were low compared to the other simulations performed in the thesis.

Next steps: Two further MDs will be continued in the SPS, which has more reliable inherent multipole behaviour.

Contribution 6B: Fine-tuned octupole strength applied at slow extraction conditions in the PS can reduce losses at the septum and improve extraction efficiency.

Octupoles can shift the extracted beam distribution sufficiently to reduce local losses at SEH23 (15 %) and SMH57 (45 %) in exchange for marginally higher global losses ([Fig. 6.14](#)).

First identification of the parabolic relation between octupole strength and ring BLM measurements. It was observed that the inherent multipole behaviour in the machine is oriented towards benefiting from amplitude detuning (i.e. near the parabola minimum).

Extent of study: A full re-optimisation of non-PPM septa orientation is required to maximize the geometry to suit the distribution. An improvement in extraction efficiency was not observed, as no optimisation was applied at the F61 transfer line.

Next steps: Either during commissioning or during a dedicated MD, a steering optimisation algorithm should be performed on the SEH23 position, angle and kick for strong octupoles and slight sextupole increase. The same should be applied at SMH57 and SMH61 and the F61 line. A dedicated study would also allow for more use of the BTV57 to track extraction distribution more precisely. For both PS studies, simulations require a more accurate model of the inherent PS octupole strength at 24 GeV.

Contribution 7A: High emittance beams and faster extraction rates can be extracted with existing optics/hardware

Emittance becomes an issue when the initial beam lies outside of the dynamic aperture of the initial stable triangle. For betatron core extraction, there is no strong dependence on amplitude, therefore large increases in emittance (up to $6\times$), do not experience significant disadvantages. To extract via RF-KO at higher emittances, optics adjustments are necessary, which causes

low-amplitude particles to be further from the resonant stop-band width. $6\times$ higher emittance required a $3\times$ stronger kick from the exciter to extract the entire beam.

Increasing extraction rate to be within 100 ms for the PIMMS set-up required up to 12 μ rad AM RF-KO kick. For 400 MeV/u, this was equivalent to a 4 kV signal, compared to ≈ 300 V usually applied. Such voltage would require a dedicated hardware design of the exciter.

Extent of study: This extraction applies a fixed setting of FM - with a Gaussian noise bandwidth around a single sinusoidal frequency, and AM - described via a set exponential equation, with 8 free parameters.

It not clear if the either results apply operationally for conventional extraction, as it is not common for the entire beam to be extracted within one cycle, and therefore will be less dependent on higher amplitude kick to provide the sufficient statistics towards the end of the spill. UHDR extraction would want to benefit from the whole beam to maximise intensity, so this is an additional operational difference that should be factored compared to conventional extraction.

Next Steps: Improving the efficiency of the FM signal reduces the required strength of kick, and having an AM feedback loop means the system can auto-adjust to provide only the necessary kick. Both of these should be applied to provide a more realistic expected kick and therefore voltage for the RF-KO exciter.

Contribution 7B: UHDR extraction can be simulated from HeLICS.

Extraction elements were located in the available spaces of the three straight-sections. Extraction solutions were found for two working points, 2.6 (in [Sec. B.1.1](#)) and 2.3. Solutions were compared for quadrupole-driven and RF-KO extraction. The PID controller for the RF-KO kick is an advancement to the previous hand-optimisation of exponential functions. Four simulations were performed: quadrupole-driven and RF-KO, for both continuous spills and burst-spills of the same intensity. For maximum energy helium ions, this was equivalent to 60 ms of spill, or ten lots of 3 ms bursts, with 3 ms gaps between them.

Extent of study: Quadrupole-driven extraction required ppf-Gaussian distribution for a uniform spill due to amplitude effects dominating small tune spreads. Proper control of the PID is limited without a tuning optimiser, producing undesirable spills.

Next steps: To determine if the linear quadrupole ramp of $0.27 \text{ T m}^{-1} \text{ s}^{-1}$ is under current hardware limits. To evolve the PID controller for simpler user usage, via an optimisation algorithm. To apply advanced FM techniques to aim for lower AM kicks.

Contribution 8: Slow extraction can be performed on scaling fixed-field accelerators.

FFA resonance crossing studies have been performed before, but this study is the first investigation of slow extraction from fixed field accelerators at the third-order resonance.

A suitable working point was explored, which required an additional resonant sextupole to the FFA. An extraction simulation was performed with RF-KO (Fig. 8.7).

Extent of study: The simulation was performed without analysis of spill quality, without physical geometry of the extraction septa, and simplification assuming a constant FFA extraction orbit.

Next steps: The FFA lattice should be redesigned with longer straight sections to fit in the injection and extraction hardware. An extraction orbit should be chosen, and the beam should be able to reach this orbit independent of its energy. The chromatic effects from the additional sextupole should be studied. The ADTS should be measured using the tools in Sec. B.1.1. The beam distortion from ES to MS should be tracked. PDE extraction and other FFA-related extraction concepts should be investigated.

Thank you for those who engaged with this journey - I hope that the content and results were enjoyable and digestible. Now please excuse me - as I have some muons to go and cool.

Bibliography

- [109] R. Taylor E.C. Cortes Garcia P. Niedermayer. “Interpretation of the horizontal beam response near the third integer resonance”. 2024.
- [141] G Bisoffi et al. “Energy comparison of room temperature and superconducting synchrotrons for hadron therapy”. In: *Journal of Physics: Conference Series* 2420.1 (Jan. 2023), p. 012109. DOI: 10.1088/1742-6596/2420/1/012109.

A

Appendix A: Simulation Models

A.1 MADX Momentum

The sixth coordinate of particle dimensions, representing the longitudinal momentum, has two standards of definition, represented by **Eq. A.1** and **Eq. A.2**. I.e. it is either the difference in total energy, normalised by the reference momentum, or the difference in momentum normalised by the reference momentum.

$$p_t = \frac{E - E_0}{P_0} \quad (\text{A.1})$$

$$\delta_p = \frac{P - P_0}{P_0} \quad (\text{A.2})$$

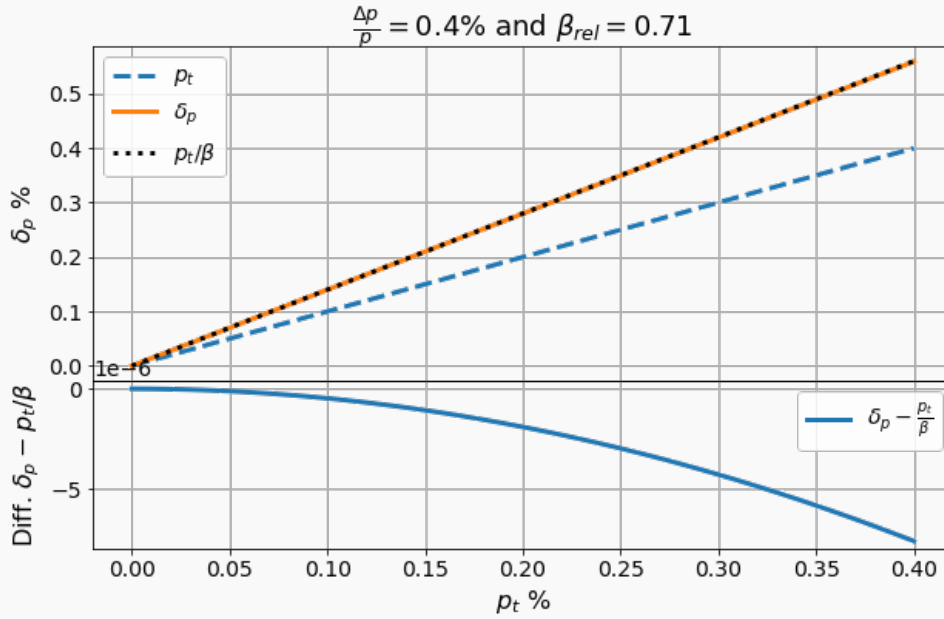
The equation relating these two definitions is derived from the MADX manual, Chapter 39 [97], the conclusion of which is an exact relation, **Eq. A.3**, which is most commonly in the accelerator community represented by a small-momentum approximation, of **Eq. A.4**. This approximation is valid when either $p_t \gg p_t^2$, or when $\beta_{\text{rel}} \approx 1$.

$$\delta_p = \sqrt{p_t^2 + 2\frac{p_t}{\beta_0} + 1} - 1 \quad (\text{A.3})$$

$$p_t \approx \beta \delta_p \quad (\text{A.4})$$

Neither of these approximations are obvious in the case of a PIMMS slow extracted beam for 400 MeV u^{-1} carbon, as $\frac{\Delta p}{p} = 0.4\%$ and $\beta_{rel} = 0.71$. **Fig. A.1** shows the comparison of the value of δ_p compared to the approximation of p_t/β_{rel} . The errors on this approximation increase quadratically, but within the maximum expected momentum spread and relativistic beta, this difference is only up to 7×10^{-6} .

Figure A.1.: Difference between δ_p and p_t representation of momentum. Difference in the approximation of $\delta_p = p_t/\beta$.



It is important to consider this difference of β_{rel} for every calculation within MADX involving δ_p , including in dispersion and in chromaticity. The treatment of δ_p is the same in MADX-PTC, unless the PTC_SetSwitch, Time=False flag is used, which means the final particle coordinate is δ_p instead of p_t .

A.2 Code Benchmarking

Grids of coordinates in (x, px) , (y, py) and (x, p_t) are compared at the PIMMS electrostatic septum for Xsuite vs MADX-PTC (**Fig. A.2**), Xsuite vs maptrack (**Fig. A.3**) and MADX-PTC vs maptrack (**Fig. A.4**). The top row of each figure shows the grid of particles in each plane. The middle and bottom rows show the error on one coordinate as a function of its initial value.

As MADX-PTC and maptrack are for the same flag settings **Lst. A.1** tracked for the same order, they show stronger agreement compared to Xsuite. All codes have the smallest error at the closed-orbit, and increase as a function of amplitude. The difference in momenta is due to the effect explained in **Sec. A.1**.

Listing A.1: PTC-Track Flags

```
1   PTC_create_universe;  
2   ptc_create_layout,model=2,method=6,nst=5, exact;  
3   PTC_TWISS,  icase=5, no=4;  
4   PTC_START, x=0, px=0, y=0, py=0, t=0, pt=0;  
5   PTC_OBSERVE, place=es_marker;  
6   PTC_TRACK, turns=100, icase=5, file=".txt", ONETABLE=True;  
7   PTC_TRACK_END; PTC_END;
```

Figure A.2.: 1-Turn grid track comparing XSuite & PTC

Grid of particles with a spread in horizontal phase-space (left), vertical phase-space (middle) and X-PT (right). (Top) difference in grid tracking between XSuite & PTC (middle) error in first coordinate as per its initial value (bottom) error in second coordinate as per its initial value.

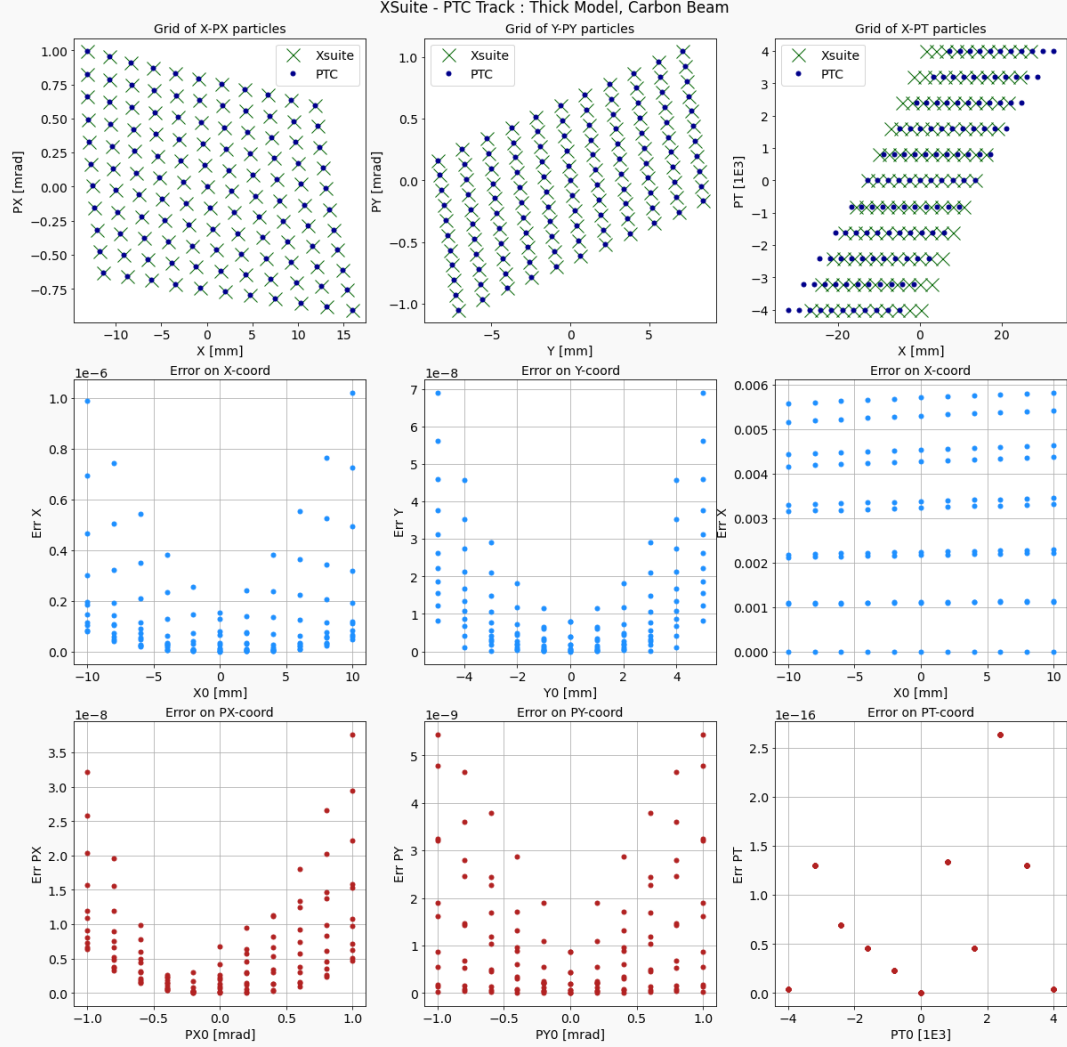


Figure A.3.: 1-Turn grid track comparing XSuite & maptrack

Grid of particles with a spread in horizontal phase-space (left), vertical phase-space (middle) and X-PT (right). (Top) difference in grid tracking between XSuite & maptrack (middle) error in first coordinate as per its initial value (bottom) error in second coordinate as per its initial value.

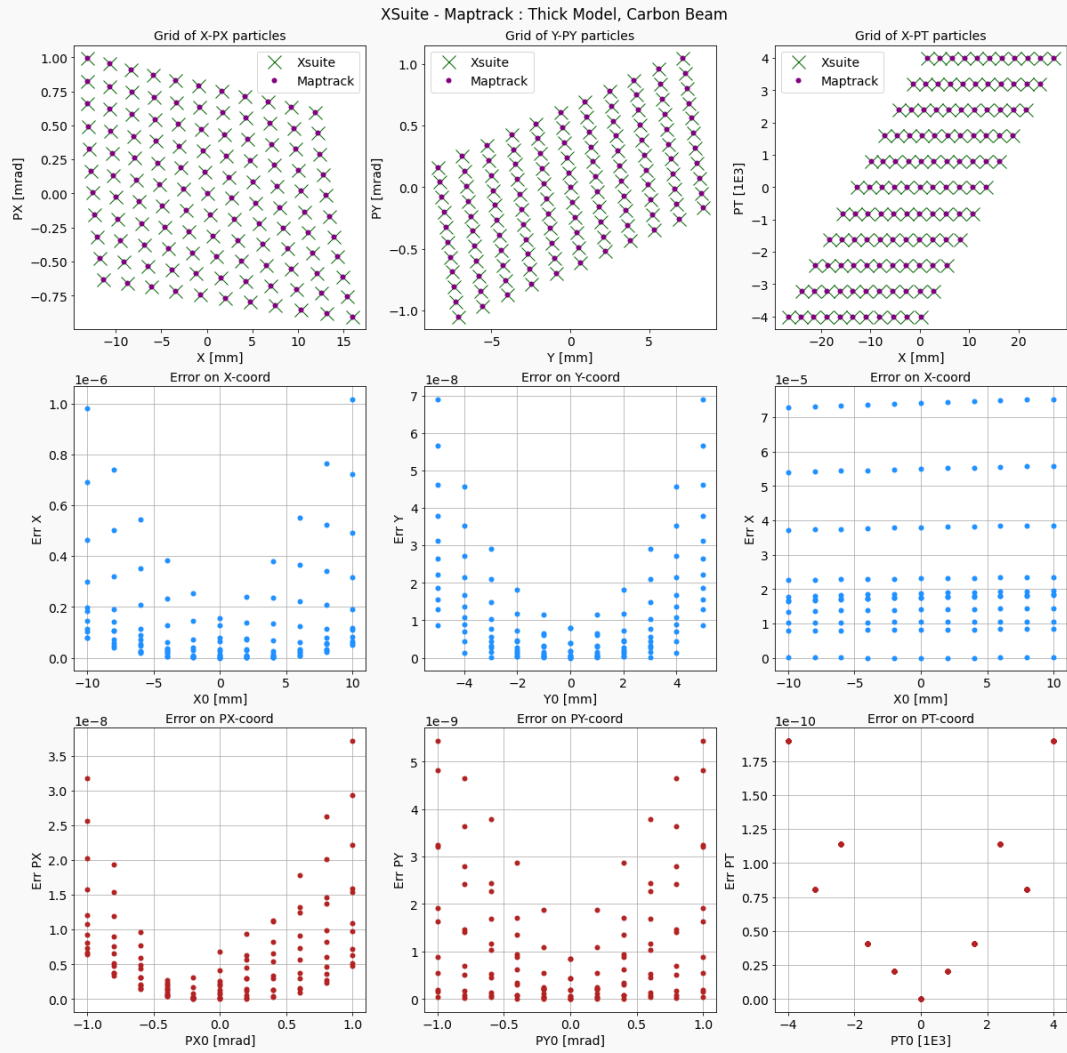
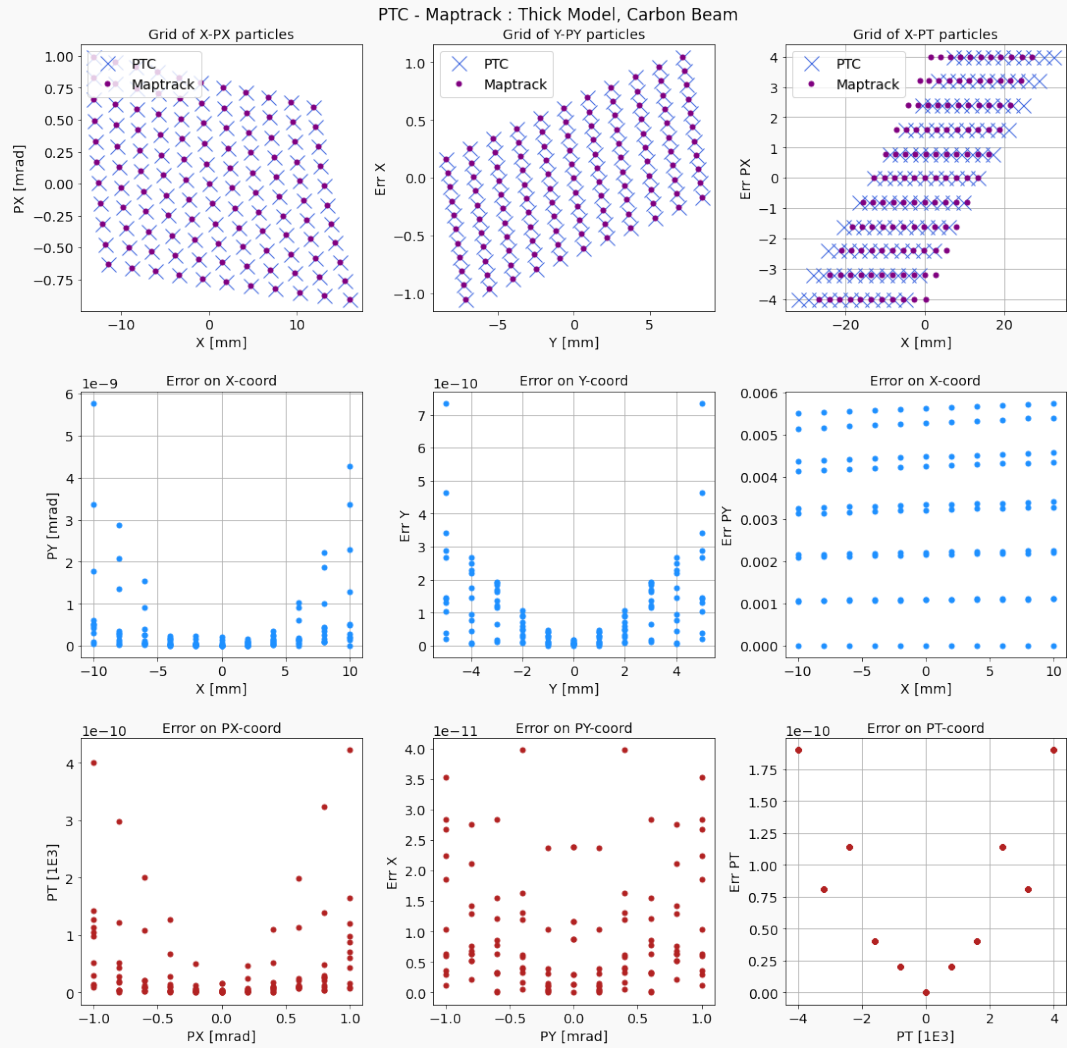


Figure A.4.: 1-Turn grid track comparing PTC & maptrack

Grid of particles with a spread in horizontal phase-space (left), vertical phase-space (middle) and X-PT (right). (Top) difference in grid tracking between PTC & maptrack (middle) error in first coordinate as per its initial value (bottom) error in second coordinate as per its initial value.

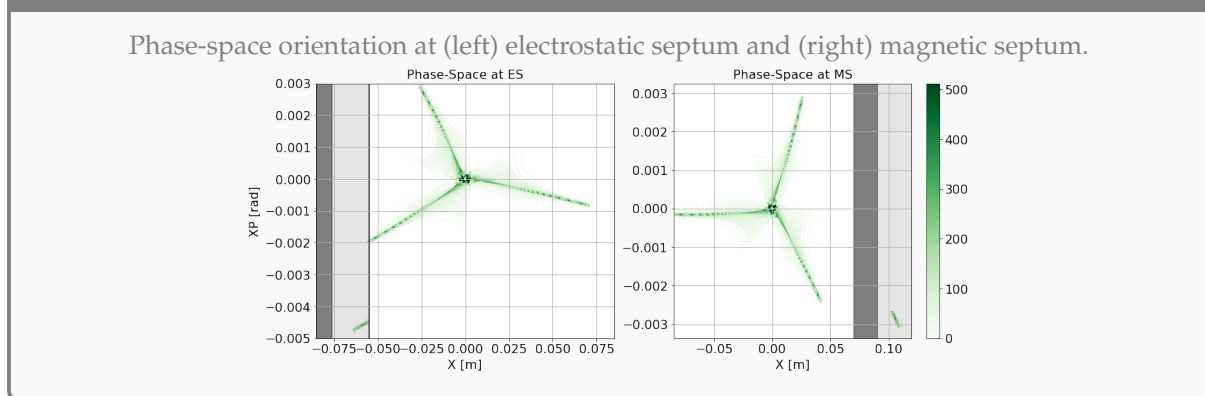


Appendix B: HeLICS - Extra Content

B.1 Initial lattice schematic

The original HeLICS lattice was for a 2.6 horizontal tune design, without defocusing quadrupoles. An extraction schematic was established for this layout, and is represented in **Fig. B.1** and **Fig. B.2**. Upon reflection, the layout is challenging at the MS, as a positive kick would be provided to an extracted beam with negative angle, which would steer it towards the direction of the septum anode. Or a negative kick would be provided, extracting from the inside of the synchrotron.

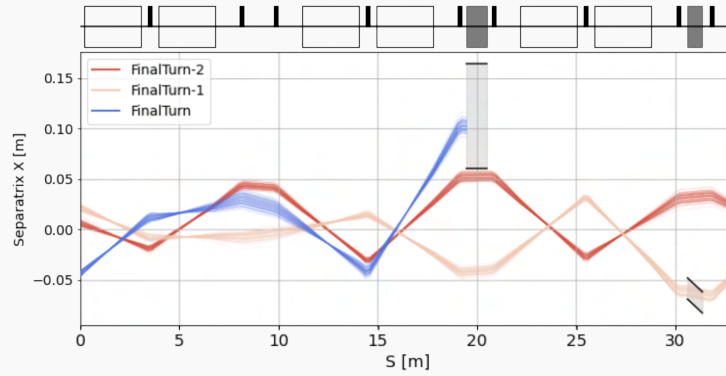
Figure B.1.: Separatrix and extracted beam distribution the two septa for $Q_x = 2.6$



One advantage of this layout is that the MS is positioned in the second straight-section, with the ES after it. This has the benefit that a small kick at the ES propagates for twice as long as the

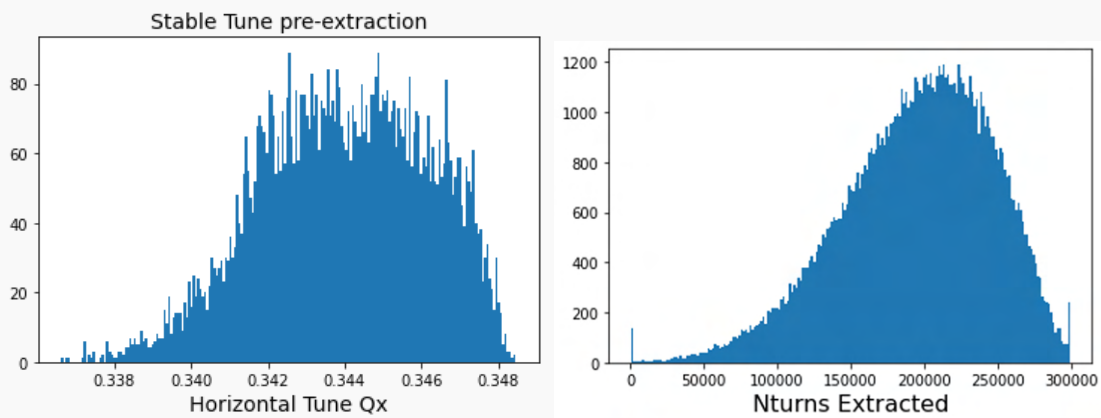
current schematic, so gives a large effect at the MS. This contrasts with the current extraction arrangement where -2.5 mrad is insufficient to reach the field region of the MS.

Figure B.2.: Separatrix trajectory of the X-position throughout HeLICS for $Q_x = 2.6$. Final two turns (red, light red) of the particles before their kick at the ES (blue).



When applying a quadrupole-ramp to extract from this lattice, difficulties were found in acquiring uniform spill distributions. In particular, it was observed that uniform momentum distributions applied in a stable beam close to the resonance were exhibiting a non-uniform tune spread, even at natural chromaticities. An example of such a distribution is in Fig. B.3 (left). It was assumed that this distribution was due to Amplitude Dependent Tune Spread (ADTS). When simulating a linear tune sweep through the 2.6 resonance, the corresponding tune sweep (right) was found to mirror this distribution. To control the machine chromaticity,

Figure B.3.: Comparison of the initial tune distribution prior to simulation, and the resulting spill after a linear quadrupole-driven ramp.



three chromatic sextupoles were positioned in the dispersive regions in-between the dipole bends, and which further emphasized this effect.

An investigation was launched to determine the extent and cause of this effect. In the end it was concluded that this effect was initiated from the linear machine, exacerbated by the single resonant sextupole. There is a strong possibility that the effects were worsened by the working-point chosen, which was in close proximity to a coupling resonance. Given the lack of defocusing quadrupoles, it would not have been possible to move the vertical tune of this lattice. The effect was dramatically reduced by moving to the new optimised lattice at a 2.3 working point.

Researchers at GSI designing the SIS-100 ring have experienced similar non-linear detuning effects [142]. Whilst it is true that amplitude detuning occurs the closer one is to the third order resonance, additional studies performed by H. HUTTUNEN imply that the ADTS emerges directly from the lattice itself, when in a working point away from resonances [121]. This effect is further apparent when considering longitudinal dynamics and space-charge effects.

B.1.1 Analytical Investigation

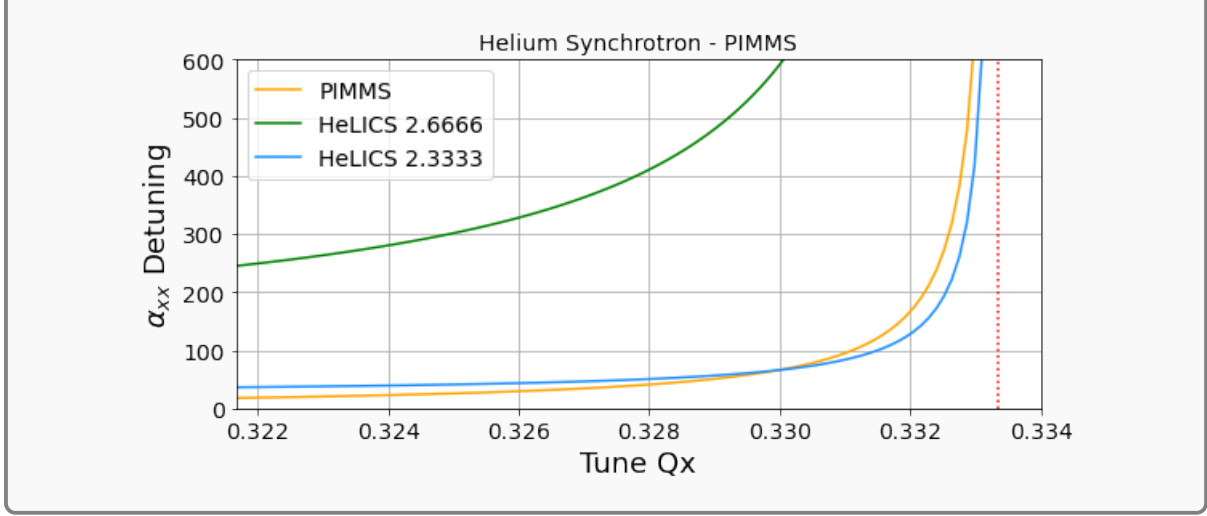
S. Y. Lee (Chapter 7.3: Nonlinear Detuning from Sextupoles and Octupoles) defines the horizontal amplitude detuning α_{xx} resulting from a concatenation of sextupoles in a ring in Eq. 2.30. The equation requires a summation over all combinations of sextupole pairs, where the indices i, j connotes any given sextupole pair.

With chromatic sextupoles applied to each lattice, the analytical expression is calculated for the initial HeLICS lattice (green), the updated HeLICS lattice of Sec. 7.2 (blue), and PIMMS (orange) for comparison. The results are represented in Fig. B.4, which shows the three curves asymptotically tending towards infinity when approaching the third-order resonance.

This approach to quantifying the detuning effect is problematic when only one sextupole is present in the machine, as the ATDS is theoretically zero. Despite that, ATDS was still observed with just the resonant sextupole present in the zero-dispersive straight-section.

To quantify this effect further, tracking was performed with 50 particles initiated with a linear dependence on x , and zero in all other coordinates. These particles were tracked for 1024 turns, whereafter their tune was calculated via pyNAFF. Fig. B.5 expresses this x_0 vs Q_x relation as a function of the initial $\frac{\Delta p}{p}$ of the beam. The solid line represents natural chromaticity, and the

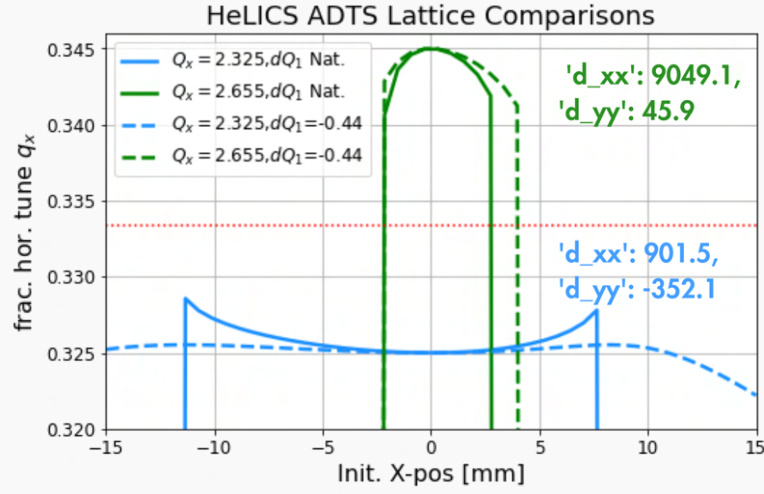
Figure B.4.: Analytical expression of horizontal detuning α_{xx} for three different machine extraction settings as function of horizontal tune tending towards the $1/3$ resonance [39]



dashed line shows chromaticity matched to a small negative value (-0.44). When the NAFF is unable to calculate the tune, due to an unstable or extracted beam, it is assigned to zero. For the initial lattice at 2.3, the stable region is as small as 5 mm radius. Within that region, a parabolic relationship with respect to detuning is observed. If there was purely an octupole relation, this would be expected to be linear only. This relation is a large indicator that higher order non-linear dynamics are also in effect. The values of d_{xx} and d_{yy} on the figure are calculated from Xsuite's *ActionMeasAmplDet* function. It is possible to match multipole functions to minimise this value. Octupole strengths were added to the lattice to try to minimize the effect, however it would never fully counteract the higher order effects.

As mentioned, the 2.6 initial lattice (green) working point is relatively close to some third-order coupled resonances, shown in Fig. B.6 (top). It is not trivial to change the vertical tune further from this point. The corresponding tune distribution can be seen in Fig. B.6 (bottom). It is clear that for the same initial momentum spread, the initial lattice (green) has a detuning effect compared to the more uniform updated lattice (blue). Both of the Q_x, Q_y tune distributions are rectangular. The shift in optics only means that the ADTS is suppressed sufficiently to perform the slow extraction study. For further lattice tracking and acceleration from injection to extraction, this effect may continue to be significant.

Figure B.5.: Tune calculation of single-particles with a initial X-spread over 1024 turns. Compare for the 2.3 (blue) and 2.6 (green) settings, at natural (solid) and low (dashed) chromaticity.



B.2 RF-KO Controller Optimisation

The HeLICS RF-KO simulation had a PID controller developed to optimise the spill. These are used to simulate a number of particles N_p over a series of turns, N_T . The controller has three key parameters, K_p , K_i and K_d , which define the proportional, integral and derivative response to the error. There are three further parameters required for the simulation: *window length*, which defines the number of turns the extracted particles are measured over, *setpoint*, which is $\frac{N_p}{N_T}$ the desired number of particles extracted per turn, and *limit*, which is the initial amplitude kick in [rad]. There are maximum and minimum constraints on *limit* to prevent exponential-trending kicks. An optional parameter is *turn waist*, before which the kicks are reducing, after which the kicks are increasing (to follow the behaviour of the bathtub function Eq. 7.3).

The error is calculated from the difference between the setpoint and the average particle extraction per turn over *window length*. Every window length, P, I and D are calculated depending on the error as the following:

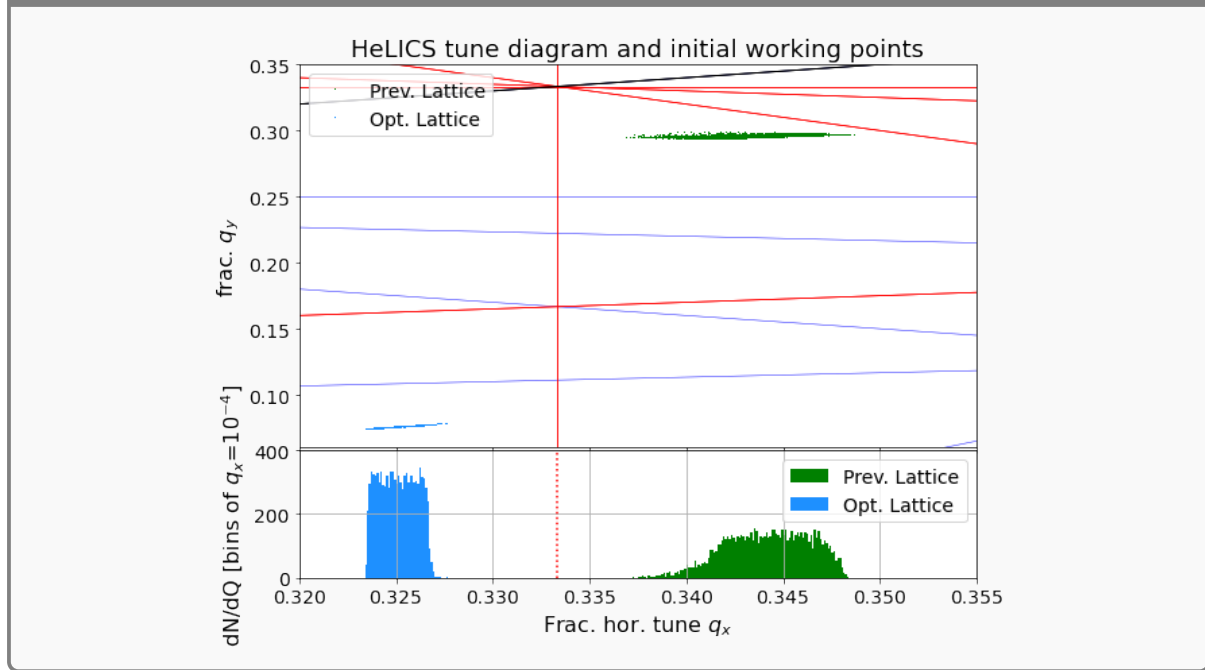
Listing B.1: PID Definitions

```

1   P = Kp * error;
2   I = RFK0FeedbackData_get_I(e1) + Ki*error*window_length;

```

Figure B.6.: Working Points and tune distribution for 2.6 (green) and 2.3 (blue) lattices



3

```
D = Kd * prev_err;
```

Then $P + I + D$ is added to the previous value of limit. The user defines a FM array of N_T turns with maximum amplitude of -1 to 1. Every turn the current limit is multiplied by the FM array value at that turn.

For burst extraction, an additional parameter is added t_{burst} which defines that every t_{burst} the FM kick and setpoint remains at 0, and the limit is set to the previous limit.

When the simulation is performed, a script is used to save the error, limit, kick and number of extracted particles each turn.

The list of parameters used for the final results of Fig. 7.17 and are in Tab. B.1. The parameters are the same for Fig. 7.20, but with a t_{burst} of 15 000.

B.2.1 Beam Physicist's Guide to Hand-Tuning PIDs

PID controllers work most optimally when applied to a solved system with a given equation of dynamical behaviour. As RF-KO is a stochastic process, finding parameters that maximize the smoothness of spill require an additional optimiser. Without this, the three initial controller parameters need to be hand-optimised. When doing so, it is usual to gain an intuition to the

Table B.1.: RF-KO Parameters used in **Ch. 7**

K_p	1.5×10^{-5}
K_i	5×10^{-9}
K_d	1.5×10^{-6}
N_p	1×10^5
N_T	3×10^5
Window length	300
Setpoint	0.3
Limit	5×10^{-7}
Max. limit	10^{-2}
Min. limit	10^{-8}

behaviour of such a system.

PID controllers feature a rise time, which is the time for the output to tend from zero to the setpoint. The controller will likely overshoot beyond the setpoint and then oscillate around it. Ideally the oscillations will dampen until it is within the desired errors.

Firstly, fast simulations can be used to obtain a rough estimate of the initial parameters. One should begin with first a Proportional controller ($K_i, K_d = 0$) to ensure that it just follows the setpoint, rather than overfitting or missing the setpoint. It is not necessary to simulate a large number of turns to confirm this, but the particle number should remain the same, as the controller is dependant on statistics.

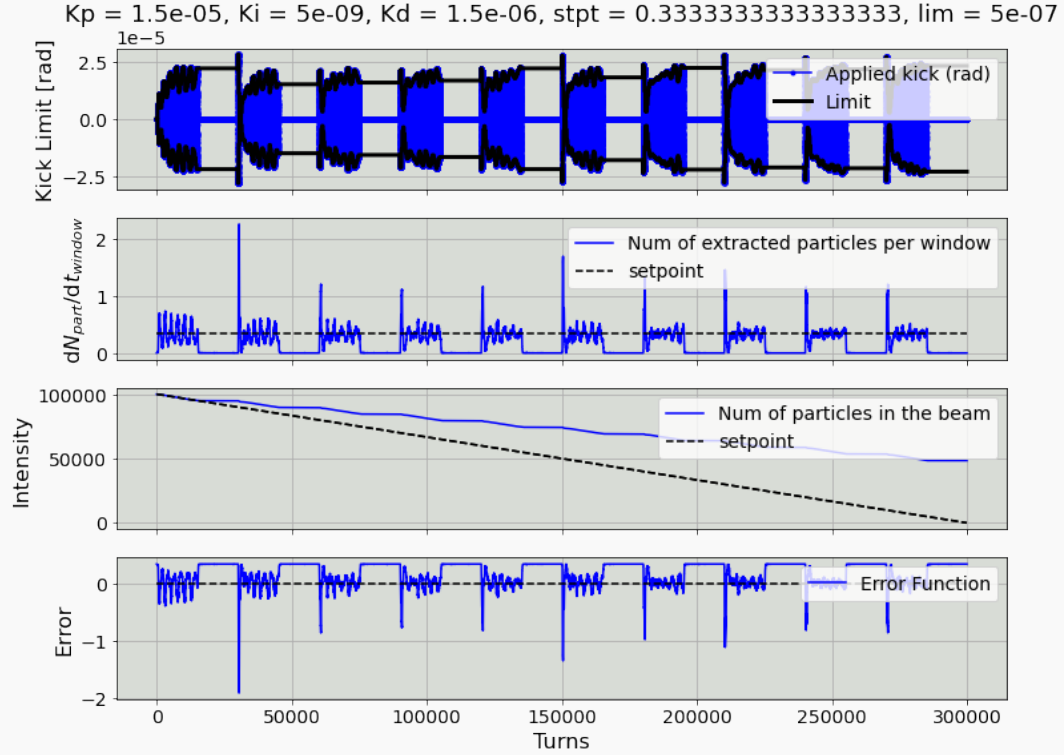
If the oscillatory response is large, one can introduce the Derivative component K_d to reduce these. As oscillations change as a function of time, it is recommended to run longer simulations to ensure the solution is truly stable. As a starting parameter, one can expect the relevant parameter to roughly corresponding to $K_d \approx \frac{K_p}{2}$.

Without the integral term, the steady-state error is not considered, and there is no settling time. The coefficient of the integral term can be initialised around $K_i \approx \frac{K_d}{2} \frac{1}{\text{window length}}$. The figures of **Fig. 7.17** and **Fig. 7.20** show increasing oscillations of time. In a typical controller this is indicative of a large K_d component, whereas in simulations this is due to from insufficient statistics available in the machine towards the end of the spill.

For the burst RF-KO simulation **Fig. 7.20**, as it is a different scenario, it should have been re-optimised to minimise the oscillations within the burst, however it was decided to keep it the same as the settings for continuous spill, for comparison purposes. Burst RF-KO simulations should have double the setpoint compared to continuous extraction, as the total extraction

Figure B.7.: Output from the RF-KO controller for burst extraction at half-setpoint

As a function of turn number, (1) the kick provided to the beam in radian (2) the number of particles extracted per time window (3) the intensity reduction of the beam in the machine (4) the difference between the setpoint and the extracted particles.



time is being halved.

It is essential that the number of simulated particles is significantly higher than the number of extracted particles. **Fig. B.7** demonstrates that the limit of the kick does not increase exponentially when twice the number of particles are simulated than extracted. This is in contrast to **Fig. 7.20**, where the AM of the final two bursts increase exponentially.



Appendix C: Proton Synchrotron

C.1 PS Methodology

Some methodological explanations of Ch. 6 are presented here.

Tune Measurements

To perform a conventional bunched BBQ (base band tune) measurement, a chirp excitation kicks the beam in both horizontal and vertical planes, the range of which is provided in the Qmeter GUI [143]. An example of such a measurement within QMeter is shown in Fig. C.1. From there, the isocenter of the beam is measured via either the Long or Short pickups. An FFT is performed on the signal and detected within a range specified in the GUI, with a defined FFT Window (i.e. Rectangular, Hann [106], etc.). The application identifies the major peak within the FFT spectra and display it as a function of time in ms in intervals set by the user.

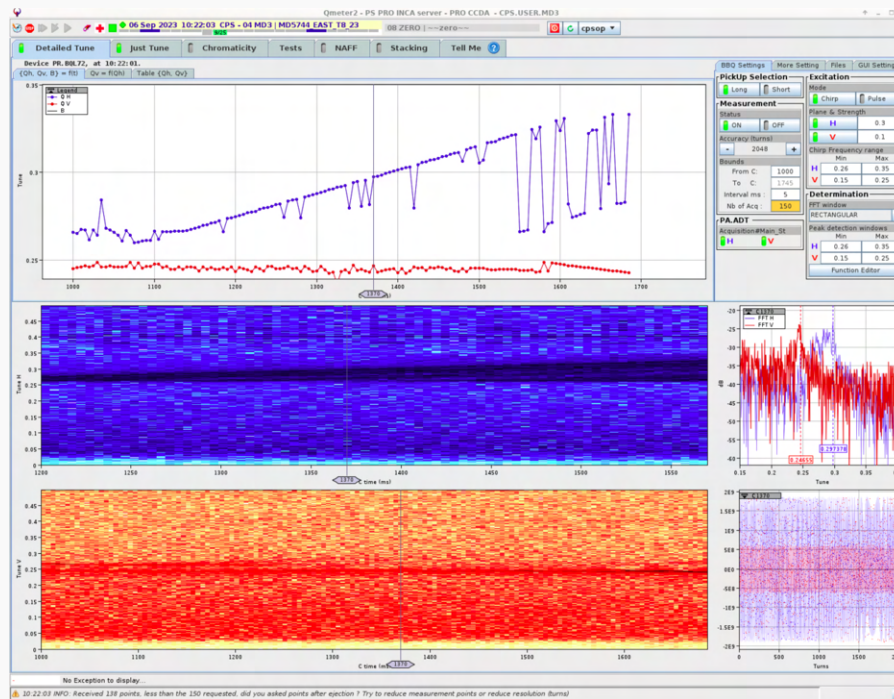
To improve upon the tune signal, connection filters can be set in the horizontal and vertical planes, more turns of data can be acquired, and the number of acquisitions can be increased. By fitting the detection windows and chirp range to be constrained around the measurement, the signal improves, but this does not provide flexibility if the tune is expected to move, i.e. for a chromaticity measurement.

With the help of T. PREBIBAJ, a technique was established to perform Qmeter BBQ measurements for a coasting (unbunched) beam. This can be achieved by having large Acquisition

Gains in the vertical and horizontal plane up to ≈ 60 dB, increasing the excitation strength and turning off filters. Users should confirm that the raw data of the pickup, shown in **Fig. C.1** bottom right plot, is not saturated (i.e. maximised at 2×10^9 arb. units).

It is easiest to measure when the beam is not experiencing losses - i.e. not extraction conditions - so either with the XSE sextupole off, the beam moved away from the resonance via the QSE, or both. **Fig. C.1** (top) shows the linear increase in the beam tune, which becomes unreliable once it reaches the resonance at 0.3. The tune spread of the coasting beam can be seen in the 2D histogram (left middle), where it shows the spread of the beam increasing as it tends towards the resonance.

Figure C.1.: Screenshot of the QMeter application showing the measurement of de-bunched beam



Chromaticity Measurements

Octupoles alter the machine's non-linear chromaticity. The chromaticity is measured by taking the tune measurement at every time-interval for a range of momenta. In the PS, this is performed by changing the frequency of the RF cavities, **Fig. C.2**. This changes the revolution frequency of the particles, and from the momentum compaction factor η , the momentum distribution of the beam will change. Due to dispersion, this affects the orbit of the beam, which

The diagram shows a feedback control loop. It starts with a block labeled f_{RF} , which is connected to a block labeled $\frac{\Delta f}{f_{rev}}$. This block is then connected to a block labeled $\frac{\Delta p}{p}$ via a gain block $\frac{1}{\eta}$. Finally, the $\frac{\Delta p}{p}$ block is connected to a block labeled x via a gain block D_x .

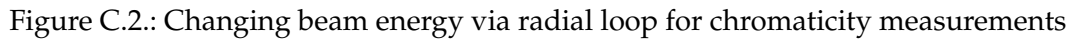
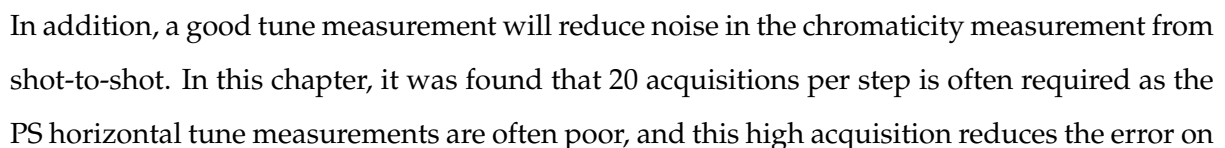


Figure C.3.: Screenshot of the QMeter application showing the measurement of non-linear chromaticity for 20 data points per momentum.



the polynomial fit. **Fig. C.3** shows the 220 datapoints which make up the chromaticity measurement, as there are 20 acquisitions for 11 steps of the radial loop. The linear and non-linear polynomial fits are shown by the straight and curved cyan and yellow lines in horizontal and vertical planes.

Chromaticity measurements required a bunched beam, otherwise it is unknown what the momentum shift of the beam is.

YASP

YASP (Yet Another Steering Programme) is a steering algorithm which can correct the closed orbit of the beam [144]. For the 24 GeV beam, this is corrected via the DHZ high energy correctors. In this MD, YASP was applied to try to reduce the global losses once the septum losses had been minimized. In particular, large sextupole strength increases the spiral step which increases losses on the injection septa SMH41. Whilst YASP was successfully able to reduce losses at BLM41, it would increase losses at other regions of small aperture.

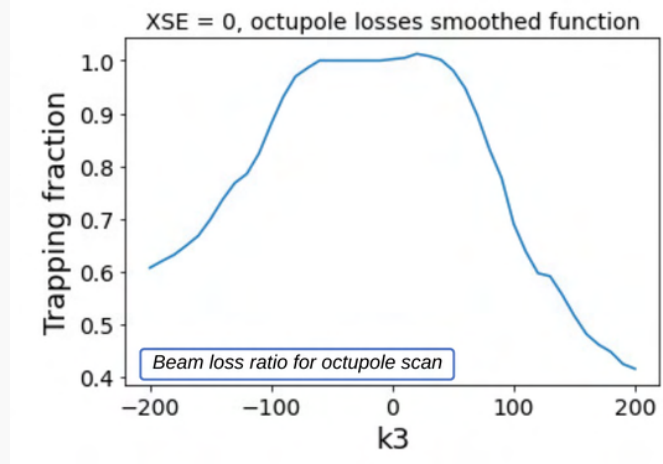
C.2 Octupole Trapping Dynamics

The Beam Current Transformer (BCT) was used to observe if strong octupoles caused a trapping effect in the PS. **Fig. 6.3** shows two BCT signals - the left plot has the resonant sextupole active and experiences complete loss of the beam intensity. The right plot has neither the sextupole nor octupole active, and has a constant beam intensity. The ratio of the average initial current (from the white line) and the final current (white dot at 1400 ms) is used to express the beam trapping ratio.

As mentioned in **Ch. 6**, at the injection energy of 2 GeV, the space-charge becomes significant enough that losses are inherent in the machine, even with no resonant sextupole, and these losses increase as a function of ONO octupole strength. **Fig. C.4** shows this loss relation as a function of the BCT ratio. The smoothed version of this function was subtracted from each datapoint in **Fig. 6.7**.

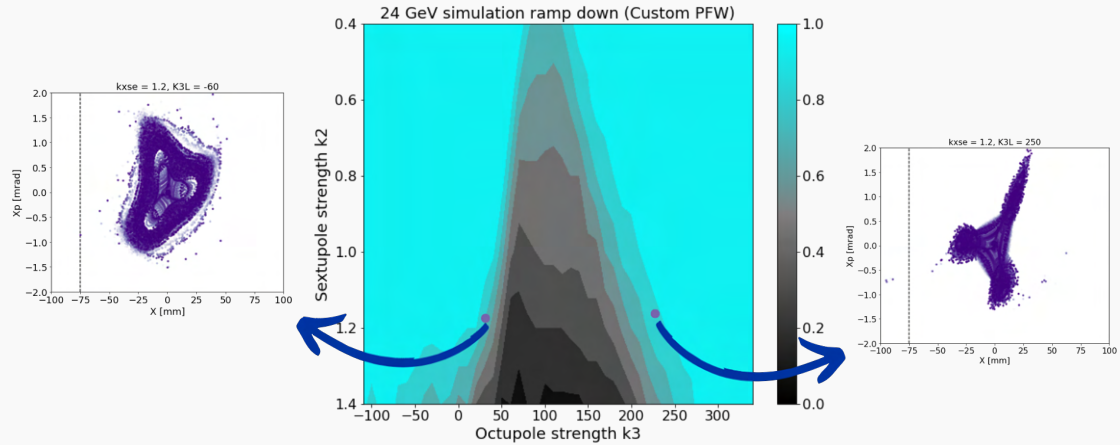
When looking at the octupole Kobayashi-Hamiltonian of **Eq. 2.32** and **Fig. 2.6**, there are three symmetries which affect the orientation of the phase-space distribution. The first is the polarity of the virtual octupole strength S_{oct} . **Fig. C.5** shows a contour plot from a series of simulations

Figure C.4.: BCT trapping ratio as a function of ONO strength at 2 GeV (no XSE).



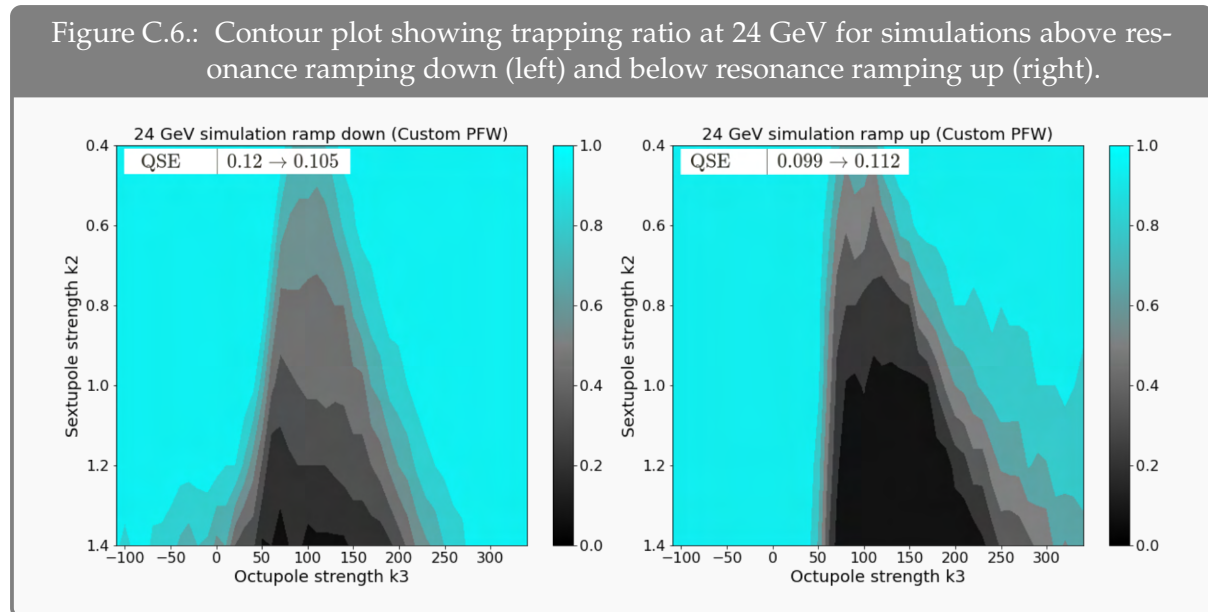
in changing multipole strengths. Two datapoints are taken, both at $XSEk_2 = 1.2$, one from the left side of the trapping triangle, and one from the right side.

Figure C.5.: Two datapoints within the simulated trapping triangle, showing their phase-space distribution for octupole trapping and inverse-trapping.



The simulation with relative positive polarity experienced island formation in phase-space, as expected. The simulation with relative negative polarity demonstrates a depletion of the three islands, with the particle contour lines tracing the non-linear behaviour outside the island distribution. Fully trapped islands will lose less particles compared to when they are trapped outside the islands, hence the increase in losses on the left. It was from this asymmetry of

the trapping triangle that one could observe a mistaken polarity difference in the operational ONO value. The offset of the triangle is due to the MADX PFW strengths. This simulation was performed with an initial horizontal tune above the 6.3 resonance.



When one changes the polarity of ϵ , the modified tune distance, then this effect is reversed. This is clear from Fig. C.6, where the difference in the triangle from starting above resonance (left) and below resonance (right) is shown. The side of the triangle that experiences more losses is on the left. If the simulations or measurement were continued into negative sextupole k_2 strength then this trend would be mirrored, with the Hamiltonian flipped 180° .

C.3 Pole-Faced Windings

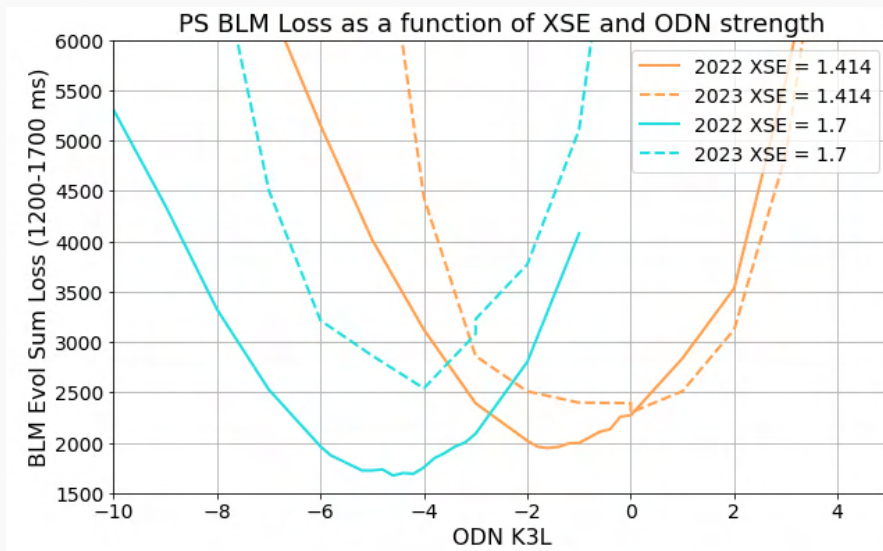
The PS Main Units (MU) have extra windings mounted on their poles, for extra control over the quadrupole, sextupole and octupole components. These Pole-Faced Windings (PFWs) are split into five circuits: Wide and narrow windings on both the focusing (WFW, WFN) and defocusing (WDW, WDN) parts of the poles, and a figure-of-eight loop (W8F) which crosses between focusing and defocusing parts [145].

The effect of the PFWs across all MD studies at the PS involving octupoles are substantial. Whilst helpful in controlling higher-order fields in the machine, these windings are highly non-linear, with all five variables having an effect on horizontal and vertical tune and chromaticity. They are studied sufficiently to understand first-order chromaticity, but they also

introduce a constant and non-local second-order chromaticity, which results in an ambient octupolar effect throughout the ring.

In 2021, the octupole component of the PFWs was first determined by studying the offset of

Figure C.7.: Sum of ring BLMs as a function of ODN strength comparing East22 (solid) vs East23 (dashed) cycle loss relations at nominal sextupole strength (orange) and increased sextupole strength (cyan).

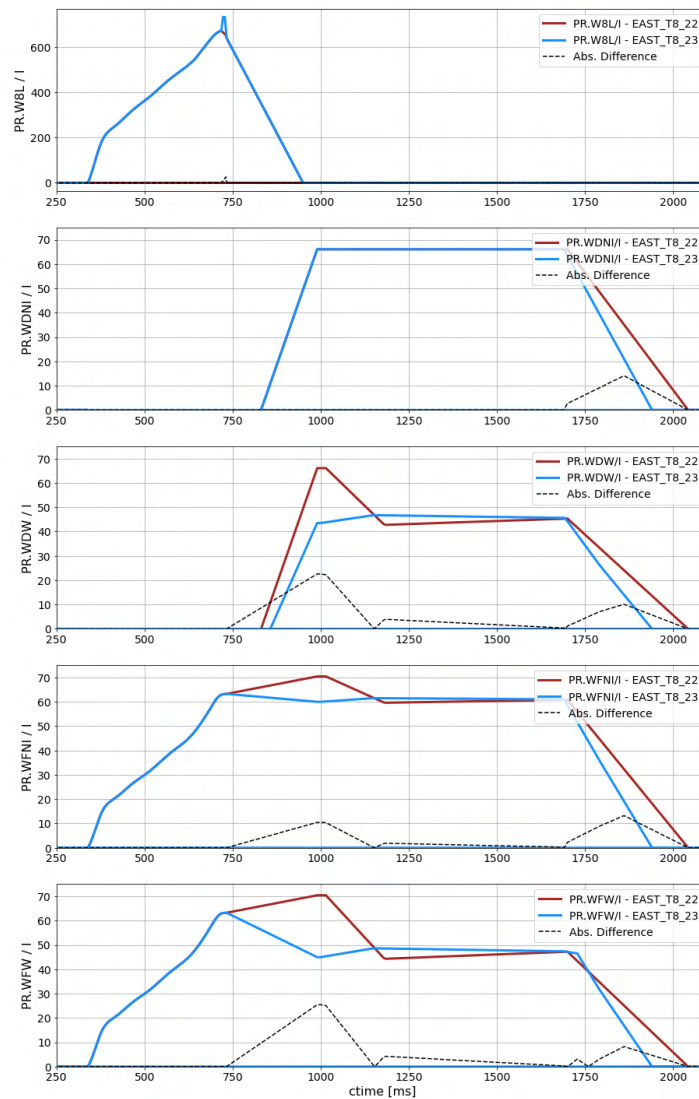


the trapping triangles at 24 GeV and 2 GeV (where the PFWs are not required for stability). In 2022 and 2023, they were analysed directly by taking a high-acquisition chromaticity scan at large radial loop, and matching this fitted chromaticity and non-linear chromaticity to $\text{PFW}(k_2)$ and $\text{PFW}(k_3)$ term in MADX. In both years, the QMeter chromaticity scan settings fitted a 4th order polynomial from -10 mm to 10 mm in steps of 2 mm, with 20 acquisitions per step. The setup used in this measurement is shown in Fig. C.3. The chromaticity measurements were performed with no octupoles active, no extraction sextupoles (XSE) active, and the QSE away from resonance ($Q_x = 6.28, Q_y = 6.2$).

The 2022 measurement demonstrates sufficient stability and accuracy to minimize fluctuations in the third-order coefficient of the chromaticity polynomial. In 2023 however, the horizontal tune measurement was well-known to be unreliable, as the FFT response had a wide and noisy peak, as in the plot of Fig. C.1 (Tune-dB plot on the right). Use of filters and chirp window ranges were used to clean the signal as much as reasonably possible.

From the description of **Ch. 6**, it is clear that the loss dependency on octupole and sextupole strengths experienced a significant difference from the East 22 cycle compared to the East 23 cycle. This difference can be seen in **Fig. C.7**. The solid lines (*East_T8_22*) show a clear improvement by increasing the sextupole strength, and the dashed lines (*East_T8_23*) have worse losses by increasing sextupole strength and also worse minimum losses. There are no significant differences at nominal settings ($k_2 = 1.414$, $k_3 = 0$).

Figure C.8.: Defined currents for each PFW windings in *East_T8_22* (red) and *East_T8_23* (blue) cycles. Difference between the two (black) shown.

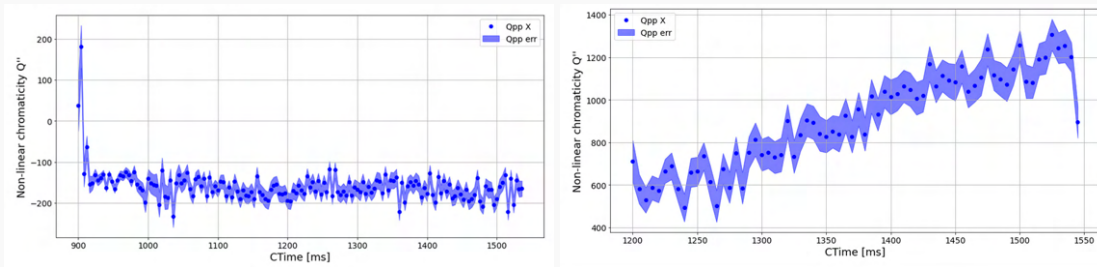


It was hypothesized at the time that the cause of this is from the difference in the PFW currents from the two cycles. **Fig. C.8** plots the LSA current functions for each winding. The

dashed line is the difference between the two values. For slow extraction, the flat-top between 1200 ms-1500 ms is significant. It is clear to see an unintentional difference in gradient at flat-top between the two cycles for WDW, WFN and WFW.

Fig. C.9 (left) shows a near constant but high variance non-linear chromaticity measurement of $Q''_x = -163 \pm 22$. On the contrary, **Fig. C.9** (right) shows a linearly increasing non-linear

Figure C.9.: Measurement of PS non-linear chromaticity as a function of time in *East_T8_22* (left) and *East_T8_23* (right)



chromaticity from $Q''_x = 600$ to 1200. This is a substantially larger value, positive instead of negative, and doubles its value from the start of extraction at 1200 ms to the end of extraction at 1500 ms.

It is not possible to measure the octupole component directly, how it can be predicted from MADX by matching the machine's non-linear chromaticity to the above values to the k_3 focusing and defocusing coefficients. The result of this is in **Fig. C.10**. In 2022 (left) there is a surprisingly good agreement between the MADX default strengths in the optics repository for East slow extraction (*pe_se_east.str* dashed line) and the measurement (solid line). Both MADX focusing and defocusing octupole coefficients are within 1 standard deviation of the mean.

By contrast, 2023 (right) has an increasing focusing strength and a decreasing defocusing strength as a function of time. Both measurements are the opposite polarity to the MADX predicted value.

The first attempt to correct for this was to keep the same PFW for the accelerating cycle of East23, but during flat-top, match by hand the PFW current to be the same as *East_22* within the range 1200 ms-1500 ms. The produced cycle was stable, and the resulting chromaticity measurement is shown in **Fig. C.11**. This result successfully shows a linear, negative non-linear chromaticity, but with a larger variance of $Q''_x = -240 \pm 152$.

Figure C.10.: Calculated PS k_3 focusing (red) and defocusing (blue) strength from the non-linear chromaticity as matched to MADX (dashed line) in *East_T8_22* (left) and *East_T8_23* (right)

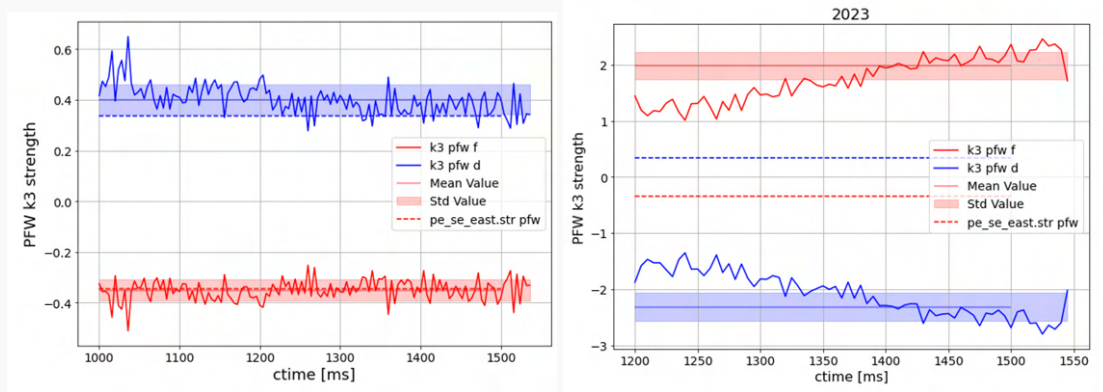
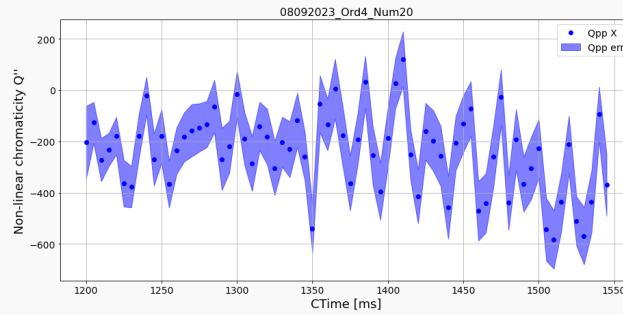


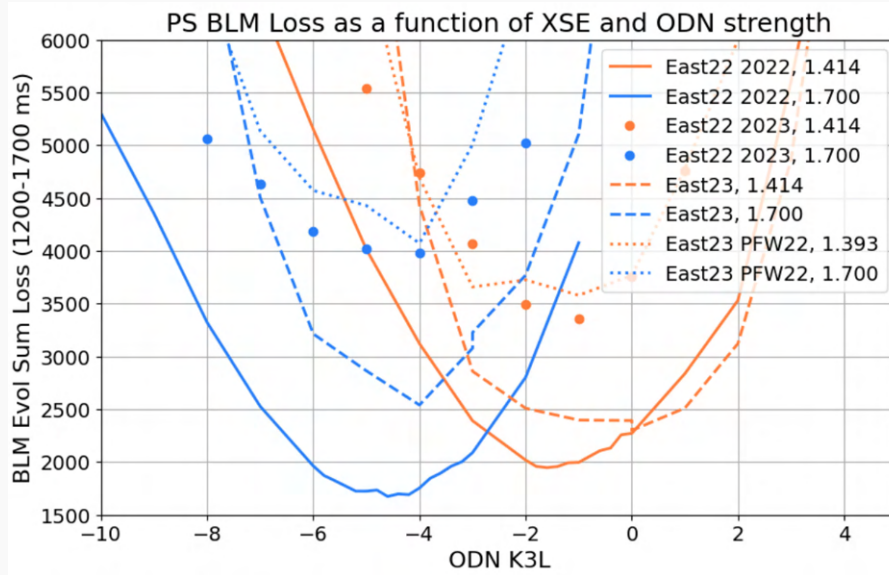
Figure C.11.: *East_T8_23* non-linear chromaticity with corrected PFW currents



The resulting octupole-loss relation for this cycle is shown by the square dotted lines of Fig. C.12 (*East23 PFW22*). This figure shows the two relations plotted in Fig. C.7. The addition of the *East_23* cycle with the PFWs of 2022 shows the worst losses observed so far, with no improvement with changing octupole strength. This is certainly because the 2023 steering performed during commissioning was optimised for the PFW settings of 2023, which have different quadrupole, sextupole and octupolar effect.

An additional attempt to correct for the large difference on PFW k_3 component was to restore the *East22* cycle in 2023, in the hopes of returning previous cycle settings. This was done with the help of M. DELRIEUX. This cycle was not stable, and a few adjustments had to be made for the extraction to perform successfully. The result of that cycle is shown by the round circles of Fig. C.12 (*East22 2023*), which is very similar in behaviour to *East23 PFW22*.

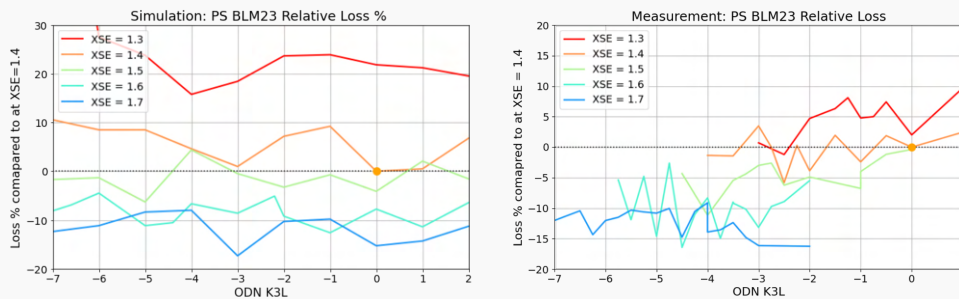
Figure C.12.: Sum of ring BLMs as a function of ODN strength comparing *East.T8.22* (solid line), *East.T8.23* (dashed line), corrected *East.T8.23* (dotted line), and *East.T8.22* cycle applied in 2023. Compared at nominal sextupole strength (orange) and increased sextupole strength (blue).



The rest of the MD is continued with the conventional *East.23* cycle. This investigation demonstrates how challenging it is to replicate the MD results of 2023 in simulations, as the k_3 component of all PFWs must change as a function of time throughout extraction. As the PS results were performed with Maptrack and MADX-PTC tracking, this type of dynamic simulation was not possible.

The closest simulation comparison made in 2023 is displayed in Fig. C.13 which is at the

Figure C.13.: BLM23 signal as a function of octupole strength in simulation (left) and measurement (right) as a function of sextupole strength (red = low, blue = high).



SEH23, only because it has no strong dependency on octupoles.

For future users of octupoles in the proton synchrotron, it is recommended each year to take a similar non-linear chromatic measurement and try with XSuite to reproduce this effect.

Steering Algorithm

The steering algorithms for septum loss reduction was performed in GeOFF (Generic Optimisation Framework) [146]. This was run via *acc-app-optimisation* with the *east_losses_optimiser* script written by E. JOHNSON. The algorithm applied was BOBYQA (Bound Optimization BY Quadratic Approximation) which works well for minima and maxima that have smooth functions and low variation.

When the optimiser was run, non-PPM variables such as septum angle or position could not be changed during a parallel MD slot, as it harms beam intensity going to East Area experiments.’ This means the steering algorithm is limited to parameters such as the extraction bumps to the electrostatic and magnetic septa (BSW23, BSW57) and the fields in the magnetic septa (SMH57, SMH61).

An initial range of 20% around the nominal values of these four parameters was applied. Should the true global minimum be beyond these values, the algorithm would tend towards their minimum or maximum constraints. As the algorithm did not contain any functions from the F61 extraction line, the optimiser could successfully minimise losses in the ring, but not gain increases in extracted intensity from the XSEC61 counter.

Bibliography

- [39] S. Y. Lee. *Accelerator physics; 3rd ed.* Singapore: World Scientific, 2012. URL: <https://cds.cern.ch/record/1425444>.
- [97] L. Deniau et al. “The MAD-X Program (Methodical Accelerator Design) User’s Reference Manual”. In: (Feb. 2022). URL: <https://madx.web.cern.ch/madx/releases/last-rel/madxguide.pdf>.
- [106] *NumPy v1.26 Manual* — [numpy.org](https://numpy.org/doc/stable/reference/generated/numpy.hanning.html). <https://numpy.org/doc/stable/reference/generated/numpy.hanning.html>. [Accessed 19-12-2023].
- [121] F. Asvesta H. Huttunen et al. “Optics design of a compact helium synchrotron for advanced cancer therapy ” (Nashville, USA, June 2024). presented at IPAC’24, Nashville, USA, June 2024, unpublished.
- [142] B. Gålnander et al. “Status of SIS100 slow extraction design including effects of measured magnetic field errors”. In: *Proc. IPAC’23* (Venice, Italy). International Particle Accelerator Conference 14. JACoW Publishing, Geneva, Switzerland, Sept. 2023, pp. 2443–2446. ISBN: 978-3-95-450231-8.

- [143] P Freyermuth. *Qmeter2 interface description: Accelerator Controls Wikis (BE/CSS)*. <https://wikis.cern.ch/display/ELENAOP/QMeter2+interface+description>. Apr. 2021.
- [144] J. Wenninger. *YASP Steering Program User Guide*. <https://jwenning.web.cern.ch/documents/YASP/YASP-user-guide.pdf>. 2005.
- [145] P Freyermuth et al. "CERN Proton Synchrotron working point Matrix for extended pole face winding powering scheme". In: (2010). URL: <https://cds.cern.ch/record/1287599>.
- [146] N. Madysa. *Generic Optimisation Frontend and Framework (GeOFF)*. <https://gitlab.cern.ch/geoff/geoff-app>.